Topics in early and late Universe cosmology

by

Supranta Sarma Boruah

A thesis
presented to the University of Waterloo
in fulfillment of the
thesis requirement for the degree of
Doctor of Philosophy
in
Applied Mathematics

Waterloo, Ontario, Canada, 2020

Examining Committee Membership

The following served on the Examining Committee for this thesis. The decision of the Examining Committee is by majority vote.

External Examiner:	Dragan Huterer Department of Physics, University of Michigan, Ann Arbor
Supervisor(s):	Ghazal Geshnizjani Michael J. Hudson
Internal Member:	Florian Girelli Achim Kempf
Internal-External Member:	Will Percival

Author's Declaration

This thesis consists of material all of which I authored or co-authored: see Statement of Contributions included in the thesis. This is a true copy of the thesis.

I understand that my thesis may be made electronically available to the public.

Statement of Contribution

I was the sole author for Chapters 1 and 7 which were written under the supervision of Ghazal Geshnizjani and Michael Hudson. This thesis consists in part of five manuscripts written for publication. Exceptions to sole authorship of material are as follows:

Research presented in Part I:

The research in part I is based on two published papers (Boruah et al., 2017; Boruah et al., 2018), that were written under the supervision of Ghazal Geshnizjani in collaboration with Hyunjin (Tony) Kim and Michael Rouben. The original project idea was conceptualized by Ghazal Geshnizjani. I did the original calculations presented in chapters 2 and 3, except the calculations and analysis presented in section 3.2, which was originally done by Ghazal Geshnizjani and I later reproduced these. I was the main author of the manuscripts with contributions from all co-authors.

Research presented in Part II:

The research presented in part II was done under the supervision of Michael Hudson and Guilhem Lavaux. The computational analysis presented in the both the chapters is my work. I was the main author of both manuscripts which had inputs from Michael Hudson and Guilhem Lavaux.

Chapter 4 is based on Boruah et al. (2019), which has been submitted to arXiv and the journal MNRAS. The probabilistic model used in the work was previously presented before in the literature. We extended the model to simultaneously fit for distance indicator data in this work.

Chapter 5 is based on a manuscript, which is currently being prepared for submission to MNRAS. The study was conceived by Michael Hudson, Ofer Lahav and Cullan Howlett. The study design was finalized in consultation with Michael Hudson and Guilhem Lavaux.

Research presented in Part III:

Chapter 6 is based on research done in collaboration with Ghazal Geshnizjani and Guilhem Lavaux. I conceptualized the original idea in consultation with Ghazal Geshnizjani and Guilhem Lavaux. I derived the probabilistic framework, designed the tests and applied it to the GW170817 data on my own under the supervision of Ghazal Geshnizjani and Guilhem Lavaux. I was the sole author of the chapter, with inputs from Ghazal Geshnizjani and Michael Hudson.

Abstract

In this thesis, we explore different problems in various areas of cosmology.

The inflationary paradigm has been very successful in explaining cosmological observations. However, some problems still linger on. In the first part of the thesis, we investigated the evolution of perturbations in an alternative bouncing scenario described by cuscuton gravity. We first derived the formulation describing the evolution of perturbation in cuscuton gravity. Then, using a toy model, we showed that unlike other bouncing scenarios, it is possible to have a regular bouncing scenario without catastrophic instabilities in cuscuton gravity.

In the second part of the thesis, we investigate the peculiar velocity field in the local Universe using observational data. We study two aspects of the local peculiar velocity field. First, by comparing the reconstructed velocity field with the observations, we constrained the cosmological parameter combination, $f\sigma_8$. We also compiled the largest peculiar velocity catalog based on low redshift Type Ia supernovae. Using an extended forward-likelihood method that self-consistently calibrates the distance indicator relationship, we find $f\sigma_8 = 0.400 \pm 0.017$. The peculiar velocity field in the local Universe is also useful for correcting redshifts of galaxies for measuring the Hubble constant and distances to galaxies. We compare some of the commonly-used peculiar velocity models of the local Universe. By comparing the various peculiar velocity models to additional peculiar velocity observations, we show that reconstruction-based velocity field performs better than kernel-smoothed peculiar velocity fields.

In the final part of the thesis, we describe a new statistical method of constraining H_0 standard sirens. Our method relies on using a reconstructed density field. Using a mock simulation, we show that our method gives an unbiased estimate of H_0. We also infer H_0 using this method for the GW170817 data.

Acknowledgements

This thesis would not have been possible without the help of others. Such a list by its nature would always be incomplete. I apologize beforehand if I miss anyone.

First and foremost, I would like to thank my supervisors, Ghazal Geshnizjani and Mike Hudson, for their patience and help throughout the course of my PhD. Even though Guilhem Lavaux is not my official supervisor, he has played a huge role in guiding me and helping me grow as a researcher. Writing this thesis would not have been possible without the guidance of Ghazal, Mike and Guillhem. I would also like to thank my collaborators and other researchers for stimulating discussions over the period of my PhD. This includes Tony Kim, Niayesh Afshordi, Tianyi Yang, Tom Charnock, Jens Jasche, Fabian Schmidt, Doogesh Kodi Ramanah, Cliff Burgess and Lukas Graf.

Before joining Waterloo, my educational journey began in my hometown, Jorhat and took me to Guwahati, where I finished my high school and to Kanpur, where I finished my undergraduate. And along the way, it was with the help of many teachers and friends that I was able to understand what science really means. I would like to thank the numerous teachers and friends who contributed to my education over this period.

Moving to a different country on the opposite side of the globe is never easy and would have been extremely difficult without the support of friends and family members back home and here in Canada. I would like to thank: Siddhartha da and Ponchi ba for helping me out when I first moved here. Tim, Tony, Juan, Keegan, Rishi (and others) for the soccer we played together. Rath, Somani, Chandra and Sahu, for keeping me sane with the weekend conversations. Deeksha, Nitica and Soham, for being the most reliable friends here in Canada. Alankrita for being the perfect companion in every way and for always having my back. And finally and most importantly, thanks to my family for always believing in me. Thank you Ma and Deuta for always supporting me in my decisions and helping me follow my own path.

I thank Dom Pesce and Jim Braatz for providing the distance measurement samples from the Megamaser Cosmology Project (MCP).

I would also like to thank the numerous administrative staff members who have worked hard behind the scenes to ensure smooth running of the University. I thank MITACS for the MITACS Globalink award, which enabled my research visit to Institut d'Astrophysique de Paris (IAP) in the Fall of 2018. I acknowledge the support of the Natural Sciences and Engineering Research Council of Canada (NSERC) for my research during my PhD program. Work presented in this thesis has made use of the Horizon cluster hosted by the

IAP. This research was enabled in part by the computing support provided by Compute Ontario[1] and Compute Canada[2].

[1] https://computeontario.ca/
[2] https://www.computecanada.ca/

Dedicated to Ma and Deuta.

Table of Contents

List of Figures

List of Tables

Chapter 1

Introduction

Over the last century, research in cosmology has advanced through a striking synergy between theory, simulations and observations. We are living in an interesting time for cosmology. Developments in observations over the last few decades has led to the establishment of the ΛCDM cosmological model as the standard model of cosmology. The inflationary paradigm, originally proposed to solve some classic problems of the standard Big Bang model, has succeeded in describing the initial seed perturbations in the Universe from which the observed structures form. Despite the successes of the ΛCDM + the inflationary paradigm, some issues still remain. Currently, multiple observations are hinting at a tension in the measurement of some of the cosmological parameters from different observations. On the theoretical front, model building for inflation is not solid and suffers from various issues.

In this thesis, we explore a variety of different questions in theoretical and observational cosmology. In order to lay the foundation for these topics, in this chapter, we review the essential cosmological background. In section 1.1 we introduce the equations for describing the homogeneous and isotropic Universe without any perturbations. Section 1.2 reviews the theory of inflation along with its current status as constrained by observations. The theoretical understanding of the formation of the large-scale structure of the Universe is reviewed in section 1.3. We then review the cosmological observations in section 1.4. In Section 1.5, we give a more extensive background on the theory and observations of direct probes of peculiar velocity, which form the basis for part II.

1.1 Background Cosmology

One of the first mathematical solutions to Einstein's equations that was found was that of an uniformly expanding Universe. The so-called, Friedmann-Lemaitre-Robertson-Waker (FLRW) metric can be used to described the evolution of the expanding isotropic and homogeneous Universe. The FLRW metric is given as,

$$\mathrm{d}s^2 = -\mathrm{d}t^2 + a^2(t)\left[\frac{\mathrm{d}r^2}{1-\kappa r^2} + r^2\mathrm{d}\Omega^2\right], \tag{1.1}$$

where, $a(t)$ is the scale factor, $\mathrm{d}\Omega$ denotes the angular element in the metric. κ is the spatial curvature with dimensions $(\text{length})^{-2}$, denoting the length scale over which curvature is important. If κ is positive, the Universe is close, while it is open for negative κ. A flat Universe has $\kappa = 0$. The dynamics of the scale factor is described by the Einstein's equations. The time-time part of the Einstein's equations gives the *Friedmann equation*,

$$H^2 = \frac{8\pi G}{3}\rho_{\mathrm{tot}} - \frac{\kappa c^2}{a^2} \tag{1.2}$$

where, $H = \dot{a}/a$, is the Hubble parameter and κ is the curvature of the spatial slice. Here, the dot denotes the partial time derivative. ρ_{tot} is the total energy density of the fluids in the Universe. The evolution of the Hubble parameter is governed by another combination of the Einstein's equation, which gives,

$$\dot{H} + H^2 = -\frac{4\pi G}{3}\left(\rho_{\mathrm{tot}} + \frac{3p_{\mathrm{tot}}}{c^2}\right), \tag{1.3}$$

p_{tot} being the pressure of the fluid. There are different type of fluids that contribute to the stress-energy tensor of the Universe so that, $\rho_{\mathrm{tot}} = \sum_i \rho_i$ and $p_{\mathrm{tot}} = \sum_i p_i$. Usually, each is parameterized by a single equation-of-state parameter, w, which describes the relation between the pressure and the density of the fluid as,

$$\frac{p_i}{c^2} = w\rho_i. \tag{1.4}$$

The main types of cosmological fluids are: *i)* non-relativistic matter, which has $w = 0$. *ii)* Radiation, with $w = 1/3$. *iii)* Cosmological constant, with negative pressure, $w = -1$. From the conservation of the stress energy tensor, one obtains the equation for evolution of the density of a fluid,

$$\dot{\rho}_i = -3H\left[\rho_i + \frac{p_i}{c^2}\right]. \tag{1.5}$$

Using equation (1.4), we can then solve for the density as a function of the scale factor, $\rho(a) \propto a^{-3(1+w)}$. Therefore, the density of radiation, ρ_r, decays rapidly with the expansion of the Universe, $\rho_r \propto a^{-4}$. The cosmological constant gives a constant density independent of the scale factor, $\rho_\Lambda = C$. And finally, the density field evolution of non-relativistic matter is given as, $\rho_m \propto a^{-3}$.

It is often convenient to define the density terms in the Friedmann equation as a fraction of the critical density. The critical density is defined as,

$$\rho_c = \frac{3H^2}{8\pi G}. \tag{1.6}$$

In a spatially flat Universe, $\kappa = 0$, the density of the Universe is equal to the critical density. The density parameters are defined as the fraction of the critical density, $\Omega_i = \rho_i/\rho_c$.

Expressing the Friedmann equation in terms of Ω and using the scale factor dependence of the densities, we get,

$$H^2(a) = H_0^2\left[\Omega_{\Lambda,0} + \frac{\Omega_{m,0}}{a^3} + \frac{\Omega_{r,0}}{a^4} + \frac{\Omega_{K,0}}{a^2}\right]. \tag{1.7}$$

Here, the subscript, '0' signifies that these quantities are measured in the present day.

1.2 Inflation

The theory of inflation in the early Universe has been very successful in explaining some of the cosmological observations. In this section, we will review the basic theory, observational constraints and the successes and the shortcomings of the theory of inflation.

1.2.1 Puzzles of the standard Big Bang model - circa 1980

The beginning of the Universe in a hot, dense state was accepted as the standard paradigm of the Universe following the discovery of CMB by Penzias & Wilson (1965). However, under the standard Big Bang picture, a few observations seemed to require extreme fine-tuning of the initial conditions which puzzled cosmologists. We review two such problems - the horizon problem and the flatness problem.

The Horizon problem

The particle horizon is defined as the biggest region with which a particle could be in causal contact. In an FRW Universe, this is given as,

$$r_{\rm hor}(t) = ca(t) \int_0^t \frac{dt'}{a(t')}. \tag{1.8}$$

Note that the scale factor in the front is used to convert the comoving scale to physical scale. Using this formula to calculate the particle horizon for a cosmological model with $\Omega_m = 0.3$, we get that the particle horizon scale subtends an angle of 1.16° on the CMB sky (Baumann, 2011). Hence, the CMB sky consists of ~ 20000 such patches which appear to be causally disconnected. However, the temperature of the CMB is observed to be isotropic across the whole sky at 10^{-5} level. Without a causal mechanism, explaining this isotropy requires a homogeneous initial conditions over causally disconnected patches of spacetime.

Flatness problem

From the Friedmann equation (1.7), we see that the spatial curvature term, $\Omega_{K,0}a^{-2}$, dilutes more slowly than the matter term, $\Omega_{m,0}a^{-3}$. Under the standard big bang picture, the curvature term should dominate at late times unless the initial conditions somehow are fine-tuned. For example, at the Higgs scale, the scale factor was $a_{\rm Higgs} \sim 10^{-13}$. Therefore, assuming a present day spatial curvature of $\Omega_K \lesssim \mathcal{O}(1)$, we get that the initial curvature of the Universe at the Higgs scale must be, $\Omega_K \lesssim 10^{-26}$. Hence, it requires a fine-tuning of the initial spatial curvature of the Universe.

Inflation as a solution to the Horizon and Flatness problem

In early 1980's, a number of independent researchers (Guth, 1981; Sato, 1981; Linde, 1982; Starobinsky, 1982) proposed inflation as a mechanism to solve the horizon and flatness (and other) problems in a causal way. Inflation refers to the exponentially fast expansion of the Universe right after the Universe began in a Big Bang. During inflation, the spacetime metric of the Universe can be described by an almost de Sitter spacetime, where $a(t) = \exp(H_{\rm inf}t)$. With this metric, the horizon scale is given as,

$$r_{\rm hor} \approx \frac{ce^N}{H_{\rm inf}}, \tag{1.9}$$

where N is the number of e-folds of inflation, and $H_{\rm inf}$ is the Hubble constant during inflation. Without inflation, the particle horizon in the FLRW Universe is of the order of the Hubble radius, c/H. However, for 40-60 e-folds of inflation, the particle horizon is much larger than the Hubble radius, thus solving the horizon problem. Moreover, because the inflaton energy density behaves like an effective cosmological constant and scale factor grows exponentially, the curvature fraction becomes negligible compared to the inflaton fraction, thus, solving the flatness problem.

1.2.2 Background evolution in Inflation - Slow roll Inflation

Consider the background evolution of the Universe in the presence of a scalar field, ϕ, with a potential, $V(\phi)$. The dynamics of the background is governed by the Friedmann equation and the Klein-Gordon equation in the expanding FLRW background,

$$3H^2 = \frac{1}{M_{\rm pl}^2}\left[\frac{1}{2}\dot{\phi}^2 + V(\phi)\right], \tag{1.10}$$

$$\ddot{\phi} + 3H\phi = -V'(\phi). \tag{1.11}$$

The slow-roll parameter for inflation is defined as,

$$\epsilon = -\frac{\dot{H}}{H^2} = \frac{\frac{1}{2}\dot{\phi}^2}{M_{\rm pl}^2 H^2} = 3\frac{\frac{1}{2}\dot{\phi}^2}{\frac{1}{2}\dot{\phi}^2 + V(\phi)}. \tag{1.12}$$

Hence, if the kinetic energy of the scalar field is much smaller than the potential energy, the Universe expands in an almost de Sitter ($\dot{H} \approx 0$) phase expansion. Thus, an inflationary solution is realised if $\epsilon \ll 1$. Therefore, a scalar field 'slowly rolling' down a potential can drive the dynamics of the inflationary Universe.

In order to sufficiently explain the isotropy of the CMB, one needs 50-60 e-folds of inflation. In order to have sufficiently long inflationary period, one also requires the derivative of the slow-roll parameter to be small. This motivates the definition of a second slow-roll parameter,

$$\eta = \frac{\dot{\epsilon}}{H\epsilon}. \tag{1.13}$$

1.2.3 Perturbations from Inflation

While inflation was initially proposed to solve the horizon and the flatness problem, it was realized that inflation also provides a causal mechanism to generate the initial perturbations from which structures formed in the late times. In particular, it was realized that quantum fluctuations in an expanding inflationary Universe could provide the mechanism to generate these initial fluctuations. One can calculate the spectrum of perturbations using the framework of quantum field theory on curved spacetime[1]. It is convenient to calculate the spectrum in the co-moving gauge (Maldacena, 2003). For single-field models, in the co-moving gauge, the scalar perturbation is captured entirely by the perturbation in the spatial curvature, ζ. Quantum fluctuations also excite tensor modes in the metric, denoted as γ_{ij}, which can lead to unique observational signatures from inflation. Note that, by definition, the tensor mode, is transverse ($\nabla_i \gamma^{ij} = 0$) and traceless ($\gamma^i_i = 0$). The perturbed spatial metric in this gauge can be expressed as,

$$h_{ij} = a^2[(1 - 2\zeta)\delta_{ij} + \gamma_{ij}] \tag{1.14}$$

In order to investigate the dynamics of the perturbations, one can calculate the second-order action for ζ and γ_{ij}. This gives us (Maldacena, 2003),

$$S^{(2)}_{\text{scalar}} = \int dt d^3x a^3 \frac{\dot{\phi}_0^2}{H^2}\left[\dot{\zeta}^2 - \frac{1}{a^2}\partial^i\zeta\partial_j\zeta\right] \tag{1.15}$$

$$S^{(2)}_{\text{tensor}} = \int dt d^3x a^3 \left[\dot{\gamma}_{ij}^2 - \frac{1}{a^2}(\partial\gamma_{ij})^2\right] \tag{1.16}$$

where, ϕ_0 is the background field. In order to calculate the quantum effects, it is convenient to use the canonically normalized *Mukhanov-Sasaki* variable instead of ζ,

$$v = a\frac{\dot{\phi}_0}{H}\zeta, \tag{1.17}$$

Quantizing the variable v, with a choice of the Bunch-Davies vacuum, one can calculate the spectrum of these perturbations. It can be shown that ζ is conserved on super-Hubble scale ($k < aH$). Since ζ freezes after crossing the Hubble radius, the evolution of the Hubble radius is imprinted on the spectrum of perturbations. During inflation, the Hubble parameter is almost constant, but is slowly decreasing, this leads to an almost scale-invariant spectrum of perturbations with a slight red tilt. The red tilt implies that there is more

[1] See Mukhanov & Winitzki (2007a) for a review.

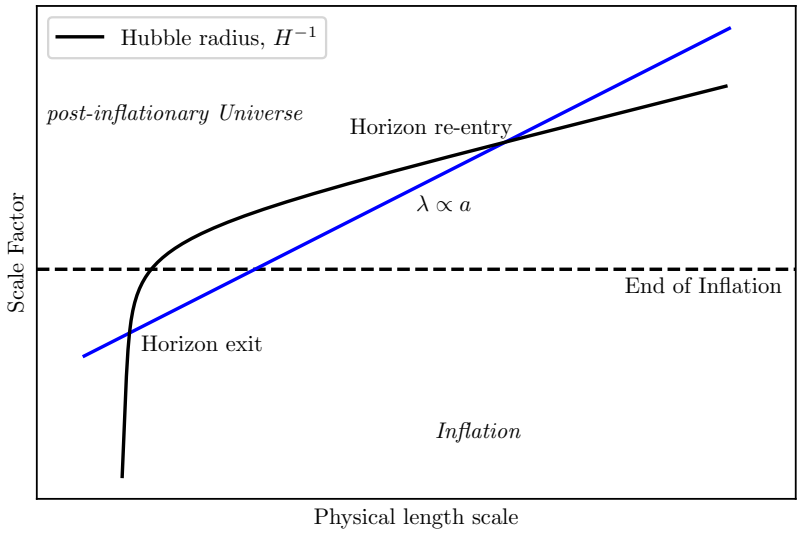

Figure 1.1: Illustration of the evolution of the Hubble radius (denoted in black) and a wave mode (denoted in blue) during inflation. The vertical axis shows the scale factor, and therefore denotes a direction of time. The physical scale of the co-moving wave modes is proportional to the scale factor. The Hubble radius is almost constant during inflation. Therefore, the wave modes, with a physical scale of $\lambda \propto a$ exits the horizon. After the end of inflation, during radiation domination, the Hubble radius grows as, $H^{-1} \propto a^2$, which is faster than the growth of the wave modes. Therefore, the frozen wave modes 're-enter' the horizon and start to evolve again.

power on the large scales compared to small scales. The conserved super-horizon perturbations start evolving on their 're-entry' into the Hubble horizon, leaving an imprint on observables such as the CMB temperature anisotropies and large-scale structure perturbations. An illustration of the exit and the re-entry of modes during and after inflation is shown in Figure 1.1.

Furthermore, one can also show that single-field inflation only excites adiabatic perturbations. In the presence of multiple fields, there are entropy perturbation between different components. Thus, detection of entropy/isocurvature perturbations can provide strong constraints on multi-field inflation.

1.2.4 Observational constraints

At present, CMB anisotropies provide the strongest observational constraints on inflation. In particular, the current CMB temperature and polarization anisotropy power spectrum allows us to constrain three main observational quantity: *i)* The amplitude of fluctuations, which is quantified by the power spectrum of ζ, *ii)* the tilt of the power spectrum, n_s, and *iii)* the tensor-to-scalar ratio, r. These quantities can be related to the slow role parameters, ϵ and η as below,

$$\Delta_\zeta = \frac{1}{8\pi^2}\frac{H^2}{\epsilon} \tag{1.18}$$

$$n_s - 1 = -2\epsilon - \eta, \tag{1.19}$$

$$r = 16\epsilon. \tag{1.20}$$

Slow-roll to observations

For a simple slow-roll inflation, the inflationary slow-roll parameters can be approximated in terms of the potential slow-roll parameters, $\epsilon_{\mathbf{v}} \approx \epsilon$ and $\eta_{\mathbf{v}} \approx \eta + \epsilon_{\mathbf{v}}$. The potential slow-roll parameters are related to the potential as below.

$$\epsilon_{\mathbf{v}} = \frac{M_{\rm pl}^2}{2}\left(\frac{V'}{V}\right)^2 \tag{1.21}$$

$$\eta_{\mathbf{v}} = M_{\rm pl}^2\left(\frac{V''}{V}\right)^2 \tag{1.22}$$

Finally, the Lyth bound suggest that for slow-roll inflation,

$$\frac{\Delta\phi}{M_{\rm pl}} \sim \left(\frac{r}{0.01}\right)^{1/2}, \tag{1.23}$$

where, $\Delta\phi$ denotes the change in the value of ϕ during inflation. The constant of proportionality is $\mathcal{O}(1)$ for a few decades of e-folding. Therefore, slow roll inflation where the field rolls down a large (Planckian) value, the tensor-to-scalar ratio is predicted to be high. One can also use Equations (1.19) and (1.20) to relate the parameter, η in terms of the observables. Doing this, we get,

$$\eta = 1 - n_s - 2\epsilon. \tag{1.24}$$

Constraints from observations

Observations from experiments such as WMAP and Planck give tight constraints on the initial fluctuations that seeded the CMB anisotropies. The constraints on the parameters, n_s and r from the Planck satellite CMB results are shown in Figure 1.2. Below, we summarize the main findings of the current observational constraints and their implication for simple slow-roll inflation.

i) *Scale invariance*: The power spectrum measured by Planck is almost scale invariant with a slight red tilt. The tilt of the scalar power spectrum is measured to be, $n_s = 0.9649 \pm 0.0042$ (Planck Collaboration, 2018b). Note that an almost scale invariant spectrum with a slight red tilt is a generic prediction of the inflationary paradigm.

ii) *Amplitude of fluctuations*: From the CMB temperature anisotropies as measured by Planck, the amplitude of scalar fluctuations are constrained to, $A_{\rm s} = \Delta_\zeta = (2.099 \pm 0.029) \times 10^{-9}$, where, $A_{\rm s}$ is the amplitude of the curvature power spectrum.

iii) *Gaussianity*: No non-Gaussianity has been detected in the CMB so far. Models of inflation with multiple fields or driven by the kinetic terms can produce high non-Gaussianity. Constraints on local $f_{\rm NL}$ can be used to already tightly constrain models of multi-field inflation. Observations also put some constraints on the parameters of DBI inflationary model (Silverstein & Tong, 2004), which is an inflationary model driven by the kinetic term and has a small speed of sound, c_s. With the Planck data, the speed of sound for DBI inflation is constrained to $c_s > 0.086$ (Planck Collaboration, 2019).

iv) Adiabatic fluctuations: Detection of isocurvature perturbations can provide crucial clues for multi-field inflation. The inflationary models with non-negligible isocurvature contribution, known as curvaton models are currently disfavored by the Planck data at high significance (Planck Collaboration, 2018b).

v) Tensor modes: Inflation generically predicts a background of primordial gravitational waves. The predicted value of r is high for large-field models (from the Lyth bound). Therefore, non-detection of tensor modes in the current CMB data prefers the small field models of inflation.

It is worth noting that the current constraints are consistent with some of the main predictions of simple inflationary models. For example, the prediction of a scale-invariant power spectrum with a slight red tilt is a generic model-independent prediction of inflation. Other predictions are slightly model dependent, thus allowing for the Planck data to constrain different models[2]. For single field models considered here, the Planck data prefers small field models with a concave potential. Simple power law models, such as the ϕ^2 and the ϕ^4 potentials are ruled out at high significance.

1.2.5 Problems with Inflation

As we saw in the previous section, the Planck data is consistent with the predictions of some inflationary model. In this section, we review some of the commonly noted problems with the inflationary models.

i) Initial conditions for the inflaton: As we saw in the previous section, the Planck data prefers small-field inflationary models. An appealing property of large field inflationary models is that there usually exists an attractor solution which generically result in an inflationary solution. However, the situation is not the same for small-field models. Generically, getting an inflationary solution with the required e-foldings of sufficiently slow-roll requires fine tuning in the initial conditions of the inflaton. This has led to claims that generically, the inflationary models which are currently allowed by the data require fine-tuning of the initial conditions.

ii) Homogeneity of the initial conditions: While inflation smooths the inhomogeneities once it starts, it has also been argued (Ijjas et al., 2013) that starting inflation

[2]See Martin et al. (2014) for an extensive Bayesian model comparison of several inflationary models with the Planck data.

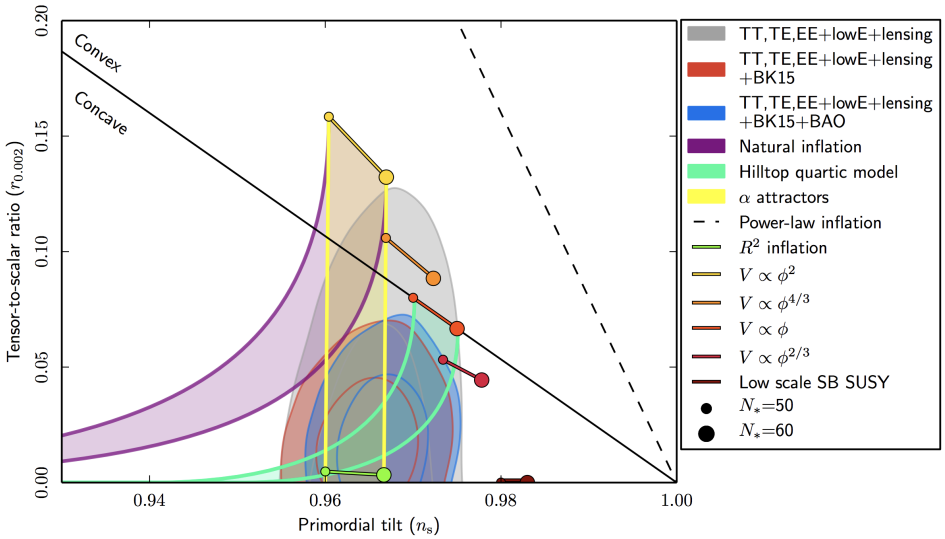

Figure 1.2: Constraints on inflation from the Planck satellite. As can be seen, the current data prefers concave potential for slow-roll inflation. Figure taken from Planck Collaboration (2018b).

requires homogeneity over a large patch of the Universe, thus requiring fine-tuned homogeneous initial conditions. This is a problem in the small-field inflationary models. However, using full numerical relativity simulations, it was shown that, at least for some inhomogeneous initial conditions, inflation indeed arises in a small field model (East et al., 2016).

iii) *Singularity*: It has been shown that inflationary spacetimes are incomplete in the past direction (Borde et al., 2003). While this is not a fundamental problem given the existence of other singularities such as black holes in nature, it indicates that studying the initial conditions of inflation would necessarily require physics beyond what is usually used in the study of inflation.

iv) *Trans-Planckian problem*: The study of inflation in certain models of inflation require invoking predictions at super-Planckian regime. That leads to the question: whether quantum field theory on curved spacetime, the framework within which inflation is typically studied, is a valid framework in the study of inflation (Martin & Brandenberger, 2001). This is what is usually called the *Trans-Planckian problem*. The Trans-Planckian problem mainly affects the large field models.

v) *Eternal inflation*: In general, inflation progresses through the scalar field rolling down

the potential, ending with the phase of reheating. In the classical picture, the scalar field always rolls down the potential. However, due to quantum fluctuations, the field may take occasional steps higher up the potential. Thus, if the quantum evolution dominates over the classical evolution, it leads to the inflationary phase not ending, thus resulting in 'eternal inflation' (Guth, 2007). Most inflationary models generically predict such scenarios (Gibbons et al., 1983; Vilenkin, 1983). This leads to a multiverse, where there are pockets where inflation ends. However, different patches will have different properties and these cannot be well predicted due to the 'infinite' nature of the inflationary Universe. This is known as the *measure problem*. Hence, in eternal inflation, it is hard to predict what are the 'generic predictions' of the theory, thus ruining the predictability of the inflationary theory.

1.3 Large-scale structure: theory

As we saw in section 1.2, there is strong evidence that quantum fluctuations in the early Universe seeded small perturbations in the density/potential field. We need a framework to describe the evolution of these perturbations in the late Universe when quantum effects are no longer important. Describing perturbations on the scale of the horizon necessarily requires General Relativity. However, on sub-horizon scales, one can simply use Newtonian physics on an expanding background to describe the evolution of these perturbations. In particular, one can use the equations of hydrodynamics to describe the evolution of these perturbations. The fluid dynamics description is valid as long as the mean free path of the described object is much smaller than the scales of our interest. This turns out to be the case for the various kinds of cosmological fluids.

1.3.1 Newtonian Cosmological Perturbation Theory

The properties of a fluid are described in terms of its density, pressure, velocity, etc. One can track the evolution of these properties by either following these properties in a fixed point in space, or by following the fluid packet as it evolves. The former approach is known as the *Eulerian* description, and the latter as the *Lagrangian* description of fluid mechanics. In this subsection, we will describe the Eulerian approach. We will elaborate on the Lagrangian approach in section 1.3.2. The discussion in this section is inspired from Mo et al. (2010).

The starting points for the fluid description of the cosmological fluid are the continuity and Euler equations for fluid mechanics which are based on conservation of mass and

momentum. We can also capture the effect of gravity on the fluid using the Poisson equation.

$$\frac{\partial \rho}{\partial t} + \nabla \cdot (\rho \boldsymbol{u}) = 0\,, \tag{1.25}$$

$$\frac{\partial \boldsymbol{u}}{\partial t} + (\boldsymbol{u} \cdot \nabla)\boldsymbol{u} = -\frac{\nabla P}{\rho} - \nabla \phi\,, \tag{1.26}$$

$$\nabla^2 \phi = 4\pi G \rho\,, \tag{1.27}$$

These equations describe a fluid under the influence of gravitational and pressure forces. The Newtonian description is valid as long as we focus on scales much smaller than the Hubble radius. However, we have to take into account the expansion of the Universe. In this section, we make a distinction between the 'physical' coordinates, $\boldsymbol{r}$, and the co-moving coordinates, $\boldsymbol{x}$. The equations, (1.25) - (1.27) still correctly describe the fluid evolution in the physical coordinates. The physical and the co-moving coordinates are related as,

$$\boldsymbol{r} = a(t)\boldsymbol{x}. \tag{1.28}$$

We make a distinction between the derivative with respect to the physical coordinates and with respect to the co-moving coordinates. Using chain rule, we can relate these as follows,

$$\left.\frac{\partial}{\partial \boldsymbol{r}}\right|_{\text{fixed } t} = \frac{1}{a(t)} \left.\frac{\partial}{\partial \boldsymbol{x}}\right|_{\text{fixed } t}, \tag{1.29}$$

$$\left.\frac{\partial}{\partial t}\right|_{\text{fixed } \boldsymbol{r}} = \left.\frac{\partial}{\partial t}\right|_{\text{fixed } \boldsymbol{x}} - \frac{\dot{a}}{a}\boldsymbol{x} \cdot \frac{\partial}{\partial \boldsymbol{x}}. \tag{1.30}$$

We drop the suffixes in what follows. The continuity equation in an expanding background expressed in the co-moving coordinates can be therefore expressed as,

$$\frac{\partial \rho}{\partial t} + 3\frac{\dot{a}}{a}\rho + \frac{1}{a}\nabla_{\boldsymbol{x}} \cdot (\rho \boldsymbol{v}) = 0, \tag{1.31}$$

The basic quantity used for describing the perturbations in the density field is the over-density, δ, which is defined as,

$$\rho(\boldsymbol{x}, t) = \bar{\rho}(t)[1 + \delta(\boldsymbol{x}, t)], \tag{1.32}$$

where, $\bar{\rho}(t)$ is the mean density of the Universe. Often, we define the overdensity for each different species of matter, such as matter, radiation or baryon, in the same way,

but for overdensity in the given species. After using stress-energy conservation for the homogeneous fluid, we can rewrite equation (1.31) to express the evolution equation for δ,

$$\frac{\partial \delta}{\partial t} + \frac{1}{a}\nabla_{\boldsymbol{x}} \cdot [(1+\delta)\boldsymbol{v}] = 0. \tag{1.33}$$

The velocity of the fluid in the physical coordinates can be expressed as,

$$\boldsymbol{u} = \dot{a}\boldsymbol{x} + \boldsymbol{v}. \tag{1.34}$$

The first term in the above expression is the velocity due to Hubble expansion and the second term is the peculiar velocity. Expressing the Euler equation in terms of the peculiar velocity, we obtain,

$$\frac{\partial \boldsymbol{v}}{\partial t} + \frac{\dot{a}}{a}\boldsymbol{v} + \frac{1}{a}(\boldsymbol{v}\cdot\nabla)\boldsymbol{v} = -\frac{\nabla\Phi}{a} - \frac{\nabla P}{a\bar{\rho}(1+\delta)}, \tag{1.35}$$

where, Φ is the perturbed gravitational potential. Modelling the fluid component as an ideal monoatomic gas, the pressure forces on the acting on the fluid can be expressed as,

$$\frac{\nabla P}{\bar{\rho}} = c_{\rm s}^2 \nabla\delta + \frac{2}{3}(1+\delta)T\nabla S, \tag{1.36}$$

where, $c_{\rm s}$ is the adiabatic sound speed, S is the entropy, and T is the temperature of the fluid. Finally, restricting only to the linear orders in perturbations (i.e., to linear order in δ and $\boldsymbol{v}$), we obtain,

$$\frac{\partial \delta}{\partial t} + \frac{1}{a}\nabla\cdot\boldsymbol{v} = 0, \tag{1.37}$$

$$\frac{\partial \boldsymbol{v}}{\partial t} + \frac{\dot{a}}{a}\boldsymbol{v} = -\frac{1}{a}\left[\nabla\Phi + c_{\rm s}^2\nabla\delta + \frac{2}{3}T\nabla S\right]. \tag{1.38}$$

The perturbed Poisson equation yields,

$$\nabla^2\Phi = 4\pi G\bar{\rho}a^2\delta. \tag{1.39}$$

Adiabatic vs Isocurvature initial conditions

As discussed in section 1.2, in a single-field inflation, only adiabatic fluctuations are activated. There is also a tight observational constraint on the adiabaticity of the initial conditions. For example, Planck constrains the deviation from adiabatic fluctuations at $\lesssim$ 2% (Planck Collaboration, 2018b). Adiabatic initial condition imply, $\nabla S = 0$. Therefore, for the rest of the section, we restrict to adiabatic fluctuations and set $\nabla S = 0$.

Decay of vorticity

A crucial insight that can be gleaned from equation (1.38) is that on large scales, the vorticity of the velocity field decays. In order to see this, we can apply the curl operator on both sides of equation (1.38). Since the curl of a gradient is zero, the right hand side of the equation vanishes and we get,

$$\begin{aligned} \frac{\partial[\nabla \times \boldsymbol{v}]}{\partial t} + \frac{\dot{a}}{a}[\nabla \times \boldsymbol{v}] = 0 \\ \implies \nabla \times \boldsymbol{v} \propto a^{-1}. \end{aligned} \tag{1.40}$$

The decay of the vorticity is a consequence of conservation of angular momentum in an expanding Universe. In linear theory, therefore, the peculiar velocity field can be modelled as a potential flow. The lack of a rotational part along with equation (1.37) results in a Poisson-like equation for the velocity potential. Solving for it, we therefore get that the velocity field is proportional to the acceleration. The integral solution for the velocity, thus obtained gives (Peebles, 1993),

$$\boldsymbol{v}(\boldsymbol{x}) = \frac{afH}{4\pi} \int \mathrm{d}^3\boldsymbol{x}' \delta(\boldsymbol{x}') \frac{\boldsymbol{x}' - \boldsymbol{x}}{|\boldsymbol{x}' - \boldsymbol{x}|^3}\,, \tag{1.41}$$

where, $f = \frac{d \ln D}{d \ln a}$ is the growth function. We will elaborate on the growth function shortly.

Jeans Instability

The physics describing the evolution of perturbations on sub-horizon scales can be intuitively understood as a competition between pressure and gravitational forces. The over-dense regions in the initial perturbations attract matter from nearby regions because of gravity, resulting in the growth of these perturbations. On the other hand, excess pressure in over-dense regions have the opposite effect, i.e., because of the random motion, matter flows outward from dense regions. This competition between gravity and pressure determines the growth of structure on the sub-horizon scale.

Taking another time derivative of equation (1.37) and replacing the $\partial \boldsymbol{v}/\partial t$ term using equation (1.38), we obtain (after assuming adiabatic initial conditions) a second order differential equation. This can be written as,

$$\frac{\partial^2 \delta}{\partial t^2} + 2H\frac{\partial \delta}{\partial t} = \left[\nabla^2\Phi + \frac{c_s^2}{a^2}\nabla^2\delta\right]. \tag{1.42}$$

To connect this equation with the physical intuition of competition between the gravitational and pressure forces, note that the first term on the right hand side denotes the gravitational force and the second term is the pressure force. It is convenient to rewrite the equation in Fourier space. The overdensity field can be expressed in terms of the Fourier wave mode, $\delta_{\boldsymbol{k}}$, as,

$$\delta(\boldsymbol{x}, t) = \sum_{\boldsymbol{k}} \delta_{\boldsymbol{k}}(t) \exp(i\boldsymbol{k} \cdot \boldsymbol{x}). \tag{1.43}$$

Note that there are other conventions that may be used for the Fourier transform. The corresponding inverse transform may be expressed as,

$$\delta_{\boldsymbol{k}}(t) = \frac{1}{V} \int d^3\boldsymbol{x}\ \delta(\boldsymbol{x}, t) \exp(-i\boldsymbol{k} \cdot \boldsymbol{x}), \tag{1.44}$$

where, V is the volume of the region were the density field is assumed to be periodic.

Any linear differential equation yields a linear algebraic equation in the Fourier space. This means that different wave modes evolve independently. Therefore, when we use linear perturbation theory, the evolution of different wave modes are independent of one another. The fact that different wave modes do not mix is another reason why using the Fourier space density is useful.

Writing equation (1.42) in the Fourier space and using the Poisson equation, we get,

$$\ddot{\delta}_{\boldsymbol{k}} + 2H\dot{\delta}_{\boldsymbol{k}} + \left[4\pi G\bar{\rho} - \frac{c_s^2}{a^2}k^2\right]\delta_{\boldsymbol{k}} = 0. \tag{1.45}$$

Note that the above equation is a damped harmonic oscillator. Defining, $\omega^2 = k^2 - k_J^2$, where,

$$k_J = \frac{2a\sqrt{\pi G\bar{\rho}}}{c_s}. \tag{1.46}$$

we get,

$$\ddot{\delta}_{\boldsymbol{k}} + 2H\dot{\delta}_{\boldsymbol{k}} - \omega^2\frac{c_s^2}{a^2}\delta_{\boldsymbol{k}} = 0. \tag{1.47}$$

For such a damped harmonic oscillator system, the qualitative solution depends on the sign of ω^2:

- Case I: $\omega^2 > 0$ or $k > k_J$

  In this case, we have a oscillating solution to the damped harmonic oscillator solution. However, because of the damping term, the amplitude of oscillations decays with time. This is the case for modes with wavelength smaller than the Jeans length, $\lambda_J = 2\pi/k_J$.

- Case II: $\omega^2 < 0$ or $k < k_J$

  In this case, there is a growing and a decaying solution. However, since the growing solution dominates at late times, for a generic initial condition, only the growing solution is important. This is the case for wave modes larger than the Jeans length.

This reflects our intuition for the competition between gravitational and pressure forces. At small scales (smaller than the Jeans length), the random motion of the particles and therefore the pressure forces dominate over the gravitational forces. However, on scales larger than the Jeans length, the gravitational forces dominate and can induce an instability, resulting in formation of these structures.

The second term in equation (1.47) is often called the 'Hubble drag'. The expansion of the Universe induces a friction term in the evolution of the density and slows down the growth of structure. Therefore, faster the expansion of the Universe, slower the growth of structures. Some of the cosmological observations rely partly on this fact to constrain cosmological parameters. We will discuss this further in section 1.4.

Evolution in different era

We have established that structures grow through gravitational instability on large scales. Let us now look at the evolution of the density perturbations through different eras in the Universe.

Radiation domination:

The density perturbations that enter the Hubble horizon during the radiation domination do not grow as fast as the modes that enter the horizon during matter domination. This leads to a characteristic break in the shape of the power spectrum.

Matter domination:

Once the Universe enters the matter-dominated phase, the speed of sound quickly drops to 0. Therefore, the evolution equation becomes,

$$\ddot{\delta}_{\boldsymbol{k}} + 2H\dot{\delta}_{\boldsymbol{k}} + \frac{3H^2\Omega_m}{2}\delta_{\boldsymbol{k}} = 0. \tag{1.48}$$

We used the Friedmann equation to rewrite the third term in the equation. Note that this equation is valid as long as $c_s \approx 0$, or $k < k_J$. Therefore, this equation is valid for both matter domination as well as Λ-dominated Universe. Using the Friedmann equations, one can show that, for a matter dominated Universe, $a(t) \propto t^{2/3}$ and $H(t) = 2/(3t)$. Plugging

these values into equation (1.48), we obtain two solutions, $\delta_+(t) \propto a(t)$ and $\delta_-(t) \propto t^{-1}$. The first solution grows with time while the second solution decays with time. Therefore, for any generic initial conditions, in the late times, the growing solution will dominate.

Dark energy domination:

If the Universe is dominated by the cosmological constant, the Hubble constant freezes to a constant value. The third term in equation (1.48) vanishes as $\Omega_m = 0$. Therefore, the equation for evolution of the density perturbations is,

$$\ddot{\delta}_{\boldsymbol{k}} + 2H_0\dot{\delta}_{\boldsymbol{k}} = 0. \tag{1.49}$$

The solutions to this equation are $\delta_+(t) = A_1$ and $\delta_-(t) \propto \exp(-2H_0 t)$. The first solution is a constant, while the second decays exponentially. Note that, for a Λ dominated Universe, the density perturbations do not grow at all. This is in line with the intuition that for a Universe which is expanding faster, Hubble drag slows down the growth of perturbations.

Growth of perturbations in the late Universe:

As we saw, in general the equation (1.48) has two solutions. However, we can safely ignore the decaying solution at late times. In the late Universe (i.e., long after matter-radiation equality), we have a mixture of matter and dark energy. The growing solution in such a model is often parameterized by the growth factor, $D(a)$. The growth factor is defined so that the solution to equation (1.48) is given as,

$$\delta_{\boldsymbol{k}}(a) = D(a)\delta_{\boldsymbol{k}}(a = 1). \tag{1.50}$$

Therefore, by definition, the growth factor equals 1 at the present time. We plot the growth factor for 3 different cosmological models in Figure 1.3. Normalized to the present, we see that the rate of growth is the highest in an flat Universe with no dark energy, i.e, $\Omega_m = 1$ and slowest for an open Universe with $\Omega_m = 0.3$.

As we saw in equation (1.41), the velocity field depends on the time derivative of the growth factor, $f = \frac{d\ln D}{d\ln a}$. In a matter-dominated Universe, $D(a) = a$. Therefore, $f = 1$ in a matter dominated Universe. This is shown in the right hand panel of Figure 1.3 by the red dashed-dotted line. In general, the growth rate in a flat ΛCDM Universe is well approximated by,

$$f_{\rm approx}(\Omega_m) = \Omega_m^{0.55}. \tag{1.51}$$

We show the validity of the approximation in Figure 1.4. We see that the approximation is valid to $\lesssim 1\%$ error for Ω_m values of our interest.

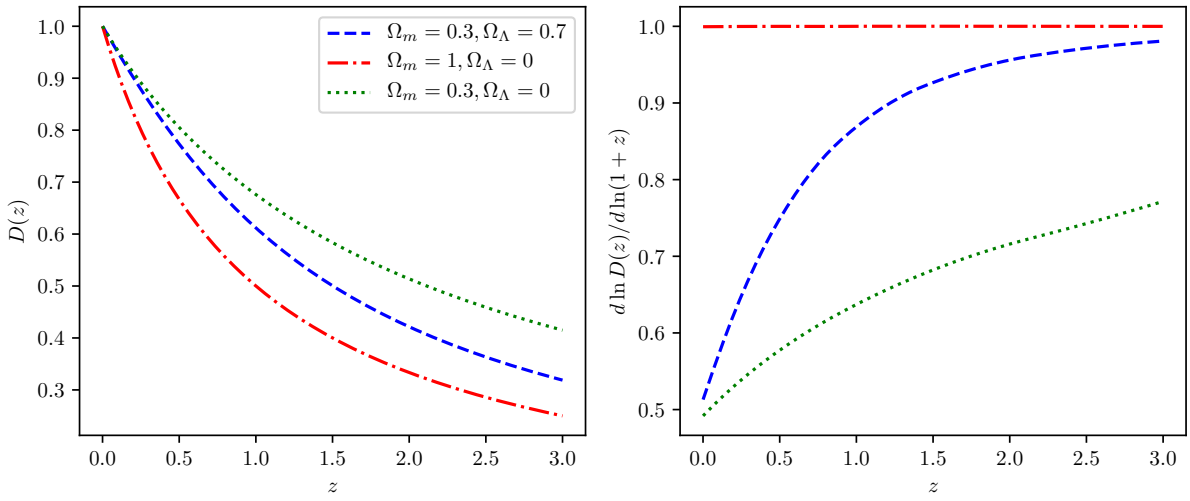

Figure 1.3: *(Left)* The growth factor, $D(z)$ as a function of the redshift, z in three different cosmological models: *i)* flat ΛCDM model with $\Omega_m = 0.3$ (blue dashed), *ii)* Flat Universe with $\Omega_m = 0.3$ (red dashed dotted), *iii)* open Universe with $\Omega_m = 0.3$. *(Right)* The growth rate, $d\ln D/d\ln a$ for the same cosmologies as a function of redshift.

Finally, note that the growth rate in ΛCDM is scale-independent. This is a prediction of general relativity. In modified theories of gravity, this may not be true, thus allowing for a test of gravity.

1.3.2 Lagrangian Perturbation Theory

In this section, we will review the Lagrangian perturbation theory (LPT) for a cosmological fluid. We will follow closely the discussion of Bernardeau et al. (2002). In LPT, one follows the motion of fluid packets in space and time. The displacement field, $\boldsymbol{\psi}$, is the main dynamical field in LPT and is used to relate the final position of a fluid packet with its initial position, $\boldsymbol{q}$. This relation is given simply as,

$$\boldsymbol{x} = \boldsymbol{q} + \boldsymbol{\psi}(\boldsymbol{q}, \tau). \tag{1.52}$$

In this section, we will use the conformal time, τ, instead of proper time, t. The two are related as, $dt = a(\tau)d\tau$. Defining, $\mathcal{H} = \frac{1}{a}\frac{\mathrm{d}a}{\mathrm{d}\tau} = aH$, the equation of motion for a fluid

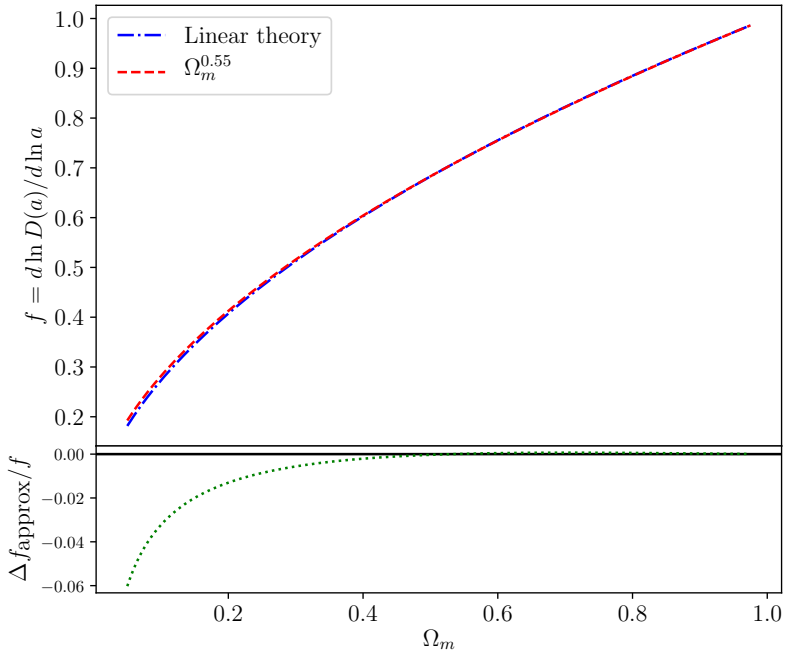

Figure 1.4: The growth rate f as a function of Ω_m. The approximation, $f = \Omega_m^{0.55}$ is shown with red dashes. The residual between the two is shown in the bottom panel. Note that the approximation is valid to $\lesssim 5\%$ for almost all values of Ω_m. For $\Omega_m \gtrsim 0.23$, the approximation yields sub-percent accuracy.

moving in a gravitational potential, Φ is given as,

$$\frac{\mathrm{d}^2\boldsymbol{x}}{\mathrm{d}\tau^2} + \mathcal{H}\frac{\mathrm{d}\boldsymbol{x}}{\mathrm{d}\tau} = \nabla_{\boldsymbol{x}}\Phi. \tag{1.53}$$

We make a distinction between the spatial derivative with respect to $\boldsymbol{x}$ and $\boldsymbol{q}$. Taking another gradient on both sides of Equation (1.53), we get,

$$\nabla_{\boldsymbol{x}}\left[\frac{\mathrm{d}^2\boldsymbol{x}}{\mathrm{d}\tau^2} + \mathcal{H}\frac{\mathrm{d}\boldsymbol{x}}{\mathrm{d}\tau}\right] = \nabla^2_{\boldsymbol{x}}\Phi. \tag{1.54}$$

The right-hand side of this equation can be rewritten in terms of δ using the Poisson equation, (1.39). We can also relate the left-hand side to derivatives of $\boldsymbol{\psi}$. Since $\boldsymbol{\psi}$ only depend on $\boldsymbol{q}$, we use the chain rule to write the derivatives with respect to $\boldsymbol{q}$.

$$\frac{\partial}{\partial x_i} = \frac{\partial q_j}{\partial x_i}\frac{\partial}{\partial q_j} = (\delta^K_{ij} + \psi_{i,j})^{-1}\frac{\partial}{\partial q_j}. \tag{1.55}$$

In the above and for the rest of the section, we use Einstein's notation to compress the summation notation. δ^K is the Kronecker delta.

To relate the Eulerian density field to the dynamical quantities of LPT, we assume that the Lagrangian coordinates are chosen such that the density is uniform in the Lagrangian coordinates. One can then use conservation of mass in the two coordinates to arrive at,

$$1 + \delta(\boldsymbol{x}, \tau) = \left|\frac{d^3q}{d^3x}\right| = \frac{1}{J(\boldsymbol{x}, \tau)}, \tag{1.56}$$

where, $J(\boldsymbol{x}, \tau)$ is the Jacobian of transformation between the coordinates, $\boldsymbol{x}$ and $\boldsymbol{q}$. Therefore, using equations (1.55) and (1.56), we can rewrite equation (1.54) as,

$$J(\delta^K_{ij} + \psi_{i,j})^{-1}\left[\frac{d^2\psi_{i,j}}{d\tau^2} + \mathcal{H}\frac{d\psi_{i,j}}{d\tau}\right] = \frac{3}{2}\mathcal{H}^2(\tau)\Omega_m[J - 1]. \tag{1.57}$$

This is the 'master equation' governing the dynamics of the displacement fields in LPT. Note that this equation is highly non-linear. One can solve this system of equations perturbatively by taking a perturbative expansion of the displacement field,

$$\boldsymbol{\psi}(\boldsymbol{q}, \tau) = \boldsymbol{\psi}^{(1)}(\boldsymbol{q}, \tau) + \boldsymbol{\psi}^{(2)}(\boldsymbol{q}, \tau) + \dots \tag{1.58}$$

In the literature, perturbative solutions up to 4th order has been calculated (Tatekawa, 2013). However, in practice, one rarely goes beyond the 2nd order Lagrangian perturbation

theory (2LPT). We can separate the displacement field into a time dependent growth factor, $D(\tau)$, and a spatial part. Up to second order, the spatial part is curl-free, and therefore can be written as a gradient of a scalar, Lagrangian potential, ϕ. Hence, up to second order, we can write,

$$\boldsymbol{x} = \boldsymbol{q} - D_1(\tau)\nabla_{\boldsymbol{q}}\phi^{(1)}(\boldsymbol{q}) + D_2(\tau)\nabla_{\boldsymbol{q}}\phi^{(2)}(\boldsymbol{q}), \tag{1.59}$$

where, $\phi^{(1)}$ and $\phi^{(2)}$ are the first and second order term in the perturbative expansion of ϕ. In the following, we will derive the perturbative solutions upto second order of LPT.

First order solution - Zeldovich Approximation

Solving Equation (1.57) and keeping only the linear terms, we get,

$$\frac{d^2\psi^{(1)}_{i,i}}{d\tau^2} + \mathcal{H}\frac{d\psi^{(1)}_{i,i}}{d\tau} = \frac{3}{2}\mathcal{H}^2(\tau)\Omega_m\psi^{(1)}_{i,i}. \tag{1.60}$$

Using the split into time dependent and spatial part of equation (1.59), we see that the spatial part drops out of the equation and that D_1 satisfy Equation (1.48). Thus, the linear order growth rate for LPT is the same as that of Eulerian perturbation theory. In order to solve for the spatial part, we expand equation (1.56) to linear order. This yields,

$$\nabla^2_{\boldsymbol{q}}\phi^{(1)}(\boldsymbol{q}) = \delta(\boldsymbol{q}). \tag{1.61}$$

Thus, solving equations (1.61) and using the linear growth factor, $D_1(\tau)$, we can solve the Lagrangian perturbation theory equations at the linear order.

Second Order Lagrangian Perturbation Theory (2LPT)

Solving Equation (1.57) up to second order, we obtain the equation governing the dynamics of $\boldsymbol{\psi}^{(2)}$,

$$\left[\frac{d^2\psi^{(2)}_{i,i}}{d\tau^2} + \mathcal{H}\frac{d\psi^{(2)}_{i,i}}{d\tau} - \frac{3}{2}\mathcal{H}^2(\tau)\Omega_m\psi^{(2)}_{i,i}\right] = -\frac{3}{4}\mathcal{H}^2\Omega_m\left[\psi^{(1)2}_{k,k} - \psi^{(1)}_{i,j}\psi^{(1)}_{j,i}\right] \tag{1.62}$$

Using the split of equation (1.59), we obtain the following equation for the growth factor at second order,

$$\frac{d^2D_2(\tau)}{d\tau^2} + \mathcal{H}\frac{dD_2(\tau)}{d\tau} - \frac{3}{2}\mathcal{H}^2(\tau)\Omega_m D_2(\tau) = -\frac{3}{2}\mathcal{H}^2\Omega_m D_1^2(\tau) \tag{1.63}$$

The solution to this equation for a flat ΛCDM Universe can be approximated to better that 1% as (Bernardeau et al., 2002),

$$D_2(\tau) \approx -\frac{3}{7}D_1^2(\tau)\Omega_m^{-1/143}. \tag{1.64}$$

The spatial part of equation (1.62) yields,

$$\nabla^2_{\boldsymbol{q}}\phi^{(2)} = \sum_{i>j}[\phi^{(1)}_{,ii}\phi^{(1)}_{,jj} - (\phi^{(1)}_{,ij})^2]. \tag{1.65}$$

The final transformation from the initial Lagrangian coordinates to the final Eulerian position is therefore given by equation (1.59). Differentiating this equation with respect to time, we get the velocity field,

$$\boldsymbol{v} = -\mathcal{H}f_1\nabla_{\boldsymbol{q}}\phi^{(1)} + \mathcal{H}f_2\nabla_{\boldsymbol{q}}\phi^{(2)}, \tag{1.66}$$

where, $f_i = d(\ln D_i)/d(\ln a)$ and $\phi^{(1)}$ and $\phi^{(2)}$ can be solved using the Poisson-like equations (1.61) and (1.65). As we saw in section 1.3.1, the linear growth rate, f_1 can be approximated as, $f_1 \approx \Omega_m^{0.55}$. The second order growth rate, can similarly be approximated as, $f_2 \approx 2\Omega_m^{6/11}$.

1.3.3 Galaxy bias and nonlinear structure formation

Perturbation theory predicts the properties of the matter density perturbations. However, what is observed are luminous tracers of this matter field such as galaxies. Therefore, we need a prescription to relate the galaxy overdensity, δ_g to the matter overdensity, δ_m. Observationally, the clustering of galaxy clusters was observed to be different from clustering of galaxies in early observations (see e.g., Bahcall & Soneira, 1983), implying that clusters and galaxies are biased in different ways with respect to the underlying density.

In general, δ_g could be an arbitrary function of δ_m and its derivatives. However, from physical considerations of equivalence principle, one finds that the bias must be a functional of the second derivative of the gravitational potential (Desjacques et al., 2018),

$$\delta_g = \mathcal{F}[\partial_i\partial_j\Phi]. \tag{1.67}$$

With the use of Poisson equation and keeping up to second order, one finds that this relation can be written as (Desjacques et al., 2018),

$$\delta_g = b_1\delta_m + \frac{1}{2}b_2\delta_m^2 + b_{s^2}K_{ij}K^{ij} + \dots, \tag{1.68}$$

where, K_{ij} is the tidal field. Note that, the first two terms are *local* terms, while the tidal term is *non-local*. When focusing on linear scales, i.e, $|\delta_m| \ll 1$, we can only keep the linear term and the relation now become,

$$\delta_g \approx b_1\delta_m. \tag{1.69}$$

Therefore, on large scales, one can assume that galaxies are linearly biased. While this simplifies the relation, this also means that only considering galaxy clustering, there is a degeneracy between the linear bias parameter and σ_8. The b_1-σ_8 degeneracy can however be broken by considering the higher order bias parameters of equation (1.68) (See e.g., Schmidt et al., 2020).

To go further in the discussion of halo bias, it is convenient to use the Press-Schechter formalism.

Spherical Collapse and the Press-Schechter formalism

In the spherical collapse model, the dynamics of an overdense region can be shown to mimic the evolution of a closed Universe. In particular, an overdense region collapses into a virialized object if $\delta > \delta_c = 1.686$ [3]. (Press & Schechter, 1974) used the spherical collapse model to predict the abundance of halo masses. In this formalism, overdensities in the initial matter field is identified. For a density field smoothed at some scale, R, the overdensities with $\delta_R > \delta_c$ are assumed to be collapsed objects of mass,

$$M(R) = \frac{4\pi}{3}R^3\bar{\rho} \tag{1.70}$$

Thus, one can calculate the number density of collapsed objects at a given mass using the Press-Schechter formalism. In order to go further, we need to make an assumption that the density field is Gaussian. Therefore the probability distribution of the density smoothed at a scale, R is given as,

$$\mathcal{P}(\delta; R)\mathrm{d}\delta = \frac{1}{\sqrt{2\pi\sigma_R^2}}\exp\left[-\frac{\delta^2}{2\sigma_R^2}\right]\mathrm{d}\delta \tag{1.71}$$

[3]There is a very weak dependence on Ω_m. In a ΛCDM Universe, this dependence is $\delta_c = 1.686[\Omega_m(t_{\rm col})]^{0.0055}$ (Mo et al., 2010). $t_{\rm col}$ is the time of collapse.

Note that the length scale , R can easily be converted into a mass scale, M using equation (1.70). The variance in the smoothed density field can then be calculated as,

$$\sigma_R^2 = \frac{1}{2\pi^2}\int_0^\infty P(k)\tilde{W}^2(kR)k^2 dk\,, \tag{1.72}$$

where, $\tilde{W}(kR)$ is a smoothing kernel with an associated length scale of R.

We show the plot of R vs $\sigma(R)$ and M vs $\sigma(M)$ in Figure 1.5. In the Press-Schechter formalism, we can calculate the fraction of collapsed objects for a given mass scale as,

$$f(M) = \int_{\delta_c}^\infty \mathrm{d}\delta\mathcal{P}(\delta; M) \tag{1.73}$$

This equation however suffers from the following problem: as $M \to 0$, $f(M) \to 1/2$, implying that only half of the mass in the Universe is in collapsed objects. The problem essentially arises from the assumption that only overdensities result in collapsed objects. In order to solve this problem, Press & Schechter (1974) introduced a fudge factor such that $f(M) \to 2f(M)$. The fraction of collapsed objects can be converted into the number of collapsed objects as,

$$\begin{aligned}\frac{\mathrm{d}n}{\mathrm{d}M}\mathrm{d}M &= \frac{\bar{\rho}}{M}\left|\frac{\mathrm{d}f(M)}{\mathrm{d}M}\right|\mathrm{d}M \\ &= \frac{\bar{\rho}}{M}f_{\rm PS}(\nu)\left|\frac{\partial \ln \nu}{\partial \ln M}\right|\mathrm{d}M,\end{aligned} \tag{1.74}$$

where, $\nu = \delta_c/\sigma_M$, and

$$f_{\rm PS}(\nu) = \sqrt{\frac{2}{\pi}}\nu \exp\left[-\frac{\nu^2}{2}\right]. \tag{1.75}$$

Equation (1.74) gives the abundance of halos of a given mass, also known as the mass function.

Peak-Background split

The physical picture of formation of dark matter halos can be intuitively understood using the *peak-background split* formalism. This formalism was first used to explain the difference in clustering of galaxies and galaxy clusters in Kaiser (1984). In this formalism, one looks at the formation of halos in the presence of a long wavelength density perturbation. That

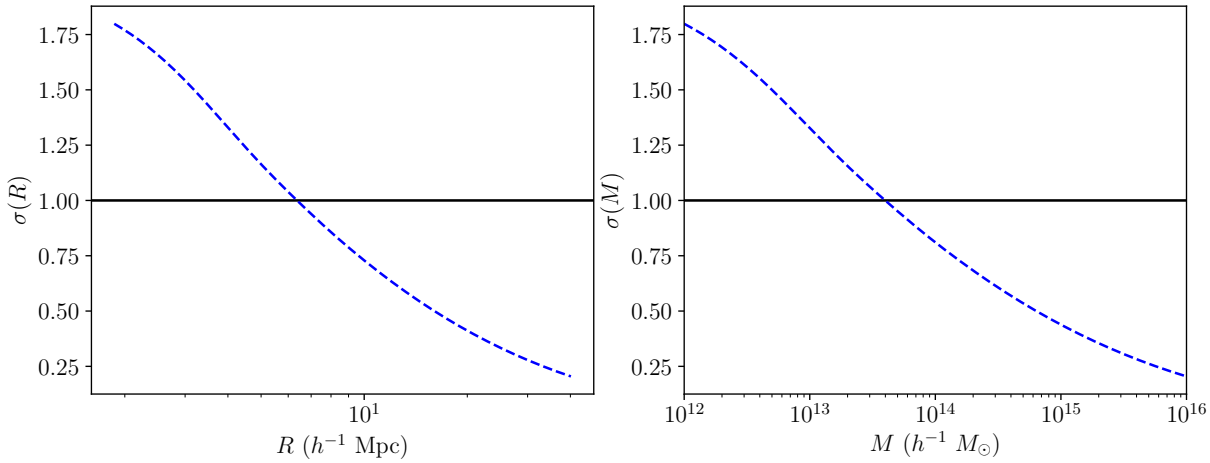

Figure 1.5: *(Left):* R vs σ_R. *(Right):* M vs σ_M calculated using equation 1.72 for a flat ΛCDM cosmology with $\Omega_m = 0.3$.

is, the density field is expressed as a sum of the long wavelength density mode, $\delta_L(\boldsymbol{x})$ and a short wavelength mode, $\delta_S(\boldsymbol{x})$. The long wavelength modulates the peaks of the density field. Therefore, it is more likely that the small scale fluctuations cross the δ_c threshold near the peak of the long wavelength. An illustration of the peak-background split is provided in Figure 1.6.

When considering the Press-Schechter formalism, the long wavelength mode has the following effect: since the long wavelength mode modulates the density fluctuation, it has the effect of lowering the threshold density in spherical collapse to $\delta_c - \delta_L(\boldsymbol{x})$. Therefore, the number density of objects in the spatial position, $\boldsymbol{x}$ in the presence of the long wavelength mode is given as,

$$\frac{\mathrm{d}n(\boldsymbol{x})}{\mathrm{d}M}\mathrm{d}M = \frac{\bar{\rho}}{M} f_{\mathrm{PS}}(\nu_L) \left| \frac{\partial \ln \nu}{\partial \ln M} \right|_{\nu=\nu_L} \mathrm{d}M, \tag{1.76}$$

where, $\nu_L = \frac{\delta_c - \delta_L(\boldsymbol{x})}{\sigma_M}$. The halo bias is then given as,

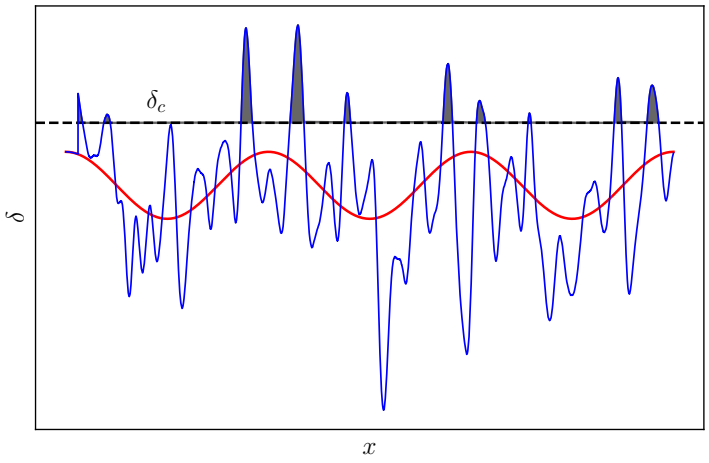

Figure 1.6: Illustration of peak-background split. The red line shows the long wavelength perturbation which modulates the small scale densities. Virialized objects form when $\delta > \delta_c$. These regions are shown with shaded grey region. Note that the structures preferentially form near the peak of the long wavelength mode.

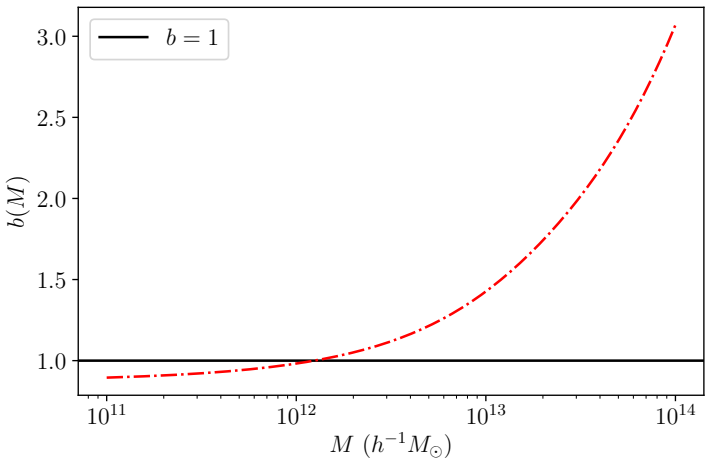

Figure 1.7: Halo bias calculated using the press-Schechter formalism as a function of halo mass.

$$
\begin{aligned}
\delta_h(\boldsymbol{x}) &= \frac{\mathrm{d}n(\boldsymbol{x})}{\mathrm{d}n} - 1 \\
&\approx \frac{f_{\rm PS}(\nu_L)}{f_{\rm PS}(\nu)} - 1 \\
&= \frac{\nu_L}{\nu} \exp\left[- \frac{(\nu_L - \nu)^2}{2} \right] - 1 \\
&= \left[1 - \frac{\delta_L(\boldsymbol{x})}{\delta_c} \right] \exp\left[- \frac{(\delta_L^2 - 2\delta_c\delta_L)}{2\sigma_M^2} \right] - 1 \\
&\approx \left[\frac{1}{\delta_c}(\nu^2 - 1) \right] \delta_L(\boldsymbol{x})
\end{aligned} \tag{1.77}
$$

The term in the square braces in equation (1.77) is the bias factor we want. However, note that in the Press-Schechter formalism, we calculate the bias in the initial density field. Therefore, this is the 'Lagrangian bias'. As noted in Equation (1.56), the volume element in the Lagrangian and the Eulerian space is related as, $V_{\rm L}/V_{\rm E} = 1 + \delta$. Therefore, the relation between the Lagrangian bias and the Eulerian bias (bias in the final density field) is given as, $b_E = 1 + b_L$. Hence, the linear Eulerian bias recovered from Press-Schechter formalism is given as,

$$
b_E(M) = 1 + \left[\frac{1}{\delta_c}(\nu^2 - 1) \right] \tag{1.78}
$$

We show the relation of M vs $b(M)$ as calculated from Press-Schechter formalism in Figure 1.7. As can be seen from the Figure, the bias of tracers at large masses increases. Therefore, galaxy clusters are more strongly clustered than galaxies. Another interesting thing to note is that halos of mass, $M \lesssim 10^{12} M_\odot$ are less clustered than the dark matter.

1.4 Cosmological Observations

As we saw, the expansion history as well as the perturbations in the Universe contain information about the nature of dark matter and dark energy. To extract this information, one needs to connect the theory to observation. The dramatic advancement in cosmological observations over the last few decades has led cosmology to become a 'precision science'. Multiple cosmological observations have converged on a standard model of cosmology, known commonly as the ΛCDM model. The main ingredients of the model consist of the cosmological constant, Λ which models the dark energy, and the cold dark matter (CDM)

which interacts weakly with the baryonic matter and with itself. The ΛCDM model consists of 6 parameters[4] that can be fitted from the data:

- the scalar tilt, n_s. We discuss the implications of inflation for the scalar tile in section 1.2.
- Total matter density parameter, Ω_m
- Total baryonic matter density parameter, Ω_b
- Amplitude of fluctuations quantified with σ_8. σ_8 is defined as the root mean squared fluctuations of the matter overdensity in a sphere of radius $8h^{-1}$ Mpc.
- Expansion rate of the Universe, measured by the Hubble constant, H_0
- The reionization depth, τ.

In this section, we review some of the major cosmological probes, the past, present and the future of cosmological observations.

1.4.1 Cosmological Probes

In this section, we review some of the observational probes of the large-scale structure of the Universe and of the expansion history.

i) Galaxy Clustering: As we saw in section 1.3, density perturbations contain a wealth of information on the underlying physics. However, most of the matter in the Universe is invisible. As we saw in the section 1.3.3, galaxies are a biased tracer of the density field. However, since, on sufficiently large scales, the galaxy bias is linear, the cosmic density field can be probed by using galaxies as tracers of the matter field. It is worth mentioning that non-linear galaxy bias remains as a major source of systematic uncertainty in many cosmological observations. Studying the clustering of galaxies in different settings and on different scales, one can extract unique information.

- Large-scale galaxy clustering: There is a qualitative difference in the evolution of the wave modes that enter the horizon before and after the matter-radiation equality.

[4] One may also consider the temperature of the CMB, $T_{\rm CMB}$, as an additional parameter, which is related to Ω_r. However, this is well-constrained from observations compared to other parameters mentioned here.

The potential for the wave modes that entered the horizon during matter domination (large scales) remains constant, and therefore retains its scale invariant spectrum. On the other hand, the growth of wave modes that entered the horizon during the radiation domination (small scales) is retarded and has a different spectrum. This leads to a characteristic break in the power spectrum, the scale of which is determined by the matter-radiation equality. Since the matter-radiation equality is sensitive to the parameter, $\Gamma = \Omega_m h$ (also known as the shape parameter), studying galaxy clustering at large scales can constrain this parameter combination.

- Clustering in the redshift space: Galaxy redshift observations capture their three dimensional information. However, the redshift of a galaxy gets a contribution from both the Hubble recession as well as its peculiar velocity. Because of the radial peculiar velocity, the clustering signal in the radial direction is different from the clustering in the transverse direction, leading to an anisotropic clustering signal. On large scales, coherent flows of galaxies lead to an increase in the correlation in the redshift space (Kaiser, 1987). On the other hand, on small scales, the non-linear velocities in clusters and groups lead to the opposite effect, i.e, a decrease in the correlation as compared to real space correlation. This effect is known as the *Finger-of-god effect*. Comparing the quadrupole and the dipole of the clustering signal, one can then measure the quantity, f/b, where, f is the growth rate of structures and b is the linear galaxy bias. More generically, RSD measurements have been used to constrain the parameter combination $f\sigma_8$. The state-of-the-art measurement (Alam et al., 2017) of this parameter from RSD comes from the Baryon Oscillation Spectroscopic Survey (BOSS), yielding a $\sim 6\%$ constraint on $f\sigma_8$ in 3 redshift bins.

- Baryon acoustic oscillations: Before recombination, the photons and the baryons were tightly coupled into a single fluid. At recombination, as the photons decoupled from the baryons, there was an excess correlation of baryons at the scale of the 'sound horizon'. This leads to a characteristic 'bump' in the correlation function at sound horizon during recombination. Measuring the Baryon Acoustic Oscillation (BAO) in the correlation function require galaxies over a large volume of the Universe. Therefore, galaxy redshift surveys for which measuring the BAO is a major scientific goal are designed to observe galaxies over a very large volume. CMB measurements from WMAP and Planck have measured this scale with very high precision ($\sim 0.5\%$). Hence, this scale serves as a 'standard ruler'. Using the measurement of the BAO scale in galaxy correlation at various redshifts therefore allows for a determination of the expansion history of the Universe.

  The BAO signal in the transverse and the radial direction are sensitive to different

quantities - thus allowing to constrain different cosmological parameters. The BAO signal in the angular direction at a redshift, z, is sensitive to the angular diameter distance at that redshift, $D_A(z)$. On the other hand, the radial BAO signal is sensitive to $H(z)^{-1}$.

ii) Direct probes of peculiar velocity: As we saw in the section 1.3, peculiar velocities are sourced by the density fluctuations in the Universe. Furthermore, the typical amplitude of peculiar velocity is also proportional to the growth rate of structure, f. Therefore, the cosmological parameter peculiar velocity probes are most sensitive to is the combination, $f\sigma_8$. Another feature that makes peculiar velocities appealing as a cosmological probe is that it is sensitive to the very large scale density perturbations. We elaborate more on using direct measurements of peculiar velocity as an observational probe in section 1.5.

iii) Weak gravitational lensing: The trajectories of light rays are deflected by the gravitational potential of density perturbations. This leads to a small change in the galaxy shapes which can be studied statistically. These contain information about cosmological perturbations. Weak lensing observations are sensitive to the perturbations in the total matter density, including dark matter, making it an excellent probe for the growth of structures. Since it probes the perturbation, it is sensitive to the parameter σ_8. It is however, also sensitive to Ω_m. The dependence on Ω_m enter through two factors: *i)* The growth of structure across redshifts depends on Ω_m, *ii)* Typically lensing perturbations are probed by the shear-shear angular correlation function. The angular diameter distance is depends on Ω_m. The parameter combination that weak lensing is most sensitive to is $S_8 = \sigma_8\sqrt{(\Omega_m/0.3)}$ (Jain & Seljak, 1997).

iv) Cluster abundance: As we saw in section 1.3.3, the abundances of the most massive clusters in the Universe are exponentially suppressed. As can be seen from equation (1.75), the abundance of the massive clusters is sensitive to the power spectrum. Hence, abundance of these clusters are a sensitive probe of cosmological structure growth. Cosmology dependence of the cluster abundance arises from: *i)* the dependence of growth factor as a function of redshift, and *ii)* the volume element which also depends on Ω_m. It is therefore, sensitive to some combination of Ω_m and σ_8. Observationally, the main challenge lies in calibrating the observable-mass relationship for clusters.

v) Standard candles and standard sirens: The peak magnitude of Type Ia Supernovae is correlated with the decay time of the light curve (Phillips, 1993). This relationship allows for the use of Type Ia supernovae as a 'standard candle' and to measure distance to high redshifts with high precision ($\lesssim$ 5-10% uncertainty). By also observing the redshift of the supernova (by identifying its host galaxy), they can be used to measure the redshift-luminosity distance relationship. Type Ia supernovae can be used to measure cosmological

parameters in two ways. First, the redshift-distance relationship diverges at high redshifts for different values of Ω_m, Ω_Λ and Ω_K because of different powers of the scale factor associated with each of these parameters in the Friedmann equation. Therefore, the Hubble rate evolves differently for different parameters. Note that, in order to measure these parameters one does not need the absolute value of the Hubble parameter. One only needs to know how the expansion rate changes with redshift. Therefore, there is no need to calibrate the supernovae to local distance ladder. The other parameter Type Ia supernovae are used to measure is the Hubble constant. However, this requires calibration of the supernovae to local distance measurements such as that of Cepheids or the Tip of red giant branch (TRGB) stars.

A similar probe to measure the expansion rate of the Universe is by using the gravitational wave observations. Gravitational wave signals can be used to measure the luminosity distance to the event. This distance measurement only relies on general relativistic predictions and do not require any intermediate calibration. Therefore, if one also detects an optical counterpart to the gravitational wave event, we can measure the redshift – distance relationship, and therefore measure the Hubble constant[5], H_0. We will discuss this further in Chapter 6.

1.4.2 Establishment of the ΛCDM model

Starting in the late 1990s, multiple observational probes matured so as to give meaningful constraints on different cosmological parameters. Since then, multiple lines of evidence has led to the establishment of a standard ΛCDM model of cosmology consisting of a flat Universe dominated by dark energy and dark matter described a cold dark matter (CDM) component.

The first notable detection of dark energy was made by two groups of supernovae cosmologists (Riess et al., 1998; Perlmutter et al., 1999), who by investigating the redshift-magnitude relation of a handful of supernovae measured a non-zero Ω_Λ at high significance. However, claims for departure from the 'standard' $\Omega_m = 1$ were being made from multiple lines of evidence starting in the early 1990's. In particular, investigation of the large-scale galaxy clustering in the APM galaxy survey (Efstathiou et al., 1990; Maddox et al., 1990) led the authors to claim that, *"the successes of the CDM theory can be retained and the new observations accommodated in a spatially flat cosmology in which as much as* 80% *of the*

[5]In principle, one can also measure Ω_m, Ω_Λ, etc. However, that requires detection of binary neutron stars to high redshifts. From the current generation of gravitational wave detectors, it is possible to detect these to fairly low redshift.

critical density is provided by a positive cosmological constant". Cosmological constraints from redshift space distortions and peculiar velocities were somewhat mixed [6]. While some studies measured a low value of $\beta = f/b \sim 0.5$ (e.g., Hudson, 1994a; Fisher et al., 1994; Willick & Strauss, 1998). On the other hand, there were other studies which preferred a value of $\beta \sim 1$ (e.g., (Peacock & Dodds, 1994; Dekel et al., 1993; Nusser & Dekel, 1993)). In White et al. (1993b) it was argued that $\Omega_m \sim 0.2$ can explain the observations of baryon-to-total matter ratio from clusters combined with BBN constraints. Ostriker & Steinhardt (1995) summarized the results from different observations to argue that ΛCDM model fits the existing data of the time the best. Finally, detection of high redshift clusters also implied a low value of Ω_m (Donahue et al., 1998; Bahcall & Fan, 1998).

Then, in 1998, two independent groups of supernova cosmologists analyzed the data from high redshift supernovae, thus measuring a non-zero value for the dark energy at high significance (Riess et al., 1998; Perlmutter et al., 1999). Within a short span of a few years, multiple probes started converging on a model for the Universe with a flat geometry and dominated by dark energy. The 2dF galaxy redshift survey was the first redshift survey with $> 10^5$ galaxy redshifts. Analysis of bispectrum and the RSD in the 2dF galaxies led to a constraint of $\Omega_m = 0.27 \pm 0.06$ (Verde et al., 2002; Peacock et al., 2001). Analysis of cluster abundance at the same time led to constraints of $\Omega_m = 0.35^{+0.13}_{-0.10}$ and $\sigma_8 = 0.66^{+0.06}_{-0.05}$ (Borgani et al., 2001). Around the same time, cosmic shear was first detected and led to a constraints on σ_8 (assuming $\Omega_m \sim 0.3$) in the range of $\sim$ 0.8-1.0 (see e.g, Van Waerbeke et al., 2000; Wittman et al., 2000; Bacon et al., 2000)). Finally, it culminated with the analysis of CMB anisotropies. Observation of the first peak in CMB anisotropies from the balloon experiments, BOOMERanG (de Bernardis et al., 2000) and MAXIMA (Balbi et al., 2000), constrained tightly the spatial curvature of the Universe, suggesting a flat Universe. Then in 2003, WMAP year-1 data (Spergel et al., 2003) was used to put much tighter constraints on the cosmological model. The model that emerged as the preferred model was that of a flat Universe dominated by dark energy and having amplitude of perturbations, $\sigma_8 \sim 0.8$. One can consider the WMAP study to be the one that finally established the ΛCDM model as the standard model of cosmology.

1.4.3 Current state of cosmological observations: H_0 and σ_8 tensions

Since its establishment, the ΛCDM model has been very successful in explaining the observations from multiple independent cosmological probes. The tightest constraints on

[6] See Table 1 of Dekel (1994) for a summary of results from peculiar velocity and RSD from 1994.

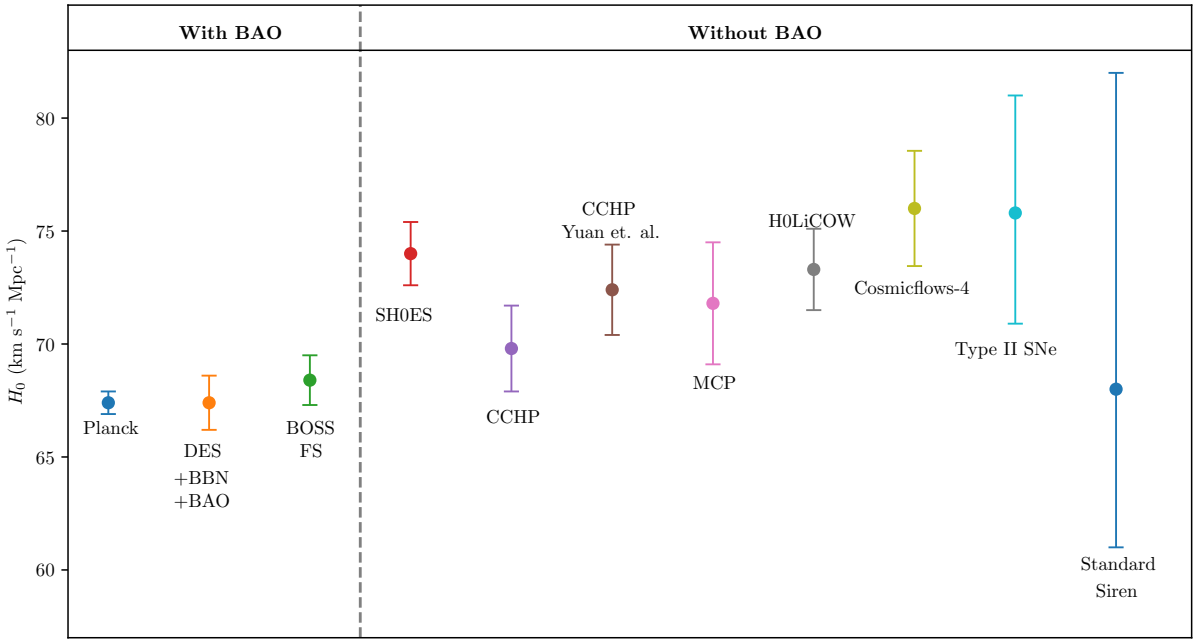

Figure 1.8: Different measurements of H_0. Note that the measurements relying on the BAO tends to give a lower value of H_0. See Table 1.1 and text for details.

Table 1.1: Comparison of H_0 values for different studies. See Figure 1.8 for a visual representation and text for details.

	Dataset	H_0 (km s^{-1} Mpc^{-1})	Reference
Early	Planck	67.4 ± 0.5	Planck Collaboration (2018a)
	DES + BBN + BAO	67.4 ± 1.2	Abbott et al. (2018b)
	BOSS Full Shape	68.6 ± 1.1	Philcox et al. (2020)
Late	SH0ES	74.0 ± 1.4	Riess et al. (2019)
	CCHP	69.8 ± 1.9	Freedman et al. (2019)
	CCHP (Recalibrated)	72.4 ± 2.0	Yuan et al. (2019)
	MCP	71.8 ± 2.7	Pesce et al. (2020)
	H0LiCOW	$73.3^{+1.7}_{-1.8}$	Wong et al. (2019)
	Cosmicflows-4	76.0 ± 2.6	Kourkchi et al. (2020)
	Type II SNe	$75.8^{+5.2}_{-4.9}$	de Jaeger et al. (2020)
	GW Standard sirens	68^{+14}_{-7}	LIGO and Virgo Collaboration (2019)

cosmological parameters come from the temperature anisotropies measured by the *Planck* satellite (Planck Collaboration, 2018a). The sample of high-z supernovae has been expanded to include 1000's of supernovae (Scolnic et al., 2018), resulting in a much tighter constraints in the Ω_m-Ω_Λ space. Weak lensing has come to play an increasingly important role in the determination of cosmological parameters by probing the growth of structures at several redshifts. With massive increase in the size of spectroscopic surveys, BAOs have been detected with high significance and RSD been used to measure growth rate of structure. Broadly, all the different probes have been consistent with the predictions of the ΛCDM model. However, some tensions have emerged in the measurement of some cosmological parameters recently. In particular, the measurement of H_0 and σ_8 from different probes seem to suggest slightly different values.

Measuring the Hubble constant requires either a standard ruler (e.g, BAO) or some standard distance indicator (e.g., Type Ia Supernovae). The measurements of H_0 relying on the BAO scale has been found to discrepant with other methods of measuring H_0 (See Verde et al. (2019) for a review). For example, the SH0ES collaboration (Riess et al., 2016) uses Type Ia supernovae calibrated on nearby Cepheid variables to measure the Hubble constant. The current measurement (Riess et al., 2019) from the SH0ES collaboration, $H_0 = 74.03 \pm 1.42$ km s^{-1} Mpc^{-1}, is in tension with the H_0 measurement of the Planck collaboration (Planck Collaboration, 2018a), $H_0 = 67.4 \pm 0.5$ km s^{-1} Mpc^{-1} at a 4.4σ level. Note that the CMB measurement of H_0 is sensitive to the location of the acoustic peak. Other estimates of H_0 that relies of the BAO measurement similarly tends to give an estimate of H_0 which is somewhat lower (Abbott et al., 2018b; Philcox et al., 2020). On the other hand, independent constraints from strong lensing time delays (Wong et al., 2019) gives a value of $H_0 = 73.3^{+1.7}_{-1.8}$ km s^{-1} Mpc^{-1}, an approximately 3σ tension with the Planck results. There are other results from Megamaser Cosmology Project (MCP, Pesce et al., 2020)), and Tully-Fisher relations (Kourkchi et al., 2020) which similarly are in mild tension with the early Universe results. It is worth noting that there are other measurements such as that of the Chicago-Carnegie Hubble program (CCHP, Freedman et al., 2019), that is in mild tensions with both the SH0ES and Planck measurement. However, Yuan et al. (2019) contested the calibration techniques applied in their measurement and claimed that the revised calibration still gives $\sim$ 2.5σ tension. The standard siren measurement of H_0 is still in its early days. Nonetheless, H_0 has been measured from gravitational waves (Abbott et al., 2017b; LIGO and Virgo Collaboration, 2019). Note that the distance indicator based H_0 measurements are not independent and may rely on same calibrator samples. Among these, Megamasers and standard sirens do not require any calibration to local distance measurements. We summarize these results in Table 1.1 and show the different measurements of H_0 in Figure 1.8.

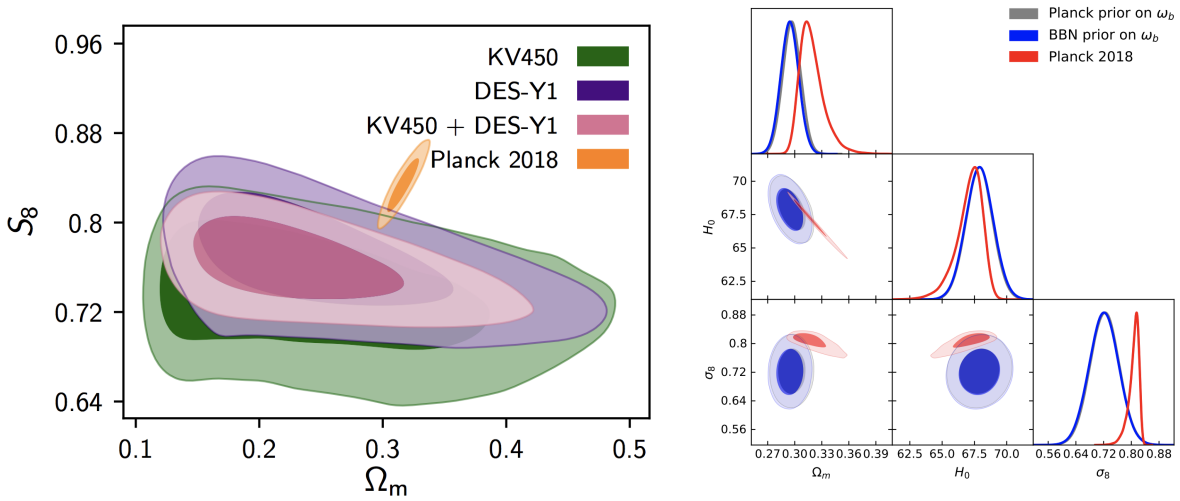

Figure 1.9: *(Left)* Measurement of S_8 and Ω_m for the weak lensing measurement in DES-Y1 and KiDS+VIKINGS-450 surveys. Figure taken from Joudaki et al. (2019). *(Right)* Measurement of σ_8 from the full shape galaxy power spectrum in the BOSS survey. Figure taken from Philcox et al. (2020). The Planck value of S_8/σ_8 is higher than the estimates from lensing and the BOSS measurements.

Similarly, the value of the amplitude of perturbations, σ_8, as measured from the CMB and the late Universe has been found to be discrepant, albeit at a slightly lower significance. As seen in Section 1.4.1, σ_8 can be measured in the late Universe from a variety of probes such as weak lensing, cluster abundances, RSD, peculiar velocities, etc. The probe which gives the tightest constraints currently is weak lensing. Multiple weak lensing surveys (Joudaki et al., 2017; Dark Energy Survey Collaboration, 2018; Joudaki et al., 2019; Hikage et al., 2019) have measured a value of σ_8 which is 2-3σ lower than the value expected from CMB measurements. There are also other measurements from the full-shape power spectrum measurement in redshift surveys which seems to give a similarly low value of σ_8 (Philcox et al., 2020). The results from cluster abundances are mixed. (Bocquet et al., 2019) used Sunyaev-Zeldovich clusters from the South Pole telescope measured a value of S_8 which is $\sim 1.5\sigma$ away from the Planck constraints. However, other studies of cluster abundances are consistent with the Planck results of σ_8. While there is no single study which on its own is in significant ($> 3\sigma$) tension with the CMB measurements, the existence of multiple surveys with this mild tension is interesting.

1.4.4 Looking into the Future

We are living in an interesting time in cosmology. On one hand, many probes converge on very similar constraints on the ΛCDM model, while on the other hand, there are hints of tensions in the standard ΛCDM model. In the near future, multiple observational surveys will start its operations, studying cosmology with various probes.

Future surveys

In the near future, many new surveys are going observe the Universe with improved capabilities. A massive upgrade in spectroscopic as well as photometric capabilities will revolutionize cosmological observations. The so-called Stage IV probes of the dark energy aim at uncovering the nature of dark energy by probing both the expansion history and the growth of structures in exquisite detail. The major probes of these missions include weak lensing, cluster growth and galaxy clustering. On the spectroscopic front, the Dark Energy Spectroscopic Instrument (DESI, DESI Collaboration et al., 2016) will acquire the redshifts of $\gtrsim 30$ million galaxies, a massive upgrade on the current spectroscopic capabilities. DESI will improve the measurement of the expansion history with BAOs as well as of the growth rate through RSDs. The Vera Rubin Observatory (VRO, formerly known as LSST, (LSST Science Collaboration, 2009)) will provide a very large imaging survey to probe among other things, weak lensing and cluster abundances. Euclid (Laureijs et al., 2011) and the Nancy Roman Observatory (formerly WFIRST (Doré et al., 2018)) will have both photometric and spectroscopic instruments to probe the Universe through a large number of complementary cosmological probes.

Development in techniques

With the increase in the statistical power from the above mentioned surveys, there is an increasing need for methods and techniques which are better able to deal with systematic effects of specific observations. This usually involves improving the physical and statistical modelling of the cosmological data.

Traditionally, most cosmological probes involve comparing summary statistics such as the 2-point correlation function for constraining cosmological parameters. Given that different probes are sensitive to different systematics and are often complementary, it is useful to be able to combine different cosmological probes in a unified analysis framework. A direction of research which has been used for combining different cosmological probes

is to model the cross-covariance between different probes in addition to the covariance of individual probes (Krause & Eifler, 2017). This techniques often goes by the name, '3x2 point analysis'. Such multiprobe analysis has been used to combine galaxy clustering with weak lensing in DES (Abbott et al., 2019), and galaxy clustering with thermal Sunyaev-Zeldovich effect (Makiya et al., 2018).

Modelling the non-linear structure formation is important to extract information from cosmological probes in an unbiased and optimal way. In the linear regime, the field is approximately Gaussian and therefore, the two point correlation function contains all the information about the large-scale modes. However, due to non-linear structure formation, at small scales, one needs to model higher order correlations to be able to extract information in an unbiased manner. One way of dealing with this is by improving the perturbation theory at the quasi-linear scales. This includes methods like the Effective Field Theory (EFT) of the large scale structures (Carrasco et al., 2012), which has recently been applied to cosmological data from the BOSS survey (d'Amico et al., 2020). There are other methods which uses forward modelling of structure formation to evolve Gaussian initial density field to the present and then comparing the observations at a field-level, i.e., without compressing into summary statistics. This includes the method of Bayesian Origin Reconstruction from Galaxies (BORG Jasche & Wandelt, 2013; Jasche & Lavaux, 2019) and Exploring the Local Universe with reConstructed Initial Density field (ELUCID Wang et al., 2014). In such models, one can use non-linear structure formation models to evolve the initial density, thus, capturing the higher order correlation function in the process. While computationally expensive, developments of faster computational methods have made these techniques computationally tractable. We will talk in detail about the BORG algorithm in Chapter 6.

1.5 Direct probes of peculiar velocities

As we saw in section 1.3, growth of structure is intimately related to the peculiar velocity of galaxies. In linear perturbation theory, the peculiar velocity at a comoving location, $\boldsymbol{x}$, is given by equation (1.41). The peculiar velocity is therefore related to the growth rate of structures, f, and the amplitude of density fluctuations, typically quantified with σ_8. In fact, using linear perturbation theory, we can only constrain the degenerate parameter combination, $f\sigma_8$, using peculiar velocities. Written in Fourier space, Equation (1.41) can be written as,

$$\boldsymbol{v}_{\boldsymbol{k}} = ifaH\frac{\boldsymbol{k}}{k^2}\delta_{\boldsymbol{k}}. \tag{1.79}$$

Because of the $1/k$ dependence, the velocity field is also sensitive to large-scale density perturbations. At low redshifts ($z \lesssim 0.06$), probes like RSD, are limited by smaller volume. Observations of peculiar velocity provide the only way to measure structure growth in the very low redshift Universe. The observed redshift of a galaxy gets a contribution from both the Hubble recession, $H_0 d$, and the radial peculiar velocity, v_p^r,

$$cz_{\rm obs} \approx H_0 d + v_p^r. \tag{1.80}$$

Therefore, to determine the peculiar velocity of a galaxy, one needs to accurately determine both the redshift and the distance to the galaxies. Estimates of the redshift are fairly easy and have an error, $\Delta cz \lesssim 30$ km/s. Determining distances, on the other hand, is quite difficult. We will discuss the distance measurements used for peculiar velocity surveys in the next subsection.

1.5.1 Peculiar velocity data

Measuring distances to galaxies is observationally challenging. The most widely used peculiar velocity data currently and historically relies on empirical galaxy scaling relations. This include the Tully & Fisher (1977) relation and the Fundamental Plane relation (Dressler et al., 1987; Djorgovski & Davis, 1987). Historically, the D_n-σ relation, which is closely related to the Fundamental Plane relation was used for many peculiar velocity studies (see e.g. Lynden-Bell et al. (1988)). The Tully-Fisher relation is an empirical relation between the rotational velocity width and the luminosity of spiral galaxies. This can in turn be used to measure distances to these galaxies. The Fundamental Plane and the D_n-σ relation are used to measure distances to elliptical galaxies whose velocity dispersion, brightness and the size has been empirically determined to be linearly related. These galaxy-scaling relations typically provide a $\sim$ 15-25% estimate of the distances to the galaxies. Often, it is desirable to obtain the peculiar velocity data to groups of galaxies than that of individual galaxies. Averaging over the redshifts of galaxies suppresses the non-linear motion that might affect the redshift estimates of its members. Besides, multiple distance measurements to its member galaxies may gives us a more precise estimate for the distance.

The other widely used distance indicator for peculiar velocity studies is the Type Ia supernovae. The use of supernovae as a standard candle for measuring the acceleration of the expansion of the Universe is well-known in cosmology. The nearby supernovae can also be used for measuring peculiar velocities to their host galaxies. Compared to the galaxy scaling relations, Type Ia supernovae give a much more precise, $\sim$ 5-15% distance estimate. Note that, for its use in peculiar velocity studies, we need relative distances (i.e, in units

of h^{-1} Mpc) rather than absolute distance. Therefore, there is no need to calibrate the distances with respect to nearby distances for its use in peculiar velocity studies. Other relations such as the Surface Brightness Fluctuations (SBF), Tip of Red Giant branch (TRGB) has also been used as distance indicators for peculiar velocity estimates (see e.g, Pike & Hudson, 2005; Tully et al., 2016).

Currently, peculiar velocity of galaxies have been measured by several surveys. The SFI++ (Masters et al., 2006; Springob et al., 2007) and the 2MTF (Masters et al., 2008; Hong et al., 2019) surveys have measured the distances to thousands of galaxies using the Tully-Fisher relation. The SFI++ uses the I-band Tully-Fisher relation while 2MTF uses 3 infrared bands to measure the distances. The I-band TF relations with an intrinsic scatter of $\sigma_{\rm int} \sim 0.3$ mag is more precise than the infrared TF relation ($\sigma_{\rm int} \sim 0.4$ mag). However, the infrared bands are less susceptible to some of the systematic effects such as dust extinction. Currently, the largest peculiar survey is the 6dF peculiar velocity survey (Springob et al., 2014), which uses the Fundamental Plane relation to measure distances. The 6dF peculiar velocity sample consists of distance and peculiar velocity estimates to 8885 galaxies. Type-Ia Supernovae has also been widely used for peculiar velocity estimates. In chapter 4, we will describe our work where we compiled the largest low redshift peculiar velocity catalog based on Type Ia supernovae.

In the near future, we anticipate an order-of-magnitude increase in peculiar velocity data from new surveys. The "Transforming Astronomical Imaging surveys through Polychromatic Analysis of Nebulae" (TAIPAN) survey (da Cunha et al., 2017) will acquire the distances to $\sim 45,000$ galaxies up to $z \sim 0.1$ in the southern sky using the FP relation. The Widefield ASKAP L-band Legacy All-sky Blind Survey (Koribalski et al., 2020) survey is a HI-survey which will observe 3 quarters of the sky. Using the Tully-Fisher relation, it is expected to acquire distances to $\sim 40,000$ galaxies (Howlett et al., 2017). In comparison, at present, the largest Tully-Fisher catalogue is the SFI++ catalogue with $\sim 4,500$ galaxies. It has been forecast that using a combination of the WALLABY and the TAIPAN peculiar velocity data, the constraints on $f\sigma_8$ will reach $\sim 3\%$ (Howlett et al., 2017; Koda et al., 2014). There will also be an increase in the number of low-redshift Type Ia supernovae usable for peculiar velocity studies. The full Foundation supernovae sample will consist of up to 800 supernovae at $z \lesssim 0.1$ (Foley et al., 2018; Jones et al., 2019). In the near future, Large Synoptic Survey Telescope (LSST) will also start taking data. It is expected to greatly increase the number of supernovae known in the local universe, although many will be at redshifts $z \gtrsim 0.2$ and will therefore have large uncertainties (Garcia et al., 2019). Observing nearby supernovae in the infrared frequencies can provide distance estimates with much smaller uncertainty. Together, the use of these peculiar velocity estimates could provide us with unprecedented constraints on the growth rate in the local universe. There

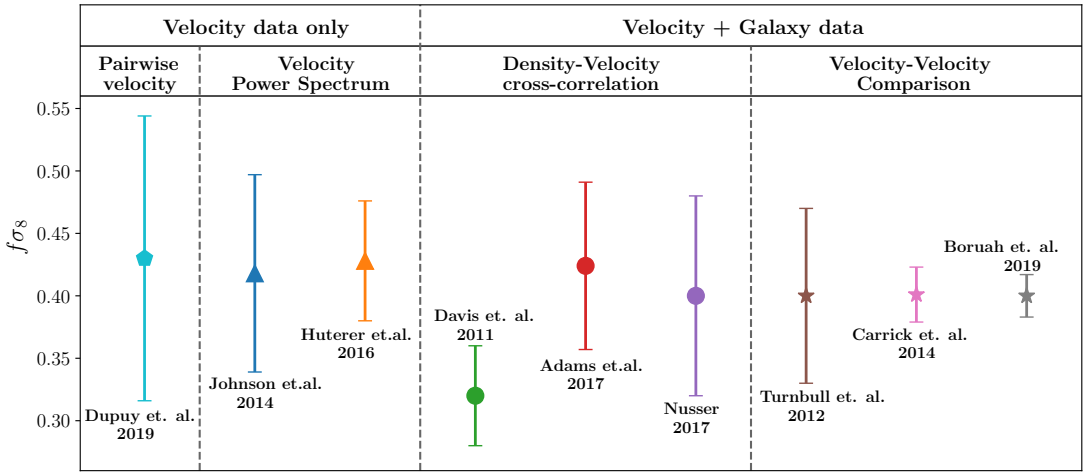

Figure 1.10: $f\sigma_8$ constraints from recent peculiar velocity studies. The first two panels on the left only use peculiar velocity data, while the two panels on the right use both peculiar velocity and galaxy redshift data. See text for more details on the methods and the different studies used in the plot.

have also been proposals to study the peculiar velocities using gravitational wave events from future GW detectors such as the Einstein Telescope (Palmese & Kim, 2020; Wang et al., 2018).

1.5.2 Peculiar velocity analysis methods

In this section, we review the different methods that has been used to constrain the growth rate from peculiar velocity analysis. Broadly, we categorize the methods into the ones that only use peculiar velocity data and the ones that use both the velocity data and an overlapping galaxy redshift survey. For each of these, we review two different methods. We also review some of the recent cosmological constraints obtained using each methods. These constraints are compared in Figure 1.10.

Methods relying only on peculiar velocity data: Methods that rely only on the peculiar velocity data do not require the modelling of galaxy bias. On the other hand, peculiar velocity estimates are very noisy, thus making these methods susceptible to other problems.

- *Pairwise velocity measurement*: For two randomly-selected galaxies, the peculiar velocity of a galaxy relative to the other is directed towards each other because of gravitational attraction. Intuitively, since the galaxies trace over-dense regions, their velocity is directed towards each other. ΛCDM model can be used to model the pair-wise velocity of galaxies, and thus can be used for constraining cosmological parameters. Recently, this method was used on the *Cosmicflows-3* data set in Dupuy et al. (2019) to constrain, $f\sigma_8 = 0.43 \pm 0.03$ (statistical) ± 0.11 (systematic). This technique has also been used to detect the kinetic Sunyaev-Zeldovich (kSZ) effect using the combined Planck and BOSS data sets (De Bernardis et al., 2017).

- *Velocity Power spectrum / correlation function*: The peculiar velocities of galaxies in a ΛCDM Universe are correlated. The ΛCDM model can be used to model the covariance of peculiar velocities at some separation, for different cosmological parameters. Thus, comparing the measured correlation to the ΛCDM predictions provides a way to put constraints on the cosmological parameters. This method has been used in Johnson et al. (2014) and Huterer et al. (2017) to measure the cosmological parameter combination, $f\sigma_8$. This method can also be used to measure a scale-dependent growth rate in the Universe (see e.g., Johnson et al., 2016). While GR predicts a scale-independent growth rate, some modified gravity theories diverge from this prediction. Therefore, measuring the scale-dependent growth rate can provide a test for modified theories of gravity.

Methods relying on peculiar velocity + redshift survey data: There are other methods that uses both a peculiar velocity data set as well as a galaxy survey to obtain constraints on the cosmological parameters. These methods necessarily require modelling of the galaxy bias. Using galaxy surveys can compensate for the sparseness and the noisy nature of velocity data, thus yielding larger statistical power.

- *Velocity-Velocity comparison*: Velocity-velocity comparison methods for analyzing peculiar velocity involves predicting the peculiar velocity field of the local Universe and then comparing it to the observations. In this method, a galaxy redshift survey is used to 'reconstruct' the density and the velocity field of the local Universe. The predicted velocity depends on the cosmological parameters. Therefore, by comparing the predicted and the observed velocities, one can obtain constraints on the cosmological parameter combination, $f\sigma_8$. This method has a long history of being used for constraining cosmological parameters (See e.g. Kaiser et al., 1991; Hudson, 1994a; Branchini et al., 1999; Pike & Hudson, 2005). Some of the recent results for $f\sigma_8$ constraints obtained using the velocity-velocity comparison method includes Turnbull

et al. (2012); Carrick et al. (2015); Boruah et al. (2019). These results are shown in Figure 1.10.

- *Density-velocity cross-correlation*: A closely related method for constraining the cosmological parameters is to compute the cross spectrum between the density field, measured from a galaxy redshift survey, and the velocity field. The cross-variance between the density and velocity field can be computed from the ΛCDM model similar to the velocity power spectrum. In Adams & Blake (2017), this method was applied (the authors also modelled the density-density and velocity-velocity autocorrelation function) on the 6dF galaxy and peculiar velocity data set to obtain $f\sigma_8 = 0.424^{+0.067}_{-0.064}$. Nusser (2017) used a velocity-density correlation method on the *Cosmicflows-3* peculiar velocity data and 2MASS galaxy survey to obtain $f\sigma_8 = 0.40 \pm 0.08$. A similar method was earlier used by Davis et al. (2011) on the SFI++ peculiar velocity data and the 2MASS galaxy survey to obtain a constraint, $f\sigma_8 = 0.32 \pm 0.04$.

1.6 Outline of the thesis

In this thesis, we will investigate a variety of different questions in early and late Universe cosmology. The thesis is divided into three parts, each of which is independent of the others and therefore can be read independently.

As we saw in section 1.2.5, the theory of inflation suffers from a number of theoretical problems. Various bouncing cosmological models have been considered in the literature (e.g, Khoury et al. (2001); Ijjas & Steinhardt (2017)) to circumvent some of these problems. However, perturbations in these bouncing scenarios generically suffer from instabilities as a consequence of violating the Null Energy Condition (Dubovsky et al., 2006). In part I, we investigate the evolution of perturbations in a modified theory of gravity known as Cuscuton gravity, that can provide an alternative to inflationary paradigm. We study in particular the evolution of perturbations in a bouncing model driven by a single scalar field within Cuscuton gravity. We found that perturbations in the bouncing model do not suffer from any instability, providing one of the very few bouncing model to not suffer from such instabilities. In chapter 2, we derived the general formulation of cosmological perturbations in Cuscuton gravity around FLRW backgrounds and showed the theory is ghost free. In chapter 3, we used a toy model to show that it is possible to have a bouncing scenario in Cuscuton gravity without catastrophic instability in the perturbations.

Part II is an observational study of the peculiar velocity fields in the local Universe. In chapter 4, we used a velocity-velocity comparison method to constrain the cosmological

parameter combination, $f\sigma_8$. Previously, Carrick et al. (2015) used this method with a reconstruction on the 2M++ galaxy catalogue to constrain $f\sigma_8$. In this work, we extended the *Forward Likelihood* method to simultaneously calibrate the Tully-Fisher and Supernovae distance indicator relation. Furthermore, we also compiled a larger set of supernovae for its use in peculiar velocity analysis. Chapter 5 compares the different peculiar velocity fields of the local Universe. These peculiar velocity corrections are important for a variety of different cosmological studies.

Finally in part III, we introduce a new statistical method to measure H_0 from standard sirens. We show some initial results that show that our method gives unbiased estimate of H_0 on mock simulations. We also apply our method to the gravitational wave event, GW170817 to get a constraint on H_0 from the real world data.

Part I

Cuscuton Bounce

Chapter 2

Theory of Cosmological Perturbations with Cuscuton Gravity

2.1 Introduction

Cuscuton gravity (Afshordi et al., 2007a,b) was originally proposed as an infrared modification of General Relativity (GR), with no additional degrees of freedom. Interestingly, since then, it has been rediscovered in other independent works to address different questions in early or late universe. For instance, it arises in the low energy limit (Afshordi, 2009; Bhattacharyya et al., 2018) of the Hořava gravity (Horava, 2009). It was also seen to emerge in various limits of new inflationary models (Adshead et al., 2016), in alternative models for inflation (Bessada et al., 2010), and in new approaches to resolve cosmological constant problem (D'Amico et al., 2011; Afshordi et al., 2014), among others. In a more recent work, a Galileon generalisation of the cuscuton was realised to be one of the three generalisation of the Galileon theories that do not form spherical caustics (de Rham & Motohashi, 2017).

The cuscuton model can be simply formulated by introducing a non-canonical[1] scalar field to General Relativity and requiring the field to be incompressible (Afshordi et al., 2007a). One notices that in that limit, the equation of motion of this field does not have any time derivatives. This means that the cuscuton field does not have its own dynamics, but rather modifies the dynamics of other dynamical fields. In other words, cuscuton acts

[1]In a non-canonical scalar field theory, the kinetic energy term is differs from the canonical kinetic term, $X = g^{\mu\nu}\nabla_\mu\phi\nabla_\nu\phi$

as an auxiliary field and it does not introduce new degrees of freedom. It is also manifest through all the equations of motion that it only modifies general relativity on large scales. As such, although it appears to be a scalar field theory, one should really think of it as a non-local modification of gravity. In this chapter and the next, we would use cuscuton to mean both points of view. When referring to the field, we call it the cuscuton field or simply cuscuton (analogous to the inflaton). When referring to the modification to gravity, we call it 'cuscuton gravity'.

In this chapter, we present the derivation of the quadratic action for cuscuton gravity as presented in Boruah et al. (2017). Note that the cuscuton equation of motion is a constraint equation which introduces non-local operators in the action, making it a non-trivial derivation. To evade this problem, we carried out our analysis in Fourier space. The other difficulty is that a priori, it is not clear what variable would be a best candidate for describing a conserved quantity ζ, if it even exists in cuscuton gravity. In standard theory of cosmological perturbations, there are different ways one can define this quantity based on a particular gauge or matter components in the model (Bardeen, 1980; Bardeen et al., 1983; Brandenberger et al., 1994; Maldacena, 2003). For instance, it can be defined as curvature perturbation with respect to the comoving gauge for one of the matter components or alternatively with respect to the total matter (Bardeen, 1980). It can also be defined in terms of metric fluctuations and the over all equation of state in Newtonian/longitudinal gauge (Brandenberger et al., 1994). For single component models, these definitions either coincide or merge on super horizon scales. Furthermore, on these scales they all contain a conserved mode and a time dependent mode which often decays away. However, for cuscuton, even though it does not introduce any additional degree of freedom, it does resemble multi-field models. To be more explicit, its formulation starts by modifying the right hand side of Einstein equation. Naively, it seems that it contributes to energy density and momentum density. Therefore, the question is which of these definitions will be best suited for defining ζ. In the end, it was evident to us that all these definitions generate a conserved mode at large scales and they merge on small scales. However, it turns out that if ζ is defined as comoving curvature perturbation with respect to only the source field, the computations are significantly simplified.

Derivation of the action for ζ provides a rigorous proof that indeed cuscuton models do not have any ultraviolet pathologies. Furthermore, it provides fascinating new possibilities for beginning of our universe that could not be explored within the realm of General Relativity. One example of that is the possibility of a regular bounce initial condition within cuscuton gravity which we will present in chapter 3. In General Relativity that entails breaking energy conditions which lead to different types of instabilities. However, as our work shows, cuscuton can evade breaking those conditions.

This chapter is organized in the following way: in Section (2.2), we review the background equations in a Friedmann-Lemaitre-Robertson-Walker (FLRW) universe in presence of cuscuton. We then outline the derivation of second order action for curvature perturbations in presence of the cuscuton field in section (2.3). In case readers are interested to repeat our analysis, a more detailed version of this derivation can be found in Appendix (A). In section (2.4), we discuss why the quadratic action for ζ implies that cuscuton theories are ghost free. We also study the conditions for appearance of other types of instabilities in cuscuton models and conservation of ζ in the infrared (IR). Our concluding remarks are presented in (2.5).

2.2 Theory

2.2.1 Review of theory

Consider a scalar field theory where the Lagrangian is an arbitrary function, $P(X, \varphi)$, of, $X = \partial_\mu \varphi \partial^\mu \varphi$, and φ, on a FLRW cosmological background. In terms of the conformal time, τ, the metric is given as,

$$ds^2 = a^2(\tau)(-d\tau^2 + \delta_{ij} dx^i dx^j). \tag{2.1}$$

Note that, Einstein's summation convention is used for this chapter. The background field equation for such a theory is,

$$(P_{,X} + 2X P_{,XX})\varphi'' + 3\mathcal{H} P_{,X}\varphi' + P_{,X\varphi}\varphi'^2 - \frac{1}{a^2} P_{,\varphi} = 0. \tag{2.2}$$

Considering the limit where the coefficient of the second derivative term vanishes, leads to

$$P_{,X} + 2X P_{,XX} = 0. \tag{2.3}$$

The unique theory where this condition is satisfied everywhere in phase space is given by the following action,

$$S_{\rm cusc} = \int d^4x \sqrt{-g}\big[\pm \mu^2 \sqrt{X} - V(\varphi)\big]. \tag{2.4}$$

The field equation obtained from the action(2.4) is given by,

$$(g_{\mu\nu} - \frac{\partial_\mu \varphi \partial_\nu \varphi}{X}) D^\mu D^\nu \varphi \pm \frac{1}{\mu^2} \sqrt{X} V'(\varphi) = 0, \tag{2.5}$$

where D^μ denotes the four dimensional covariant derivative. There are different ways that one can show this equation does not have any propagating modes (Afshordi et al., 2007a). This will be manifest in our analysis later in this chapter at linear order as well. However, the main argument holds at any order in perturbation theory.

2.2.2 Background Cosmology

As mentioned above, cuscuton is a field with no dynamics and acts as a non-local modification to Einstein's gravity. Therefore, to produce dynamical cosmological solutions in a cuscuton scenario, there needs to be other sources with propagating degrees of freedom. In our work, we consider the scalar mode to be sourced by a scalar field, π, with a canonical kinetic term and minimally coupled to the cuscuton field, φ. So we start with the action[2]

$$S = \int d^4x\sqrt{-g}\big[\frac{1}{2}R - \frac{1}{2}D_\mu\pi D^\mu\pi - U(\pi) \pm \mu^2\sqrt{-D_\mu\varphi D^\mu\varphi} - V(\varphi)\big]\,. \tag{2.6}$$

We now substitute the FLRW metric (2.1) in this action and assuming homogeneity and isotropy, derive the the background equations

$$3\mathcal{H}^2 = \frac{1}{2}\pi_0'^2 + V(\varphi_0)a^2 + U(\pi_0)a^2 \tag{2.7a}$$

$$\mathcal{H}^2 - \mathcal{H}' = \frac{1}{2}\pi_0'^2 \pm \frac{\mu^2}{2} \mid \varphi_0' \mid a. \tag{2.7b}$$

In our notation, $\mathcal{H} \equiv \frac{a'}{a}$, where $'$ denotes the derivative with respect to conformal time, $\frac{d}{d\tau}$. We are also denoting the background homogeneous values with a subscript, $_0$. If we introduce the following dimensionless quantities,

$$\alpha \equiv \frac{\pi_0'^2}{2\mathcal{H}^2} \tag{2.8}$$

$$\epsilon \equiv \frac{\mathcal{H}^2 - \mathcal{H}'}{\mathcal{H}^2}, \tag{2.9}$$

then equation (2.7b) can be written as

$$\sigma \equiv \epsilon - \alpha = \pm\frac{\mu^2}{2\mathcal{H}^2} \mid \varphi_0' \mid a. \tag{2.10}$$

[2]We use the units, where the Planck mass, $M_{\rm pl} = 1$.

In the standard single field inflationary models, the quantities ϵ and α[3] coincide and in inflationary context, they are referred to as *the first slow-roll* parameter. Therefore, σ denotes the deviations from standard GR due to cuscuton. Furthermore, its sign is dictated by the sign of μ^2 taken in the action. Note that if we choose $+\mu^2$ in the action, ϵ will automatically be positive.

Next, we can obtain the equation of motion for cuscuton

$$\pm 3\mu^2 \text{sign}(\varphi_0')\mathcal{H} = -aV_{,\varphi}(\varphi_0), \tag{2.11}$$

which, as expected, is only a constraint equation for $\mathcal{H}$. For a specific cuscuton potential, equation (2.11) can be inverted to express φ_0 as a function of $\mathcal{H}$. Combining that with (2.7a), we can then explicitly see that at background level, cuscuton simply modifies the Friedmann equation

$$3\mathcal{H}^2 = \frac{1}{2}\pi_0'^2 + U(\pi_0)a^2 + V\left(V_{,\varphi}^{-1}\left(-\frac{\pm 3\mu^2 \text{sign}(\varphi_0')\mathcal{H}}{a}\right)\right)a^2. \tag{2.12}$$

Therefore, the functional form of the potential $V(\varphi)$, dictates the form of modified Friedmann equation (2.12). Also there is no consistent cuscuton FRW solution if the cuscuton potential is set to zero. Equation (2.11) also leads to

$$V_{,\varphi\varphi}(\varphi_0) = \frac{3\mu^4}{2}\left(1 + \frac{\alpha}{\sigma}\right) \tag{2.13}$$

which tells us if we choose $+\mu^2$ in the action ($\sigma > 0$), then there is a lower bound on $V_{,\varphi\varphi}$.

We end this section by including the equation of motion for the scalar field, π,

$$\pi_0'' + 2\mathcal{H}\pi_0' - a^2\frac{\partial U}{\partial \pi}\pi_0' = 0. \tag{2.14}$$

2.3 The quadratic action for curvature perturbations in cuscuton gravity

This section presents our main result. Similar to the standard method of deriving the quadratic action, we start with the ADM formalism (Arnowitt et al., 2008). ADM variables provide a convenient way for splitting the $3+1$ space-time into a space-like foliation and a

[3] In the notation of section 1.2, $\alpha = \epsilon_{\mathbf{v}}$.

time direction. In this approach, metric is written in terms of the lapse, N, shift, N_i and the 3-dimensional metric h_{ij} as,

$$ds^2 = -N^2 d\tau^2 + h_{ij}(dx^i + N^i d\tau)(dx^j + N^j d\tau). \tag{2.15}$$

Rewriting the action (2.6) in terms of Eintein-Hilbert part, the scalar field, π and Cuscuton part and then substituting for ADM variables we get

$$S = S_{EH} + S_\pi + S_\varphi, \tag{2.16}$$

where

$$S_{EH} = \frac{1}{2}\int d\tau d^3x\sqrt{h}\Big[NR^{(3)} + N^{-1}(E_{ij}E^{ij} - E^2)\Big], \tag{2.17}$$

$$S_\pi = \frac{1}{2}\int d\tau d^3x\sqrt{h}\Big[N^{-1}(\pi' - N^i\partial_i\pi)^2 - Nh^{ij}\partial_i\pi\partial_j\pi - 2NU(\pi)\Big], \tag{2.18}$$

$$S_\varphi = \frac{1}{2}\int d\tau d^3x\sqrt{h}\Big[\pm 2\mu^2\sqrt{((\varphi' - N^i\partial_i\varphi)^2 - N^2h^{ij}\partial_i\varphi\partial_j\varphi)} - 2NV(\varphi)\Big]. \tag{2.19}$$

$R^{(3)}$ represents the Ricci scalar of the spacial hyper-surfaces and E_{ij} is defined as

$$E_{ij} = \frac{1}{2}h'_{ij} - \frac{1}{2}(\nabla_i N_j + \nabla_j N_i). \tag{2.20}$$

∇ represents the covariant derivative with respect to the spatial metric, h_{ij}, while ∂ denotes the partial derivative with respect to the comoving coordinates. Variation of action (2.16) with respect to lapse and shift leads to momentum and Hamiltonian constraints,

$$\nabla_i(N^{-1}(E^i_j - \delta^i_j E)) = q_{,i} \tag{2.21a}$$

$$R^{(3)} + N^{-2}(E^2 - E^{ij}E_{ij}) = 2\rho. \tag{2.21b}$$

Here $q_{,i}$ is the momentum density and the ρ is the total energy density, including cuscuton contributions. We now proceed to perform perturbative analysis around FLRW background. There are two gauge degrees of freedom associated with the scalar perturbations. We can remove one of them by choosing uniform field gauge with respect to π field

$$\delta\pi = 0. \tag{2.22}$$

In this gauge, the time foliation is taken to be the π constant hyper-surfaces. One can transfer from any other gauge with $\delta\pi \neq 0$ to $\delta\pi = 0$ through a time coordinate transformation $t \to t + \xi^0(x,t)$ and choosing $\xi^0(x,t) = \frac{\delta\pi(x,t)}{\dot{\pi}_0}$ since

$$\delta\pi(x,t) \to \delta\pi(x,t) - \dot{\pi}_0\xi^0. \tag{2.23}$$

Of course, there is an underlying assumption here that $\dot{\pi}_0 \neq 0$. The other gauge freedom can be fixed by setting the off-diagonal components of the spatial metric to zero[4]

$$h_{ij} = a^2(1+2\zeta)\delta_{ij} \ . \tag{2.24}$$

In the literature, ζ is often referred to as comoving curvature perturbation. Note that comoving here refers only with respect to π field. As we will see, this particular choice produces a viable conserved quantity and makes the computations considerably simpler. The scalar contributions to lapse and shift function in the metric can be written as,

$$N_i = \nabla_i \psi, \quad N = a\ (1+N_1) \ . \tag{2.25}$$

Finally, we denote the perturbations associated with the the cuscuton field by $\delta\varphi$. Writing the momentum constraint (2.21a) and the Hamiltonian constraint (2.21b) to linear order in perturbations yields

$$N_1 = \frac{\zeta'}{\mathcal{H}} \pm \frac{1}{2}\mu^2 a\ \text{sign}(\varphi_0')\frac{\delta\varphi}{\mathcal{H}} \tag{2.26a}$$

$$\nabla^2\psi = -\frac{1}{\mathcal{H}}\nabla^2\zeta + \frac{\pi_0'^2}{2\mathcal{H}}N_1 \ . \tag{2.26b}$$

The next step is to perturb the action (2.16) to second order in the perturbative variables, N_1, ψ, ζ and $\delta\varphi$. This calculation is involved and readers can refer to Appendix A for the details. We then remove N_1 and ψ using the constraint equations (2.26a) and (2.26b). The result for the second order action after taking into account the background equations, is

$$S^{(2)} = \int d\tau d^3x\ a^2 \left[\alpha\zeta'^2 - \epsilon(\partial\zeta)^2 + \sigma\left(\frac{\mathcal{H}\delta\varphi}{\varphi_0'}\right)\left(\alpha\mathcal{H}\zeta' - \partial^2\zeta\right)\right] \ . \tag{2.27}$$

In the $\sigma \to 0$ limit in which contributions from cuscuton vanish, the action (2.27), simplifies to the standard quadratic action for curvature perturbations.

$$S^{(2)} = \int d\tau d^3x\ a^2\alpha\left[\zeta'^2 - (\partial\zeta)^2\right] \tag{2.28}$$

As we pointed out before, the field equation for cuscuton (2.5) provides another constraint equation. At linear order this equation reduces to

$$\nabla^2\delta\varphi - \mathcal{H}^2\alpha\big[3+\alpha-\epsilon\big]\delta\varphi = \frac{\varphi_0'}{\mathcal{H}}\left[\nabla^2\zeta - \alpha\mathcal{H}\zeta'\right] . \tag{2.29}$$

[4]We are using similar convention and notation to Maldacena (2003).

In order to eliminate $\delta\varphi$ from the action (2.27), we need to invert the above equation. However, since this involves inverting derivative operators, we continue our derivation in Fourier space. This allows us to substitute $\delta\varphi_k$ in terms of ζ_k and ζ_k' using this formula

$$\delta\varphi_k = \frac{\varphi_0'}{\mathcal{H}} \frac{\mathbf{k}^2\zeta_k + \alpha\mathcal{H}\zeta_k'}{\left[\mathbf{k}^2 + (3+\alpha-\epsilon)\alpha\mathcal{H}^2\right]}. \tag{2.30}$$

After Fourier transforming the action (2.27), substituting for $\delta\varphi_k$ and some algebraic calculations, we finally arrive at

$$S^{(2)} = \int d^4x\ z^2 \left[\zeta_k'^2 - c_s^2\ \mathbf{k}^2\zeta_k^2\right]. \tag{2.31}$$

$z(\mathbf{k},\tau)$ and $c_s(\mathbf{k},\tau)$ in above action are both time and scale dependent functions given by

$$z^2 \equiv a^2\alpha\left(\frac{\mathbf{k}^2 + 3\alpha\mathcal{H}^2}{\mathbf{k}^2 + \alpha\mathcal{H}^2(3-\sigma)}\right) \tag{2.32}$$

$$c_s^2 \equiv \frac{\mathbf{k}^4 + \mathbf{k}^2\mathcal{H}^2\mathcal{B}_1 + \mathcal{H}^4\mathcal{B}_2}{\mathbf{k}^4 + \mathbf{k}^2\mathcal{H}^2\mathcal{A}_1 + \mathcal{H}^4\mathcal{A}_2}, \tag{2.33}$$

and we have introduced the following additional notation,[5]

$$\eta \equiv \frac{\epsilon'}{\mathcal{H}\epsilon} \tag{2.34}$$

$$\beta \equiv \frac{\alpha'}{\mathcal{H}\alpha} \tag{2.35}$$

$$\mathcal{A}_1 \equiv 6\alpha - \alpha\sigma \tag{2.36}$$

$$\mathcal{A}_2 \equiv 9\alpha^2 - 3\alpha^2\sigma \tag{2.37}$$

$$\mathcal{B}_1 \equiv \mathcal{A}_1 + \sigma(6+\eta+\beta-2\epsilon) + \alpha(\eta-\beta) \tag{2.38}$$

$$\mathcal{B}_2 \equiv \mathcal{A}_2 + \sigma\alpha(12-4\sigma+3\eta) + 3\alpha^2(\eta-\beta). \tag{2.39}$$

It is also evident here that in the $\sigma \to 0$ limit, we get back the standard single scalar field result of $c_s^2 \sim 1$ and $z^2 \sim a^2\alpha$.

2.4 Ghosts, instabilities and conservation of ζ

It is manifest from the action (2.31), that cuscuton is ghost free around FLRW background. As expected, the leading $\mathbf{k}$ terms in the action do not have cuscuton dependence. Therefore,

[5] A detailed calculation is presentation in Appendix A.

in the UV limit ($\mathbf{k} \to \infty$), we get the standard single scalar field result of $z^2 \sim a^2\alpha > 0$. This implies that the theory is ghost free regardless of the sign or value of ϵ, or which sign for μ^2 is taken in the action. In fact, one generic feature is that for $-\mu^2$ in the action, since σ is automatically negative, z^2 always remains positive regardless of scale. On the other hand if we pick the $+\mu^2$ factor in the original cuscuton action (2.4), then $\sigma > 0$. In this case, one may ask what happens in a region of parameter space with $\sigma \geq 3$. In other words, is there a pathology associated to z^2 diverging or becoming negative. Note that producing such a model would require engineering peculiar potentials and tuning of μ^2 which seems very contrived. Nevertheless, that would not indicate a ghost in the theory. The notion of ghost is only a meaningful statement in the UV limit and as we have pointed earlier, that limit is always fine. When we deviate from the limit of flat background or time independent actions, energy conservation and plain wave description of modes breaks down. One may still evaluate the Hamiltonian and it can be negative but that doesn't necessarily tell us if there is an instability in the system or not. In fact, even in standard inflationary models, the Hamiltonian becomes negative on super horizon scales and resembles excited states with negative energy but theory is still healthy (Mukhanov & Winitzki, 2007b).

A theory might be ghost free but still suffer from other types of instabilities such as gradient instability. However, as long as instabilities are not in UV, they are only indicative of a growing solution that can be circumvented by tuning the parameters of the model. Whether a particular cuscuton scenario exhibits such an instability in a specific region of phase space or not, will depend on the details of the model. To elaborate, let us write down the equation of motion for ζ_k derived from the action (2.31):

$$\zeta_k'' + \left(2 + \beta + \frac{\mathcal{C}_1\mathcal{H}^2k^2 + \mathcal{C}_2\mathcal{H}^4}{\mathbf{k}^4 + \mathbf{k}^2\mathcal{H}^2\mathcal{A}_1 + \mathcal{H}^4\mathcal{A}_2}\right)\mathcal{H}\zeta_k' + c_s^2k^2\zeta_k = 0 \tag{2.40}$$

where,

$$\mathcal{C}_1 = (\beta + 2\alpha - 2\alpha^2 - 2\alpha\sigma)\sigma + 3\alpha^2(\eta - \beta) \tag{2.41}$$

$$\mathcal{C}_2 = 3\alpha^2(\eta - \beta). \tag{2.42}$$

As we see there are quite a few parameters that can determine the sign and behaviour of c_s^2 and coefficients of ζ_k'. While we cannot make conclusive statement for every cuscuton scenario, we comment on some generic features. First, in the UV limit, all the cuscuton contributions go away and $c_s^2 \to 1$. Therefore, there is no gradient instability in that limit.

Second, the non-trivial denominator shared in one of the coefficients of ζ_k' and c_s^2 can be factored as

$$\mathbf{k}^4 + \mathbf{k}^2\mathcal{H}^2\mathcal{A}_1 + \mathcal{H}^4\mathcal{A}_2 = (\mathbf{k}^2 + 3\alpha\mathcal{H}^2)(\mathbf{k}^2 + \alpha\mathcal{H}^2(3 - \sigma)). \tag{2.43}$$

Therefore, for $-\mu^2$ in the action or $+\mu^2$ with $\sigma < 3$, the equation of motion for ζ_k is not singular. Models with $+\mu^2$ and $\sigma \geq 3$ can allow for poles which make the equation of motion for ζ_k singular. Singular ODEs are not necessarily catastrophic and they may be treatable. In fact, as we mentioned before for $+\mu^2$, Equation 2.10, dictates that $\epsilon > 0$ at all times. Therefore, an expanding universe can not go through a bounce. It turns out for $+\mu^2$ and $\epsilon > 0$, one can write the equation of motion for Φ potential in longitudinal gauge and there the equation is not even singular (Afshordi et al., 2007b).

Next, we check the behaviour of ζ_k in the IR to see if it is conserved or not. In the $k \to 0$ limit, as long as $\sigma \neq 3$, $z^2 c_s^2$ remains finite and equation of motion can be estimated as

$$\frac{d}{d\tau} z^2 \zeta_k' \approx 0. \tag{2.44}$$

Similar to the standard case, the solutions to this equation include a desirable constant mode for ζ_k as well as a time dependent mode that goes as $\int d\tau/z^2$. One can investigate under what conditions this mode decays away or grows outside the horizon. Substituting z^2 from Eq. 2.32, taking the IR limit and rewriting the time dependence of this mode in terms of e-folding number, $N \equiv \ln a$, we find

$$\zeta_{IR}^{(time)} \propto \int \frac{d\tau}{z^2}\bigg|_{IR} \approx \int \left(\frac{1-\frac{\sigma}{3}}{\alpha}\right)\left(\frac{dN}{e^{3N-\int \epsilon d\tilde{N}}}\right). \tag{2.45}$$

Therefore, generically in an expanding universe (N is increasing in time), $\epsilon < 3$ can lead to a decaying mode outside the horizon but $\epsilon \geq 3$ can produce a growing mode. On the other hand, in a contracting model since N is decreasing, we expect the reverse. Of course, this is no different from ordinary cosmological perturbation theory, except that here a cuscuton model may compensate for these effects by having the time variation of σ cancel the exponential term in the integral. It is also interesting to note that $\sigma \geq 3$ models which as we said can only be realized in $+\mu^2$ actions and expanding scenarios lead to $\epsilon = \alpha + \sigma > 3$.

Last, let us also comment on how are definition of ζ differs from other definitions in literature. For example, in single field models, sometimes a conserved parameter ζ_s is defined in longitudinal/Newtonian gauge[6] as

$$\zeta_s = \Phi + \frac{\Phi' + \mathcal{H}\Phi}{\epsilon \mathcal{H}}. \tag{2.46}$$

[6]In this gauge, shift function, N_i is set to zero and $h_{ij} = a^2(1+2\Phi)\delta_{ij}$ which implies $N_1 = -\Phi$.

A time transformation $t \to t - \psi$ shows that ζ_s is related to our choice of ζ in the following way

$$\zeta_s = \zeta - \frac{\sigma \mathcal{H} \delta\varphi}{\varphi_0'}. \tag{2.47}$$

Substituting for $\delta\varphi$ from (2.30), we can obtain an explicit relation for ζ to the Newtonian potential Φ in Fourier space

$$\zeta_k = \Phi_k + \frac{\Phi_k' + \mathcal{H}\Phi_k}{\epsilon\mathcal{H}} \left[1 - \frac{3\mathcal{H}^2\sigma}{\mathbf{k}^2 + 3\mathcal{H}^2\epsilon}\right]. \tag{2.48}$$

As we see, these equations show that as $\sigma \to 0$ and in the UV limit, these two definitions merge. In the IR limit we get

$$\zeta_s \simeq \zeta + \frac{\sigma}{\mathcal{H}(3-\sigma)}\zeta', \tag{2.49}$$

which implies if ζ is conserved ζ_s will be conserved too. We can also perform the time transformation $t \to t + \frac{\sigma}{\epsilon}\frac{\delta\varphi}{\varphi_0'}$ to go the comoving gauge with respect to the total momentum of both the cuscuton and the π field ($T_i^0 = 0$). In that case, the comoving curvature perturbation is

$$\zeta_t = \zeta + \frac{\sigma \mathcal{H} \delta\varphi}{\epsilon\varphi_0'}, \tag{2.50}$$

which leads to similar results in different limits. Therefore, from physical point of view there does not seem to be any advantage in choosing one definition over the other as long as ζ does not have a growing mode outside the horizon. However, from the computational point of view, we found that the derivation of the equations and the action was considerable simpler when we used the comoving gauge with respect to the source field.

We end this discussion by emphasising again that, similar to usual model buildings in GR scenarios, the question of instabilities will depend a lot on the details of the potentials. If anything, with cuscuton there is more room to evade these problems.

2.5 Conclusion

The main goal of this chapter was to obtain the quadratic action for comoving curvature perturbations, ζ, in cuscuton models. We started from an action that included the standard Hilbert-Einstein term, a canonical scalar field and a cuscuton field. We then used the ADM formalism and the uniform field gauge with respect to the scalar field to obtain the quadratic action for ζ. In order to eliminate the cuscuton dependence from this action we

had to invert the cuscuton constraint equation. Therefore, we carried out the derivation in Fourier space. As expected, our final action (2.31) had a complicated form but it explicitly shows that cuscuton models are ghost free and have no instabilities in UV limit. Basically, in the UV limit, the action becomes the standard quadratic action for a scalar field, minimally coupled to gravity. Upon further investigation of the equation of motion for ζ_k in section 2.4, we also saw that there are no out of ordinary instabilities on non-UV scales either. This analysis shows that depending on the details of a particular cuscuton model and the potential of the scalar field, some corners of parameter space may lead to growing modes. Interestingly, it seems that if we choose a $-\mu^2$ for cuscuton kinetic term in the action, there is more room for different background evolutions and less chance of developing instabilities. That will be very useful in exploring bounce scenarios. In order to get a bounce one has to choose $-\mu^2$ in the action and make the parameter ϵ become negative. However, with cuscuton that does not lead to ghosts since the source field does not violate the null energy condition. That is the subject of the next chapter. We also showed that our choice of ζ was consistent with producing a conserved mode on super horizon scales. We noticed that although other common definitions of ζ are different physical quantities, they also produce a conserved mode and all of these definitions merge on small scales. From the computational point of view, we found that derivation of equations and action were considerably simpler when we picked ζ as the comoving curvature perturbation with respect to the source field.

Chapter 3

Cuscuton Bounce

3.1 Introduction

As reviewed in Chapter 1, precise observations of the CMB and large scale structure have provided tight constraints on our cosmological models. Cosmology on the theoretical front has also been very successful in building models of early universe that can match these observations. The inflationary paradigm is arguably the most popular among the current models. However, as we saw in section 1.2.5, inflationary models do not address all the fundamental questions about the beginning of universe. For instance, it has been argued that inflationary space-times are not past-complete (Borde et al., 2003). In other words, inflation doesn't provide a resolution to singularity problem. It is generally posited that quantum gravity effects might lead to the resolution of this problem. However, invoking the unknown powers of quantum gravity to address any initial condition problem that we can not resolve, can be a double-edged sword. For instance, if quantum gravity effects are important, the framework of quantum field theory on curved space-time, which is used to make predictions for inflation becomes invalid at the scales of interest and leads to the so-called trans-Planckian problem (Martin & Brandenberger, 2001; Brandenberger, 2010). One would hope that if quantum gravity is relevant at early universe, its effects can be formulated in systematic ways, that can also be tested.

One way in which the singularity problem can be evaded is by considering bouncing cosmologies, in which an initially contracting universe 'bounces' and starts expanding. Many models of regular bouncing cosmologies using different scalar fields have been proposed in the literature (Khoury et al., 2001; Ijjas & Steinhardt, 2017; Fertig et al., 2016; Cai et al., 2012, 2013; Easson et al., 2011; Qiu et al., 2011; Creminelli et al., 2006; Cai et al., 2017a,b;

Dubovsky et al., 2006; Creminelli et al., 2010). One of the obstacles that regular bouncing scenarios face is that, in general relativity, a bounce requires the violation of the Null Energy Condition (NEC). This generally leads to instabilities or superluminal speed of sound in the models (Dubovsky et al., 2006). In fact, stable NEC violation is also an interesting topic for other areas of gravitational physics, such as traversable wormhole solutions or models which require universe to be initially static (Creminelli et al., 2010). There are few proposals in the literature regarding stable ways to violate the NEC. For example, the 'Kinetic Gravity Braiding' model, a sub-class of the Horndeski action, was introduced in Deffayet et al. (2010) to stably violate the NEC in late universe. Later, the bouncing scenario using this model was realized in Easson et al. (2011); Qiu et al. (2011). Other proposals include the Ghost condensate (Creminelli et al., 2006) as well as new approaches that describe a bounce through effective field theories (Cai et al., 2017a,b).

In this chapter, we present a new resolution for instabilities associated with NEC violating scenarios. We show that the cuscuton modification of gravity (Afshordi et al., 2007a,b) allows for an effective violation of the NEC in FRW backgrounds while the actual matter sources satisfy the NEC. As seen in the previous chapter, the kinetic term of the cuscuton field is such that it has no dynamical degree of freedom. Instead, it modifies gravity in infrared (IR) regime. Due to its non-dynamical nature, cuscuton models still need other fields to produce dynamics. Note that recently it has been shown that NEC violation derived by single non-canonical scalar field, $P(X, \phi)$, in the region of validity of the EFT leads to violation of unitarity condition (de Rham & Melville, 2017). However, our model does not fall under the category of models discussed there as it does not belong to single field theories. In other words, cuscuton is instrumental to make the background bounce but the actual dynamical degree of freedom does not violate NEC. We would like to also point out that cuscuton terms have previously been shown to be important in realizing a bounce solution within k-essence models[1] (Romano, 2017) as well as a stable matter bounce scenario in massive gravity models (Lin et al., 2018).

This chapter is structured in the following way: in Section 3.2, we present a toy model for a cuscuton bounce scenario. In Section 3.3, we analyze the existence of ghosts and other instabilities in this model. We end with our concluding remarks in Section 3.4.

[1]There, cuscuton term is part of the single field non-canonical kinetic terms.

3.2 A toy model for cuscuton bounce

Consider the following action for a scalar field with a noncanonical kinetic term,

$$S = \int d^4x\sqrt{-g}L(\varphi, X) \ , \tag{3.1}$$

where L is an arbitrary function of the scalar φ and $X \equiv \frac{1}{2}\partial_\mu\varphi\partial^\mu\varphi$ [2].

This action is compatible with a perfect fluid description

$$T_{\mu\nu} = (\rho + P)u_\mu u_\nu - Pg_{\mu\nu} \tag{3.2}$$

assuming

$$u_\mu \equiv \frac{\partial_\mu\varphi}{\sqrt{2X}} \tag{3.3}$$

is time-like. The energy density and the pressure in the comoving fame of u_μ are

$$\rho = T_{\mu\nu}u^\mu u^\nu = 2XL_{,X} - L \tag{3.4}$$

$$P = L. \tag{3.5}$$

We use $_{,X}$ to denote the partial derivative with respect to the variable X.

In a flat FRW background

$$ds^2 = dt^2 - a^2(t)\delta_{ij}dx^i dx^j, \tag{3.6}$$

the homogeneous field equation (3.1) reduces to,

$$(L_{,X} + 2XL_{,XX})\ddot{\varphi}_0 + 3HL_{,X}\dot{\varphi}_0 + L_{,X\varphi}\dot{\varphi}_0^2 - L_{,\varphi} = 0 \ , \tag{3.7}$$

where H represents the Hubble constant and we denote the time derivative with an overdot. *Cuscuton* modification of gravity is achieved by taking the incompressible limit of the above perfect fluid such that everywhere on (φ, X) plane

$$L_{,X} + 2XL_{,XX} = 0. \tag{3.8}$$

As we see in that limit, the equation of motion is no longer second order since the second time derivative of φ vanishes (see Afshordi et al. (2007a,b) for more details). A Lagrangian that satisfies the above requirement everywhere in phase space corresponds to

$$L(\varphi, X) = \pm\mu^2\sqrt{2X} - V(\varphi), \tag{3.9}$$

[2] We will use units with $M_p^2 = 1/8\pi G$ and the metric signature is $(+, -, -, -)$.

which is called the *Cuscuton* Lagrangian. What is more interesting about this Lagrangian is that when we substitute it in 3.7, not only does the $\ddot{\varphi}$ dependence vanishes but the $\dot{\varphi}$ dependence cancels as well, leading to the following constraint equation

$$\pm \text{sign}(\dot{\varphi}) 3\mu^2 H + V'(\varphi) = 0 \ . \tag{3.10}$$

μ can in principle depend on φ but that dependence can be absorbed into a field redefinition such that a new cuscuton action with constant μ and a new potential is obtained.

Since the cuscuton equation is not dynamical, contributions of dynamical matter sources in the universe are necessary to obtain any cosmological evolution. Here, we consider a toy bounce model where the universe consist of a barotropic fluid $p_{\text{fl}} = w\rho_{\text{fl}}$ in addition to the cuscuton field. A desirable model would initially be a contracting universe where in very early times the cuscuton modifications of gravity are negligible. However, as it gets smaller the cuscuton modification becomes important, causing the universe to bounce into an expanding phase. For simplicity we assume $w = 1$ so $\rho_{\text{fl}} \propto a^{-6}$, making cuscuton contributions grow even faster close to the bounce and be dominant over anisotropies. However, this assumption is not fundamental for our result. A simple way to produce such an equation of state from the action is to include a canonical scalar field, π, with no potential and which is minimally coupled to gravity. That will later allow us to consistently study the behaviour of perturbations during the bounce.

A main feature of a regular bounce ($H \neq \pm\infty$) is that universe goes from a contracting phase ($H < 0$) into an expanding one ($H > 0$) at finite value of scale factor, a_b, where b denotes the bounce. . This criteria automatically implies

$$H_b = 0 \tag{3.11}$$

$$\dot{H}_b > 0, \tag{3.12}$$

In general relativity, the second condition necessitates the violation of NEC for a perfect fluid source.

We now investigate the possibility of a bounce solution in a framework, consisting of cuscuton and a barotropic fluid ρ_{fl}. The Friedmann and continuity equations can be obtained from action or Einstein's equations

$$H^2 = \frac{1}{3M_p^2}[V(\varphi) + \rho_{\text{fl}}] \tag{3.13}$$

$$\dot{H} = -\frac{1}{2M_p^2}[\pm\mu^2\sqrt{2X} + (1+w)\rho_{\text{fl}}]. \tag{3.14}$$

Therefore, requiring the energy condition $\rho_{\text{fl}} > 0$ and (3.11) be satisfied at the bounce leads to

$$V(\varphi_b) < 0. \tag{3.15}$$

On the other hand, condition (3.12) implies that only the choice of the negative sign for cuscuton kinetic term could lead to a bounce solution. So from here on we only consider

$$L(\varphi, X) = -\mu^2\sqrt{2X} - V(\varphi). \tag{3.16}$$

This, in turn, means that Eq. (3.10) becomes

$$-\text{sign}(\dot{\varphi})3\mu^2 H + V'(\varphi) = 0\ . \tag{3.17}$$

Taking the time derivative of this equation leads to

$$3\mu^2\dot{H} = V''(\varphi)|\dot{\varphi}|. \tag{3.18}$$

Therefore, in the regimes in which the NEC is valid ($\dot{H} < 0$), the cuscuton potential must satisfy

$$V'' < 0, \qquad \text{for NEC}, \tag{3.19}$$

but close to the bounce,

$$V'' > 0, \qquad \text{for NEC violation}. \tag{3.20}$$

In addition, substituting H from Eq. (3.10) back into Eq. (3.13), we arrive at

$$\frac{M_p^2}{3\mu^4}V'^2(\varphi) = V(\varphi) + \rho_{\text{fl}}\ . \tag{3.21}$$

This equation demonstrates how for a particular potential $V(\phi)$, the evolution of cuscuton depends on other matter/fluid sources in the universe. We can also use this relation to derive further constraints on the cuscuton potential. Taking a time derivative of Eq. (3.21), combining it with continuity equation for the additional fluid, $\dot{\rho}_m = -3H(\rho_{\text{fl}} + p_{\text{fl}})$, and Eq. (3.10) we get[3]

$$\frac{2M_p^2}{3\mu^4}V''(\varphi) - 1 = -(1+w)\frac{\rho_{\text{fl}}}{\mu^2|\dot{\varphi}|} < 0, \tag{3.22}$$

for $w > -1$ or that

$$V''(\varphi) < \frac{3\mu^4}{2M_p^2}. \tag{3.23}$$

[3]This equation together with (3.21) also demonstrates, how $\dot{\varphi}$ is uniquely determined as a function of φ.

This enables us to conclude that while the shape of the potential in the NEC violating era (around the bounce) is convex (3.20), its convexity is in this range:

$$0 < V''(\varphi_b) < \frac{3\mu^4}{2M_p^2}. \tag{3.24}$$

However, as we argued before, potential has to become concave, $V''(\varphi) < 0$, in regions that NEC is restored. Setting additional assumptions such as far from the bounce cuscuton modifications of gravity are negligible, can also be used to obtain additional restriction about the shape of the potential. This assumption can be applied by requiring

$$\lim_{t\to\pm\infty} H^2 = \lim_{t\to\pm\infty} \frac{1}{3M_p^2}\rho_{\rm fl} \to 0, \tag{3.25}$$

$$\lim_{t\to\pm\infty} \dot{H} = \lim_{t\to\pm\infty} -\frac{1+w}{2M_p^2}\rho_{\rm fl} \to 0, \tag{3.26}$$

where $t = 0$ corresponds to the bounce. Using the above conditions in combination with Eq. (3.22), Eq. (3.10) and Eq. (3.21), one can show

$$\lim_{t\to\pm\infty} V'(\varphi_\infty) = 0 \tag{3.27}$$

$$\lim_{t\to\pm\infty} \frac{3\mu^4}{M_p^2}\frac{|V(\varphi_\infty)|}{V'^2(\varphi_\infty)} \ll 1 \tag{3.28}$$

$$\lim_{t\to\pm\infty} V''(\varphi_\infty) \ll -\frac{3\mu^4}{\sqrt{2}M_p^2} \tag{3.29}$$

Note that Eq. (3.24) and Eq. (3.29) imply

$$|V''(\pm\varphi_\infty)|/V''(\varphi_b) \gg 1. \tag{3.30}$$

We now introduce a toy model, where the potential contains a quadratic, an exponential and a constant term, such that it meets all the above conditions:

$$V(\varphi) \equiv m^2(\varphi^2 - \varphi_\infty^2) - m^4[e^{(\varphi^2-\varphi_\infty^2)/m^2} - 1], \tag{3.31}$$

with

$$\frac{\varphi_\infty^2}{m^2} \gg 1. \tag{3.32}$$

The constant term is set to a value that ensures $V(\varphi) = 0$ at $\varphi = \pm\varphi_\infty$ and the large value of φ_∞^2/m^2, guarantees that $|V''(\pm\varphi_\infty)|/V''(\varphi_b) \gg 1$. The viable range for μ consistent with Eq. (3.24) and Eq. (3.29) is then

$$\frac{m^2}{M_p^2} \ll \frac{\mu^4}{M_p^4} \ll \frac{\varphi_\infty^2}{M_p^2}. \tag{3.33}$$

Figure (3.1) displays a schematic shape of a potential where parameters, m and φ_∞ are set to $m = 0.05M_p$ and $\varphi_\infty = 0.25M_p$ so $\varphi_\infty^2/m^2 = 25$. For these choice of parameters the

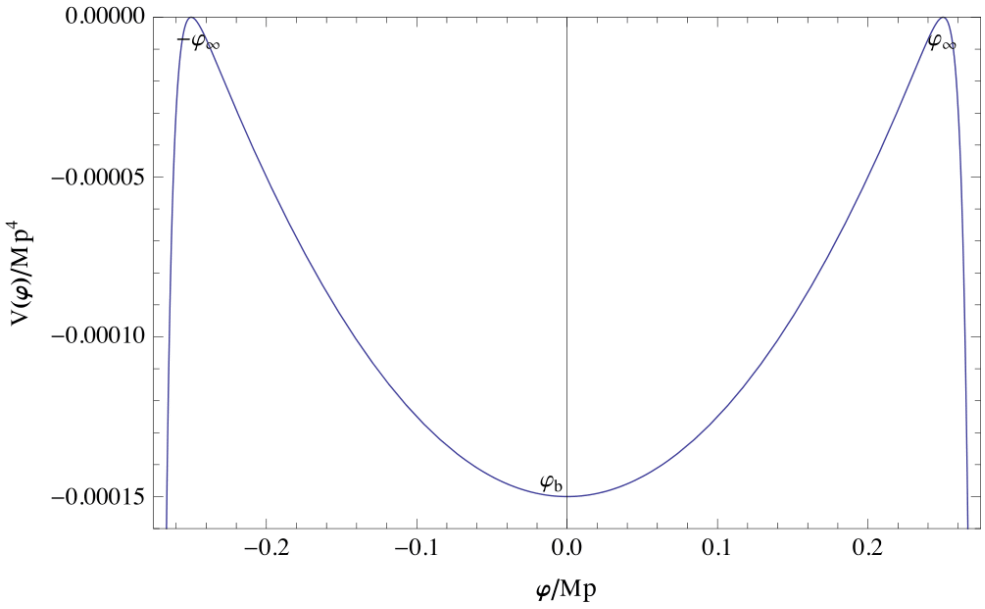

Figure 3.1: $V(\varphi)$ as a function of φ for $m = 0.05M_p$, $\varphi_\infty^2/m^2 = 25$.

allowed range of μ is $0.22 < \frac{\mu}{M_p} < 0.5$. For the rest of the discussion we keep the values of the parameters in our model to be fixed at $m = 0.05M_p$, $\varphi_\infty^2/m^2 = 25$ and $\mu = 0.3M_p$. Substituting the potential described by Eq. (3.31) into Eq. (3.21), one can derive the evolution of ρ_{fl} and H as functions of φ. Figure (3.2) demonstrates the φ dependence of these quantities, including $\rho_{cus} \equiv V(\varphi)$ and figure (3.3) shows the ratio of $\rho_{\text{fl}}/\rho_{cus}$. As expected the magnitude of ρ_{cus} is negligible far from the bounce and it is always less than ρ_{fl}, except at the bounce where they cancels off in order to yield $\dot{H}_b = 0$.

Assuming $\omega = 1$ ($\rho_{\text{fl}}(\varphi) = \rho_b(a/a_b)^{-6}$), one can obtain the evolution of background parameters numerically in terms of cosmic time or conformal time. Figures (3.4) and (3.5)

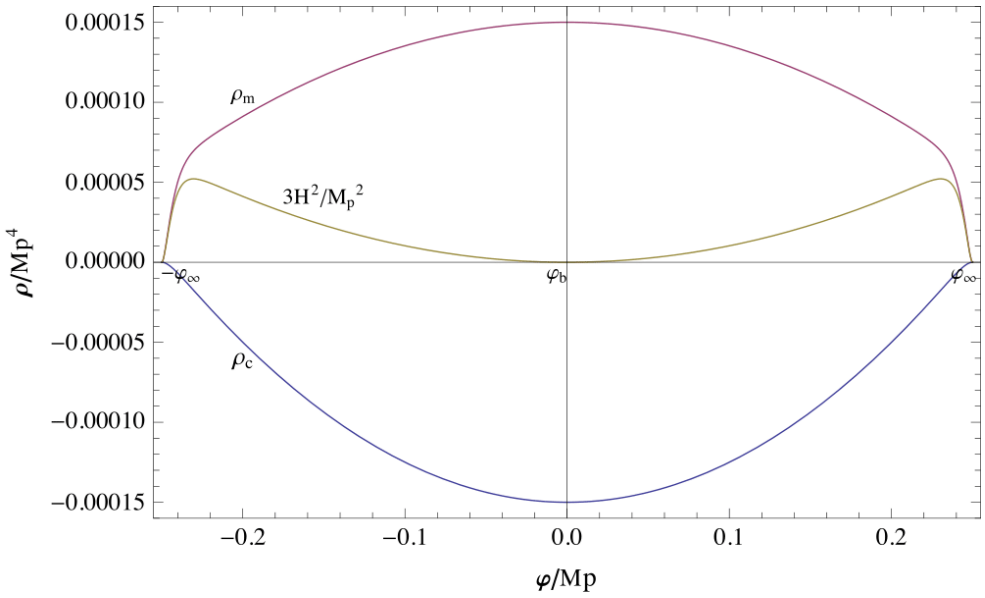

Figure 3.2: Densities and Hubble parameter as functions of φ for $m = 0.05M_p$, $\varphi_\infty^2/m^2 = 25$ and $\mu = 0.3M_p$. ρ_c is the density of the cuscuton field.

illustrate that the cosmological evolution of the scale factor, $a(t)$, and Hubble constant, $H(t)$, are consistent with our picture for a regular bounce cosmology. Note that for simplicity we have chosen $\text{sign}(\dot{\varphi}) > 0$ so $\varphi < 0$ coincides with Hubble parameter being negative and universe contracting. Therefore, when φ evolves into the positive region, the universe undergoes a smooth bounce and enters an expanding phase.

Having developed a consistent picture of the background bounce, next we study the behaviour of cosmological perturbations around this background.

3.3 Perturbations in the cuscuton bounce

3.3.1 Absence of ghosts in the cuscuton bounce

One of the generic instabilities that occurs in NEC-violating models is the ghost instability. This instability is, by definition, a UV instability which can be identified though a wrong sign for the kinetic term for excitations around flat space-time. In order to investigate the existence of such an instability in our cuscuton model, we have to study the corresponding

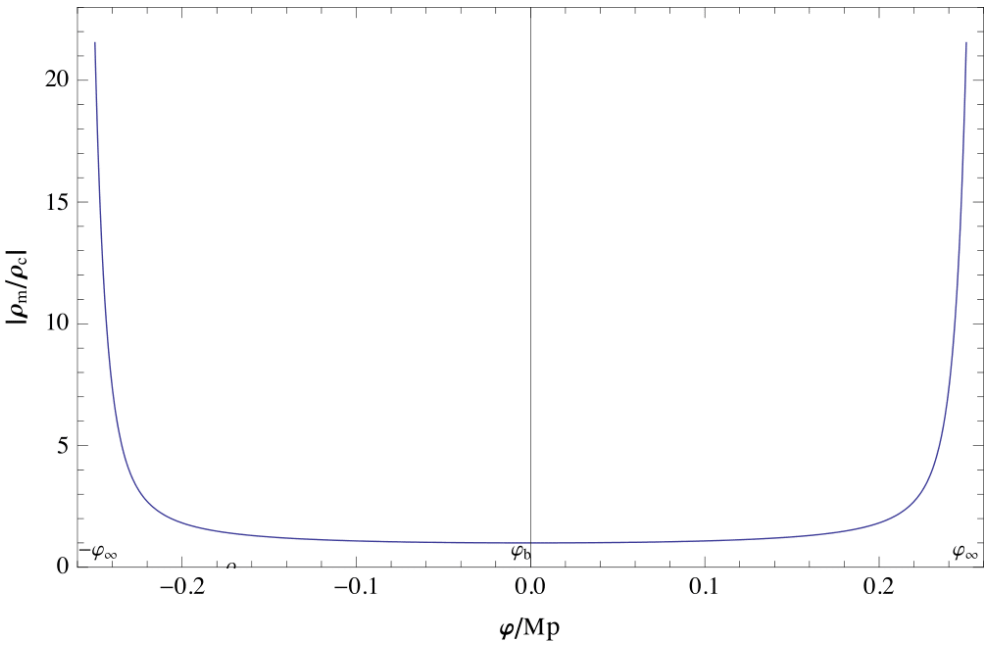

Figure 3.3: Ratio of densities as functions of φ for $m = 0.05M_p$, $\varphi_\infty^2/m^2 = 25$ and $\mu = 0.3M_p$. For this choice for the values of the parameters in the model, ρ_{cus} becomes more than twenty times smaller than $\rho_{\rm fl}$ far away from the bounce.

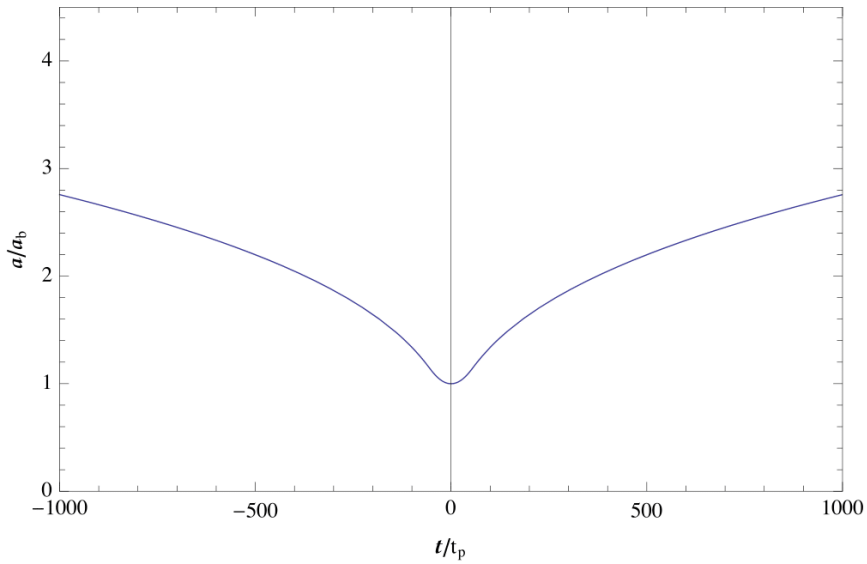

Figure 3.4: The evolution of scale factor, $a(t)$ in time is consistent with universe contracting, undergoing a regular bounce and then expanding.

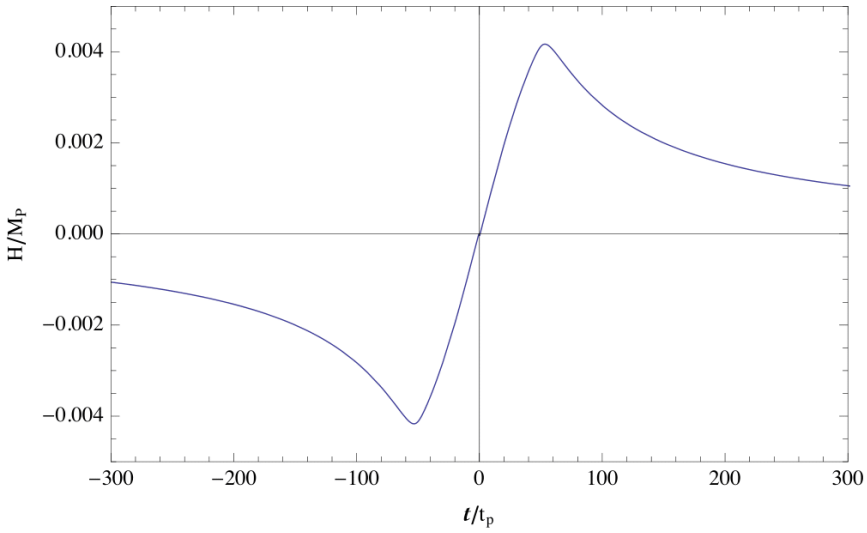

Figure 3.5: The evolution of Hubble constant, H, as a function of time. Hubble constant vanishes at the bounce and far from the bounce and there exists a NEC violating region around the bounce where $\dot{H} > 0$.

action for quantum fluctuations. As we mentioned before, adding a canonical scalar field, π, that doesn't have a potential to cuscuton action, can automatically produce a dynamical source with $w = 1$. This allows us to study fluctuation in a framework consistent with the background evolution described in section 3.2.

The full action after including the canonical scalar field is given by,

$$S = \int d^4x\sqrt{-g}\left[\frac{M_p^2}{2}R - \frac{1}{2}D_\mu\pi D^\mu\pi - \mu^2\sqrt{-D_\mu\varphi D^\mu\varphi} - V(\varphi)\right], \tag{3.34}$$

where D_μ denotes covariant derivatives, φ represents the Cuscuton field and π stands for the canonical scalar field.

This action is in fact a subclass of actions that we have studied in chapter 2. There, we probed the existence of ghosts in cuscuton gravity with generic canonical scalar field content. We found that, in general, such models do not contain ghosts.

In proper time, the quantities, c_s^2 and z^2 can be written similar to equations (2.33) and (2.32),

$$c_s^2 \equiv \frac{(k/a)^4H^2 + (k/a)^2\mathcal{B}_1 + \mathcal{B}_2}{(k/a)^4H^2 + (k/a)^2\mathcal{A}_1 + \mathcal{A}_2} \tag{3.35}$$

$$z^2 \equiv 2\,a^2P\left(\frac{(k/a)^2 + 3P}{(k/a)^2H^2 + (P)(3H^2 + P + \dot{H})}\right). \tag{3.36}$$

where, $P = \frac{1}{2M_p^2}\dot{\pi}_0^2$ and the functions $\mathcal{A}_{1/2}/\mathcal{B}_{1/2}$ are the same functions as given in equations (2.36) - (2.39).

As is seen from the quadratic action, (2.31), Cuscuton gravity is free from ghosts if the coefficient of the kinetic term, z^2 is positive. The terms, $(k/a)^2$ and P, appearing in the numerator of z^2 are both positive. Hence, positivity of z^2 depends on the sign of the denominator. The denominator can be simplified using the background equation to,

$$(k/a)^2H^2 + P(3H^2 + \frac{\mu^2}{2M_p^2}|\dot{\varphi}_0|). \tag{3.37}$$

Written in this form, it is apparent that the denominator is always positive. Hence, this class of Cuscuton Gravity, including our bounce model is ghost-free[4]. Furthermore, positivity of denominator and non-vanishing contribution from cuscuton modification, guarantees

[4]As discussed in Boruah et al. (2017) (chapter 2) the other class with $+\mu^2$ in the Lagrangian, also turns out to be ghost free.

the absence of any poles in this coefficient regardless of wavelength and at the bounce ($H = 0$).

3.3.2 Absence of dynamical instabilities in cuscuton bounce

We next investigate the dynamical stability of the perturbations in different regimes.

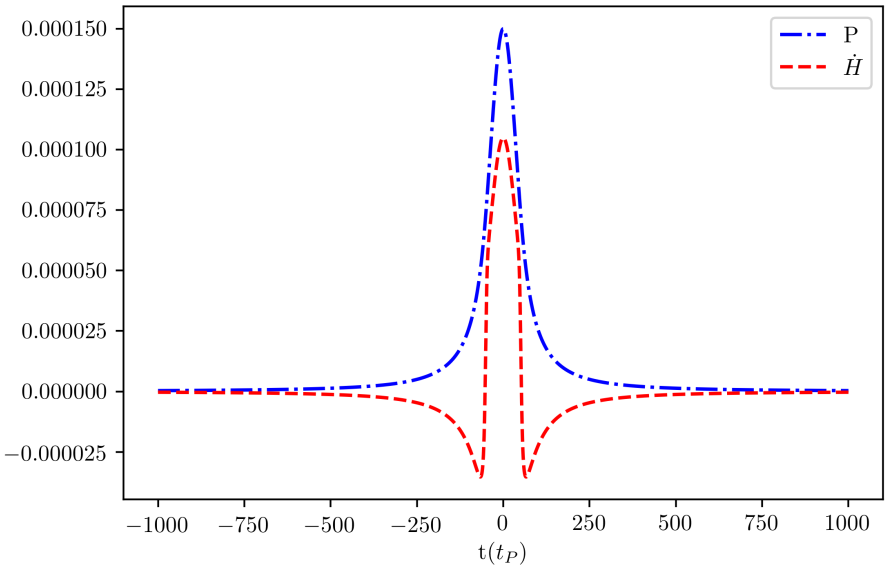

Figure 3.6: The quantities, P, and $\dot{H}$ plotted as a function of time. It can be seen that both quantities are of the same order at the bounce($t = 0$)

As mentioned earlier, the dynamics of the perturbations can be described through the perturbation quantity, ζ. The equations of motion determining the evolution of ζ was derived in Boruah et al. (2017). Similar to action, it is convenient to express this equation in the Fourier space

$$\ddot{\zeta}_k + (H + 2\frac{\dot{z}}{z})\dot{\zeta}_k + \left(\frac{c_s^2 k^2}{a^2}\right)\zeta_k = 0, \tag{3.38}$$

where the quantities c_s and z are given in equations (3.35) and (3.36) and we find

$$2\frac{\dot{z}}{z} = -4H - 2H\left(\frac{((k/a)^2+9P)}{(k/a)^2+3P}\right) - \left(\frac{(k/a)^2(2H\dot{H}-2H^3)+P(\ddot{H}-12HP-18H^3)}{(k/a)^2H^2+P(3H^2+P+\dot{H})}\right). \quad (3.39)$$

We would like first to point out that equation (3.38) does not become singular for any value of k at any time. That's because $P > 0$, $P + \dot{H} = \frac{\mu^2}{2M_p^2}|\dot{\varphi}| > 0$ and c_s^2 is always finite [5].

We now proceed to numerically explore the dynamics of the perturbations for different scales and as they pass through the bounce. Since at the bounce $H_b = 0$ and $\ddot{H}_b = 0$, there are two relevant mass scales in equation (3.38), corresponding to quantities $\sqrt{\dot{H}_b}$ and $\sqrt{P_b}$. Figure 3.6, demonstrates the time dependence of $\dot{H}$ and P for our model. As we see, both $\sqrt{\dot{H}_b}$ and $\sqrt{P_b}$ are comparable and around $\sim 10^{-2}M_p$ at the bounce. Therefore, we can associate a bounce length scale, $l_B \sim 1/\sqrt{\dot{H}_b}$ to this scale and classify our modes with respect to that. We refer to modes as Ultra-Violet (UV)/Infra-Red (IR), if they are shorter/longer with respect to this length scale.

The equation governing the evolution of the perturbations, (3.38), is a second-order differential equation, which implies the existence of two independent solutions for each k. We have to check the stability for both of these modes to ensure that perturbations are stable on this bouncing background. To do that, we chose two solutions such that one is non-zero at the bounce but has zero derivative there, while the other is zero at the bounce but has non-zero derivative. Since the Wronskian for these solutions is non-zero at the bounce, they are independent.

To examine the evolution in different regimes, we evolved three wavelength modes, with $\lambda = 0.1l_B, l_B, 10l_B$ numerically. The results of the numerical evolution for the two independent solutions, is shown in Figures 3.7. Our result confirms that there are no instabilities associated with the evolution of modes in different wavelengths scales. As we mentioned before, the value of $\sqrt{\dot{H}_b}$ is $\sim 0.01M_{\rm pl}$. Therefore, the wavelengths we are investigating are of the order of $10\ell_P, 100\ell_P$ and $1000\ell_P$.

We conclude that there is no pathology associated with the perturbations at the bounce or at the transition into NEC violating region ($|t| \sim 60\,t_p$), neither for UV or IR or intermediate scales.

[5] The denominator of c_s^2 is always positive since the quantities $\mathcal{A}_1$ and $\mathcal{A}_2$ simplify to $\mathcal{A}_1 = P(6H^2 + \frac{\mu^2}{2}|\dot{\varphi}|)$ and $\mathcal{A}_2 = 3P^2(3H^2 + \frac{\mu^2}{2}|\dot{\varphi}|)$.

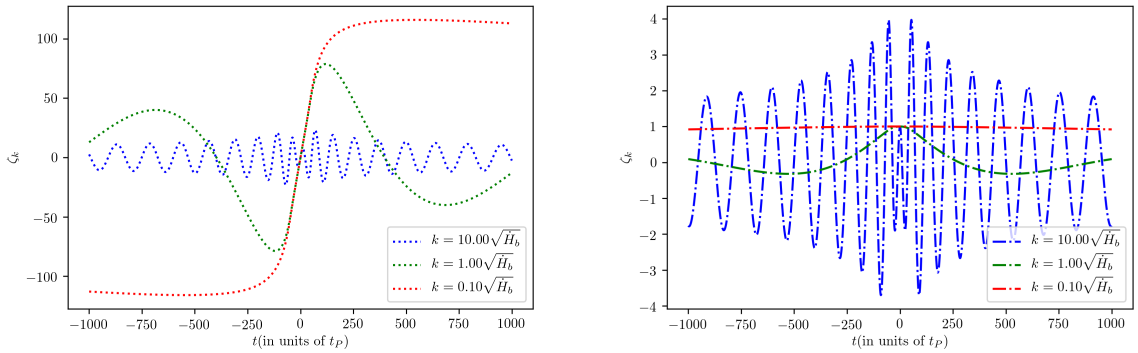

Figure 3.7: Evolution of perturbations at three different length scales, $k/\sqrt{\dot{H}_b} = 0.1, 1.0, 10.0$. The two panels correspond to different initial conditions which leads to linearly independent solutions. The left panel has $\zeta_b = 0, \dot{\zeta}_b \neq 0$. The right panel has $\zeta_b \neq 0, \dot{\zeta}_b = 0$

3.4 Conclusions

In this work, we found a cuscuton bounce solution that has no pathologies associated with NEC violation. Our solution corresponds to a toy model consisting of a cuscuton field, φ, in addition to a dynamical fluid, π. At the background level, we required that, away from the bounce (in the contracting or expanding phase), the cuscuton density be sub-dominant to the additional fluid. However, we looked for a cuscuton potential such that it would grow faster than the fluid density as universe contracted and would make the background bounce into expansion. After finding an appropriate potential, we used the cosmological perturbation theory to scrutinize the existence of ghosts and other instabilities in the model. We found that the theory is healthy. We think the underlying reason for absence of instabilities in our model, is that unlike GR, the field which governs the background, i.e. cuscuton, does not have its own dynamical degree of freedom. Therefore, we expect our result can be extended beyond bounce models to more generic classes of solutions with NEC violation, which would otherwise suffer from instabilities.

Part II

Peculiar velocities

Chapter 4

Cosmological constraints from peculiar velocities

4.1 Introduction

As we saw in chapter 1, peculiar velocities are sourced by inhomogeneities in the universe, making them an excellent probe of its large-scale structure. In fact, the peculiar velocity field is the only probe of very large-scale structures in the low-redshift universe.

In linear perturbation theory, the relationship between peculiar velocity, $\boldsymbol{v}$, and the dark matter overdensity, δ, is given by equation 1.41. As can be seen from the equation, the velocity field is sensitive to the dimensionless growth rate, $f = \frac{\mathrm{d}\ln D}{\mathrm{d}\ln a}$ and the typical amplitude of density fluctuations. Consequently, the peculiar velocity field has been used to constrain the degenerate cosmological parameter $f\sigma_8$ (Pike & Hudson, 2005; Davis et al., 2011; Carrick et al., 2015; Adams & Blake, 2017; Dupuy et al., 2019). In the ΛCDM cosmological model, $f \approx \Omega_m^{0.55}$ Wang & Steinhardt (1998). However, in modified theories of gravity, the growth rate could be different, i.e. $f = \Omega_m^{\gamma}$ with $\gamma \neq 0.55$. Therefore, peculiar velocities can also be used to constrain theories of gravity (Abate & Lahav, 2008; Nusser & Davis, 2011; Hudson & Turnbull, 2012; Huterer et al., 2017).

However, analysing peculiar velocities poses several challenges. The measured redshift, cz, of a galaxy gets a contribution from both the recessional velocity due to Hubble flow, Hr, and the peculiar velocity, $\boldsymbol{v}$. Therefore, to analyse peculiar velocities, one needs to determine the distances to these galaxies in order to separate these two contributions. There are several ways to measure distances directly. The most popular of these use

empirical galaxy scaling relations. For example, SFI++ (Masters et al., 2006) and the 2MTF (Masters et al., 2008) catalogues use the Tully-Fisher (TF) relation (Tully & Fisher, 1977), and the 6dF velocity survey (Springob et al., 2014) uses the Fundamental Plane relation (Dressler et al., 1987; Djorgovski & Davis, 1987). Another distance indicator relies on Type Ia supernovae (Riess et al., 1997; Radburn-Smith et al., 2004; Turnbull et al., 2012; Huterer et al., 2017; Mathews et al., 2016). Since the distance errors from Type Ia supernovae ($\mathcal{O}$[5-10%]) are much lower than those obtained using galaxy scaling relationships ($\mathcal{O}$[20-25%]), a smaller sample of Type Ia supernovae can give comparable results to that of a larger catalogue based on the TF or FP relations. In this work, we combine low redshift supernovae from various surveys to produce the largest peculiar velocity catalogue based on Type Ia supernovae to date.

As described in section 1.5.2, the different approaches to analysing peculiar velocities can be separated into two categories: i) those which use only the distance indicator data for peculiar velocity analysis, and ii) those which 'reconstruct' the cosmic density field from a redshift survey and then compare the velocity field predictions with the observed peculiar velocity data. Some examples of the first category are the POTENT (Dekel et al., 1993) and the forward-modelled VIRBIUS (Lavaux, 2016) method. Our approach falls into the second category, where we compare the reconstructed velocity field to distance observations. In particular, we use the distribution of galaxies (δ^g) as a tracer of the mass density field, δ. We can then use a modified version of Equation (1.41) to predict the peculiar velocities. In this approach, we can constrain the degenerate parameter combination $\beta = f/b$, where b is the linear galaxy bias. The cosmological parameter combination $f\sigma_8$ is then related to β as $f\sigma_8 = \beta\sigma_8^g$, where, σ_8^g is the typical fluctuation in the galaxy overdensity field at a radius of 8 h^{-1} Mpc. Specifically, we compare the observed data from the peculiar velocity surveys to the reconstructed velocity field from the 2M++ redshift compilation. In doing so we use an inverse reconstruction scheme which was used in Carrick et al. (2015). More examples of reconstruction-based peculiar velocity analyses are given in Lavaux et al. (2010) and Erdoğdu et al. (2006).

This chapter is structured as follows: Section 4.2 describes the peculiar velocity catalogues we use in this work, primarily, the new compilation of type Ia supernovae. Section 4.3 describes the 2M++ galaxy catalogue and the reconstruction scheme used in this work. In Section 4.4, we elaborate on the methods used to compare the reconstructed velocity field to the observations of the peculiar velocity catalogue. The results are presented in section 4.6. We compare our results to other results in the literature and discuss future prospects of peculiar velocity analysis in section 4.7 before we summarise our results in section 4.8. Throughout this work, $h = H_0/(100\,\mathrm{km\,s^{-1}\,Mpc^{-1}})$, where H_0 is the local Hubble constant. Unless otherwise mentioned, throughout this work, we adopt a flat ΛCDM cosmological

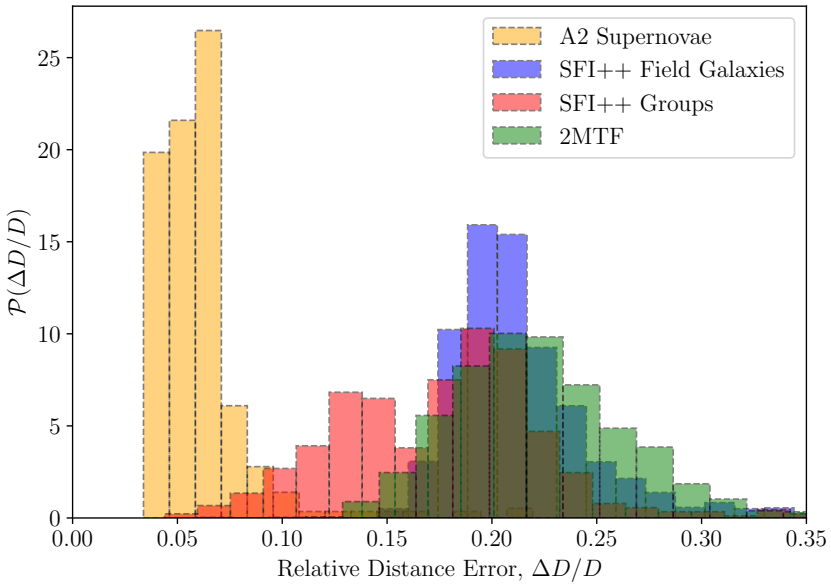

Figure 4.1: The normalised distribution of the relative distance errors of the different peculiar velocity datasets. The distribution of the relative errors of the A2 compilation is shown in orange, that of the SFI++ groups is shown in red, the SFI++ field galaxies are shown in blue and the 2MTF galaxies are shown in green. The typical errors on the distances of the supernovae is much lower than that of the other datasets.

model with $\Omega_m = 0.3$.

4.2 Peculiar velocity catalogue

In this section, we describe the two main peculiar velocity catalogues used in this chapter. In Section 4.2.1, we present a new compilation of low redshift Type Ia supernovae from various different surveys. In Section 4.2.2, we summarise the data from the SFI++ and 2MTF catalogues, where the distance has been estimated using the Tully-Fisher relationship.

4.2.1 Second amendment (A2) supernovae compilation

Several distance indicators have been used over the past decades. Among these, distances from the FP and TF relations have found a central place in peculiar velocity analysis. In this section, we focus on distances derived from SNe-Ia light curves. Among the current distance indicators, SNe distances (typically $\sim 5\%$) are the best in terms of distance errors (see Figure 4.1). The peak luminosity of a Type Ia supernova is correlated with the rate of decline of its light curve, making these 'standardisable candles' (Phillips, 1993). Type Ia supernovae have been previously used in many works to probe the velocity field of the nearby universe (Riess et al., 1997; Radburn-Smith et al., 2004; Turnbull et al., 2012; Huterer et al., 2017).

The 'First Amendment' (A1) compilation of Type Ia supernovae in the local universe was previously presented in Turnbull et al. (2012). This was based on the addition of 26 SNe from the first data release (DR1) of the Carnegie Supernovae Project (CSP, Folatelli et al. (2010)) to the low-z set of 'Constitution' supernovae (Hicken et al., 2009). In this work, we add to the First amendment catalogue additional supernovae from the third data release (DR3) of CSP (Krisciunas et al., 2017), the Lick Observatory Supernova Search (LOSS, Li et al. (2000)) and the Foundation Supernova Survey data release 1 (DR1) (Foley et al., 2018; Jones et al., 2019), resulting in the 'Second Amendment' (A2) compilation of SNe peculiar velocities. For each of these sub-catalogues, we only use the supernovae that are within the 2M++ volume and remove the duplicates from different catalogues. We also do a simple χ^2 fit (described in section 4.4.1) to determine the 'flow model', which refers to the set of four parameters consisting of the rescaling factor, β and the three components of the residual bulk flow velocities. We then reject iteratively the outliers from this fit until there are no outliers. While it is common to choose a fixed rejection threshold for all samples (such as 3σ), in principle the threshold for outlier rejection should depend on the size of the sample. Suppose that the residuals are Gaussian then we expect a given object to lie in the tail of the distribution with some small probability p. If there are N objects in the sample, the number of objects in the tails will be Np. We choose the threshold p such that $Np = 0.5$. For the different samples, this value is 2.6σ for the LOSS and CSP-DR3 samples and 2.9σ for the Foundation sample. The LOSS supernova sample was taken from Ganeshalingam et al. (2013). Removing the duplicates from the A1 catalogue and outliers from the χ^2 fit, we arrive at a sample of 55 SNe. We reject a total of 4 outliers: (SN2005ls, SN2005mc, SN2006on, SN2001e) in the process. The data set for the CSP-DR3 was obtained from Burns et al. (2018). From this catalogue, we remove the duplicates in the First Amendment or the LOSS sample. We also remove supernovae outside the 2M++ volume or the outliers of the χ^2 fit. This yields us a total of 53 supernovae after rejection

of 2 outliers (SN2006os, SN2008gp). Note that changing the duplicate selection criteria among A1, LOSS and CSP-DR3 changes the inferred value of β by less than 0.1σ. We use the given selection criteria for easy comparison with earlier results (Carrick et al., 2015; Turnbull et al., 2012). For the Foundation DR1 sample we rejected a total of 12 outliers in the fitting procedure: (SN2016cck, SN2016gkt, ASASSN-15go, ASASSN-15mi, PS15akf, SN2016eqb, SN2016gfr, SN2017cju, ASASSN-15la,PS15bbn, SN2016aqs, SN2016cyt).

The Foundation DR1 and the LOSS sample provides the supernovae light-curve stretch parameter, x_1, color parameter c and the amplitude, m_B after fitting the light curves using the SALT2 (Guy et al., 2007) fitter. The distance modulus for the SALT2 model is given by the Tripp formula (Tripp, 1998),

$$\mu = m_B - M + \alpha x_1 - \mathcal{B}c\,. \tag{4.1}$$

To determine the global parameters, we use a self consistent method to jointly fit for the flow model and the global parameters to determine the distances. We fit for the global parameters $\alpha, \mathcal{B}$, M and the intrinsic scatter for this sample of supernovae in addition to the flow model using a modified forward likelihood method, which is described in section 4.4.2. We note that, conventionally, the parameter $\mathcal{B}$ is denoted with β in the SN literature. We avoid this notation to avoid confusion with $\beta = f/b$.

It is useful to have a metric that summarise the power of a sample. Here we discuss two such metrics. First, we define a sample's uncertainty-weighted "characteristic depth" as

$$d_* = \frac{\sum_{i=1}^{N} r_i/\sigma_i^2}{\sum_{i=1}^{N} 1/\sigma_i^2}\,, \tag{4.2}$$

where σ_i is the uncertainty in the distance estimates. The characteristic depth of the different sub-samples of supernovae and the combined catalogue is presented in Table 4.1. Note that the newly added LOSS and Foundation samples probe higher redshifts compared to the earlier A1 sample. The characteristic depth of the full A2 sample is 41 h^{-1} Mpc. Second, we introduce a metric designed to assess the overall power of a peculiar velocity survey that combines the number, depth and uncertainty of the peculiar velocity tracers. If all galaxies in the sample were located in the same direction in the sky, and there was a bulk flow in that direction, then the uncertainty in the mean peculiar velocity, $\Delta\bar{V}$, of the sample is simply

$$\frac{1}{\Delta\bar{V}^2} = \sum_{i=1}^{N} \frac{1}{\sigma_i^2 + \sigma_v^2}, \tag{4.3}$$

where the distance uncertainty, σ_i, is reported in km s^{-1} and we assume a value of $\sigma_v = 150$ km s^{-1}. $\Delta\bar{V}$, is related to the expected error on bulk flow that can be obtained using a given

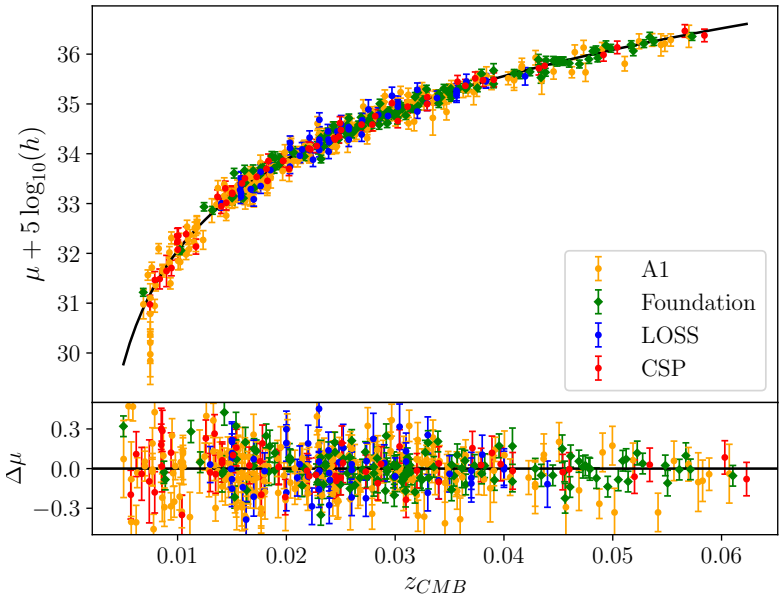

Figure 4.2: The Hubble diagram for the supernovae in the A2 compilation. The error bars for the magnitude include the intrinsic scatter for each sample. The black solid line is the expected distance-redshift relation in a ΛCDM cosmological model with $\Omega_m = 0.30$. The lower panel shows the residual from the given relation.

peculiar velocity sample and hence is a Figure-of-merit for the peculiar velocity sample. We show the value of $\Delta\bar{V}$ for the different samples in Table 4.1.

A Hubble diagram for the supernovae in our compilation is shown in Figure 4.2. The redshift distribution and the sky distribution of the supernovae in the A2 compilation is shown in Figure 4.3. Note that the CSP sample is distributed primarily in the southern sky.

4.2.2 Tully-Fisher catalogues

The Tully & Fisher (1977) relation is an empirical scaling relationship between the luminosity and the velocity width of spiral galaxies. It is commonly expressed in terms of the variable, $\eta = \log W - 2.5$, where W is the velocity width of the galaxies in km s^{-1}. This relationship can be used to determine distances to galaxies. The distance modulus to a

Table 4.1: Properties of the different peculiar velocity catalogues showing the number of objects, the characteristic depth and the uncertainty in the mean peculiar velocity.

Catalogue	$N_{\rm objects}$	d_* (h^{-1} Mpc)	ΔV (km/s)
A1	232	31	28
CSP (DR3)	53	40	49
LOSS	55	61	85
Foundation	125	59	38
A2	**465**	**41**	**16**
SFI++ field galaxies	1996	40	24
SFI++ groups	599	22	21
2MTF	1247	26	21
Combined	**4308**	**27**	**13**

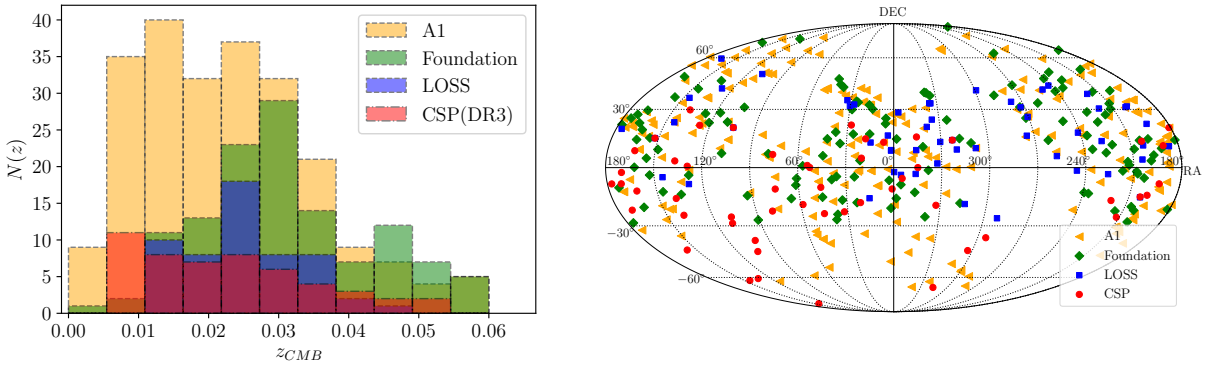

Figure 4.3: *(Left)* The redshift distribution of the supernovae in the different catalogues in the A2 compilation. Note that the LOSS and the Foundation samples probe higher redshifts, i.e., they have a higher characteristic depth ($r_* \sim 60\ h^{-1}$ Mpc) compared to the A1 and CSP samples. The characteristic depth is shown in Table 4.1. *(Right)* The sky distribution of the A2 supernovae in Equatorial coordinates. The above shows the Mollweide projection of the right ascension and the declination of the supernovae in the different samples. As can be seen in the figure, the CSP sample is primarily in the southern hemisphere.

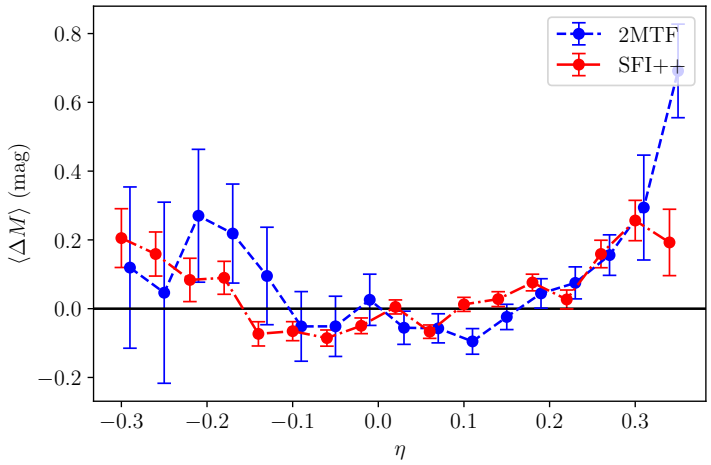

Figure 4.4: The deviation from the inferred linear Tully-Fisher relationship in bins of η. We calculated the mean absolute magnitude in bins of η of width 0.04 and calculate its deviation from the inferred linear relationship (shown on the y-axis). As can be seen, it deviates from the linear relationship in both in the faint end (low η) and in the bright end (high η).

galaxy in terms of the apparent magnitude (m), and η is given as,

$$\mu = m - (a_{\rm TF} + b_{\rm TF}\eta)\,, \tag{4.4}$$

where $a_{\rm TF}$ and $b_{\rm TF}$ are the zero-point and the slope of the Tully-Fisher relationship. The intrinsic scatter is denoted with $\sigma_{\rm int}$.

For the analysis of the Tully-Fisher samples, we jointly fit for the distances and the flow model using the method described in section 4.4.2. This requires fitting for three additional TF parameters, $a_{\rm TF}$, $b_{\rm TF}$ and $\sigma_{\rm int}$ in addition to the flow model. In this work, we use the data from two TF catalogues: the SFI++ catalogue and the 2MASS Tully-Fisher (2MTF) survey. We present the details of data processing for the two catalogues in the next subsections. The value of the TF parameters for the SFI++ and the 2MTF catalogues as inferred in our fitting procedures are presented in Table 4.2.

SFI++

The SFI++ catalogue (Masters et al., 2006; Springob et al., 2007) consists of 4052 galaxies and 736 groups. After restricting to the groups and galaxies inside the region covered by

Table 4.2: Tully-Fisher parameters inferred using our fitting procedure

	$a_{\rm TF} + 5\log_{10}(h)$	$b_{\rm TF}$	$\sigma_{\rm int}$ (mag)
SFI++	-20.915 ± 0.008	-6.42 ± 0.07	0.299 ± 0.006
2MTF	-22.556 ± 0.013	-6.56 ± 0.13	0.392 ± 0.010

2M++, we are left with 3915 galaxies and 734 groups. For the set of galaxies, we then use the redshift distance as the distance estimate and fit for the Tully-Fisher relations. It was noted in Davis et al. (2011) that the I-band Tully-Fisher relation deviates from a linear relationship at the faint end. Since we are fitting using a forward method, the selection cuts should be a function of η only for an unbiased estimate. We plot the mean relation as inferred from the data and how it deviates from the inferred linear relationship in Figure 4.4. As can be seen from the figure, there is a deviation from the inferred linear relationship in both the faint end (low η) and the bright end (high η). Therefore, we reject the objects with $\eta < -0.15$ and $\eta > 0.2$ from the SFI++ dataset. We then iteratively reject the points which are not within 3.5σ of the inferred TF relation in the magnitude. Finally, we compare the peculiar velocity predicted using bulk flow parameters inferred using the χ^2 minimization method (described in section 4.4.1) to the reported peculiar velocities in the SFI++ dataset. We reject the 3.5σ outliers (17 objects) from this comparison.

For fitting the bulk flow parameters, we use both the galaxy and the group catalogues from the SFI++ dataset. Therefore, we remove the duplicates from the galaxy catalogue in the group catalogue. We also reject the groups for which all the corresponding galaxies in the dataset are rejected during one of the cuts described in the earlier paragraph. After these cuts, we are left with a total of 1996 field galaxies and 599 groups (containing 1167 galaxies). The characteristic depth of the field galaxy sample was found to be 38 h^{-1} Mpc and that of the group sample is 22 h^{-1} Mpc.

2MTF

The 2MTF survey (Masters et al., 2008; Hong et al., 2019) contains TF data for 2062 galaxies in the nearby Universe. It is restricted to distances < 100 h^{-1} Mpc. For objects which are in both SFI++ and 2MTF catalogues, we use the objects in the SFI++ catalogue. This is because the TF relation in the I-band (used by SFI++) is found to have a smaller scatter compared to the TF relation in infrared (employed in the 2MTF) frequency. It is reflected in our results of scatter as found for the SFI++ catalogue and the 2MTF (See Table 4.2). To remove duplicates, we cross-match the galaxies by considering all 2MTF galaxies with an angular separation of ≤ 20 arcseconds and a redshift difference

$|\Delta cz| < 150$ km s^{-1} of SFI++ galaxies. We find 384 galaxies that are in both catalogues, and we remove these from the 2MTF sample. We also include only galaxies that are in the 2M++ region, which removes another 22 galaxies. The 2MTF survey provides galaxy magnitudes in the H, J and K bands. For the purposes of this chapter, we only use the K band magnitudes. As with the SFI++ data, we observe a deviation from the inferred linear relationship at the faint and bright ends of the sample. We therefore keep only galaxies with $-0.1 < \eta < 0.2$. We then fit the Tully-Fisher relationship by using the redshift-space distance and iteratively exclude the 3.5σ outliers. The final sample has a total of 1247 galaxies. The characteristic depth of the 2MTF sample is 21 h^{-1} Mpc.

4.3 Density and velocity field reconstruction

In this section, we present details on the density and velocity reconstruction that we use for predicting the peculiar velocities. In section 4.3.1, we describe the 2M++ redshift compilation, which has been used in our reconstruction. In section 4.3.2, we present details of the reconstruction scheme used.

4.3.1 2M++ galaxy redshift compilation

Peculiar velocities are sourced by the density fields on large scales. Therefore, to study peculiar velocities, we require our galaxy catalogue to have a large sky coverage and be as deep as possible. With this as a goal, the 2M++ compilation of galaxy redshifts was constructed in Lavaux & Hudson (2011a). The 2M++ redshifts are derived from the 2MASS redshift survey (2MRS) (Erdogdu et al., 2006), 6dF galaxy redshift survey-DR3 (Jones et al., 2009) and the Sloan Digital Sky Survey (SDSS) Data Release 7 (Abazajian et al., 2009). The apparent K-band magnitude was corrected by taking into account Galactic extinction, k-corrections, evolution and surface brightness dimming. The Zone of Avoidance (ZoA) due to the Galactic Plane is masked in the process. The resulting catalogue consists of a total of 69160 galaxies. The catalogue was found to be highly complete up to a distance of 200 h^{-1} Mpc (or $K < 12.5$) for the region covered by the 6dF and SDSS and up to 125 h^{-1} Mpc (or $K < 11.5$) for the region that is not covered by these surveys. Hereafter, '2M++ volume/region' is restricted to less than 200 h^{-1} Mpc for the region in the 2M++ catalogue which is covered by SDSS and 6dF survey and to less than 125 h^{-1} Mpc for the region covered only by 2MRS.

In Carrick et al. (2015), the ZoA was filled by "cloning" galaxies above and below the

plane. We elaborate on the reconstruction process in section 4.3.2. For further details on the 2M++ catalogue, see Lavaux & Hudson (2011a) and the references therein.

4.3.2 Reconstruction scheme

In Carrick et al. (2015), the density field was reconstructed with an iterative scheme modelled on Yahil et al. (1991). We use the luminosity-weighted density field from Carrick et al. (2015) in this work. A luminosity weight was assigned to each galaxy in the 2M++ catalogue after fitting the luminosity function with a Schechter function. Galaxy bias depends on luminosity: Westover (2007) found that

$$\frac{b}{b_*} = (0.73 \pm 0.07) + (0.24 \pm 0.04)\frac{L}{L_*}\,, \tag{4.5}$$

where b_* is the bias of an L_* galaxy. This luminosity-dependent bias function was used to normalize the density contrast to a uniform b_* at all radii.

Finally, the mapping from the redshift data of 2M++ to comoving coordinates is done using an iterative scheme. First, the galaxies are grouped using the 'Friends of friends' algorithm (Huchra & Geller, 1982). Then, galaxies are initially placed at the comoving distance corresponding to its redshift. Then, the luminosity-weighted density field is calculated and smoothed using a Gaussian filter at 4 h^{-1} Mpc. From this density field, the peculiar velocity is calculated using linear theory for each object. The comoving coordinates in the next iteration are then corrected for using this peculiar velocity prediction. This process is repeated, slowly increasing β from $\beta = 0$ to $\beta = 1$. For more details on this reconstruction procedure, refer to Carrick et al. (2015). The reconstructed density and the radial velocity in the supergalactic plane is shown in Figure 4.5.

4.4 Comparing Predicted and Observed Peculiar Velocities

We want to compare the reconstructed velocity field to the observations of the peculiar velocity catalogues. To do this, we fit for $\beta = f/b$ and a coherent residual bulk flow velocity $\boldsymbol{V}_{\rm ext}$, which may arise from the large-scale structures outside of the 2M++ survey area. Note that the published velocity field[1] of Carrick et al. (2015) uses $\beta = 0.43$ with the $\boldsymbol{V}_{\rm ext} = (89, -131, 17)$ km s^{-1} as given in that paper. Here we refit both β and $\boldsymbol{V}_{\rm ext}$.

[1] Available at https://cosmicflows.iap.fr

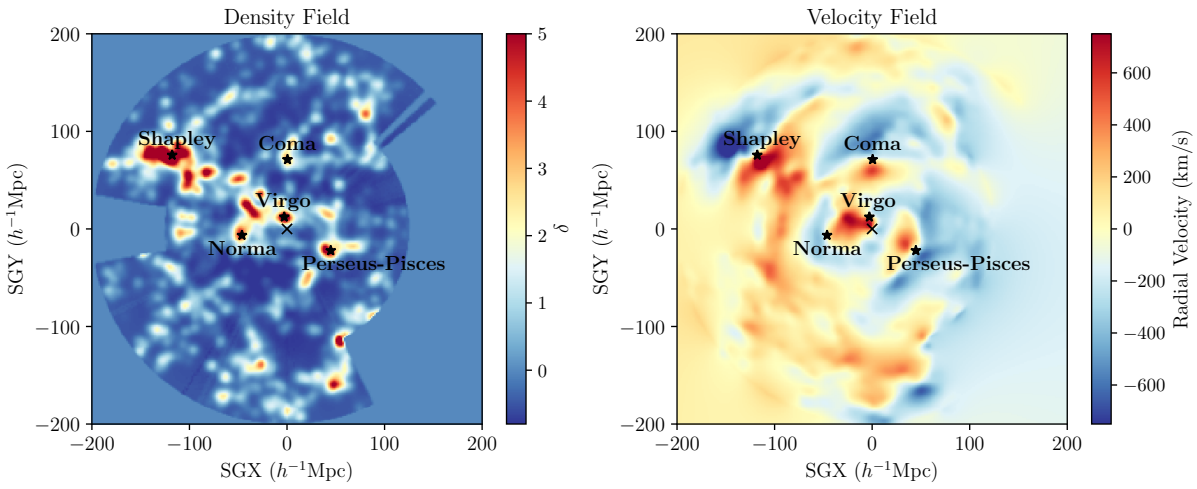

Figure 4.5: The reconstructed luminosity-weighted density (δ_g) and the radial velocity field in the Supergalactic Plane smoothed with a Gaussian filter of size 4 h^{-1} Mpc. The location of the prominent superclusters, namely, Shapley, Coma, Virgo, Norma and Perseus-Pisces are shown with a black star. The Local Group is at the origin and is denoted with a black cross.

The approaches to measuring peculiar velocities via distance indicators often come in two variants, the so-called forward and the inverse approaches. In the *forward approach*, one predicts a distance-dependent quantity (e.g. magnitude) as a function of a distance-independent quantity (e.g. velocity width). In the *inverse approach* (Aaronson et al., 1982), one predicts the distance-independent quantity as a function of a distance-dependent quantity. Note, however, that some distance indicators, such as Type Ia supernovae, only have a "forward" method. In addition to the above distinction between the forward and inverse methods, there is another distinction that is generally made between the different approaches. Predicting the peculiar velocity requires an *a priori* 'best estimate' for the position of the observed galaxies. One can use, for example, the Tully-Fisher relations to assign an *a priori* best estimate of the distance to a galaxy. Alternately, one can use the redshift as the *a priori* best estimate of the distance. The former has been called the *Method I* and the latter, *Method II* in the literature (Strauss & Willick, 1995).

Each combination of distance-indicator method and Method I/II are subject to different biases which arise due to selection effects and density inhomogeneities. However, biases are lower for some combinations: in particular, an inverse distance indicator combined with Method II is insensitive to Malmquist biases arising from the scatter in the distance indicator[2], whereas a forward distance indicator combined with Method I is less sensitive to many selection effects.

We use two different methods for our peculiar velocity analysis: a simple χ^2 minimization technique and a forward likelihood method.

4.4.1 χ^2 minimization

In the first approach, we compare the observed redshift to the predicted redshift of a galaxy by assuming it is at the distance reported in the peculiar velocity survey. This is therefore a *Forward-Method I* approach. This approach suffers from Malmquist bias (Strauss & Willick, 1995). In Section 4.4.2, we correct for the Malmquist bias by integrating the measured inhomogeneities along the line-of-sight. It is difficult to correct for it in a simple χ^2 fitting method used in this subsection. Because of this bias, the inferred value of β is biased high in this approach. Nevertheless, we use this method because of its interpretability and to check consistency.

[2]There remains a weak Malmquist-like bias due to the scatter in the flow model used to assign a distance given a redshift (Kaiser & Hudson, 2015) but this is much smaller than the one due to the scatter in the distance indicator.

The predicted redshift for a galaxy is dependent on the flow model and the reconstructed velocity. That is, $z_{\rm pred} \equiv z_{\rm pred}(\boldsymbol{r}, \boldsymbol{v}, \boldsymbol{V}_{\rm ext}, \beta)$, where $\beta = f/b$ and $\boldsymbol{V}_{\rm ext}$ is the external bulk flow arising from outside the survey region. The dependence of $z_{\rm pred}$ on these quantities is given as

$$1 + z_{\rm pred} = \left(1 + z_{\rm cos}(r)\right)\left(1 + \frac{1}{c}(\beta \boldsymbol{v} + \boldsymbol{V}_{\rm ext}) \cdot \hat{\boldsymbol{r}}\right), \tag{4.6}$$

where r is obtained by taking the distance as being equal to the reported distance in the peculiar velocity catalog and $\boldsymbol{v}$ is the velocity predicted from our reconstruction. In what follows, we do not explicitly show the dependence of $z_{\rm pred}$ on the reconstructed velocity and the flow model. For the cosmological redshift, $z_{\rm cos}$, we use a second order approximation (Peebles, 1993),

$$z_{\rm cos}(r) = \frac{1}{1+q_0}\left[1 - \sqrt{1 - \left(\frac{2H_0 r}{c}\right)(1+q_0))}\right], \tag{4.7}$$

where, q_0 is the deceleration parameter, which can be related to the cosmological parameters, Ω_m and Ω_Λ as, $q_0 = \frac{\Omega_m}{2} - \Omega_\Lambda$. This approximation is accurate to better than 2 km s^{-1} in cz for $z < 0.05$. The relation between $z_{\rm cos}$ and the comoving distance r is also robust to the adopted value of Ω_m: a 5% difference in Ω_m results in $< 0.5\%$ difference in the $z_{\rm cos}$.

Given the parameters $(\beta, \boldsymbol{V}_{\rm ext})$ and a reconstructed velocity field $\boldsymbol{v}$, the discrepancy between the observations and the predictions is given by,

$$\chi^2(\beta, \boldsymbol{V}_{\rm ext}) = \sum_{i=1}^{N_{\rm gal}} \frac{(cz_{\rm obs} - cz_{\rm pred})^2}{\sigma_d^2 + \sigma_v^2}, \tag{4.8}$$

where σ_v is the additional uncertainty in modelling the velocity field and σ_d is the error on the distance estimate converted to the units of km s^{-1}. The predicted redshift, $z_{\rm pred}$ is obtained using Equation (4.6) by assuming that the tracer is at the radial position reported in the peculiar velocity catalogue. Unless mentioned otherwise, throughout this work, we fix $\sigma_v = 150$ km s^{-1}. This value was obtained in Carrick et al. (2015) by comparing the linear theory predictions with the observed velocities of halos in N-body simulations. However, changing this value (or fitting it as an additional parameter) does not change the results.

We minimize the χ^2 given in Equation (4.8) with respect to β and $\boldsymbol{V}_{\rm ext}$ to infer the best-fit flow model.

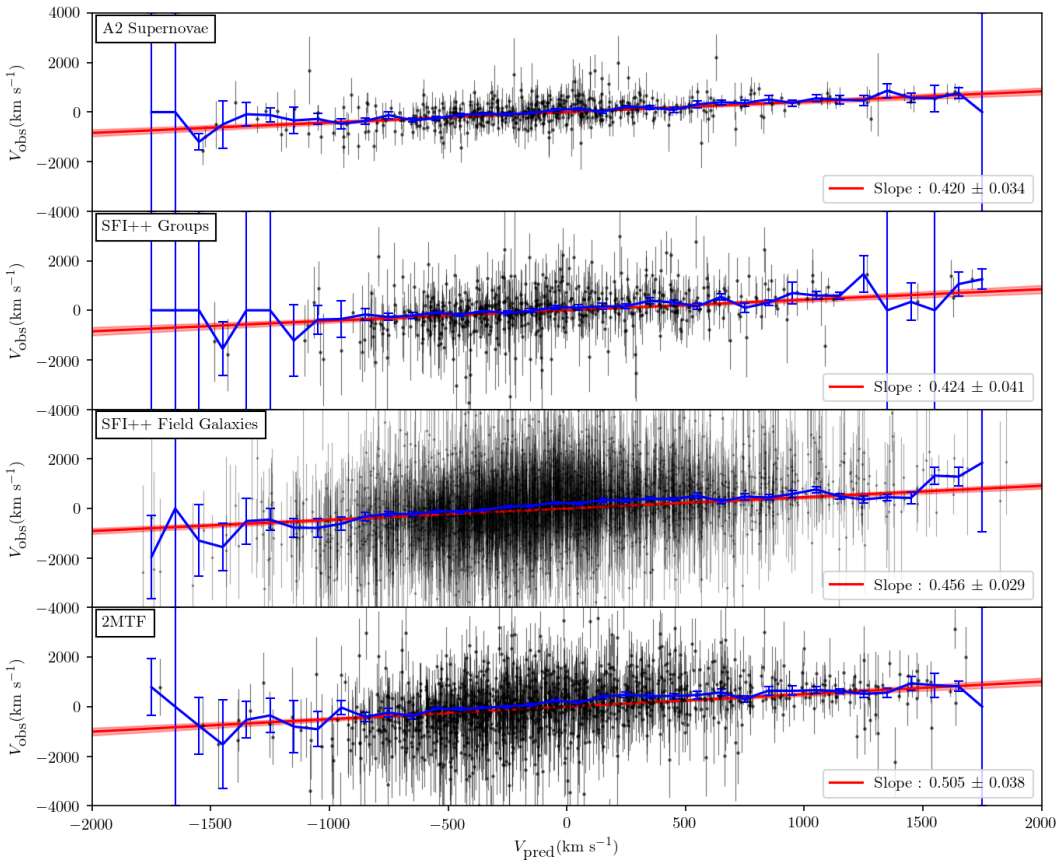

Figure 4.6: The predicted velocity ($V_{\rm pred}$) vs the observed velocity ($V_{\rm obs}$) for objects in the peculiar velocity catalogues: the A2 supernovae, SFI++ groups, SFI++ field galaxies and 2MTF. The predicted velocity is scaled to $\beta = 1$. The fitted slope therefore gives an estimate for β, although this will be biased somewhat high due to inhomogeneous Malmquist bias (see text for details). The red solid line is the best fitted line and the shaded area is the corresponding 1σ error. The blue lines are the weighted average of $V_{\rm obs}$ in bins of width 100 km/s in $V_{\rm pred}$.

4.4.2 Forward Likelihood

As mentioned in the previous section, the *Forward-Method I* approach is affected by inhomogeneous Malmquist bias. Pike & Hudson (2005) introduced an approach to take care of these difficulties. We call this approach *Forward likelihood*. A virtue of this method is that we can include any distance indicator data in this method.

Like the χ^2 minimization method introduced in section 4.4.1, the difference in the observed and predicted redshifts are minimized in this approach. To correct the inhomogeneous Malmquist bias, we need to take the inhomogeneities along the line of sight into account. Also, the measured distances have a lognormal uncertainty[3]. To correct for these deficiencies, we assume that the radial distribution is given as,

$$\mathcal{P}(r) = \frac{r^2 \exp\left(-\frac{[\mu(r)-\mu(d)]^2}{2\sigma_\mu^2}\right)[1+\delta_g(\boldsymbol{r})]}{\int_0^\infty \mathrm{d}r' r'^2 \exp\left(-\frac{[\mu(r')-\mu(d)]^2}{2\sigma_\mu^2}\right)[1+\delta_g(\boldsymbol{r'})]}\,, \tag{4.9}$$

where d is the distance reported in the peculiar velocity survey and δ_g is the overdensity in the galaxy field. The distances are converted to distance modulus using the formula $\mu(r) = 5\log_{10}(r/10\text{ pc})$. σ_μ is the error in the distance modulus of the tracer. As a proxy for the galaxy field, the luminosity weighted density was used. For the distance estimates which have already been corrected for homogeneous Malmquist bias, we drop the r^2 term from the prior. Instead, to correct for possible scale errors in the reported distance, we marginalize over a nuisance parameter, $\tilde{h}$, which rescales the reported distance

$$\mathcal{P}(r|\tilde{h}) = \frac{1}{\mathcal{N}(\tilde{h})}\exp\left(-\frac{[\mu(r)-\mu(\tilde{h}d)]^2}{2\sigma_\mu^2}\right)[1+\delta_g(\boldsymbol{r})]\,, \tag{4.10}$$

where $\mathcal{N}(\tilde{h})$ is the normalization term that depends on $\tilde{h}$. To account for the errors that arise because of the triple-valued regions and inhomogeneities along the line of sight, the likelihood is marginalized over the above radial distribution. The likelihood, $P(z_{\rm obs}|\boldsymbol{v}, \boldsymbol{V}_{\rm ext}, \beta)$, can therefore be written as

$$\mathcal{P}(z_{\rm obs}|\boldsymbol{v}, \boldsymbol{V}_{\rm ext}, \beta) = \int_0^\infty dr \mathcal{P}(z_{\rm obs}|r, \boldsymbol{v}, \boldsymbol{V}_{\rm ext}, \beta)\mathcal{P}(r), \tag{4.11}$$

where

$$\mathcal{P}(z_{\rm obs}|r, \boldsymbol{v}, \boldsymbol{V}_{\rm ext}, \beta) = \frac{1}{\sqrt{2\pi\sigma_v^2}}\exp\left(-\frac{(cz_{\rm obs}-cz_{\rm pred})^2}{2\sigma_v^2}\right), \tag{4.12}$$

[3]Although using a Gaussian distribution changes the inferred value of β by $< 0.35\sigma$

and $\mathcal{P}(r)$ is given by Equation (4.9) and $z_{\rm pred} \equiv z_{\rm pred}(r, \boldsymbol{v}, \boldsymbol{V}_{\rm ext}, \beta)$ as given in Equation (4.6).

We infer the flow model, $\{\beta, \boldsymbol{V}_{\rm ext}\}$ by sampling from the following posterior distribution,

$$\mathcal{P}(\boldsymbol{V}_{\rm ext}, \beta | \boldsymbol{v}, z_{\rm obs}) = \frac{\mathcal{P}(z_{\rm obs} | \boldsymbol{v}, \boldsymbol{V}_{\rm ext}, \beta) \mathcal{P}(\boldsymbol{V}_{\rm ext}, \beta)}{\mathcal{P}(z_{\rm obs})} \,. \tag{4.13}$$

Assuming a uniform prior on $V_{\rm ext}$, β and ignoring the denominator in Equation (4.13) as it does not depend on the parameters of interest, the posterior turns out to have the same functional form as the likelihood.

For the dataset of all galaxies, $\{z_i\}$, assuming independent probabilities, we maximize the joint posterior, which is given by

$$\mathcal{P}(\boldsymbol{V}_{\rm ext}, \beta, \tilde{h} | \{z_i\}) \propto \prod_i \mathcal{P}(z_i | \boldsymbol{V}_{\rm ext}, \beta) \,. \tag{4.14}$$

The results from the forward likelihood fit are presented in Section 4.6.1.

Jointly inferring distances and flow model with a modified Forward likelihood method

Measuring distances usually requires a calibration step for the distance indicator relationship. In this section, we introduce a method to jointly calibrate the distance indicator relationship while fitting for the flow model. To fit the LOSS and Foundation supernovae data and the field galaxies sample of the SFI++ catalogue, we modify the forward likelihood method to jointly fit for both the flow model and the parameters of the distance indicator. For the SALT2 model, the distance is a function of the global parameters, α, $\mathcal{B}$, M and $\sigma_{\rm int}$. We jointly denote these parameters with $\Theta_{\rm SN}$. Similarly, for the Tully-Fisher relationship, the distances depend on the TF parameters, $\Theta_{\rm TF} = \{a_{\rm TF}, b_{\rm TF}, \sigma_{\rm int}\}$. In order to jointly fit the parameters of distance indicator and the flow model, we therefore fit for these global parameters in addition to the flow model. In this approach, the Equation (4.9) is modified to

$$\mathcal{P}(r | \Theta) = \frac{1}{\mathcal{N}(\Theta)} r^2 \exp\left(- \frac{[\mu(r) - \mu(\Theta)]^2}{2\sigma_\mu^2(\Theta)} \right) [1 + \delta_g(\boldsymbol{r})] \,, \tag{4.15}$$

where $\mu(\Theta)$ is obtained from equation (4.1) or (4.4) and σ_μ is obtained by adding in quadrature the intrinsic scatter and the measurement uncertainty. Here, Θ stands for

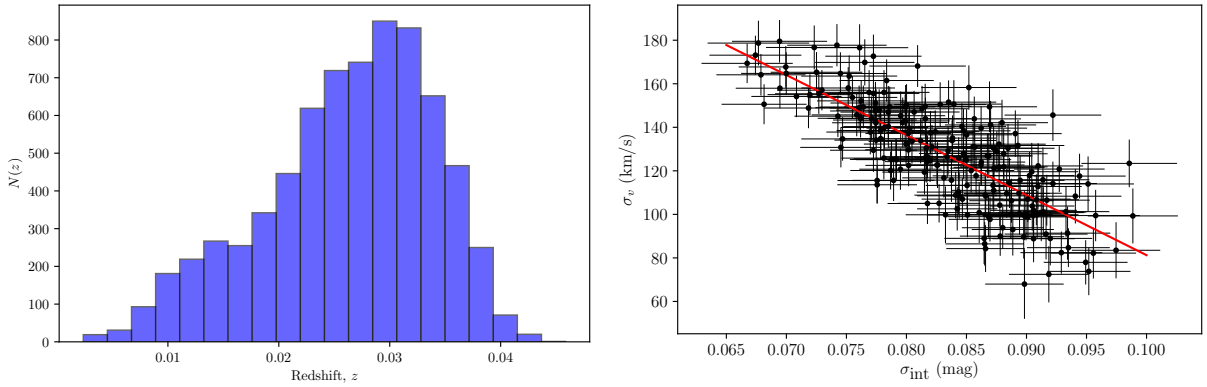

Figure 4.7: *(Left)* The redshift distribution of the simulated supernovae after the apparent magnitude cut of 16.5. *(Right)* Degeneracy in the recovered value of σ_v and $\sigma_{\rm int}$. We plot a rough best fit line, $\sigma_v = [137 + 220(\sigma_{\rm int}/0.08 - 1)]$ km/s to indicate the direction of the degeneracy. Simultaneously fitting σ_v and $\sigma_{\rm int}$ can result in significant bias in the recovered value of these parameters.

either $\Theta_{\rm SN}$ or $\Theta_{\rm TF}$. Note that we have added back the volume term which corrects fro the homogeneous Malmquist bias. $\mathcal{N}(\Theta)$ is the normalization term that depends on Θ. Using Bayes' Theorem as in the usual approach, we can then write the joint posterior for $\Theta, \boldsymbol{V}_{\rm ext}, \beta$. We sample from this posterior to infer the parameters. The results for fitting the supernovae data in using this method are presented in section 4.6. A test on mock simulations is given in section 4.5.

To sample from the posterior distribution of this section, we used the MCMC package `emcee` (Goodman & Weare, 2010; Foreman-Mackey et al., 2013). The autocorrelation time for the MCMC chains is $\mathcal{O}$(10-20)[4]. This gives an effective sample size of ~ 1000.

4.5 Testing the modified forward likelihood with simulated supernovae data

In this work, we used a modified forward likelihood method to jointly infer both the flow model and the distances to the supernovae. In this section, we use this method on simulated

[4]We note that finding the autocorrelation of an ensemble sampler is not trivial as the walkers are not independent. To get our estimate, we calculated the autocorrelation for each walker and then average over them. This has been suggested in `https://emcee.readthedocs.io/en/stable/tutorials/autocorr/`

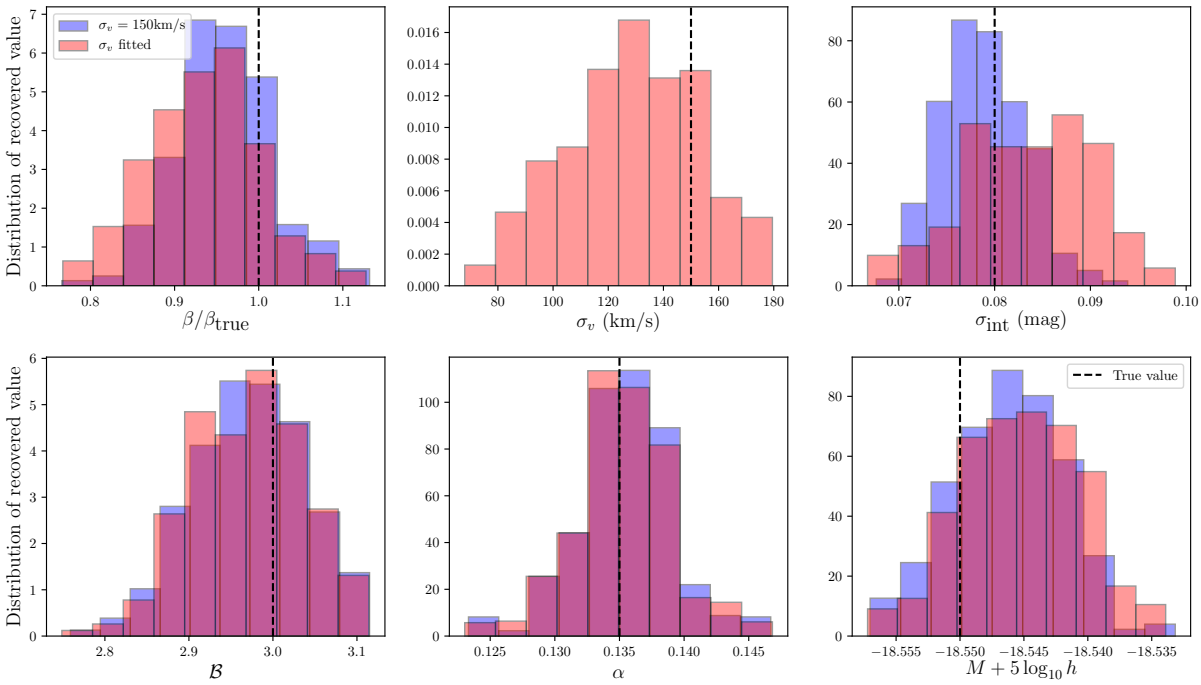

Figure 4.8: The recovered value of the various parameters from the simulated supernovae sample. We plot the histogram of the recovered values for the various parameters weighted by its uncertainty. The black dashed vertical line shows the true value of the parameter. For the adopted smoothing of 4 h^{-1} Mpc, we expect $\beta/\beta_{\rm true} = 0.95$, see text for further details.

data, where we know the true values of the global parameters of the SALT2 fitting formula.

To create the simulated data, we used a simulation from the VELMASS N-body simulation [5]. The simulation we use was performed in a cubic box of size 2 h^{-1} Gpc with a total of 2048^3 particles with mass 9.387×10^{10} $h^{-1}M_\odot$. The cosmological parameters used are as follows: $\Omega_m = 0.315, \Omega_b = 0.049, H_0 = 68$ km s^{-1} Mpc^{-1}, $\sigma_8 = 0.81$, $n_s = 0.97$ and $Y_{\rm He} = 0.248$. We identified the halos in the simulation with the ROCKSTAR halo finding software (Behroozi et al., 2013). We then populate the dark matter halos with simulated supernovae. To each supernova, we assign a value of the stretch (x_1) and color (c) parameter according to a distribution which describes the data from the Foundation supernovae survey well. We then use values of the global parameters as follows, $M = -18.55, \alpha = 0.135, \mathcal{B} = 3.00, \sigma_{\rm int} = 0.08$ mag. Using the true distance of the halo (and hence the true distance modulus, μ) and adding a Gaussian noise with a scatter of $\sigma_{\rm int}$, we can then measure the value of m_B using equation (4.1). We then apply an apparent magnitude cut of $m_B < 16.5$. The redshift distribution of the resulting simulated supernovae sample is shown in the left panel of Figure 4.7. From this data, we create 200 realizations of 500 randomly selected mock supernovae.

The density field of the VELMASS simulation is calculated using the Cloud-in-cell algorithm with grids of size 1.953 h^{-1} Mpc. We then smooth this density field with a Gaussian filter of a given size and estimate the velocity field from the smoothed density using the linear perturbation theory prediction, equation (1.41). When the Gaussian smoothing is done in conjunction with the CIC gridding, the effective smoothing length is different from the base Gaussian smoothing length. The CIC kernel in Fourier space is given as (Hockney & Eastwood, 1988; Cui et al., 2008),

$$W_{\rm CIC}(\boldsymbol{k}; l) = \prod_{i \in \{x,y,z\}} \left[\frac{\sin^2(k_i l/2)}{(k_i l/2)^2} \right], \tag{4.16}$$

where l is the grid spacing. Taylor expanding the CIC kernel, we get

$$\ln[W_{\rm CIC}(\boldsymbol{k}; l)] \approx -\frac{k^2}{2}\left(\frac{l^2}{6}\right) + \mathcal{O}(k^4 l^4). \tag{4.17}$$

Thus the CIC kernel has an effective Gaussian smoothing scale of $l/\sqrt{6}$. For a density field calculated with nearest grid-point (NGP) and Triangular Shaped Cloud (TSC) algorithms, the equivalent Gaussian smoothing length calculated in the same way turns out to be $l/\sqrt{12}$ and $l/2$ respectively. Therefore, when smoothing the CIC gridded density field with a Gaussian filter of size, R, the effective Gaussian smoothing scale is given as, $R_{\rm eff}^2 = R^2 + l^2/6$.

[5] For more details on the simulation we used, see Kodi Ramanah et al. (2019); Charnock et al. (2019)

For fitting the parameters with the forward likelihood code, we use the density field smoothed at $R_{\rm eff} = 4\ h^{-1}$ Mpc. The velocity field is calculated using linear perturbation theory prediction, equation (1.41). We jointly infer the global parameters of the Tripp parameterization and the flow model using the method of Section 4.4.2 for the 200 realizations of the mock supernovae. Note that all these realizations are not completely independent of each other. There are a total of $\sim$ 9000 mock supernovae after applying the apparent magnitude cut. Therefore, there must be repeated sampling of supernovae in our realizations. The results of the recovered value of the forward likelihood fit is shown in Figure 4.8. We plot the distribution of the recovered mean weighted by their uncertainty for the different parameters. We fit the parameters in two ways - *i)* we fix $\sigma_v = 150$ km/s, *ii)* we fit σ_v as a free parameter.

As can be seen from Figure 4.8, we recover unbiased value of the SNe parameters, α and $\mathcal{B}$ using both the methods. When simultaneously fitting σ_v, we see that the recovered value of $\sigma_{\rm int}$ has a significant scatter. This results from the fact that jointly fitting σ_v and $\sigma_{\rm int}$ results in a significant degeneracy between these parameters. This is shown in the right panel of Figure 4.7 where we plot the recovered value of σ_v and $\sigma_{\rm int}$ for the 200 realizations. Therefore, if one simultaneously fits σ_v and $\sigma_{\rm int}$, it can result in significantly biased results. For the parameter, $\beta/\beta_{\rm true}$, we recover a weighted mean of 0.96 with a mean uncertainty of 0.04. As shown in Carrick et al. (2015), the value of β obtained by using the smoothed density field from haloes is not the same as the value of β obtained, at the same smoothing length, using the reconstruction procedure in which the haloes are iteratively moved from theory positions in redshift space to their reconstructed positions in configuration space. In fact, using the haloes at their true locations results in a value of β that is biased low by $\sim 5\%$ at $4\ h^{-1}$ Mpc, as we also find here. Since the comparison in this chapter uses the Carrick et al. (2015) density field after reconstruction, we expect this to be unbiased. Finally, there is no significant bias in the value of M obtained using the two methods. The weighted value for all the simulations is -18.546 ± 0.005 mag using $\sigma_v = 150$ km/s and -18.545 ± 0.005 mag when we simultaneously fit σ_v.

4.6 Results

In this section, we will present the results of the comparison between the predicted and the measured peculiar velocities. In Section 4.6.1, we present our peculiar velocity analysis of the different catalogues. In Section 4.6.2, we present the constraints on the cosmological parameters and the external bulk flow.

4.6.1 Peculiar velocity analysis with different catalogues

In this section, we present the results of analysis of the different catalogues we use in our peculiar velocity analysis. First, we analyse these catalogues using the χ^2-minimization method. Then, we present the analysis of the same catalogues using the forward likelihood method.

χ^2 minimization

While the χ^2 minimization method is affected by the inhomogeneous Malmquist bias, it is advantageous to get interpretable results. We present the results of the χ^2-minimization method in Table 4.3. For each sub-sample, we infer the external bulk flow velocity, $\boldsymbol{V}_{\rm ext}$, its direction in the galactic coordinates, l and b. We also infer the velocity rescaling factor for the predicted velocity from reconstruction. Note that this rescaling factor is equal to $\beta = f/b$. In Table 4.3, we also report the value of the χ^2 over the number of degrees of freedom. In this section, for the SFI++ catalogue, we use the distance as reported in the catalogue. For the supernovae samples, we use a variant of the χ^2 minimization method where we also fit for the intrinsic scatter. For the LOSS and the Foundation sample, we fit for the light curve parameters in addition to the flow model parameters.

In Figure 4.6, we compare the predicted peculiar velocities to the observations from the peculiar velocity surveys. In the χ^2 minimization method, the difference between the two is minimized by fitting for the flow model. The observed peculiar velocities usually have a large uncertainty. Nonetheless, when taken together, the trend is clearly visible. We also show the results of the χ^2 fitting method in the plot. We plot the predicted velocities from the reconstruction against the observed velocities and fit for the slope. This slope roughly corresponds to the value of β. However, the obtained value is biased high due to inhomogeneous Malmquist bias. One can also observe this by comparing the value of β as found in Table 4.3 and Table 4.4.

Forward likelihood

We also analysed the peculiar velocity samples using the forward likelihood method of Section 4.4.2. The result of this analysis is presented in Table 4.4. For the analysis in this section, wherever possible, we use the modified forward likelihood method, presented in Section 4.4.2 to jointly fit for the distance indicator parameters and the flow model. For the Foundation and the LOSS SNe samples and the Tully-Fisher galaxy samples, we fit

Table 4.3: Results of the χ^2 minimization with the different catalogues. Note that the χ^2 method is affected by inhomogeneous Malmquist bias. We correct for the IHM using the forward likelihood method. Forward likelihood result is presented in Table 4.4.

Sample	β	$\lvert\boldsymbol{V}_{\rm ext}\rvert$(km/s)	l(deg)	b(deg)	χ^2/d.o.f
A1	0.445 ± 0.042	130 ± 37	314 ± 29	26 ± 17	0.901
CSP-DR3	0.588 ± 0.092	231 ± 63	14 ± 41	-50 ± 18	0.950
LOSS	0.483 ± 0.077	264 ± 100	282 ± 42	-24 ± 16	1.005
Foundation	0.389 ± 0.060	375 ± 64	251 ± 10	18 ± 7	1.032
A2	$\mathbf{0.439 \pm 0.033}$	$\mathbf{132 \pm 30}$	$\mathbf{285 \pm 17}$	$\mathbf{16 \pm 13}$	**0.768**
SFI++ Groups	0.431 ± 0.040	184 ± 41	282 ± 22	23 ± 14	0.839
SFI++ Field Galaxies	0.458 ± 0.031	192 ± 30	283 ± 11	4 ± 8	0.734
2MTF	0.504 ± 0.041	190 ± 36	285 ± 16	17 ± 11	0.938
Combined	$\mathbf{0.457 \pm 0.016}$	$\mathbf{163 \pm 17}$	$\mathbf{283 \pm 8}$	$\mathbf{15 \pm 6}$	**0.803**

Table 4.4: Results of forward likelihood analysis for different peculiar velocity datasets. For the A2 and the combined results, we jointly fit the flow model parameters and the global parameters of the each sample.

Sample	β	$f\sigma_{8,\rm lin}$	$\lvert\boldsymbol{V}_{\rm ext}\rvert$(km/s)	l(deg)	b(deg)
A1	0.421 ± 0.030	0.396 ± 0.030	156^{+32}_{-31}	310^{+13}_{-13}	7^{+9}_{-9}
CSP-DR3	0.483 ± 0.103	0.469 ± 0.097	217^{+55}_{-55}	19^{+32}_{-31}	-43^{+16}_{-17}
LOSS	0.490 ± 0.079	0.456 ± 0.073	150^{+65}_{-65}	282^{+105}_{-99}	-26^{+27}_{-27}
Foundation	0.345 ± 0.064	0.331 ± 0.062	314^{+54}_{-55}	249^{+12}_{-12}	17^{+8}_{-8}
A2	$\mathbf{0.408 \pm 0.025}$	$\mathbf{0.385 \pm 0.027}$	$\mathbf{135^{+24}_{-24}}$	$\mathbf{300^{+11}_{-11}}$	$\mathbf{-3^{+8}_{-8}}$
SFI++ groups	0.411 ± 0.027	0.385 ± 0.030	174^{+31}_{-30}	292^{+10}_{-10}	2^{+7}_{-7}
SFI++ field	0.411 ± 0.020	0.385 ± 0.022	181^{+20}_{-21}	291^{+10}_{-10}	14^{+6}_{-6}
2MTF	0.483 ± 0.022	0.444 ± 0.025	177^{+19}_{-19}	304^{+7}_{-7}	-2^{+5}_{-5}
All combined	$\mathbf{0.428 \pm 0.012}$	$\mathbf{0.401 \pm 0.017}$	$\mathbf{159^{+12}_{-11}}$	$\mathbf{301^{+4}_{-4}}$	$\mathbf{0^{+3}_{-3}}$

Table 4.5: Light curve parameters and intrinsic scatter inferred using the modified forward likelihood analysis for the LOSS, Foundation and the CSP samples

Sample	$M + 5\log_{10}(h)$	α	$\mathcal{B}$	$\sigma_{\rm int}$ (mag)
LOSS	-18.191 ± 0.022	0.121 ± 0.019	3.53 ± 0.16	0.125 ± 0.017
Foundation	-18.558 ± 0.011	0.140 ± 0.011	2.78 ± 0.12	0.082 ± 0.010
CSP-DR3	—	—	—	0.062 ± 0.018

the parameters of the distance indicator relation and the flow model for the sample. In this method, the likelihood is still given by Equation (4.11) but Equation (4.9) is modified to Equation (4.15). We jointly fit $\beta, \boldsymbol{V}_{\rm ext}, M, \alpha, \mathcal{B}$ and $\sigma_{\rm int}$ for the supernovae samples and $\beta, \boldsymbol{V}_{\rm ext}, a_{\rm TF}, b_{\rm TF}, \sigma_{\rm int}$ for the Tully-Fisher samples using this modified version of forward likelihood. Similarly, for the CSP-DR3 sample, we also fit the intrinsic scatter. The results of these fits and a comparison of the intrinsic scatter for the LOSS, CSP and Foundation sample is presented in Table 4.5.

4.6.2 Constraining $f\sigma_8$ and the bulk flow

In this section, we present the results of inferring the cosmological parameter, $f\sigma_8$, and the bulk flow using the forward likelihood method. Note that while inferring the flow model with multiple catalogues, we jointly fit the distance indicator parameters of each peculiar velocity catalogue and the flow model parameters.

Constraint on $f\sigma_8$

Using the forward likelihood method of Section 4.4.2, we inferred the parameter $\beta = f/b$ for the reconstructed velocity field. The relation between β and the factor $f\sigma_8$ is given as, $f\sigma_8 = \beta\sigma_8^g$, where σ_8^g is the root mean squared fluctuation in the galaxy field. Carrick et al. (2015) found the value of σ_8^g to be 0.99 ± 0.04. To convert our constraints on β to the constraints on $f\sigma_8$, we use this value of σ_8^g.

It should be noted however, the value of σ_8 inferred from peculiar velocities is sensitive to the non-linear evolution of structures. To compare with values of σ_8 inferred at high redshifts, we need to correct for the non-linear evolution. This is done using the recipe of Juszkiewicz et al. (2010). This linearized value is denoted by $f\sigma_{8,\rm lin}$. We assume $\Omega_m = 0.3$ to convert the constraint on $f\sigma_8$ into the constraint on σ_8. This value is then converted into the linearized value. The result for $f\sigma_{8,\rm lin}$ as inferred from the two reconstruction

schemes and the different datasets is presented in Table 4.4 and in Figure 4.9. We find consistent results from the different datasets. The value of $f\sigma_{8,\mathrm{lin}}$ inferred by comparing the combined dataset of the A2 supernovae, 2MTF and the SFI++ to the predictions of our reconstruction is 0.401 ± 0.017.

Bulk Flow

We also infer the external bulk flow in the forward likelihood method. The bulk flow may be thought of as the coherent flow in the reconstructed volume. Comparison with our reconstruction yields an external bulk flow of magnitude 159^{+12}_{-11} km s^{-1} in the direction $l = 295^\circ \pm 4^\circ, b = 5^\circ \pm 3^\circ$. We also compare the reconstructed bulk flow centred on the Local Group at an effective radius of 40 h^{-1} Mpc. At this scale, we find a bulk flow of 246 ± 11 km s^{-1} in the direction $l = 292^\circ \pm 5^\circ$, $b = 14^\circ \pm 5^\circ$. To obtain this flow, we added the external flow to the velocity obtained by smoothing the reconstructed velocity flow at $R = 40\ h^{-1}$ Mpc with a Gaussian filter. We compare our results for the bulk flow at 40 h^{-1} Mpc with other results from the literature in section 4.7.1.

4.7 Discussion

In this section, we compare our inferred value of $f\sigma_8$ and the bulk flow to that of other results in the literature and also discuss the prospects for the future.

4.7.1 Comparison with the literature

In this section, first we compare our results to other results of $f\sigma_8$ based on a variety of cosmological probes. Then we compare our results for the bulk flow to ΛCDM prediction and to other results in the literature.

Comparison of the value of $f\sigma_8$

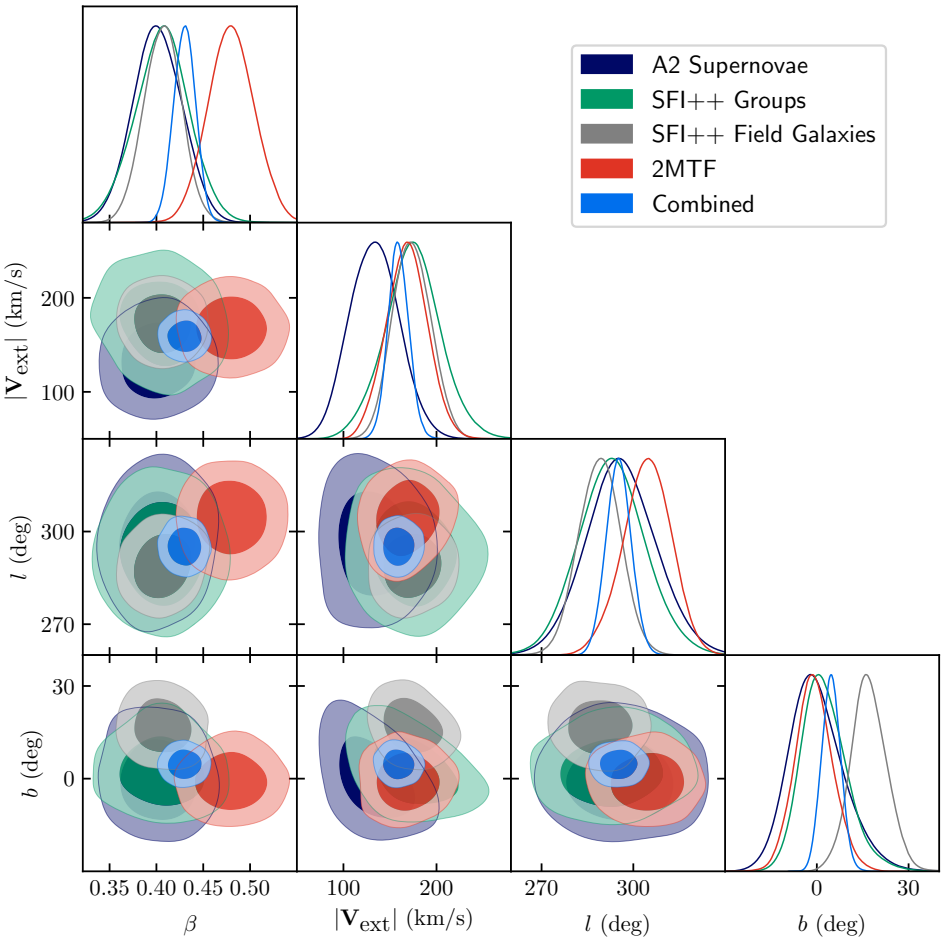

Figure 4.9: The results of forward likelihood inference with our reconstruction scheme. The numerical values are presented in Table 4.4. The panels show the two dimensional marginal posteriors for $\beta, |\boldsymbol{V}_{\rm ext}|, l, b$. The different samples corresponds to the results obtained from the taking the different datasets. The 'combined' dataset is obtained by combining the A2 supernovae, SFI++ field galaxies, SFI++ groups and 2MTF samples. The dark and light shaded regions correspond to the 68% and 95% confidence intervals respectively

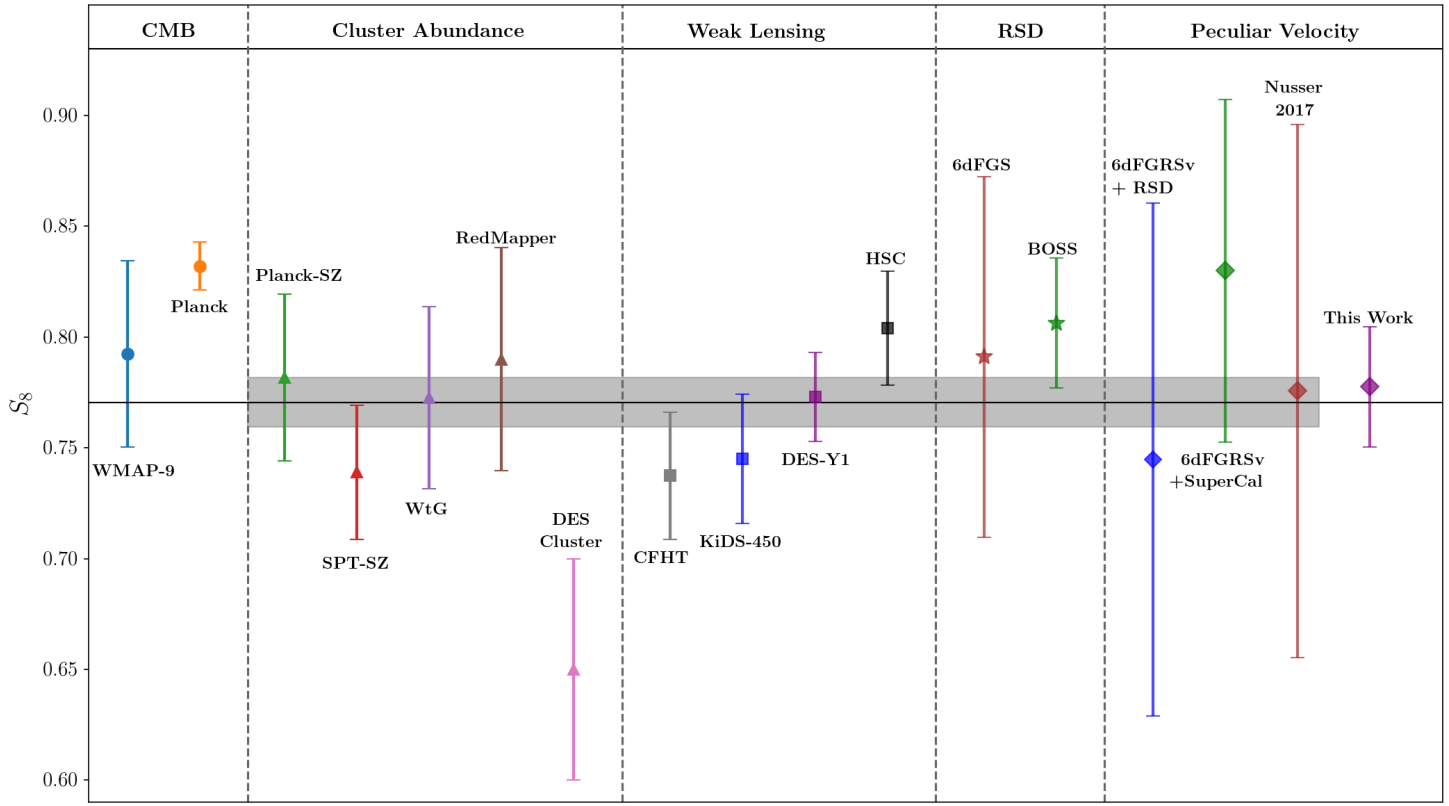

Figure 4.10: Comparison of different literature results for $S_8 = \sigma_8(\Omega_m/0.3)^{0.5}$. See Table 4.6 and section 4.7.1 for details of these studies. The horizontal line corresponds to the uncertainty weighted mean for the measurement from the different datasets, excluding the CMB and our result. The shaded grey region is the weighted uncertainty for these same studies.

Table 4.6: Comparison of the S_8 results in the literature from various cosmological probes. Along with the value of $S_8 = \sigma_8(\Omega_m/0.3)^{0.5}$, we also show the quantity and the value in terms of Ω_m and σ_8 that was reported in the original reference.

Probe		Reported Quantity	Reported Value	S_8	Reference
CMB	WMAP	MCMC Chains	—	0.792 ± 0.053	Hinshaw et al. (2013)
	Planck	MCMC Chains	—	0.832 ± 0.013	Planck Collaboration (2018a)
Cluster Abundance	Planck-SZ	$\sigma_8(\Omega_m/0.31)^{0.3}$	0.774 ± 0.034	0.782 ± 0.048	Planck Collaboration (2016)
	SPT-SZ	S_8	0.739 ± 0.041	0.739 ± 0.041	Bocquet et al. (2019)
	WtG	$\sigma_8(\Omega_m/0.3)^{0.17}$	0.81 ± 0.03	0.773 ± 0.053	Mantz et al. (2015)
	RedMapper	S_8	$0.79^{+0.05}_{-0.04}$	$0.79^{0.05}_{-0.04}$	Costanzi et al. (2018)
	DES-Clusters	S_8	0.65 ± 0.05	0.65 ± 0.05	DES Collaboration (2020)
Weak Lensing	CFHT	$\sigma_8(\Omega_m/0.27)^{0.46}$	$0.774^{+0.032}_{0.041}$	0.737 ± 0.039	Heymans et al. (2013)
	KiDS-450	S_8	0.745 ± 0.039	0.745 ± 0.039	Hildebrandt et al. (2017)
	DES-Y1	S_8	0.773 ± 0.026	0.773 ± 0.026	Abbott et al. (2018a)
	HSC	S_8	0.804 ± 0.032	0.804 ± 0.032	Hamana et al. (2019)
RSD	6dFGS	$f\sigma_8$	0.423 ± 0.055	0.791 ± 0.103	Beutler et al. (2012)
	BOSS	$f\sigma_8$	—	0.806 ± 0.029	Alam et al. (2017)
Peculiar Velocity	6dFGRSv + RSD	$f\sigma_8$	0.384 ± 0.081	0.707 ± 0.148	Adams & Blake (2020)
	6dFGRSv + SNe	$f\sigma_8$	$0.428^{+0.048}_{-0.045}$	0.780 ± 0.087	Huterer et al. (2017)
	Nusser 2017	$f\sigma_8$	0.40 ± 0.08	0.776 ± 0.120	Nusser (2017)
	This Work	$\boldsymbol{f\sigma_8}$	$\mathbf{0.401 \pm 0.018}$	$\mathbf{0.777 \pm 0.035}$	This work

In this section, we compare our result to others from the literature. These include cosmological constraints obtained from other peculiar velocity analyses, from redshift space distortions, as well as from CMB anisotropies, cluster abundances and weak lensing. Table 4.6 summarises the measurements from the literature and converts these to the parameter combination $S_8 \equiv \sigma_8(\Omega_m/0.3)^{0.5}$ where appropriate assuming $\Omega_m = 0.3$. The comparison is shown in Figure 4.10.

We first compare our result $f\sigma_{8,\rm lin} = 0.401 \pm 0.017$ to the constraints on $f\sigma_8$ from other analyses of peculiar velocity in the local universe. In Adams & Blake (2020), the authors did a joint analysis of the peculiar velocity sample and the redshift space distortions in the galaxy redshifts of the 6dF galaxy survey to obtain, $f\sigma_8 = 0.384 \pm 0.054(\rm stat) \pm 0.061(\rm sys)$. In Huterer et al. (2017), the authors used the 'SuperCal' sample of supernovae in addition to the 6dFGRSv catalogue to obtain the constraint, $f\sigma_8 = 0.428^{+0.048}_{-0.045}$. Finally we also include the results from Nusser (2017), where the authors used velocity-density cross-correlation on the *Cosmicflows-3* peculiar velocity data (Tully et al., 2016) and the 2MASS redshift survey to obtain $f\sigma_8 = 0.40 \pm 0.08$. Note that these results are not independent since they all include the same 6dFGRSv catalogue.

Redshift space distortions (RSD) are sensitive to the parameter combination $f\sigma_8$. We compared our results to the RSD results from the 6dFGRS (Beutler et al., 2012) and the results from the SDSS-BOSS survey (Alam et al., 2017). Beutler et al. (2012) probed the redshift space distortions at low redshifts with an effective redshift of $z_{\rm eff} = 0.067$. At that redshift, the value of $f\sigma_8 = 0.423 \pm 0.055$. For the BOSS study, we use a weighted mean of the 'consensus' value of $f\sigma_8$ at three different effective redshifts. for this comparison. The constraints on $f\sigma_8(z)$ is converted to a constraint at $z = 0$ by assuming a cosmological model with $\Omega_m = 0.3$ and $\Omega_\Lambda = 0.7$. In this model, we solve for $\Omega_m(z)$ and use linear theory to scale σ_8 with the linear growth factor $D(z)$.

Different cosmological probes are sensitive to different combination of parameters. In particular, while peculiar velocities are sensitive to $f\sigma_8 = \Omega_m^{0.55}\sigma_8$, cosmological constraints from weak lensing are usually reported in terms of the parameter, $S_8 = \sigma_8(\Omega_m/0.3)^{0.5}$. Note that our peculiar velocity result corresponds to $S_8 = 0.777 \pm 0.035$. We compare our results to the results from DES-Y1 (Abbott et al., 2018a), KiDS450 (Hildebrandt et al., 2017) and the HSC (Hamana et al., 2019).

Cluster abundances are another probe of cosmology that is sensitive to the cosmological parameter combination, $\sigma_8\Omega_m^\alpha$, where, α is the local slope of the matter power spectrum (White et al., 1993a). Depending on the specific survey, $\alpha \sim 0.2 - 0.4$. We compare the results of 5 cluster abundance studies. Two of them Planck-SZ (Planck Collaboration, 2016) and SPT-SZ (Bocquet et al., 2019) are based on Sunyaev-Zeldovich (SZ) clusters.

SPT-SZ, the RedMapper (Costanzi et al., 2018) study and the DES cluster abundance (DES Collaboration, 2020) give their results in terms of S_8. The Planck-SZ and Weighing the Giants (WtG) Mantz et al. (2015) gives their results using $\alpha = 0.3$ and $\alpha = 0.17$ respectively. To convert these constraints into that on S_8, we use the Ω_m value inferred in these studies and add the uncertainties in quadrature.

Finally, we compare our results also to the results obtained from CMB anisotropies. We use the publicly available MCMC chains for Planck 2018 (Planck Collaboration, 2018a) and Wilkinson Microwave Anisotropy Probe (WMAP) 9 year (Hinshaw et al., 2013) results to obtain the constraints on S_8. For the Planck results, we use the combination of TT,TE,EE+lowE+lensing results.

Our result is in good agreement with a simple error weighted average of lower redshift results: the uncertainty-weighted value of S_8 of the measurements from the different datasets, excluding the CMB and our result, is 0.770 ± 0.011. While our result appears to be in tension with Planck, the difference is not statistically significant (1.6σ) Moreover, as discussed in section 4.7.2, the systematic uncertainties in our measurement have not been fully quantified at this time.

Comparison of the bulk flow

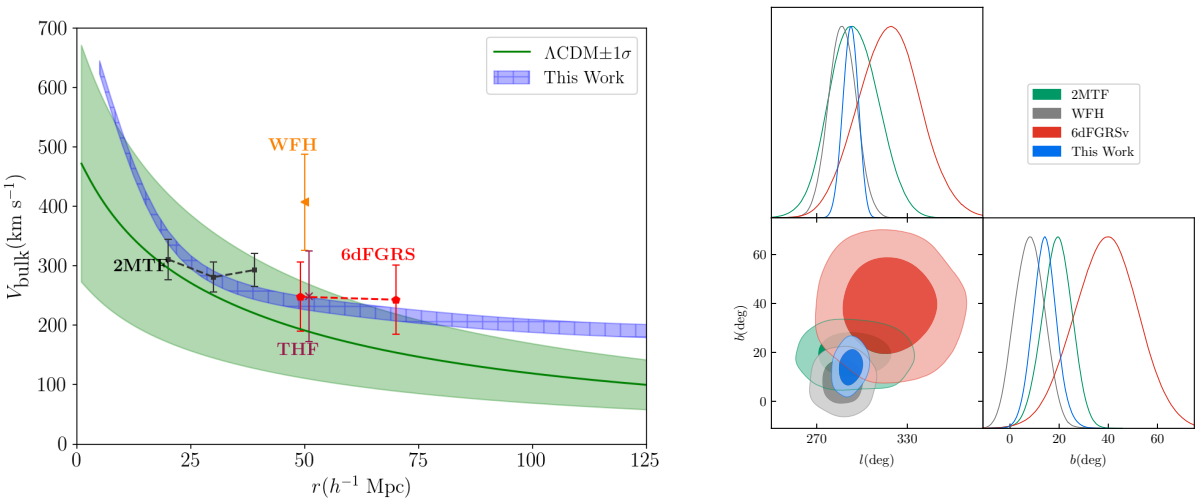

Figure 4.11: *(Left):* Comparison of the bulk flow amplitude. Our result for the bulk flow amplitude is compared to other results from the literature and to the ΛCDM prediction, which is calculated using a Gaussian filter of the given scale radius. The green shaded area shows the 68% confidence region for ΛCDM predictions. Our bulk flow amplitude is calculated by adding the residual bulk flow inferred in the earlier sections to the Gaussian smoothed bulk velocity centered on the Local Group at different scales. Our result is shown with a hatched blue region. The 2MTF (Hong et al., 2014) bulk flow is denoted with a black symbols, 6dFGRS (Scrimgeour et al., 2016) with a red pentagon, THF (Turnbull et al., 2012) with a brown cross, WFH (Watkins et al., 2009) with an orange triangle. *(Right)*: Comparison of the direction of the bulk flow at a depth of $\sim 40\ h^{-1}$ Mpc. We obtain a bulk flow in the direction $(l, b) = (293^\circ \pm 6^\circ, 9^\circ \pm 4^\circ)$ for our reconstruction. For the purposes of illustration, the other works (2MTF, WFH and 6dFGRSv) are plotted as a normal distribution in l, b with the quoted uncertainties. The dark and light shaded regions correspond to the 68% and 95% confidence intervals respectively

Table 4.7: Bulk flow results - comparison with other studies. We quote our bulk flow result at 40 h^{-1} Mpc for easy comparison with other studies

Work	Peculiar Velocity survey	Effective radius	$\lvert \boldsymbol{V}_{\rm bulk} \rvert$ (km/s)	l (deg)	b (deg)	Reference
6dFGRSv	6dFGRSv	40 h^{-1} Mpc	248 ± 58	318 ± 20	40 ± 13	Scrimgeour et al. (2016)
2MTF	2MTF	40 h^{-1} Mpc	292 ± 28	296 ± 16	19 ± 6	Hong et al. (2014)
THF	A1 Supernovae	50 h^{-1} Mpc	249 ± 76	319 ± 18	7 ± 14	Turnbull et al. (2012)
WFH	COMPOSITE	40 h^{-1} Mpc	407 ± 81	287 ± 9	8 ± 6	Watkins et al. (2009)
This Work	**A2 Supernovae + SFI++**	**40 $\boldsymbol{h^{-1}}$ Mpc**	$\mathbf{246 \pm 11}$	$\mathbf{289 \pm 5}$	$\mathbf{13 \pm 5}$	—-

The bulk flow in the local universe has been studied in the literature by many groups (See e.g. Carrick et al. (2015); Scrimgeour et al. (2016); Hong et al. (2014)). In this section, we compare our results to the predictions from the ΛCDM model and to other results in the literature.

One can use linear perturbation theory to calculate the expected bulk flow in a ΛCDM universe. The variance of the bulk flow on a scale, R, is given as (Gorski, 1988),

$$\sigma_B^2(R) = \frac{H_0^2 f^2}{2\pi^2} \int_0^\infty dk P(k) \widetilde{W}^2(k, R) \ , \tag{4.18}$$

where $P(k)$ is the matter power spectrum and $\widetilde{W}$ is the window function used to smooth the field at the scale, R. We calculate the matter power spectrum using the publicly available CAMB software (Lewis et al., 2000).

The distribution of velocity on a scale, R, with standard deviation, σ_B is given by the Maxwellian distribution if the density field is Gaussian. On large-scales, where linear theory holds, this is a valid assumption. Hence, the distribution of bulk flow velocity, V, for ΛCDM universe is given as,

$$P(V)\,\mathrm{d}V = \sqrt{\frac{2}{\pi}} \left(\frac{3}{\sigma_B^2}\right)^{3/2} V^2 \exp\left(-\frac{3V^2}{2\sigma_B^2}\right) \mathrm{d}V \ . \tag{4.19}$$

We plot the mean and standard deviation of this distribution as a function of the scale, R, in the left panel of Figure 4.11. These results are calculated assuming $\Omega_m = 0.3$. We compare our results along with other results of bulk flow in the literature. At a radius of 125 h^{-1} Mpc, up to which 2M++ has high all-sky completeness, the mean and standard deviation of the predicted bulk flow for ΛCDM is 100 km s^{-1} and 42 km s^{-1} respectively.

At large radius, the predicted bulk flow from our reconstruction at 125 h^{-1} Mpc, $V_{\rm bulk}(125h^{-1}\ \mathrm{Mpc}) = 189 \pm 11$ km/s, seems to be slightly higher than the linear theory predictions, but the $\sim 1.5\sigma$ difference is not statistically significant. This bulk flow consists of a ~ 170 km/s external bulk flow and a 19 km/s internal bulk flow from the reconstruction. Note that the bulk flows in spheres of increasing radius are highly correlated. Besides, our model of a dipolar bulk flow is not sufficient at large distances. In order to model better the external bulk flow, we need to add the higher multipoles of the bulk flow. Given the imperfect modelling, the dipole is particularly sensitive to the peculiar velocity data at low redshifts, leading to a higher inferred bulk flow. The bulk flow inferred in this study may also include contributions from sources which are missed in the reconstruction due to, e.g., the ZoA, or incompleteness in the 2M++ catalogue. At $r \approx 0$, our estimates

are consistent with the Local Group velocity. The velocity of the Local Group as inferred in our reconstruction is 706 km/s in the direction, $l = 277°$ and $b = 35°$ in agreement with the CMB dipole, given the expected scatter of 150 km/s when comparing halo peculiar velocities with the predictions of linear theory. Note that the result for the predicted bulk flow variance is also not sensitive to changes in the value adopted for Ω_m. A change of 5% changes the bulk flow by $< 0.5\%$. In summary, the results for the external bulk flow obtained from our reconstruction are not inconsistent with the ΛCDM predictions. We also compare our results with other studies of bulk flow in the literature. The details of these other studies are given in Table 4.7. In this comparison, we quote our bulk flow results at $R = 40\ h^{-1}$ Mpc. The direction of the bulk flow as found in this study is also similar to what has been found before in other studies. We compare some of these in the right panel of Figure 4.11.

4.7.2 Future Prospects

As discussed in Section 1.5, many new peculiar velocity surveys will operate in the near future increasing the volume of peculiar velocity data by an order-of-magnitude. This increase in data volume will lead the statistical error on the measurement of $f\sigma_8$ from peculiar velocities to decrease further.

Given the statistical precision of peculiar velocity studies, it would be timely to more clearly understand the systematics of the density-velocity comparison. Carrick et al. (2015) used N-body simulations to show that, when dark matter haloes are used as tracers of the density field, the inverse reconstruction procedure used here should have biases of order of 1%. However, in practice, a few approximations were made during the reconstruction. For example, luminosity-weighting is used as a proxy for halo mass, where every galaxy is assigned a weight proportional to their absolute K-band luminosity. The galaxy bias is assumed to be linear on a scale where it is known to be non-linear, with the bias factor fit from the data. The systematic errors introduced due to these approximations have not been quantified.

Improvement in the methods of analysis may also tighten these constraints. Forward-modelled reconstruction is a promising framework for the analysis of the large-scale structure. In Lavaux (2016), a forward-modelled approach, VIRBIUS, was introduced to analyse the 3-dimensional velocity field by jointly inferring the distances to the peculiar velocity data. VIRBIUS was used in Graziani et al. (2019) to analyse the CosmicFlows-3 data. It would also be interesting to compare the velocity field of the forward modelled reconstruction scheme, BORG (Jasche & Wandelt, 2013; Jasche & Lavaux, 2019), to study the peculiar

velocity field of the local universe. Non-linear structure formation models such as Second order Lagrangian Perturbation Theory (2LPT, Bouchet et al. (1995)), Particle-Mesh (See e.g. Hockney & Eastwood (1988)) and COmoving Lagrangian Acceleration (COLA, Tassev et al. (2013)) can be incorporated into BORG, likely providing a better approximation to the non-linear velocity field.

4.8 Summary

In this work, we used peculiar velocity analysis to infer the cosmological parameter combination $f\sigma_8$ and the bulk flow in the local universe. We compiled a new peculiar velocity catalogue of low-z Type Ia supernovae, called the Second Amendment (A2) sample. We also used the SFI++ and the 2MTF Tully-Fisher catalogues for our analysis. We used an inverse reconstruction scheme used in Carrick et al. (2015) to compare the predicted velocities from the reconstruction to the observations in order to infer $f\sigma_8$ and the bulk flow. To make this comparison, we introduced a variant of the original forward likelihood method, in which the distances to the peculiar velocity tracers are fitted jointly with the flow model and hence, do not require prior calibration. The comparison yielded $f\sigma_{8,\mathrm{lin}} = 0.401 \pm 0.017$, with $\sim$ 4% statistical uncertainties on the value of $f\sigma_8$. These results are consistent with other low redshift results from the literature, as shown in section 4.7.1. We also fit for an external bulk flow which is not accounted for in our reconstruction process. We compare our constraint of the bulk flow with the ΛCDM prediction in Figure 4.11. With our reconstruction method, we obtain a residual bulk flow of 159^{+12}_{-11} km s^{-1} in the direction $l = 295^\circ \pm 4^\circ, b = 5^\circ \pm 3^\circ$. At an effective radius of $40h^{-1}$ Mpc, this corresponds to a bulk flow of 246 ± 11 km s^{-1} in the direction $l = 292^\circ \pm 5^\circ, b = 14^\circ \pm 5^\circ$ for our reconstruction scheme.

Chapter 5

Comparing peculiar velocity models of the local universe

5.1 Introduction

As we saw in the previous chapter, peculiar velocities provide the only way to measure growth of structures in the low redshift Universe. Apart from their use as a probe of cosmological structure growth, one also has to account for the peculiar velocity of galaxies in other studies of cosmology and galaxy formation. For example, peculiar velocity corrections for nearby standard candles and standard sirens are an important step in trying to measure the expansion rate of the Universe. It was noted in Hui & Greene (2006) that correlated errors in the supernovae introduced due to peculiar velocities are important to account for in cosmological analyses. Neill et al. (2007) applied peculiar velocity corrections while inferring the equation-of-state from supernovae, finding a systematic bias of $\Delta w \sim 0.04$ when not corrected for the peculiar velocities. In Riess et al. (2011), peculiar velocity corrections were applied for the first time in the measurement of the Hubble constant. Peculiar velocity corrections are especially important given the increasing discrepancy (Verde et al., 2019) in the value of the Hubble constant, H_0, measured using the Cosmic Microwave Background (CMB) (Planck Collaboration, 2018a) and other low-z measurements (Riess et al., 2019; Wong et al., 2019). The current tension between the measurements from CMB and the low redshift supernovae has been estimated to be $\sim 4.4\sigma$ (see section 1.4.3). Other methods such as standard sirens and megamasers, which measure distances without any calibration to the distance ladder, are crucial in resolution of the H_0 tension. H_0 has already been measured from the first detection of gravitational waves

from a binary neutron star merger, GW170817 (Abbott et al., 2017a) yielding a value of $H_0 = 70.0^{+12.0}_{-8.0}$ km s^{-1} Mpc^{-1}(Abbott et al., 2017b). Megamaser cosmology project has also measured distances to six megamasers giving a constraint of $H_0 = 73.9 \pm 3$ km s^{-1} Mpc^{-1}.

The value of H_0 measured from local distance indicators depend on the peculiar velocity corrections. The observed redshift, $z_{\rm obs}$, for standard candles and standard sirens gets a contribution from both the recession velocity due to the Hubble flow, $H_0 r$, and the radial peculiar velocity of the object, v_r,

$$cz_{\rm obs} \approx H_0 r + v_r. \tag{5.1}$$

Therefore, in order to measure the value of H_0, the radial peculiar velocity needs to be subtracted from the observed redshift. The inferred value of H_0 can have significant differences depending on the model of velocity corrections (see Pesce et al. (2020)). To measure the peculiar velocity, we need accurate measurements of the redshifts as well as distances. Accurate distances are also important for measuring, e.g., the stellar mass of galaxies, which has implications for understanding the nature of dark matter.

To measure the peculiar velocity of galaxies, one has to rely on some distance indicator. Commonly used distance tracers for the measurement of peculiar velocity includes empirical galaxy scaling relationships such as the Tully-Fisher and the Fundamental Plane relations as well as Type Ia supernovae. However, not all galaxies have a distance estimate associated with it. And even when there is an estimate, the associated uncertainty is very high. Hence, we need some method to map out the peculiar velocities field of the nearby Universe.

In this work, we compare the performance of different methods of mapping the peculiar velocity fields by comparing the predictions to independent peculiar velocity catalogues. Broadly, we compare the velocity field predicted using density reconstruction and the velocity field predicted using the adaptive kernel smoothing technique applied to peculiar velocity data. Predicting peculiar velocities based on density reconstruction has a long history (e.g. Kaiser et al. (1991); Hudson (1994b)). In this approach, one uses the galaxy redshift surveys to 'reconstruct' the density field, which in turn is used to predict the peculiar velocity field in the local Universe. In contrast, the adaptive kernel smoothing method smooths the peculiar velocity data to map out the velocity field of the Universe. This has been used for cosmography with the 6dF (Springob et al., 2014) and the 2MTF (Springob et al., 2016) peculiar velocity surveys. The reconstructed velocity field used in this work is obtained using the 2M++ galaxy redshift compilation (Lavaux & Hudson, 2011a) and the adaptive kernel-smoothed velocity fields are obtained by smoothing the 6dF peculiar velocity catalogue and a combined Tully-Fisher catalogue from SFI++ and

2MTF. We use two different methods: a simple comparison of the mean squared error and a forward likelihood method, to compare the different velocity field predictions to the observations.

This chapter is structured in the following manner. In Section 5.2, we describe the peculiar velocity data that we use for the adaptive kernel smoothing and as tracers to test peculiar velocity models. Section 5.3 describes the two methods for predicting the peculiar velocity fields. We highlight the importance of scaling the smoothed velocity fields by a constant factor to obtain unbiased velocity estimate of the galaxies in section 5.4. In section 5.5, the predictions of the peculiar velocity models are compared to the observed peculiar velocity from the test sets. We discuss some essential features of our findings in Section 5.7 before summarising our results in Section 5.8.

5.2 Peculiar Velocity data

We use a few different peculiar velocity catalogues in this work. These catalogues serve two purposes : first, to map the velocity field of the local Universe using an adaptive kernel smoothing technique, and second, we use these as test sets to test the predictions of the peculiar velocity models. In this section, we describe the different catalogues we use in this work, their main features and the corresponding data processing required.

5.2.1 6dF peculiar velocity catalogue

The 6dF peculiar velocity sample (Springob et al., 2014) consists of galaxies from the fundamental plane survey (Magoulas et al., 2012; Campbell et al., 2014) of the 6dF galaxy survey. It is presently the largest peculiar velocity survey with a total of 8885 galaxies. The distance (and hence the radial peculiar velocity) of these galaxies is estimated using the Fundamental Plane relation. The sample is restricted to the southern hemisphere with a galactic cut of $|b| > 10^{\circ}$ and $cz < 16000$ km/s in the CMB frame. The mean distance uncertainty of the sample was found to be $\sim$ 26%. We plot the sky distribution of the 6dF peculiar velocity catalogue along with the tracers we use to compare the velocity field in the southern hemisphere in the left panel of Figure 5.1. We use the 6dF peculiar velocity sample to predict the peculiar velocity using the adaptive kernel smoothing method described in Section 5.3.2. The radial velocity field in the supergalactic plane obtained using adaptive kernel smoothing of the 6dF peculiar velocity data is shown in Figure 5.3.

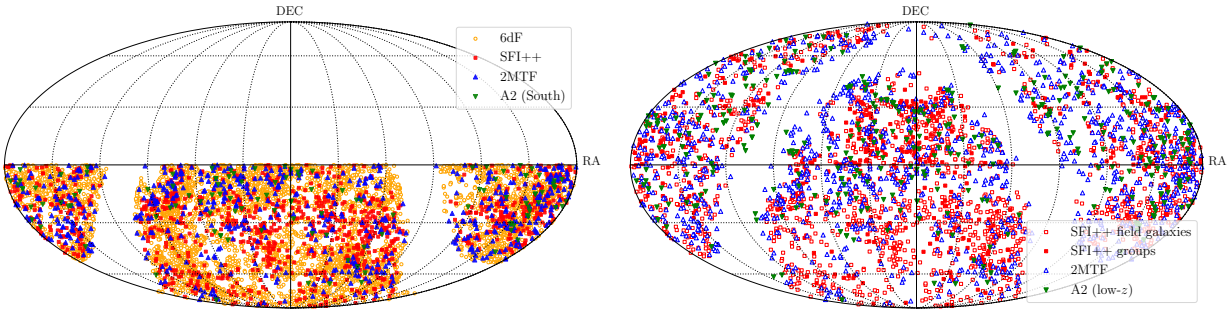

Figure 5.1: *Left:* Distribution of 6dF peculiar velocity catalogue objects and the corresponding tracer objects in the southern hemisphere plotted in the equatorial coordinates. The 6dF objects are shown with orange circles. The test set consists of objects from the SFI++, 2MTF and the A2-South catalogue - shown with red squares, blue triangles and green inverted triangles respectively. *Right:* The sky distribution of SuperTF and A2 objects plotted in the equatorial coordinates. The SFI++ objects are denoted with red squares, with the groups being a filled squared and the field galaxies are hollow squares. The 2MTF galaxies are denoted with a blue triangle and the A2 supernovae as a green inverted triangle.

5.2.2 Tully-Fisher catalogues

In this work, we use two Tully-Fisher (TF) catalogues - SFI++ and 2MTF. The TF catalogues serve dual purpose in this work. First, we use the objects in the southern hemisphere as tracers to test the predictions of the 2M++ reconstructed velocity field and the adaptive kernel smoothed velocity obtained from 6dF. Second, we use a combined TF catalogue of SFI++ and 2MTF to predict the velocity field using the adaptive kernel smoothing method and compare it with the other velocity field models.

SFI++

We used the SFI++ distance catalog in the previous chapter on constraining cosmological parameters. We apply the same data cuts and outlier selection on the SFI++ catalog as described in the previous chapter, i.e, *i)* we only use galaxies with $-0.1 < \eta < 0.2$. *ii)* we remove the outliers, by iteratively fitting the Tully Fisher relation and removing the 3.5σ outliers. For this work, we only consider the galaxies that are within $cz < 10000$ km/s. With these cuts, we have a total of 1607 field galaxies and 584 groups in our sample. Of these, 949 field galaxies and 204 groups are in the southern hemisphere. While comparing

the 6dF adaptive kernel-smoothed peculiar velocity field and the 2M++ reconstructed velocity field, we use only the galaxies in the southern hemisphere as a test set.

2MTF

The 2MTF survey (Masters et al., 2008) is a Tully-Fisher survey in the J, H and K bands. The final catalogue (Hong et al., 2019) consists of 2062 galaxies within $cz < 10000$ km/s. Like the previous chapter, we remove the duplicates from 2MTF that are already contained in the SFI++ catalogue. We only use galaxies with $-0.1 < \eta < 0.2$ and reject outliers by iteratively fitting the Tully-Fisher relation. We have a total of 1248 galaxies after these cuts. Of these, 567 galaxies are in the southern hemisphere and we use these galaxies to compare with the 6dF adaptive smoothed peculiar velocity field and the 2M++ reconstructed velocity field.

SuperTF

We also combine the SFI++ and the 2MTF catalogs into a 'super TF' catalog which we then use to produce an adaptive kernel-smoothed peculiar velocity map. Unlike 6dF, we can use this catalogue to map out the velocity field in both hemispheres using the kernel smoothing method. The I-band Tully-Fisher relation, used in the SFI++ catalogue, has a smaller intrinsic scatter compared to the TF relation in the infrared bands, which is used by the 2MTF survey (See e.g. Boruah et al. (2019)). Therefore, when there are duplicates in the SFI++ and 2MTF datasets, we use the SFI++ objects. The final data set consists of 584 SFI++ groups, 1607 SFI++ field galaxies and 1248 2MTF galaxies. We show the sky distribution of the objects in this combined catalogue in Figure 5.1. We also compare the redshift distribution of the objects in the SuperTF catalogue with the 6dF peculiar velocity catalogue in Figure 5.2. Note that the SuperTF catalogue has a higher density of objects at lower redshifts ($z \lesssim 0.015$). The velocity field of the local Universe mapped using the adaptive kernel smoothing technique on the SuperTF catalogue is shown in Figure 5.3.

5.2.3 A2 Supernovae

We also use a sample of Type Ia supernovae as a tracer population to test the peculiar velocity fields. Type Ia Supernovae are excellent tracer of peculiar velocities because of their smaller distance error. We presented the Second Amendment (A2) sample of supernovae in 4.2. It consists of low redshift (low-z) supernovae from the CfA supernovae sample

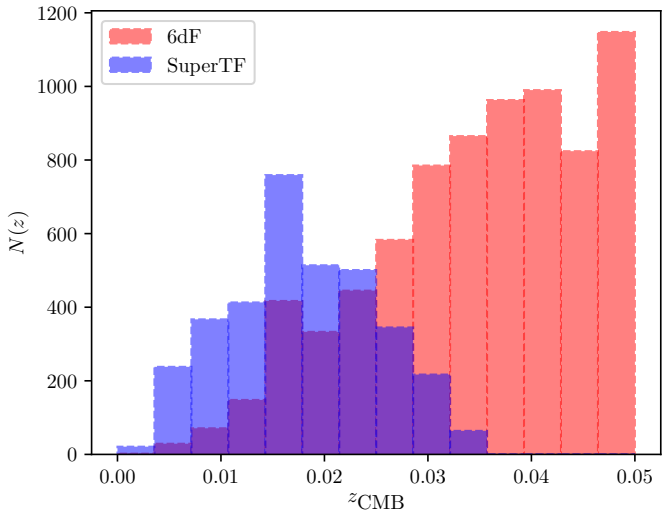

Figure 5.2: Redshift distribution of SuperTF and 6dF objects. Note that the two catalogues cover different fractions of the sky, with 6dF covering only the southern hemisphere. Also note that the SuperTF catalogue has a higher density of objects compared to 6dF at lower redshifts ($z \lesssim 0.015$).

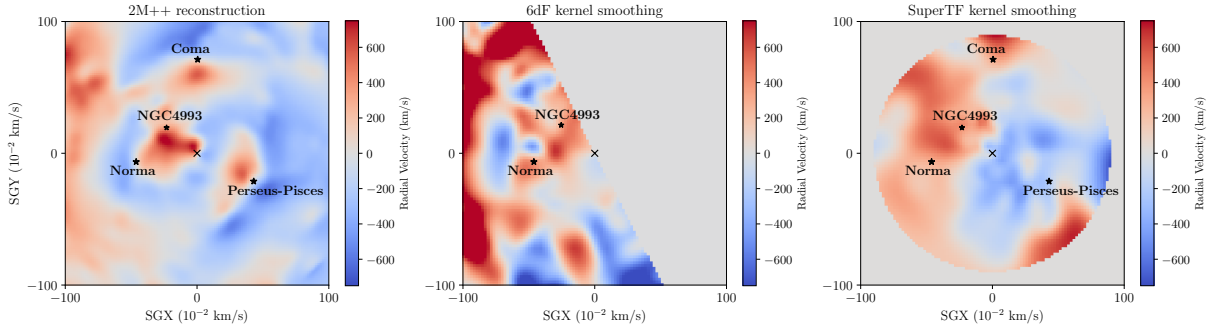

Figure 5.3: The radial peculiar velocity in the Supergalactic Plane for the 3 different peculiar velocity models: *Left:* 2M++ reconstruction, *Centre:* Adaptive kernel smoothing with the 6dF peculiar velocity catalogue, *Right:* Adaptive kernel smoothing with the SuperTF catalogue. The coordinates for the adaptive smoothed fields are in redshift space, while that for 2M++ reconstruction is in the real space. We also show the location of a few prominent superclusters and NGC4993. The adaptive kernel-smoothed velocity fields are smoothed using a fiducial smoothing scale of $\sigma' = 8\ h^{-1}$ Mpc.

(Hicken et al., 2009), Carnegie Supernovae project (Folatelli et al., 2010; Krisciunas et al., 2017), the Lick Observatory Supernova Survey (LOSS) (Ganeshalingam et al., 2013) and the Foundation supernovae sample (Foley et al., 2018; Jones et al., 2019). The final sample consists of 465 low-z supernovae, resulting in the largest peculiar velocity catalogue based on supernovae. While comparing to the 6dF adaptive smoothed peculiar velocity field, we only use the SNe in the southern hemisphere and $|b| < 10°$. We call this data set consisting of 150 SNe, 'A2-South'.

5.3 Peculiar velocity models

In this work, we compare two different types of peculiar velocity models - *i)* the velocity field reconstructed from the 2M++ galaxy redshift compilation, *ii)* velocity field mapped out using an adaptive kernel smoothing technique. In this section, we briefly describe both these methods.

5.3.1 Velocity reconstruction with 2M++

We use the luminosity-weighted density field from Carrick et al. (2015) in this work. The velocity field is predicted from the density field reconstructed using the procedure described in section 4.3.2. The predicted velocity field from the luminosity-weighted density field is scaled by a factor of $\beta = f/b$ and an external velocity, $\boldsymbol{V}_{\rm ext}$ is added to this. To fit for the value of β and the external velocity $\boldsymbol{V}_{\rm ext}$, we compared the predicted velocity to the observed velocities from the SFI++ and the A2 catalogue. The details of the fitting process can be found in Chapter 4 (Also see Carrick et al. (2015)). More details on the reconstruction procedure can be found in Carrick et al. (2015).

5.3.2 Adaptive kernel smoothing method

An adaptive kernel smoothing technique to map the peculiar velocity field using measured peculiar velocities was presented in Springob et al. (2014, 2016). We use this method to map the velocity field in the local Universe using the 6dF and the SuperTF catalogues.

In this scheme, a Gaussian kernel is used to smooth the peculiar velocity measurements from the catalogues. The measured radial velocities, $\{v_r(\boldsymbol{r}_i)\}$, in peculiar velocity catalogue at locations, $\{\boldsymbol{r}_i\}$, is used to predict the peculiar velocity at $\boldsymbol{r}$ as,

$$v(\boldsymbol{r}) = \frac{\sum_{i=0}^{N_{\rm gal}} v_r(\boldsymbol{r}_i)\cos\theta_i e^{-\Delta r_i^2/2\sigma_i^2}\sigma_i^{-3}}{\sum_{i=0}^{N_{\rm gal}} e^{-\Delta r_i^2/2\sigma_i^2}\sigma_i^{-3}}, \tag{5.2}$$

where, $\Delta r_i = |\boldsymbol{r} - \boldsymbol{r}_i|$ and $\cos(\theta_i) = \hat{\boldsymbol{r}}\cdot\hat{\boldsymbol{r}}_i$. Note that in this method, the location, $\boldsymbol{r}$, is given in the redshift space. The kernel width for each galaxy is adaptively computed using the prescription presented in Springob et al. (2014, 2016). Assuming a fiducial smoothing length, σ', the adaptive smoothing length for each object is defined as,

$$\sigma_i = \sigma'\left[\frac{\exp(\sum_{j=1}^{N}\ln(\delta_j)/N)}{\delta_i}\right]^{1/2}, \tag{5.3}$$

where δ_i is computed as,

$$\delta_i = \sum_{j=1}^{N_j}\exp\left(-\frac{|\boldsymbol{r}_j - \boldsymbol{r}_i|^2}{2\sigma'^2}\right). \tag{5.4}$$

The sum in equation (5.4) is over the N_j objects that are within distance, $3\sigma'$ of the i-th object. The quantity, δ_i roughly calculates the density of peculiar velocity tracers near the i-th object. Equation (5.3) then calculates the kernel width adaptively based on the density of the peculiar velocity tracers. The calculated kernel size in regions with larger density is thus smaller.

We use the adaptive kernel smoothing method to predict the velocity field using the 6dF Fundamental Plane and the SuperTF catalogue. In this work, we use two different fiducial smoothing lengths, $8h^{-1}$ Mpc and $16h^{-1}$ Mpc to predict the kernel smoothed velocity field. If we use a fiducial smoothing length of $\sigma' = 8\ h^{-1}$ Mpc, the mean smoothing length, $\langle\sigma_i\rangle$, for the 6dF and the SuperTF catalogues are 8.61 h^{-1} Mpc and 8.83 h^{-1} Mpc respectively. The spread of the same smoothing lengths as measured using the standard deviation of the distribution are, 3.60 h^{-1} Mpc and 4.39 h^{-1} Mpc for the 6dF and Super TF catalogues respectively. The distribution of the adaptively calculated smoothing lengths with fiducial smoothing length of $8h^{-1}$ Mpc for the 6dF and the SuperTF catalogues is shown in Figure 5.4.

A visual comparison of the peculiar velocity fields in the supergalactic plane derived using the 2M++ reconstruction, and the adaptive kernel smoothing on the 6dF and the SuperTF catalog is shown in in Figure 5.3.

5.4 Scaling the smoothed velocity

In the previous section, we presented two ways to predict the velocities of galaxies. Both these methods rely on smoothing the peculiar velocity field in some way. However, one must be careful while using a smoothed field to predict velocities since certain smoothing scales may lead to biased estimates of the peculiar velocity. In Berlind et al. (2000) and Carrick et al. (2015), the effect on smoothing radius on the inferred value of β (or Ω_m in the earlier paper) was studied in the context of constraining cosmological parameters from density-velocity comparison. Using tests on numerical simulations, it was found in Carrick et al. (2015) that using a smoothing length of $\sim 4h^{-1}$ Mpc gives unbiased estimates for the peculiar velocity. Using a smoothing length other than this value may bias our estimates of peculiar velocity. Therefore, when predicting the peculiar velocity using the 2M++ reconstruction, we used smoothed the velocity field using a Gaussian filter with a smoothing length of $4h^{-1}$ Mpc to predict the peculiar velocity.

The kernel smoothing method also predicts the velocity by smoothing the peculiar velocity data in the neighboring region. Given the large error bars and the sparse sample of

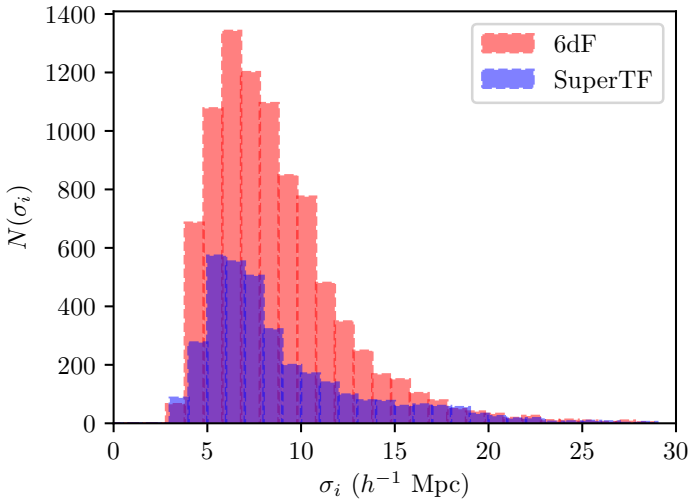

Figure 5.4: Distribution of the adaptively calculated kernel smoothing length computed using a fiducial smoothing length, $\sigma' = 8\ h^{-1}$ Mpc, for the two peculiar velocity catalogues, 6dF and SuperTF. The mean smoothing lengths for the 6dF and the SuperTF catalogues are 8.61 h^{-1} Mpc and 8.83 h^{-1} Mpc respectively.

peculiar velocity data, smoothing over a larger region is necessary to reduce the uncertainties on the predictions to an acceptable level. However, smoothing over larger regions also biases low the peculiar velocity estimates. Therefore, if we smooth the peculiar velocity field using a smoothing scale $> 4h^{-1}$ Mpc, we need to correct for this bias.

In order to correct for this bias, we use simple analytical predictions from linear perturbation theory. We assume that the smoothing scale of $R_{\rm unbiased} = 4h^{-1}$ Mpc gives unbiased estimates for the predicted peculiar velocity. If one uses linear perturbation theory to predict the peculiar velocity by smoothing at some scale, R, the variance of the estimated peculiar velocity if given as,

$$\sigma^2_{\rm PV}(R) = \frac{H_0^2 f^2}{2\pi^2} \int_0^\infty dk P(k) \widetilde{W}^2(k, R) \ , \tag{5.5}$$

where, $P(k)$ is the matter power spectrum and $\widetilde{W}$ is the window function used to smooth the field at the scale, R. We calculate the matter power spectrum using the publicly available CAMB software (Lewis et al., 2000).

In order to recover the unbiased velocity estimate, we therefore scale up the velocity by a scaling factor, A. This 'scaling factor' is obtained by using equation (5.5) and that smoothing radius of $R_{\rm unbiased}$ gives an unbiased estimate of the peculiar velocity. The scaling factor, A, is then given as,

$$A(R) = \frac{\sigma_{\rm PV}(R_{\rm unbiased})}{\sigma_{\rm PV}(R)}. \tag{5.6}$$

The peculiar velocity estimate, $v_p(R)$ obtained by using a smoothing scale, R therefore needs to be scaled by factor of A such that,

$$v_p(R) \to A v_p(R). \tag{5.7}$$

We compare both the scaled and the unscaled versions of the adaptive kernel-smoothed peculiar velocity fields in the next section.

5.5 Comparing peculiar velocity models

To compare the models of peculiar velocity of the local Universe, we use independent peculiar velocity data sets to compare the predictions of the models to observations. We propose two ways to test this : the first is based on a simple comparison of the mean squared

error between predicted and observed peculiar velocity of the tracer peculiar velocity data set. In this method, we use the velocity estimate from the peculiar velocity models at the estimated distance of the peculiar velocity tracer and compare it with the observed value of the velocity. However, this method is known to be affected by inhomogeneous Malmquist bias. The second method is the *Forward likelihood* method described in section 4.4.2. The forward likelihood method can correct for the inhomogeneous Malmquist bias. We use Bayesian model comparison with this likelihood to compare the peculiar velocity models presented in Section 5.3.

5.5.1 Comparing the mean squared error

In the first approach, we calculate the mean squared error between the predicted radial velocity from the peculiar velocity models and the measured radial peculiar velocity of the test set. The model with the better predictions for the peculiar velocity should have a lower value of mean squared error (MSE). For the adaptive kernel smoothing approach, we estimate the peculiar velocity of the test objects using the approach of Section 5.3.2. In this approach, we use the redshift space position of the test object to estimate the velocity. For the reconstructed velocity field, we predict the velocity at the reported mean position of the object. We plot the predicted velocity from 6dF adaptive kernel smoothing technique and from the 2M++ reconstruction against the observed velocity of the 2MTF, SFI++ and the A2 supernovae in Figure 5.5.

We then compare the estimated velocity to the measured radial velocity. The Mean Squared error (MSE) between the observed velocity and the predicted velocity is defined as,

$$\mathrm{MSE} = \frac{1}{N_{\mathrm{tracers}}} \sum_{i=0}^{N_{\mathrm{tracers}}} \frac{(V^r_{\mathrm{pred}} - V^r_{\mathrm{obs}})^2}{\Delta V^2_{\mathrm{obs}}} \tag{5.8}$$

The value of MSE obtained for the different models is presented in Table 5.1. Since the SuperTF catalogue consists of SFI++ and 2MTF galaxies, we do not use these data sets to compare to the velocity field obtained by using the adaptive kernel smoothing on the SuperTF catalogue. We notice that for all the test sets, the 2M++ reconstructed velocity field gives a lower value of the MSE than the adaptive kernel-smoothed velocity fields. Hence, it suggests that 2M++ reconstructed peculiar velocity is a better model for the peculiar velocity of the local Universe than the one obtained by using adaptive kernel smoothing.

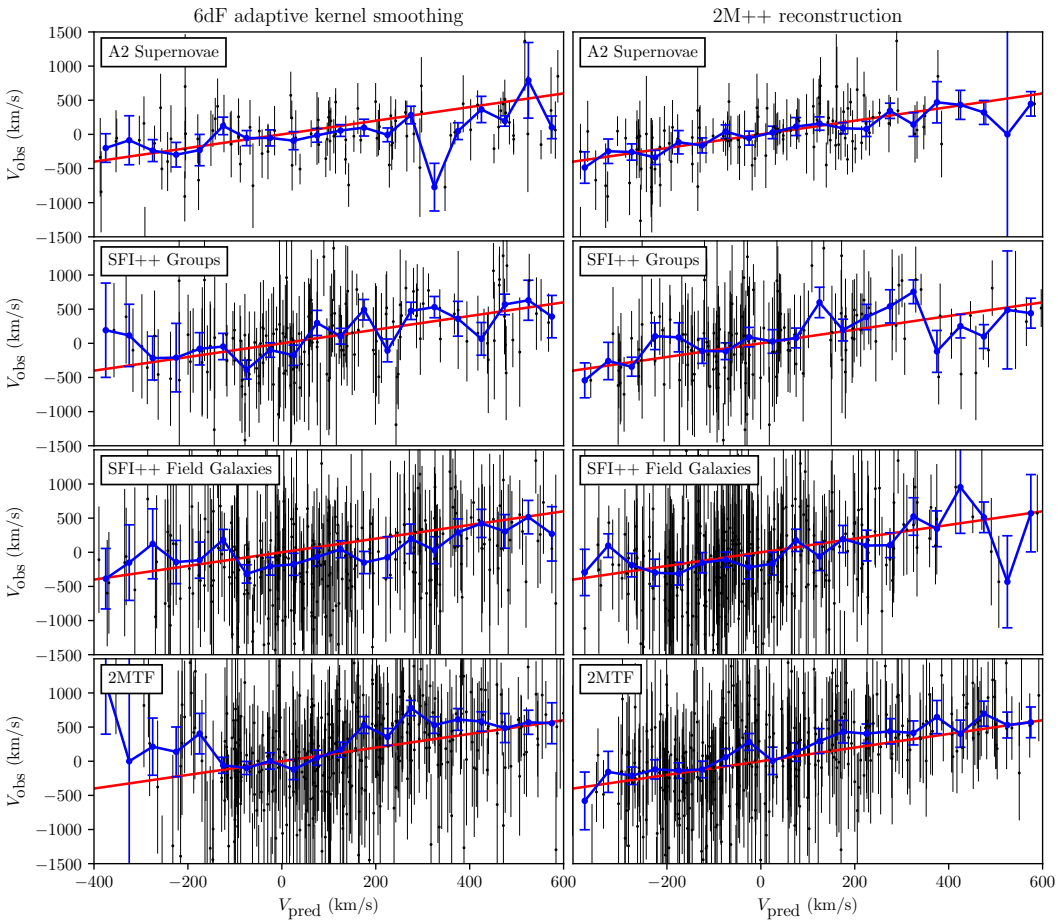

Figure 5.5: Plot of the predicted velocity, $V_{\rm pred}$, predicted using adaptive kernel smoothing on 6dF (*left*) and 2M++ reconstruction (*right*) vs the observed velocity, $V_{\rm obs}$ for the different test sets. The black markers denote the peculiar velocity estimate for each object in the test set. The blue curve denotes a binned version where we plot the weighted average of the observed peculiar velocity objects in each 50 km s^{-1} bins of predicted peculiar velocity. The red line represents, $V_{\rm pred} = V_{\rm obs}$.

Table 5.1: The value of MSE measured for different test data sets

Tracer	2M++	6dF	SuperTF
A2 (South)	0.742	1.856	1.970
A2 (low-z)	0.899	—	2.214
SFI++ groups	0.673	0.727	—
SFI++ field galaxies	0.484	0.556	—
2MTF	0.646	0.844	—

5.5.2 Forward likelihood

In this section, we use the forward likelihood approach to determine which peculiar velocity field fits the data well. The details of the method are given in section 4.4.2. The likelihood for the data given a velocity field is given by equation (4.11). However, in this case, we do not vary β and $\boldsymbol{V}_{\rm ext}$. Rather, these parameters are set to the best fit value from the fitting procedure of the previous chapter. Therefore, the forward likelihood only depends on the velocity field, $\boldsymbol{v}$,

$$\mathcal{P}(z_{\rm obs}|\boldsymbol{v}) = \int_0^\infty dr \mathcal{P}(z_{\rm obs}|r, \boldsymbol{v})\mathcal{P}(r), \tag{5.9}$$

where $\mathcal{P}(r)$ is given by equation (4.9).

In the case of adaptive kernel smoothing, the radial velocity is calculated in the redshift space. Therefore, we introduce the redshift space coordinate, $\boldsymbol{s}$, to facilitate the calculation for this case.

$$\boldsymbol{s} = \boldsymbol{r} + v_r(\boldsymbol{r})\hat{\boldsymbol{r}}. \tag{5.10}$$

Note that, in the above equation distance coordinates, $\boldsymbol{s}$ and $\boldsymbol{r}$ has the same units as that for the velocity. That is we convert the distance units into velocity units (km/s). We use this change of coordinates to calculate Equation (5.9) in the redshift space,

$$\begin{aligned}\mathcal{P}(z_{\rm obs}|\boldsymbol{v}) &= \int_0^\infty ds \left|\frac{\partial r}{\partial s}\right| \mathcal{P}(z_{\rm obs}|r(\boldsymbol{s}), \boldsymbol{v}(\boldsymbol{s}))\mathcal{P}(r(s)), \\ &= \int_0^\infty ds \left(1 - \frac{\partial v_r}{\partial s}\right) \mathcal{P}(z_{\rm obs}|r(\boldsymbol{s}), \boldsymbol{v}(\boldsymbol{s}))\mathcal{P}(r(s))\end{aligned} \tag{5.11}$$

Note that the above relation is defined only if the relation between $\boldsymbol{r}$ and $\boldsymbol{s}$ is monotonic along the line of sight of the peculiar velocity tracers. As is well-known, this is not always the case due to the phenomenon of triple-valued regions (Strauss & Willick, 1995). A triple valued region usually occurs in the neighborhood of big clusters, where, for a given value of redshift, there are 3 solutions in the real space. Since the adaptive kernel smoothing technique estimates the velocity in the redshift space, it does not take into account the effect of triple-valued points. In this work, to convert between $\boldsymbol{r}$ and $\boldsymbol{s}$ we use the peculiar velocity models to get the peculiar velocity at a given location. We only consider the objects which have a monotonic relation between $\boldsymbol{r}$ and $\boldsymbol{s}$ under the peculiar velocity model for our comparison. For such objects, Equation (5.11) gives a valid way to calculate the forward likelihood using the adaptive kernel smoothed peculiar velocity field.

Bayesian model comparison

We use Bayesian model comparison to compare the two peculiar velocity models described in Section 5.3. Given two models, $\mathcal{M}_1, \mathcal{M}_2$ describing the same data, D, Bayesian model comparison gives a way to compare the two models. The plausibility of the two models can be compared by calculating the posterior probability ratio (Mackay, 2003),

$$\frac{\mathcal{P}(\mathcal{M}_1|D)}{\mathcal{P}(\mathcal{M}_2|D)} = \frac{\mathcal{P}(\mathcal{M}_1)}{\mathcal{P}(\mathcal{M}_2)} \frac{\mathcal{P}(D|\mathcal{M}_1)}{\mathcal{P}(D|\mathcal{M}_2)}. \tag{5.12}$$

$\mathcal{P}(\mathcal{M})$ denotes the prior belief in the model, $\mathcal{M}$.

Hence, Bayesian model comparison is well-suited to compare the different peculiar velocity models. We do so by using the forward likelihood to calculate the likelihood, $\mathcal{P}(D|\boldsymbol{v})$. If we assign equal prior probability to two different peculiar velocity models, $\boldsymbol{v}_1$ and $\boldsymbol{v}_2$, i.e., $\mathcal{P}(\boldsymbol{v}_1) = \mathcal{P}(\boldsymbol{v}_2)$, the posterior probability ratio can be written as,

$$\frac{\mathcal{P}(\boldsymbol{v}_1|D)}{\mathcal{P}(\boldsymbol{v}_2|D)} = \frac{\mathcal{P}(D|\boldsymbol{v}_1)}{\mathcal{P}(D|\boldsymbol{v}_2)}. \tag{5.13}$$

The right hand side of equation (5.13) can be calculated using equations (5.9) and (5.11). We fix the value of σ_v to 150 km s^{-1}. We present the values for the ratio $\mathcal{P}(D|\boldsymbol{v})$ for the 2M++ reconstructed velocity field and the kernel smoothed velocity field in Tables 5.2 and 5.3. The fiducial smoothing radius was chosen as $8h^{-1}$ Mpc and $16h^{-1}$ Mpc for Table 5.2 and 5.3 respectively. We highlight here some of the main findings:

i) We find that the 2M++ reconstructed velocity field gives a better fit to the observed velocities for all test sets and for all range of redshifts than the adaptive kernel-smoothed velocity fields.

ii) We also find that choosing a bigger smoothing scale of $16h^{-1}$ Mpc for the adaptive kernel-smoothed velocity performs better than a smoothing scale of $8h^{-1}$ Mpc for almost all test data sets and all range of redshifts.

iii) The effect of scaling the predicted velocity field as we proposed in Section 5.4 is more pronounced when we use kernel smoothing with a smoothing radius of 16 h^{-1} Mpc. The value of A for the two smoothing scales are 1.12 and 1.34 for $8h^{-1}$ Mpc and $16h^{-1}$ Mpc respectively. For the 2MTF, SFI++ field galaxies and SFI++ groups data sets, the scaled velocity from kernel smoothing indeed gives a better fit compared to the unscaled version. However, for the supernovae data, the reverse is true.

5.5.3 Comparison of the reconstruction based and kernel smoothing method

We saw in this section that the 2M++ reconstructed velocity field gives a better fit to the different data sets compared to the velocity field calculated using adaptive kernel smoothing. In this section, we give a rough argument for why that is the case.

In equation (5.2), if N objects contribute significantly to the calculation of the kernel smoothed velocity, and if the velocity error for each object is a constant, ΔV, the error in the estimated velocity will be roughly, $\sim \Delta V/\sqrt{N}$. The relative error on the peculiar velocity measured using TF or FP is usually 15-25% of the distance given in km/s. For NGC4993, which is at ~ 3000 km/s, assuming a relative error of 20%, and $N \sim 10$, which is the number of 6dF objects within 8 h^{-1} Mpc (number of SuperTF objects within the same distance is 11), we get the velocity error of $\sim$ 180 km/s. This estimate is close to the error, 153 km/s calculated for the 6dF velocity field. However, the same argument also implies that the error on the calculated peculiar velocity field grows with distance. For redshift much larger than that of NGC4993, one would need a much higher density of peculiar velocity tracers to achieve a distance error of $\sim$ 150 km/s using the kernel smoothing technique. On the other hand, the error with the predictions of the reconstruction based approach arises from systematic error in the reconstruction and errors in the prediction from linear perturbation theory. While some dependence of this error with distance is expected, it is not as drastic as using the kernel smoothing method.

Table 5.2: Ratio of $\log(\mathcal{P})$ calculated using the 2M++ reconstructed velocity field and the adaptive kernel smoothing technique for 6dF and SuperTF. For this table, we used a fixed value of $\sigma_v = 150$ km s^{-1} and the fiducial smoothing length is 8 h^{-1} Mpc. For each test set, we make two cuts in the redshift.

Test set	Redshift selection	$\ln\left(\frac{\mathcal{P}_{\rm 2M++}}{\mathcal{P}_{\rm 6dF}}\right)$	$\ln\left(\frac{\mathcal{P}_{\rm 2M++}}{\mathcal{P}^{\rm scaled}_{\rm 6dF}}\right)$	$\ln\left(\frac{\mathcal{P}_{\rm 2M++}}{\mathcal{P}_{\rm SuperTF}}\right)$	$\ln\left(\frac{\mathcal{P}_{\rm 2M++}}{\mathcal{P}^{\rm scaled}_{\rm SuperTF}}\right)$	$N_{\rm tracers}$
A2-South	$cz < 3000$ km/s	2.21	2.70	2.41	2.88	16
	$cz < 4500$ km/s	2.33	3.86	5.07	5.89	32
	$cz < 6000$ km/s	5.21	6.05	8.85	10.21	53
	$cz < 9000$ km/s	9.19	10.58	15.56	17.80	79
A2-low-z	$cz < 3000$ km/s	—	—	11.38	11.95	49
	$cz < 4500$ km/s	—	—	20.76	21.89	92
	$cz < 6000$ km/s	—	—	49.82	52.86	168
	$cz < 9000$ km/s	—	—	85.92	92.90	310
2MTF	$cz < 3000$ km/s	24.6	24.4	—	—	108
	$cz < 4500$ km/s	39.00	36.28	—	—	247
	$cz < 6000$ km/s	55.65	53.06	—	—	379
	$cz < 9000$ km/s	69.49	69.01	—	—	483
SFI++ Groups	$cz < 3000$ km/s	12.08	11.88	—	—	61
	$cz < 4500$ km/s	9.35	9.29	—	—	100
	$cz < 6000$ km/s	18.89	17.87	—	—	165
	$cz < 9000$ km/s	18.78	17.78	—	—	170
SFI++ Field	$cz < 3000$ km/s	9.94	9.01	—	—	63
	$cz < 4500$ km/s	5.72	5.24	—	—	153
	$cz < 6000$ km/s	13.52	11.70	—	—	388
	$cz < 9000$ km/s	53.66	44.29	—	—	736

124

Table 5.3: Same as table 5.2, but with a fiducial smoothing length of 16 h^{-1} Mpc.

Test set	Redshift selection	$\ln\left(\frac{\mathcal{P}_{\rm 2M++}}{\mathcal{P}_{\rm 6dF}}\right)$	$\ln\left(\frac{\mathcal{P}_{\rm 2M++}}{\mathcal{P}^{\rm scaled}_{\rm 6dF}}\right)$	$\ln\left(\frac{\mathcal{P}_{\rm 2M++}}{\mathcal{P}_{\rm SuperTF}}\right)$	$\ln\left(\frac{\mathcal{P}_{\rm 2M++}}{\mathcal{P}^{\rm scaled}_{\rm SuperTF}}\right)$	$N_{\rm tracers}$
A2-South	$cz < 3000$ km/s	2.39	2.94	3.01	3.45	23
	$cz < 4500$ km/s	4.37	4.75	6.19	7.08	42
	$cz < 6000$ km/s	6.18	6.70	9.70	11.39	66
	$cz < 9000$ km/s	8.01	8.40	12.83	15.69	94
A2-low-z	$cz < 3000$ km/s	—	—	9.96	10.10	49
	$cz < 4500$ km/s	—	—	17.50	18.34	92
	$cz < 6000$ km/s	—	—	42.78	45.45	168
	$cz < 9000$ km/s	—	—	69.66	77.59	310
2MTF	$cz < 3000$ km/s	20.81	16.72	—	—	118
	$cz < 4500$ km/s	45.63	33.41	—	—	282
	$cz < 6000$ km/s	59.87	43.97	—	—	443
	$cz < 9000$ km/s	68.19	53.24	—	—	563
SFI++ Groups	$cz < 3000$ km/s	8.36	6.47	—	—	70
	$cz < 4500$ km/s	7.22	3.73	—	—	119
	$cz < 6000$ km/s	10.19	5.75	—	—	198
	$cz < 9000$ km/s	9.99	5.49	—	—	203
SFI++ Field	$cz < 3000$ km/s	8.93	9.96	—	—	75
	$cz < 4500$ km/s	5.16	4.44	—	—	180
	$cz < 6000$ km/s	9.40	6.05	—	—	450
	$cz < 9000$ km/s	10.87	12.90	—	—	863

125

Another problem with the kernel smoothing technique is that it does not account for triple valued regions. Triple valued regions arises when the same value of redshift has 3 solutions in the real space. To get these solution, these points in the real space must have peculiar velocities in opposing directions. Since kernel smoothing is done in the redshift space, potentially these triple valued regions are smoothed together, hence, inducing additional biases.

5.6 H_0 measurement from megamasers

As we saw in equation (5.1), the redshift of a galaxy gets a contribution from both the peculiar velocity and the Hubble recession. Therefore, one needs to correct for the contribution of the peculiar velocity in order to correctly infer H_0. In this section, we consider the peculiar velocity corrections for megamasers from the Megamaser Cosmology Project (MCP). We begin with the Bayesian model we use for the treatment of peculiar velocity for these data sets.

5.6.1 H_0 likelihood

When correcting the redshifts for the peculiar velocities, traditionally one uses a point estimate for the peculiar velocity at a given redshift. However, given the large uncertainty on the distances, we need to marginalize over the radial velocity along the line-of-sight for each object. In this section, we derive the likelihood for such a method.

We want to infer the Hubble constant, H_0, given the observed redshift to the objects, $\{z_{\rm obs}\}$, and some data, $\{x_{\rm dist}\}$, from which the distance is derived. That is, we want to calculate $\mathcal{P}(H_0|\{z_{\rm obs}\},\{x_{\rm dist}\})$. Using Bayes theorem and assuming the different distance measurements are independent, we can simplify the posterior as,

$$\begin{aligned}\mathcal{P}(H_0|\{z_{\rm obs}\},\{x_{\rm dist}\}) \propto& \mathcal{P}(\{z_{\rm obs}\},\{x_{\rm dist}\}|H_0)\mathcal{P}(H_0),\\ =&\mathcal{P}(H_0)\prod_{i=1}^{N_{\rm events}}\mathcal{P}(z^i_{\rm obs},x^i_{\rm dist}|H_0).\end{aligned} \tag{5.14}$$

In order to go further, we simplify the likelihood, $\mathcal{P}(z^i_{\rm obs},x^i_{\rm dist}|H_0)$, by expanding it in terms of the intermediate distance variable, d, and the velocity field, $\boldsymbol{v}$, used to correct the

observed redshifts.

$$\mathcal{P}(z^i_{\rm obs}, x^i_{\rm dist}|H_0) = \int {\rm d}d\mathcal{P}(z^i_{\rm obs}|H_0, \boldsymbol{v}, d)\mathcal{P}(x^i_{\rm dist}|d)\mathcal{P}(d). \tag{5.15}$$

Finally, we have to model the likelihood for the redshift, $\mathcal{P}(z^i_{\rm obs}|H_0, \boldsymbol{v}, d)$.

$$\mathcal{P}(z^i_{\rm obs}|H_0, \boldsymbol{v}, d) = \frac{1}{\sqrt{2\pi\sigma_v^2}} \exp\left[-\frac{(cz^i_{\rm obs} - cz_{\rm pred})^2}{2\sigma_v^2}\right], \tag{5.16}$$

where, $cz_{\rm pred} \equiv cz_{\rm pred}(H_0, d, \boldsymbol{v})$ and σ_v is the typical uncertainty in the predicted peculiar velocity.

5.6.2 Peculiar velocity correction for megamasers

Water megamasers in the active galactic nuclei of galaxies provide a completely geometric method to measure distances without the need for intermediate calibration. In Pesce et al. (2020), the Megamaser Cosmology Project (MCP) measured the value of H_0 from the distance measurement to 6 such megamasers. It was found that the inferred value of H_0 depended strongly on the treatment of peculiar velocities.

In this section, we reanalyze the distance data from the megamasers to infer the constraints on H_0, checking different assumptions for peculiar velocity correction. Our treatment is different from Pesce et al. (2020) in four ways:

i) We used the likelihood of section 5.6.1 to marginalize over the line-of-sight peculiar velocity as opposed to using a point estimate for the peculiar velocity.

ii) We use a volumetric prior for the distances.

iii) We use the group-corrected redshift instead of the individual redshift for each galaxy.

iv) We use two different values of σ_v to check the robustness of the result to the choice of this parameter.

We discuss the effect of each of these modelling assumptions on the inferred value of H_0 in the following. We use the peculiar velocity fields described in the previous sections to correct for peculiar velocities. Since all 6 megamasers are located in the northern sky, we cannot use the 6dF velocity field for our purpose. We used both the 2M++ and the SuperTF velocity fields for our treatment of the peculiar velocity.

Marginalizing the line-of-sight peculiar velocity: We use the probability model described in section 5.6.1, where we marginalize over the line-of-sight peculiar velocity, as opposed to a point estimate that is usually used. We compared the effect of not marginalizing the line-of-sight peculiar velocity. When using the simple point estimate of the peculiar velocity, we find that the H_0 posterior shifts by $\sim +1.5$ km s^{-1} Mpc^{-1}. This is a non-negligible effect on the inferred value of H_0. Such a shift is not present when using the SuperTF velocities, suggesting that the effect of marginalizing over the line-of-sight peculiar velocity may be non-trivial. In addition to using a fixed peculiar velocity, if we use a uniform prior on the distances, we get $H_0 = 71.5 \pm 2.7$ km s^{-1} Mpc^{-1}, which is consistent with the values obtained by Pesce et al. (2020).

Distance priors: We use a volumetric prior on the distances. It has been noted that assuming a wrong distribution biases the distance measurement, an effect usually called Malmquist (1920) bias, although the first derivation of this effect is in Eddington (1914). The fractional bias for a lognormal uncertainty is given as, $3\Delta^2$, where Δ is the fractional distance uncertainty (Lynden-Bell et al. (1988)). Therefore assuming a uniform prior on the distances, instead of a volumetric prior, will bias the distance measurements to a lower value, leading to an inferred value of H_0 that is systematically biased high. For the megamasers, the difference in the prior distribution biases the value of H_0 by ~ 1 km s^{-1} Mpc^{-1} (see Table 5.4).

Group redshift corrections: We use the group mean redshifts for the megamaser galaxies to suppress the non-linear velocity contributions. Except for NGC 4258, we identify the groups from the 2M++ catalogue. In Kourkchi & Tully (2017), it was noted that the NGC 4258 group is located directly in the foreground of the NGC 4217 group. This can lead to mistaken identification of the two groups into the same group. In the group catalogue of 2M++, the two groups are identified into a single group. Therefore, we use the group information for NGC 4258 from Kourkchi & Tully (2017). We note that for the MCP megamaser sample, using the group redshift has a small effect, leading to a value H_0 that is 0.4 km s^{-1} Mpc^{-1}higher than when using the galaxy redshifts.

Value of σ_v: We also checked the effect of using a different value of σ_v for the peculiar velocity error. The $\sigma_v = 150$ km/s uncertainty was obtained by calibrating our reconstruction with simulations. If for some reason, the peculiar velocity error is underestimated, the value of σ_v may be higher. We therefore test the effect of adopting a larger uncertainty, $\sigma_v = 200$ km/s for our measurements. The effect of different values of σ_v in non-trivial. As expected, the uncertainty increases for the higher σ_v value. The mean value of inferred H_0 is also 0.4 km s^{-1} Mpc^{-1} higher than for the fiducial value of σ_v .

We present our results in Table 5.4, where the inferred value of H_0 for different model

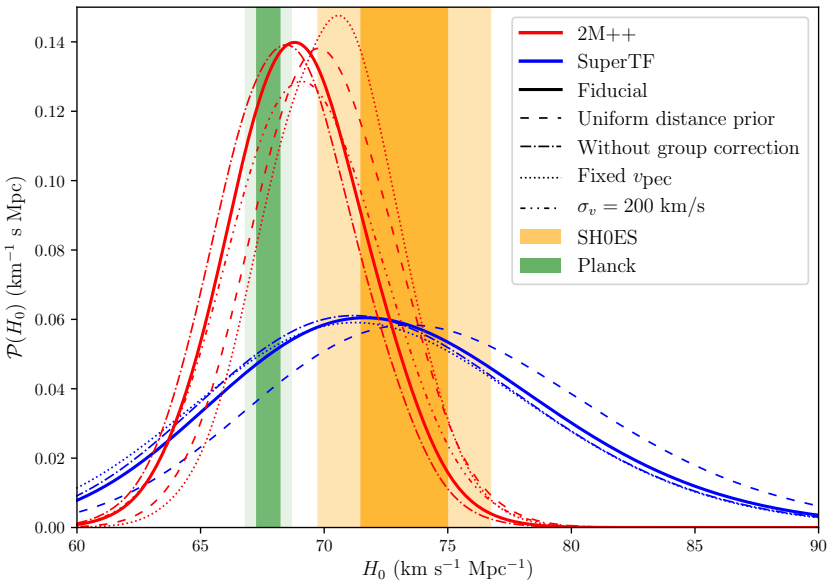

Figure 5.6: H_0 posteriors from the megamaser distances for different peculiar velocity treatments. The red curves are obtained using the 2M++ velocity field, while blue curves are obtained using the SuperTF velocity field. Different line styles corresponds to different model assumptions as indicated in the plot. The Planck and SH0ES confidence intervals are shown with green and orange vertical bands.

Table 5.4: Inferred value of H_0 from megamasers for different treatment of peculiar velocities. Results are reported as the median with 1σ confidence interval (16th to 84th percentile).

Peculiar velocity	Model Assumption	H_0 (km s^{-1} Mpc^{-1})
2M++	**Fiducial**	$\mathbf{69.0^{+2.9}_{-2.8}}$
	Fixed $v_{\rm pec}$	$70.5^{+2.6}_{-2.8}$
	Uniform distance prior	70.1 ± 2.9
	No group redshift correction	$68.6^{+2.9}_{-2.8}$
	$\sigma_v = 200$ km/s	$69.4^{+3.1}_{-3.0}$
	Pesce et al. (2020)	71.8 ± 2.7
SuperTF	**Fiducial**	$\mathbf{72.6^{+7.1}_{-6.3}}$
	Fixed $v_{\rm pec}$	$72.0^{+7.0}_{-6.5}$
	Uniform distance prior	$74.4^{+7.3}_{-6.5}$
	No group redshift correction	$72.2^{+7.0}_{-6.1}$

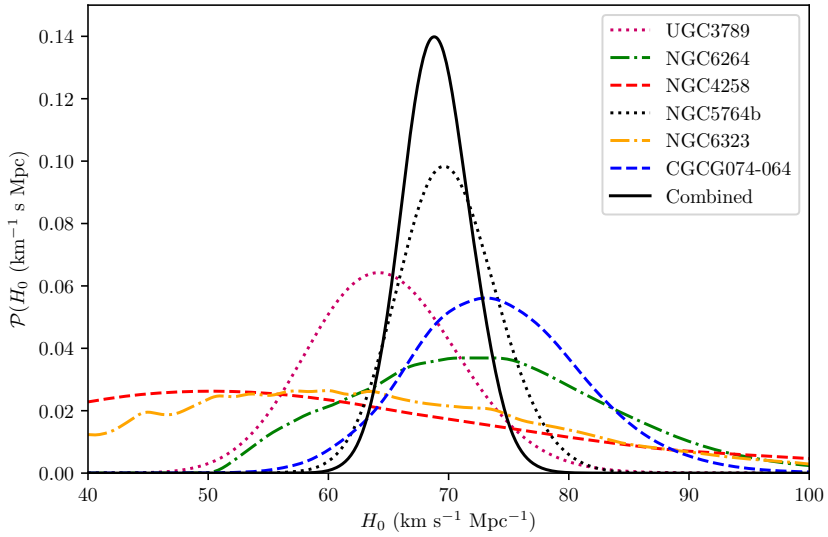

Figure 5.7: The H_0 posterior for each of the individual megamasers for our fiducial model assumptions with the 2M++ velocity field. NGC5764b provides the tightest constraint on H_0 among the 6 megamasers.

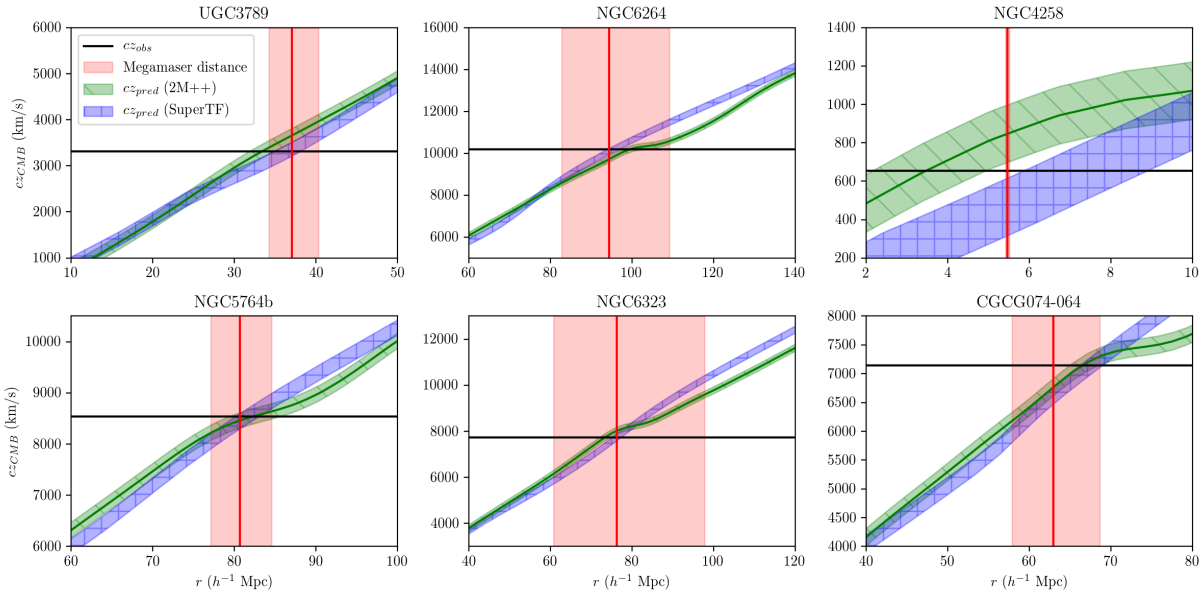

Figure 5.8: The predicted CMB frame redshifts along the line-of-sights of the 6 megamasers. The red shaded region shows the distance uncertainty as measured by Pesce et al. (2020). We use $h = 0.72$ to convert the angular diameter distances to r (measured in h^{-1} Mpc). The black horizontal line is the observed CMB frame redshift, with the group corrections. The green and the blue shaded region is the uncertainty in the predictions of cz from 2M++ and SuperTF fields respectively.

assumptions are reported for the 2M++ and the SuperTF peculiar velocity fields. For the SuperTF velocity field, we add in quadrature to $\sigma_v = 150$ km/s, the measurement uncertainty in the kernel-smoothed velocity field. As can be seen in Figure 5.2, the distribution of SuperTF galaxies at high redshift is sparse. Furthermore, as discussed in section 5.5.3, at higher redshift, the peculiar velocity uncertainties are also larger. Hence, the velocity corrections for the megamasers obtained using the SuperTF field is a very noisy, leading to the much larger uncertainty in H_0. In the 'fiducial model', we marginalize over the line-of-sight peculiar velocity, assume a volumetric prior for the distance, and the group corrected redshifts are used. For 2M++, we assume $\sigma_v = 150$ km s^{-1} for the fiducial model. The posteriors derived for the different model assumptions are shown in Figure 5.6. As can be seen from the figure, we find that using the SuperTF velocity field yields a much larger uncertainty in H_0 compared to the 2M++ velocity field. Of the different assumptions that we checked, we highlight the importance of using a volumetric prior and marginalizing the line-of-sight peculiar velocity. For the 6 megamasers, a combination of these two effects shifts the H_0 posterior by $\sim 1\sigma$. In Figure 5.7, we show the H_0 posterior from each of the 6 individual megamasers. As can be seen from the figure, NGC5764b provides the strongest constraints among the 6 megamasers. We show the predicted redshift along the line-of-sight of the megamasers from the 2M++ and the SuperTF velocity fields in Figure 5.8. The inferred value of H_0 is broadly consistent with both the value of H_0 as inferred by Planck and the SH0ES collaboration. However, it is interesting that with the 2M++ peculiar velocity field, we obtain a value of $H_0 = 69^{+2.9}_{-2.8}$ km s^{-1} Mpc^{-1}, which is lower than the value of H_0 obtained by the SH0ES collaboration Riess et al. (2019) by $\sim 1.7\sigma$.

5.7 Discussion

In this section, we discuss some essential features of the considered peculiar velocity models. In sections 5.7.1 and 5.7.2, we discuss the peculiar velocity estimates for two specific galaxies - NGC 4993 and NGC 1052 respectively, which has implications for our understanding of dark matter and dark energy.

5.7.1 Peculiar velocity of NGC 4993

The exact peculiar velocity of NGC4993 has been the discussion of many recent works (see Nicolaou et al., 2019; Howlett & Davis, 2020; Mukherjee et al., 2019). NGC4993 was the host galaxy for the binary neutron star event, GW170817 (Abbott et al., 2017a) discovered by LIGO. The distance measurement from the gravitational wave event can be used to put

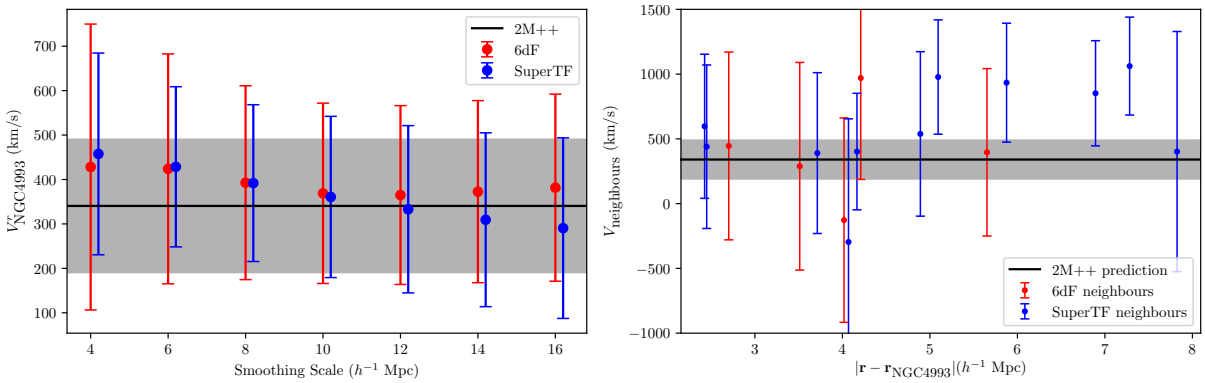

Figure 5.9: Peculiar velocity estimate of NGC4993. *(Left)* The measured peculiar velocity of the galaxies within 1 kernel width (for a fiducial smoothing length of 8 h^{-1} Mpc) of NGC4993 from the 6dF (red markers) and the SuperTF (blue markers) peculiar velocity catalogues. There are a total of 6 neighbours within 1 kernel width for the 6dF catalogue and 10 neighbors within a kernel width for the SuperTF catalogue. *(Right)* Predicted peculiar velocity for different models. The black horizontal line is the prediction from 2M++ reconstruction and the grey region is the associated error, assuming $\sigma_v = 150$ km/s. The red and the blue markers are the estimates using the adaptive kernel smoothing on 6dF and SuperTF catalogues respectively for different smoothing scales.

constraint on the value of H_0. However, because it is relatively nearby, the contribution to the redshift from the peculiar velocity is substantial ($\gtrsim$ 10%) and therefore needs to be corrected.

The original estimate of H_0 from GW170817 (Abbott et al., 2017b), used adaptive kernel smoothing on the 6dF peculiar velocity sample to predict the velocity of NGC4993. It was noted that reconstruction based method with 2M++ also gives a similar velocity estimate. Howlett & Davis (2020) tested the dependence of the peculiar velocity predictions on different assumptions, such as group assignment and different peculiar velocity catalogues for kernel smoothing. It was demonstrated that different assumptions leads to different estimates for the peculiar velocity, thus leading to a higher uncertainty in the measured value of H_0. Mukherjee et al. (2019) used the forward-modelled reconstruction framework, BORG (Jasche & Wandelt, 2013; Jasche & Lavaux, 2019), to predict the velocity field with the 2M++ catalogue, finding a velocity estimate of 330 ± 130 km s^{-1}.

In this section, we check the predictions for the peculiar velocity of NGC4993 using different choices of the peculiar velocity models considered in this work. Nicolaou et al.

(2019) noted that the estimates of the peculiar velocity for NGC4993 using the kernel smoothing technique depends strongly on the choice of kernel width and used a Bayesian model to account for the uncertainty due to the choice of the kernel width. As we already point in Section 5.4, predictions from a smoothed velocity field need to be scaled up in order to obtain unbiased estimates for the velocity. We show our results for the dependence of the predicted peculiar velocity of NGC4993 on the smoothing length in Figure 5.9. As can be seen, after scaling the velocity by the required factor, there is no longer a strong dependence on the smoothing scale. The predictions from 2M++ reconstruction and adaptive kernel smoothing give consistent results. Since our methods of estimating the peculiar velocity smooths the velocity field at a scale much larger than that of individual galaxies, it is useful to predict the velocities of groups of galaxies. Averaging the redshifts of galaxies in a group suppresses the non-linear velocity contributions. In order to correct for the grouping, we identify the groups from the 2M++ catalogue. For NGC4993, the average group redshift is $cz = 3339$ km/s, while that of the galaxy is $cz = 3216$ km/s. Using a fiducial smoothing length of 8 h^{-1} Mpc, the adaptive kernel smoothing technique predicts a velocity of $v_r = 357 \pm 160$ km/s for the 6dF catalogue and $v_r = 388 \pm 61$ km/s for the SuperTF catalogue. Since the 2M++ reconstruction gives the velocity in the real space coordinates, we use an iterative method to estimate the velocity along the line-of-sight of the galaxy. For NGC4993, we find the 2M++ predictions to be, $v_r = 456 \pm 150$ km/s. Therefore, we find consistent predictions from the 2M++ reconstruction and the kernel smoothing methods.

We then used these estimates of the peculiar velocity for NGC4993 along with the distance posterior for the GW event to get an estimate of H_0. In Figure 5.10, we show the posterior on H_0 measured using only the luminosity distance to NGC4993 [1] measured using gravitational waves (Abbott et al., 2017b). We show the effect of using the different peculiar velocity models considered in this work.

5.7.2 Distance and peculiar velocity of NGC 1052-DF2

In an interesting result, van Dokkum et al. (2018) discovered that a galaxy, NGC1052-DF2, contains little or no dark matter. This challenges the conventional wisdom about galaxy formation and shows that at least some galaxies may have baryonic component without any dark matter in it. However, their result was contested by Trujillo et al. (2019) where, using Tip of Red Giant Branch (TRGB) and other distance measurements, the authors calculated a distance of $\sim$ 13 Mpc to the galaxy as opposed to the earlier estimates of

[1] The posterior samples are publicly available at https://dcc.ligo.org/LIGO-P1800061/public

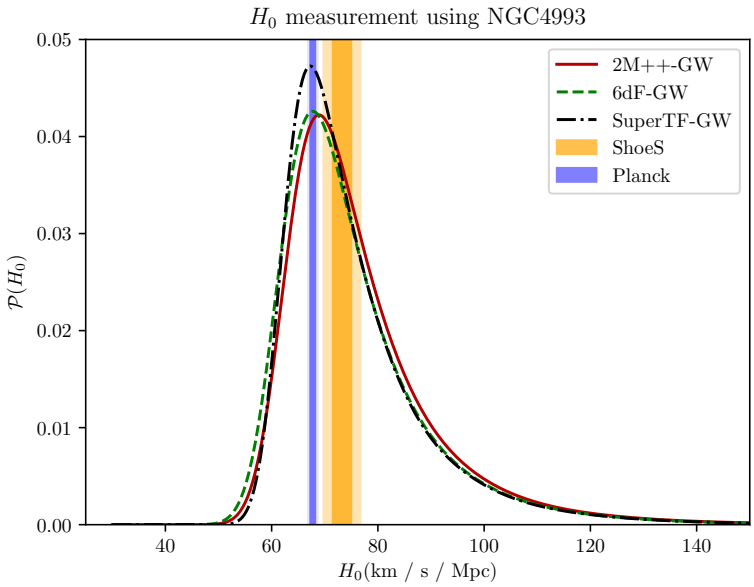

Figure 5.10: H_0 posterior for NGC4993 considering the distances measured from GW170817. The peculiar velocity is corrected for using the 2M++ reconstruction (*maroon*), 6dF adaptive kernel smoothing (*green-dashed*) and SuperTF adaptive kernel smoothing (*black dash-dotted*).

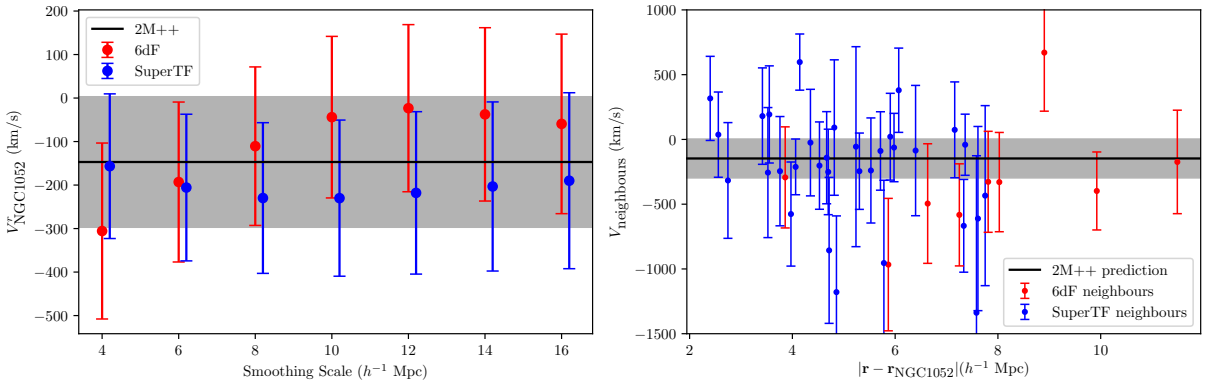

Figure 5.11: Same as Figure 5.9 but for NGC1052-DF2.

$\sim$ 19 Mpc as derived from surface brightness fluctuations in van Dokkum et al. (2018). Analysis with the shorter distance to NGC1052-DF2 results in a stellar mass fraction, $M_{\rm halo}/M_\star > 20$ as opposed of order unity derived in van Dokkum et al. (2018).

However, the shorter (13 Mpc) distance implies a radial peculiar velocity of 640 ± 25 km/s in the CMB frame for NGC 1052-DF2. While Trujillo et al. (2019) claim that the spread of peculiar velocities in this region is high, we argue that most of this spread is due to uncertainty in the distance indicator and does not reflect the real velocity noise on the underlying flow field. For example, for the TF and FP methods, the scatter in the distance indicator is $\sim 20\%$, which translates to a scatter of ~ 350 km/s in the peculiar velocity from galaxy to galaxy at the distance of NGC 1052. In this section, we infer the peculiar velocity of the galaxy by the two methods previously described. The result of this analysis is shown in Figure 5.11. The mean redshift of the 9 members of the NGC 1052 group (in which NGC1052-DF2 is assumed to reside) is $cz_{\rm CMB} = 1256$ km/s. This is in agreement with Kourkchi & Tully (2017), who find a mean CMB redshift of 1252 km/s from 16 group members. Note that this is considerably lower than the CMB redshift of NGC 1052-DF2 itself (1587 km/s). Using the 2M++ reconstruction, the peculiar velocity for NGC 1052 group is $v_r = -162 \pm 150$ km s^{-1}. Assuming $H_0 = 73 \pm 2$ km/s/Mpc, this peculiar velocity implies a distance of 19.4 ± 2.2 Mpc. The distance estimates are consistent with the Fundamental Plane distance estimate for NGC1052, $d = 21.5 \pm 4$ (Blakeslee et al., 2001) and the distance obtained from surface brightness fluctuations, $d = 19.0 \pm 1.7$ van Dokkum et al. (2018). We find consistent results from the kernel smoothing approaches: with a fiducial smoothing radius of 8 h^{-1} Mpc, with the 6dF velocity data there are a total of 9 6dF velocities within 1 kernel length of NGC1052-DF2 and these yield a kernel-smoothed mean velocity of $v_r = -124 \pm 68$ km s^{-1}. With the SuperTF data, the kernel smoothed mean velocity is $v_r = -191 \pm 38$ km s^{-1} from 32 SuperTF velocities within 1 kernel length of NGC 1052-DF2.

We also consider the possibility that NGC 1052-DF2 may be an isolated galaxy in the foreground of the NGC 1052 group with a distance of ~ 13 Mpc. In this case, the peculiar velocity needed to explain its redshift is ~ 600 km s^{-1}. In Figure 5.12, we plot the predicted redshift along the line-of-sight of NGC1052-DF2 for the different peculiar velocity models. As can be seen from the Figure, there are no locations in the foreground of the NGC 1052 group with such high outward radial peculiar velocity. Therefore, we conclude that a short distance is not the explanation for the high stellar mass fraction of NGC 1052-DF2.

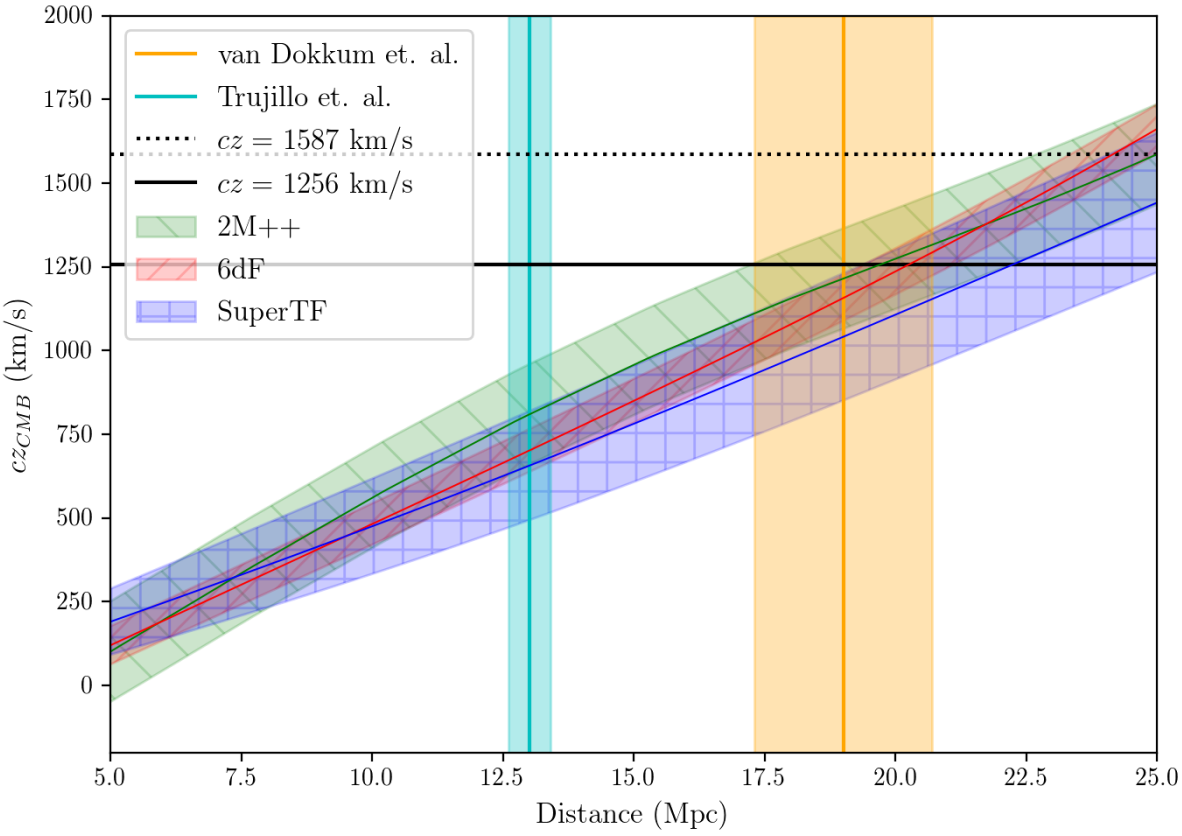

Figure 5.12: $cz_{\rm CMB}$ in the line of sight for NGC 1052-DF2. We use $h = 0.72$ to convert the distance in h^{-1} Mpc to absolute distance. The shaded regions for the 2M++, 6dF and the SuperTF radial velocities (shown in green, red and blue respectively) signify the 1σ errors associated with the velocity estimates. The observed redshifts for NGC 1052-DF2 is shown with a dotted black line. The redshift of the NGC 1052 group is shown with a solid black line. The cyan and the orange vertical lines are the distance estimates of Trujillo et al. (2019) and van Dokkum et al. (2018) respectively.

5.8 Summary

Unbiased estimates of peculiar velocity are essential for different applications in cosmology and galaxy formation. There are different methods of estimating the peculiar velocities of galaxies, e.g, using reconstruction of the density field in the local Universe or by kernel smoothing the peculiar velocity data. In this chapter, we compared the performance of different peculiar velocity models of the local Universe. First model we compare is the reconstructed velocity field from the 2M++ redshift compilation. The other is based on an adaptive kernel smoothing technique, which we apply on the 6dF peculiar velocity data and SuperTF, a compilation of the Tully-Fisher peculiar velocity data from SFI++ and 2MTF. We highlight that, when using a smoothed velocity field, we need to rescale the predictions by a scaling factor to get unbiased estimate of the peculiar velocity. We compared the peculiar velocity predictions to a few test data sets using a simple comparison of the mean squared error and a forward likelihood method. We find that the 2M++ reconstruction performs better than both the kernel smoothed peculiar velocity data for all the peculiar velocity test data sets across all range of redshifts.

We also compared the peculiar velocity estimates from these different methods for two interesting galaxies: NGC 4993 and NGC 1052-DF2. NGC 4993 was the host galaxy for the first binary neutron star event detected by LIGO. An accurate peculiar velocity is required to correct the redshift of the galaxy in order to obtain a measurement of the Hubble constant. The different models considered in this work give remarkably consistent peculiar velocity estimates for the galaxy. NGC 1052-DF2 is an ultra-diffuse galaxy which has been claimed to be almost free of dark matter. This result has been contested with the claim that a shorter distance to the galaxy solves the anomalous stellar mass fraction. However, we find that this claim is not supported by the models of peculiar velocity that we use in our study.

Part III

Standard siren H_0 measurement

Chapter 6

Measuring the Hubble Constant from standard sirens without optical counterparts

6.1 Introduction

The detection of gravitational waves from binary coalescence events has opened a new window into studying the Universe. In particular, gravitational wave measurements from binary events allows for a new way, independent of electromagnetic signals, to measure luminosity distance at cosmological scales, hence they are also called, 'standard sirens'. Independent distance measurements are particularly important because of the increasing discrepancy[1] between the value of Hubble constant measured from the early Universe and the value measured from late Universe observations. It has been reported that $\sim$ 50 standard siren events may be sufficient to resolve this tension in H_0 value (Feeney et al., 2019). A promising aspect of distance measurement from standard sirens, as opposed to the distance measurement from standard candles, is that it requires no intermediate calibration with a distance ladder. Instead, the distances are estimated directly using General Relativity. Therefore, standard sirens provide an absolute distance estimate and therefore is free from systematic effect that may arise in the calibration step.

Using standard sirens to measure the Hubble constant was first proposed by Schutz (1986). Since the original proposal, the idea has been refined and even been applied to

[1] See section 1.4.3 for more detail

measure the Hubble constant from the first detection of binary neutron star event (Abbott et al., 2017b). However, gravitational waves only provide a distance estimate on its own. To measure the Hubble constant, one also needs redshift measurements in addition to the distance measurements. Observations of electromagnetic counterparts such as a gamma-ray burst or a kilonova[2] provides one such way to measure the redshift (Holz & Hughes, 2005; Nissanke et al., 2010). Detecting an optical counterpart also reduces substantially uncertainties in other parameters. The first detection of binary neutron stars by LIGO, GW170817 (Abbott et al., 2017a), was accompanied by a kilonova. The electromagnetic counterpart was then used to infer NGC4993 as the host galaxy with $> 99.996\%$ probability. Using the electromagnetic counterpart and the distance measurement, the Hubble constant was measured to $\sim$ 14% accuracy in Abbott et al. (2017b).

However, electromagnetic counterparts are not the only way to measure the redshifts. In fact, for binary black hole event, we do not expect to observe such optical counterparts. Even with binary neutron stars, optical counterparts were not observed with subsequent events detected by LIGO (Abbott et al., 2020). An alternate method relies on using a galaxy catalogue and assume that the binary coalescence event is associated with a galaxy from the catalogue. The assumption of the binary event being associated with the galaxies, therefore gives possible redshift estimate for the source. Combining the galaxy redshifts with distance estimate therefore gives a way to measure the Hubble constant. Such a method has been called the 'statistical' method of measuring the Hubble constant. In fact, the original proposal by Schutz (1986) relied on such a statistical method. A statistical method was applied for the first time to measure H_0 from the GW170817 data without assuming an electromagnetic counterpart in Fishbach et al. (2019). In Soares-Santos et al. (2019), the method was used to measure H_0 from a 'dark siren', for which an electromagnetic counterpart was not observed, albeit with a large uncertainty. These methods have also been applied to binary black hole events from the first and second LIGO observing runs to improve the H_0 constraints from GW170817 alone (The LIGO Scientific Collaboration et al., 2019).

In this chapter, we propose a new approach to statistically measure the Hubble constant from standard sirens. Our method involves using a reconstructed density field of dark matter in the Universe. The reconstruction is performed with the Bayesian forward-modelled reconstruction software, BORG (Jasche & Wandelt, 2013; Jasche & Lavaux, 2019), where a physical structure formation model is used to evolve the initial density field to the present day and an ensemble of plausible density fields is sampled from a posterior. Our

[2]It has also been noted that it may be posible to use light curves from kilonova on its own as a standardizable candle to provide a distance measurement. See e.g., Kashyap et al. (2019); Coughlin et al. (2020)

reconstruction self-consistently accounts for the peculiar velocities which can introduce systematic uncertainty in estimating the redshift at low redshifts (Hui & Greene, 2006). Furthermore, higher order correlation functions in the density field induced because of structure formation are automatically taken into account in this reconstruction framework. The forward-modelled framework for reconstructing the density field is especially powerful in the low signal-to-noise regime, i.e., when there is a relatively modest number density of galaxies or the survey is not complete. Joint reconstruction of density and true position of galaxies from a photometric survey has also been demonstrated to be extremely powerful for improving the photometric redshift estimates to galaxies (Jasche & Wandelt, 2012). Therefore, it is interesting to develop a framework which relies only on the forward-modelled reconstructed density field to measure H_0.

This chapter is structured as follows: In section 6.2, we develop the probabilistic framework that we use for inferring H_0. In section 6.3, we describe the BORG framework that is used for reconstructing the density field. Section 6.4 describes the test of our method on a mock simulation of galaxies and binary neutron stars. Then in section 6.5, we apply our method on the binary neutron star event GW170817 before concluding in section 6.6. Throughout this chapter, $h = H_0/(100 \text{ km s}^{-1} \text{ Mpc}^{-1})$.

6.2 H_0 Inference Framework

In this section, we derive the probabilistic model for inferring H_0 from a density field reconstruction. For this section, we will consider the reconstructed density field as a given. The basic problem we want to solve is the following: we want to infer H_0, given a galaxy catalog data, $\{x_{\rm gal}\}$, and a set of gravitational wave events, $\{x_{\rm GW}\}$. That is, we want to calculate $\mathcal{P}(H_0|\{x_{\rm GW}\}, \{x_{\rm gal}\})$. Using Bayes rule, we can write this posterior as,

$$\begin{aligned}\mathcal{P}(H_0|\{x_{\rm GW}\}, \{x_{\rm gal}\}) &\propto \mathcal{P}(H_0)\mathcal{P}(\{x_{\rm GW}\}|\{x_{\rm gal}\}, H_0) \\ &= \mathcal{P}(H_0) \prod_{i=1}^{N_{\rm GW}} \mathcal{P}(x^i_{\rm GW}|\{x_{\rm gal}\}, H_0)\,. \end{aligned} \tag{6.1}$$

In the second line, we assume that the likelihood for all the standard siren events are independent of each other and therefore can be expressed as the product of likelihood for individual events.

We formulate the H_0 inference likelihood in terms of the reconstructed density field, δ. In this formulation, the galaxy catalogue enters the likelihood through the probability, $\mathcal{P}(\delta|\{x_{\rm gal}\})$, which indicates the output of the reconstruction. For BORG, the output consists of an ensemble of density fields sampled from this posterior. Galaxy catalogues provide us with the redshifts of the galaxies, which can then be mapped to the comoving space. It is also conventional to express this in units of h^{-1} Mpc [3]. Therefore, the density field is calculated in the comoving coordinates measured in units of h^{-1} Mpc, which we denote as r. The gravitational wave standard sirens, on the other hand, gives the luminosity distance to the GW event. The mapping from r to the luminosity distance, d_L, depends on H_0. We can expand the likelihood for the gravitational wave event in terms of the intermediate variables as follows,

$$\mathcal{P}(x_{\rm GW}|\{x_{\rm gal}\}, H_0) \propto \int \mathrm{d}\{\delta\}\mathrm{d}\Omega\mathrm{d}d_L\mathrm{d}r\mathcal{P}(x_{\rm GW}|d_L,\Omega)\mathcal{P}(d_L|r,H_0)\mathcal{P}(r,\Omega|\{\delta\})\mathcal{P}(\{\delta\}|\{x_{\rm gal}\})\,, \tag{6.2}$$

where, Ω stands for the angular position. The dependence of the luminosity distance on the co-moving distance and the Hubble constant is deterministic. That is, $\mathcal{P}(d_L|r,H_0) = \delta^{(D)}(d_L - \hat{d}_L(r,H_0))$, where $\delta^{(D)}$ is the Dirac delta function and $\hat{d}_L(r,H_0) = r(1+z)/h$. Therefore d_L can be easily marginalized out of the above relation. Physically, that means that, for a given value of H_0, we map the GW posterior to the co-moving space. The integration over $\mathcal{P}(\{\delta\}|\{x_{\rm gal}\})$ denotes marginalization over the BORG posterior ensemble.

Evaluating the GW event likelihood, $\mathcal{P}(x_{\rm GW}|d_L,\Omega)$, involves another use of the Bayes theorem. Gravitational wave data analysis tools usually provides the posterior of d_L and Ω given the gravitational wave data. The posterior, $\mathcal{P}(d_L,\Omega|x_{\rm GW})$ can be obtained using a full GW inference framework such as LALINFERENCE (Veitch et al., 2015) or some approximate 3D position reconstruction scheme such as BAYESTAR (Singer & Price, 2016). For this work, we use BAYESTAR to infer the 3D positions of the simulated GW events. The likelihood can be expressed as, $\mathcal{P}(x_{\rm GW}|d_L,\Omega) \propto \frac{\mathcal{P}(d_L,\Omega|x_{\rm GW})}{\mathcal{P}(d_L,\Omega)}$. Note that the prior, $\mathcal{P}(d_L,\Omega)$ must be the same prior that is used in the GW analysis to obtain the posterior. Typically, one takes a volumetric prior on the luminosity distance, $\mathcal{P}(d_L,\Omega) \propto d_L^2$.

The final remaining part in equation (6.2) is modelling the probability, $\mathcal{P}(r,\Omega|\delta)$. This is the probability of the GW event occuring at r,Ω given a certain overdensity. We model this as a Poisson process. To describe the Poissonian rate of mergers, we need to introduce two new quantities: $n_{\rm GW}$, which gives the average rate of mergers per unit volume in the Universe and $b_{\rm GW}$, which denotes the parameters governing the 'bias' of the merger events

[3] See Sanchez (2020) for a case for dropping this convention.

with respect to the matter overdensity, δ. The mean rate of mergers at a location, $\mathbf{r}$, is therefore given as, $n_{\rm GW}(1+\delta_{\rm GW}(\mathbf{r}))$, where $\delta_{\rm GW}$ depends on $b_{\rm GW}$ and δ. The Poisson intensity for an infinitesimal volume $\mathrm{d}^3\mathbf{r}$ is then given as,

$$\lambda(\mathbf{r})\mathrm{d}^3\mathbf{r} = n_{\rm GW}(1+\delta_{\rm GW}(\mathbf{r}))\mathrm{d}^3\mathbf{r}\,. \tag{6.3}$$

The Poisson probability for the event to occur at r, Ω can then be written as,

$$\mathcal{P}(\mathbf{r}|n_{\rm GW}, b_{\rm GW}, \delta) = \lambda(\mathbf{r})\exp\left[-\int \mathrm{d}^3\mathbf{r}'\lambda(\mathbf{r}')\right]\mathrm{d}^3\mathbf{r}\,. \tag{6.4}$$

The integral in the exponential can then be written as,

$$\int n_{\rm GW}(1+\delta_{\rm GW})r^2\mathrm{d}r\mathrm{d}\Omega = n_{\rm GW}V = N_{\rm GW}\,. \tag{6.5}$$

where, V is the total volume under consideration. Using this in the equation (6.4), we obtain,

$$\mathcal{P}(r, \Omega|n_{\rm GW}, b_{\rm GW}, \delta) \propto N_{\rm GW}e^{-N_{\rm GW}}(1+\delta_{\rm GW}(r,\Omega))\,. \tag{6.6}$$

If we assume an uniform prior on $N_{\rm GW}$ (or $n_{\rm GW}$), we can marginalize over $N_{\rm GW}$ analytically resulting in a constant. Therefore, it drops out of the equation. Incorporating these simplifications, we can then simplify equation (6.2) to write,

$$\mathcal{P}(x_{\rm GW}|\{x_{\rm gal}\}, H_0) \propto \int \mathrm{d}b_{\rm GW}\mathrm{d}r\mathrm{d}\Omega\mathrm{d}\delta\; r^2(1+\delta_{GW}(r,\Omega))\frac{\mathcal{P}(\hat{d}_L(r,H_0),\Omega|x_{\rm GW})}{\mathcal{P}(\hat{d}_L,\Omega)}\mathcal{P}(b_{\rm GW})\mathcal{P}(\delta|\{x_{\rm gal}\})\,. \tag{6.7}$$

A BORG run on a galaxy catalogue gives us an ensemble of density fields, which are consistent with the galaxy catalogue. Thus, we can marginalize over δ using the Monte Carlo samples provided by BORG. For all the cases considered in this work, we use a volumetric prior for the GW events.

$$\begin{aligned}\mathcal{P}(x_{\rm GW}|\{x_{\rm gal}\}, H_0) &\propto \frac{1}{N_{\rm BORG}}\sum_{i=1}^{N_{\rm BORG}}\int \mathrm{d}b_{\rm GW}\mathrm{d}r\mathrm{d}\Omega\;\frac{r^2}{d_L^2(r,H_0)}(1+\delta^i_{GW})\mathcal{P}(\hat{d}_L(r,H_0),\Omega|x_{\rm GW})\mathcal{P}(b_{\rm GW}) \\ &\propto \int \mathrm{d}b_{\rm GW}\mathrm{d}r\mathrm{d}\Omega\;\frac{r^2}{d_L^2(r,H_0)}(1+\langle\delta^i_{GW}\rangle)\mathcal{P}(\hat{d}_L(r,H_0),\Omega|x_{\rm GW})\mathcal{P}(b_{\rm GW})\,.\end{aligned} \tag{6.8}$$

Note that we only require the mean density field from BORG for the purposes of this inference.

Because of gravitational wave selection effects and volume effects, a normalization term must be included which depends on H_0. The normalization factor, as applicable to the analysis of gravitational wave has been a topic of discussion in the literature (Mandel et al., 2019; Abbott et al., 2017b). With the normalization term, the final likelihood is expressed as below,

$$\mathcal{P}(x_{\rm GW}|\{x_{\rm gal}\}, H_0) = \frac{H_0^2}{\alpha(H_0)} \int {\rm d}b_{\rm GW} {\rm d}r {\rm d}\Omega \, \frac{1}{(1+z)^2} (1+\langle \delta^i_{GW} \rangle) \mathcal{P}(\hat{d}_L(r, H_0), \Omega | x_{\rm GW}) \mathcal{P}(b_{\rm GW}) \,, \tag{6.9}$$

$\alpha(H_0)$ being the normalization term. When the galaxy catalogue has a high degree of completeness compared to the the GW events, $\alpha(H_0)$ only corrects for the volume effects of the posterior. In this regime, $\alpha(H_0) \propto H_0^3$. We will restrict to this regime for this chapter. This is the likelihood we use in our inference calculations. In principle, one can model the bias in varying levels of complexity in this framework. For our mock simulations, since the binary events are uniformly placed on the galaxies, we assume that gravitational wave events are similarly biased as the galaxies. In general, the formation of binary coalescence events is an area of active research. As such the 'bias' of binary events could be a complicated function of stellar mass or luminosity or some combination of these.

6.3 Forward modelled reconstruction of the Large-scale structure with BORG

In this section, we describe the probabilistic framework of BORG and give some essential details about the BORG runs we use in this work. For further details on the framework, see the original papers (Jasche & Wandelt, 2013; Jasche & Lavaux, 2019).

The BORG framework uses Bayesian forward modelling to reconstruct the large-scale density field of the universe. In BORG, we jointly infer the cosmic matter density field and a set of bias parameters for the galaxies/halos. The density field is set up on a simulation box. Note that, in BORG, the density in each voxel is a parameter that we infer. This typically results in $\gtrsim 10^6$ parameters. Sampling from such high dimensional parameter poses a challenge to traditional sampling methods. It is nonetheless possible with efficient sampling schemes such as Hamiltonian Monte Carlo (HMC, Neal, 1993, 1996). HMC increases the sampling efficiency by taking into account the gradient of the posterior. This

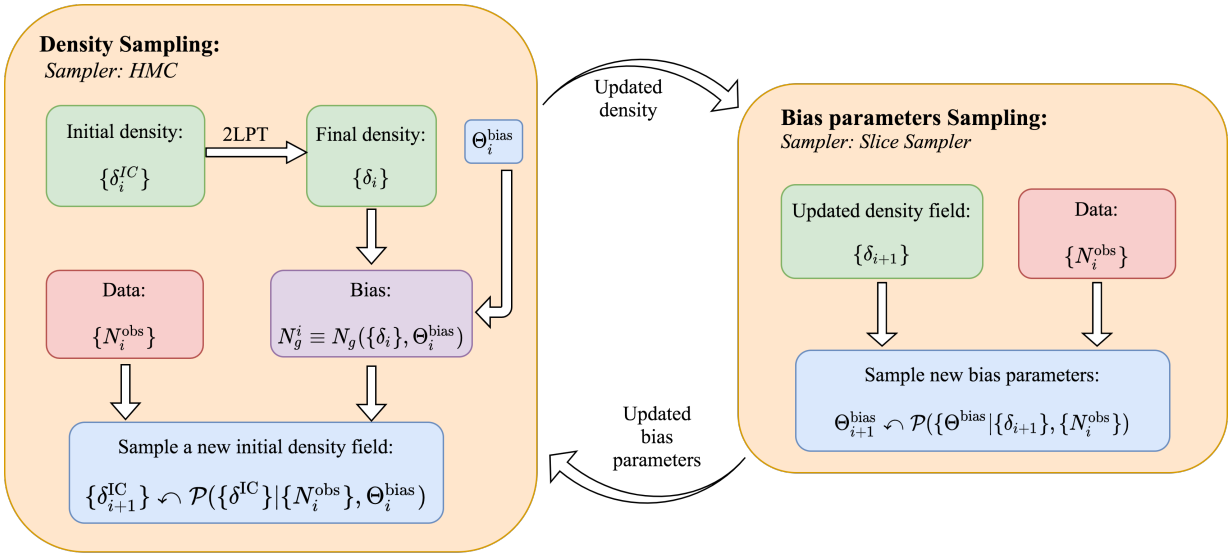

Figure 6.1: An illustration of the sampling scheme used in BORG. During the sampling of the density field, the bias parameters are kept fixed. Using a bias model, the predicted number of galaxies is compared with the observed galaxy catalogue. The density sampling is done using HMC. Then the updated density field sampled using HMC is kept fixed while sampling the bias parameters. The sampling of the bias parameters are done using slice sampling.

allows to generate proposal moves that are large, allowing the creation of independent samples from the posterior distribution, while keeping a high acceptance rate.

Due to the incorporation of the physical structure formation model, the problem of inferring the late-time non-linear density field is transformed into the problem of inferring accurately the initial conditions of the universe. Since the structure formation is deterministic, there is a unique mapping between the initial densities, $\delta_i^{\rm IC}$ and the late-time densities, δ_i, i.e.,

$$\mathcal{P}(\{\delta_i\}|\{\delta_j^{\rm IC}\}) = \prod_{i=1}^{N_{\rm voxel}} \delta^{(D)}\left(\delta_i - f_i(\{\delta_j^{\rm IC}\})\right) \ , \tag{6.10}$$

where, $\delta^{(D)}$ is the Dirac delta function.

The forward-modelling of the initial conditions to the final densities is implemented using particles. The mapping from the initial position to the final position of the particle is done using the structure formation model. In doing so, one also obtains the velocity for each particle. Using the velocity, $\boldsymbol{v}$, of the particles, we can then map their real space position, $\boldsymbol{r}$, to their redshift space position, $\boldsymbol{s}$,

$$\boldsymbol{s} = \boldsymbol{r} + \frac{a}{H} v_r \hat{\boldsymbol{r}} \ . \tag{6.11}$$

Since the observation of galaxies gives us their redshift, we estimate the density in the redshift space and then compare it to the observations. Thus, BORG systematically takes care of the redshift space distortions that arise in the reconstruction.

Apart from inferring the initial densities, BORG also consistently infers the parameters of the bias model, $\Theta_{\rm bias}$. To consistently sample both the bias parameters and the initial densities, a block sampling algorithm is used, where the density field is first sampled from the conditional posterior keeping the bias parameters fixed. Then using the updated density field, we conditionally sample the bias parameters. We illustrate this procedure in Figure 6.1.

We want to infer the posterior probability on the initial conditions given the galaxy numbers in each voxel, $\mathcal{P}(\{\delta_i^{\rm IC}\}|\{N_i^g\})$. Since, the likelihood of the observation is easily interpretable in terms of the late-time density, we can write this posterior as a marginalized posterior of the late-time density,

$$\mathcal{P}(\{\delta_i^{\rm IC}\}|\{N_i^{\rm obs}, \Theta_{\rm bias}\}) = \int \mathrm{d}\{\delta_i\} \mathcal{P}(\{\delta_i^{\rm IC}\}, \{\delta_i\}|\{N_i^{\rm obs}\}, \Theta_{\rm bias}) \ . \tag{6.12}$$

The integrand on the right-hand side can be simplified using the Bayes theorem as,

$$\mathcal{P}(\{\delta_i^{\rm IC}\}, \{\delta_i\}|\{N_i^{\rm obs}\}, \Theta_{\rm bias}) = \frac{\mathcal{P}(\{N_i^{\rm obs}\}|\{\delta_i^{\rm IC}\}, \{\delta_i\}, \Theta_{\rm bias}) \mathcal{P}(\{\delta_i^{\rm IC}\}, \{\delta_i\})}{\mathcal{P}(\{N_i^{\rm obs}\})} \ . \tag{6.13}$$

We then express the joint probability $\mathcal{P}(\{\delta_i\}, \{\delta_i^{\rm IC}\})$ in terms of the conditional probability, equation (6.10) and the prior probability, $\mathcal{P}(\{\delta_i^{\rm IC}\})$. Also, we assume that the final number of galaxies depend on $\{\delta_i^{\rm IC}\}$ only through its dependence on $\{\delta_i\}$. With these assumptions, we get,

$$\mathcal{P}(\{\delta_i^{\rm IC}\}, \{\delta_i\}|\{N_i^{\rm obs}\}, \Theta_{\rm bias}) = \frac{\mathcal{P}(\{N_i^{\rm obs}\}|\{\delta_i\}, \Theta_{\rm bias})\mathcal{P}(\{\delta_i\})|\{\delta_i^{\rm IC}\})\mathcal{P}(\{\delta_i^{\rm IC}\})}{\mathcal{P}(\{N_i^{\rm obs}\})} \,. \tag{6.14}$$

Using equation (6.10) in equation (6.14) and marginalizing using equation (6.12), we get,

$$\mathcal{P}(\{\delta_i^{\rm IC}\}|\{N_i^{\rm obs}\}, \Theta_{\rm bias}) = \frac{\mathcal{P}(\{\delta_i^{\rm IC}\})\mathcal{P}(\{N_i^{\rm obs}\}|\{\delta_i\}, \Theta_{\rm bias}))}{\mathcal{P}(\{N_i^{\rm obs}\})} \,. \tag{6.15}$$

$\mathcal{P}(\{\delta_i^{\rm IC}\})$ is the prior probability on $\{\delta^{\rm IC}\}$ which is determined by the cosmological power spectrum. The initial density field is sampled from the above posterior using HMC. For efficient sampling with HMC, one needs the derivative of the posterior with respect to $\{\delta^{\rm IC}\}$ and a well suited mass matrix. These details are provided in Jasche & Wandelt (2013) and Jasche & Lavaux (2019).

In the block sampling scheme, the bias parameters are then sampled using the updated density field. The posterior from which the bias parameters are sampled is then given by the following,

$$\mathcal{P}(\Theta_{\rm bias}|\{N_i^{\rm obs}\}, \{\delta_i\}) \propto \mathcal{P}(\Theta_{\rm bias})\mathcal{P}(\{N_i^{\rm obs}\}|\Theta_{\rm bias}, \{\delta_i\}) \,. \tag{6.16}$$

For this work, the bias parameters are sampled using the slice sampling scheme (Neal, 2003).

Modelling the non-linear bias galaxy/halo bias is a challenging task. For this work, we use a bias model proposed in Neyrinck et al. (2014) which models the galaxy bias well into void regions. It is a power-law with an exponential cut-off in the void regions. It can be expressed as below,

$$\lambda_g(\delta) = \bar{N}(1+\delta)^{\alpha} \exp\left[-\left(\frac{(1+\delta)}{r_0}\right)^{-\epsilon}\right], \tag{6.17}$$

where, λ_g is the expected number of galaxies in a region with dark matter overdensity, δ. $\bar{N}, \alpha, r_0$ and ϵ are parameters of the bias model which are inferred in BORG.

In our inference with BORG, we use a probabilistic model where the galaxies are assumed to be a Poisson sample with the Poisson intensity given by equation (6.17). Hence, given

an observation of galaxy numbers, N, in a grid, the likelihood of this observation is given as,

$$\mathcal{P}(N|\delta) = \frac{1}{N!}\lambda_g^N(\delta)e^{-\lambda_g(\delta)}\,. \tag{6.18}$$

The selection effects in the galaxy catalogue is also incorporated inside the BORG framework. The target selection completeness of a pixel is computed using the Schechter function, $\Phi(\mathbf{x})$. The completeness in a voxel labelled by V is given as,

$$c_V = \frac{\int_{\mathcal{V}_V} d^3\mathbf{x} \int_{L_{\rm app}(|\mathbf{x}|)}^{L_{\rm max}} dL\Phi(L)}{\mathcal{V}_V \int_{L_{\rm min}}^{L_{\rm max}} dL\Phi(L)}\,. \tag{6.19}$$

In the above equation, $L_{\rm app}(\mathbf{x})$ is the minimum luminosity that is visible at a position $\mathbf{x}$ due to the apparent magnitude cut. The response function is a product of the radial completeness, c_V, and the angular selection due to the survey mask. Due to the effects of radial selection and survey mask, the Poisson intensity, λ in equation (6.18) is modified to,

$$\lambda_i \to \lambda_i' = R_i\lambda_i. \tag{6.20}$$

6.4 Test on mock simulation

In order to test our method, we tested it on a mock data set of galaxies and gravitational wave data. In section 6.4.1, we describe the mock galaxy catalogue and the BORG run performed on this catalogue to reconstruct the density field. In section 6.4.2, we describe the mock GW data used in the inference and section 6.4.3 discusses the result of applying our inference framework on these mock catalogues.

6.4.1 Mock galaxy catalogue

Our mock galaxy catalogue is based on the VELMASS N-body simulation. The N-body evolution is performed using the GADGET2 (Springel, 2005) software on a cubic box of size 2 h^{-1} Gpc. The dark matter halos in the box are then identified in the $z = 0$ snapshot using the ROCKSTAR halo finder (Behroozi et al., 2013). For our mock catalogue, we use a smaller (500 h^{-1} Mpc)^3 box from the full box. We then assign to each halo in this part

of the simulation box a single galaxy using an abundance matching approach (Marinoni & Hudson, 2002; Kravtsov et al., 2004). To implement the abundance matching, we sample a set of galaxies of size equal to the number of halos in the N-body simulation and assign the galaxies to the halos by matching the brightest galaxy to the most massive halo. The luminosities of the galaxies are obtained from a Schechter function using the best-fit Schechter parameters, $\alpha = -0.94$, $M^* = -23.28$ of Lavaux & Hudson (2011b). We then choose an apparent magnitude limit of 12.5 and discard the galaxies which appear fainter than that.

We then use BORG to reconstruct the density field using this mock catalogue. The BORG run is performed on a 128^3 cubic box with each side of size 677 h^{-1} Mpc. The structure formation from the initial condition is performed using 2LPT. In general, the galaxy bias is luminosity-dependent. Therefore, we split the galaxies with absolute magnitude between -23.25 to -25.25 into 8 bins of absolute magnitude, each of width, 0.25. For each of these bins, the galaxy bias is modelled using equation (6.17). Note that in the inference process, the redshift space distortions introduced due to the peculiar velocity are consistently taken into account. The power spectrum of the initial density (and then scaled to $z = 0$ using linear perturbation theory) inferred from BORG samples is shown in Figure 6.2.

6.4.2 Mock GW catalogue

We simulate a set of GW events using the BAYESTAR software and apply our inference framework on it. We randomly select galaxies within 100 h^{-1} Mpc from our mock catalogue and assign to each of these galaxies a GW event from a $1.4M_\odot$-$1.4M_\odot$ binary system. The inclination is uniformly sampled for these events. Note that this is not meant to be a realistic representation of the detected binary neutron star events. Rather, this is meant to be a test set for testing our method. To calculate the distances to these sources, we assume a value of Hubble constant, $H_0 = 68$ km s^{-1} Mpc^{-1}. The inclination of the sources are randomly sampled from a uniform distribution. BAYESTAR is then used to infer the distance and the sky localization of each of these events. Only the events with SNR > 12 are retained. We simulate a total of 500 events. For these events, the distances and the sky distribution is inferred using BAYESTAR, yielding us the 3 dimensional volume reconstruction for the GW events. The position is reconstructed under two assumptions: *i)* The only active detectors are the current LIGO + VIRGO detectors. (HLV) *ii)* Along with the current detectors, the LIGO India and KAGRA detectors are also active (HLVIK).

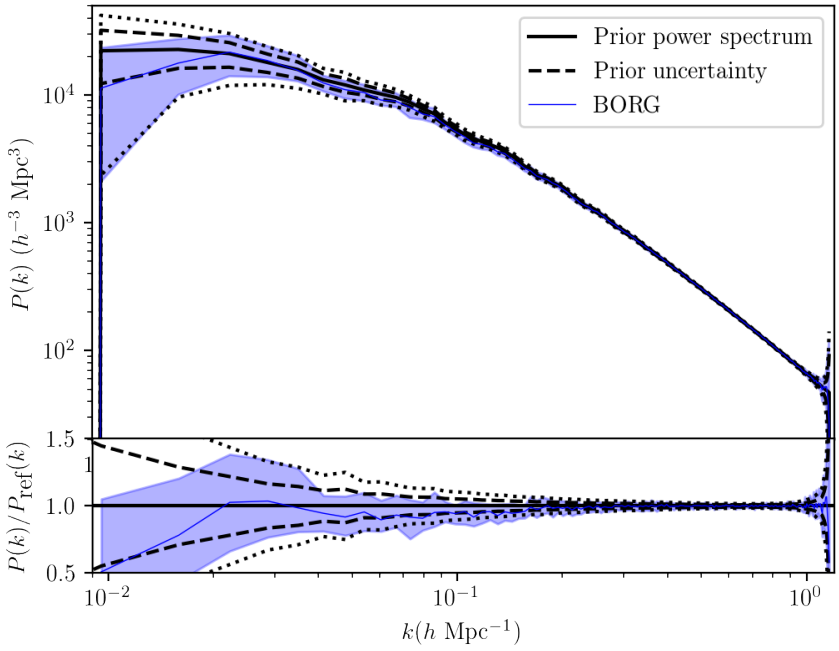

Figure 6.2: Power spectrum of the initial density field scaled to $z = 0$ using linear perturbation theory. The blue solid line shows the mean of all the BORG samples used in the inference. The blue shaded region shows the 2σ uncertainty from the BORG samples. The black solid line is the ΛCDM prediction and the dashed and the dotted lines are the expected 1σ and 2σ uncertainty assuming a Poissonian uncertainty. At large scales, the inferred power is systematically lower than the ΛCDM power spectrum.

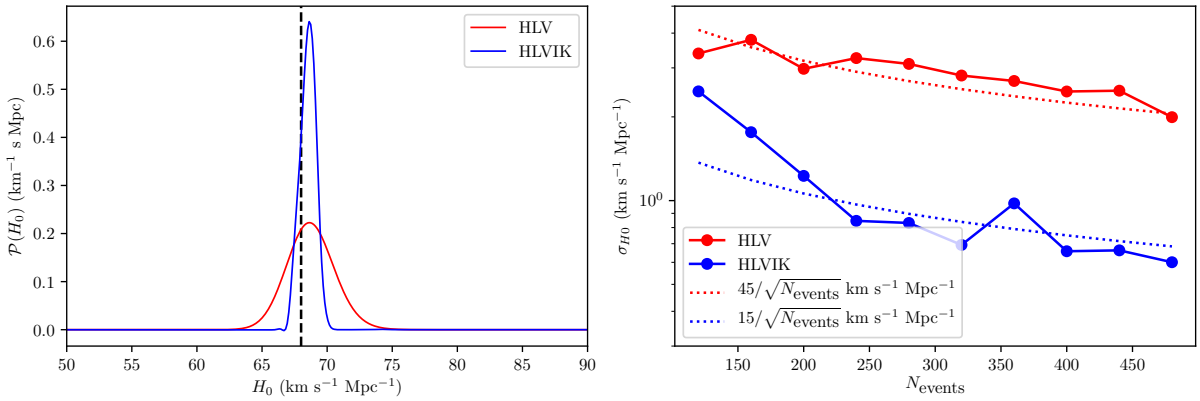

Figure 6.3: Inference of H_0 on the mock data set. *(Left):* The posterior of H_0 with the HLV and the HLVIK data sets. The black vertical line is the true injected value of H_0. As can be seen from the figure, we recover unbiased value of the Hubble constant using our inference framework. *(Right):* The uncertainty on H_0 as a function of number of events for the two configuration. The dotted lines correspond roughly to the asymptotic behaviour of the uncertainty for the two configuration.

6.4.3 H_0 inference

We used our inference framework on both the HLV and the HLVIK data sets and recover unbiased value of the Hubble constant. For the data set of 500 HLV events, we recover a value of $H_0 = 68.75 \pm 1.83$ km s^{-1} Mpc^{-1}. Similarly, for the HLVIK events, we recover a value of $H_0 = 68.53 \pm 0.64$ km s^{-1} Mpc^{-1}. The posteriors from this data sets is shown in Figure 6.3. As can be seen in the right hand panel, for a large number of events, the uncertainty drops roughly in a Poissonian manner, $\sigma_{H0} \propto 1/\sqrt{N_{\rm events}}$.

6.5 GW170817

We also used our framework on the data from the binary neutron star event, GW170817. Although for GW170817, an optical counterpart was detected, we do not use the optical counterpart in our analysis. A similar standard siren measurement of H_0 without assuming the optical counterpart for GW170817 has been performed in Fishbach et al. (2019).

We use the 2M++ galaxy compilation to reconstruct the local density field. See Section 4.3.1 and Lavaux & Hudson (2011b) for further details on the 2M++ catalogue. The BORG

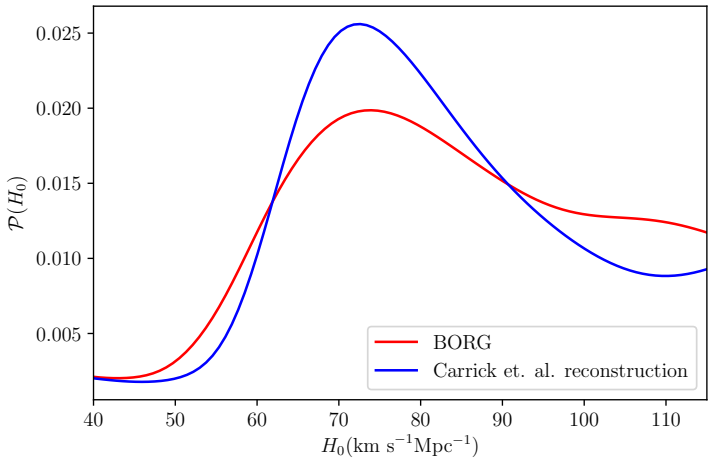

Figure 6.4: H_0 posterior for the BNS event, GW170817. We used our method using two reconstruction methods. The blue curveshows the posterior using the iterative reconstruction of Carrick et al. (2015). The red curve is the posterior obtained by using the BORG reconstruction on the 2M++ catalogue.

reconstruction on the 2M++ catalogue has been discussed in Jasche & Lavaux (2019). In this reconstruction, the structure formation is modelled using 20 steps of the particle-mesh algorithm. The galaxy bias is modelled using equation (6.17). The 2M++ galaxies with absolute magnitude between -21 and -25 are split into 8 sub-samples based on its absolute magnitude. Each bin has an equal width of $\Delta M_K = 0.5$. The galaxies in the 2M++ catalogue with apparent magnitude, $K_{\rm 2M++} < 11.5$ and those with $11.5 < K_{\rm 2M++} < 12.5$ have different selections. Therefore, the galaxies are split into two sets based on these apparent magnitude. By using the inferred bias parameters of (6.17) and the inferred density field, we can compute the inferred galaxy overdensity field for BORG, which can then be used for our analysis.

Although our discussion was focussed on BORG, our method is equally good for any reconstructed density field. Therefore, we also use the reconstruction of Carrick et al. (2015) for inferring H_0. Note that the Carrick et. al. density field is a luminosity-weighted field. The results of inferring H_0 from both these reconstruction schemes are shown in Figure 6.4.

Using a uniform prior of $H_0 \in [40, 120]$ km s^{-1} Mpc^{-1}, for BORG, we obtain a constraint of, $H_0 = 84^{+23}_{-18}$ km s^{-1} Mpc^{-1}. Using the Carrick et. al. reconstruction, we obtain, $H_0 = 82^{+20}_{-14}$ km s^{-1} Mpc^{-1}. Note that, these results are given in the form of median with

the 16-84 percentile as the lower and upper error bar.

6.6 Conclusion

In this chapter, we used our inference framework that relies on the density field reconstructed from a galaxy catalogue to constrain H_0 from dark standard sirens. We used this framework on a test data set to show that our method gives unbiased estimate of H_0. We also applied our method to the data from the binary neutron star event, GW170817 along with two density reconstructions with the 2M++ galaxy redshift catalogue. Our method also consistently corrects for the peculiar velocity, which can introduce large and correlated errors at low redshift in the inference of H_0.

It remains to be seen how our method compares with other statistical methods of inferring H_0, e.g. that of Fishbach et al. (2019). It would also be interesting to see how well our method works on more realistic simulations and on other data sets such as binary black holes. A joint reconstruction of the density field in conjunction to inferring the photometric redshifts is known to improve the estimate of the photometric redshift (Jasche & Wandelt, 2012). Such an analysis will fit in well with our approach for statistically inferring H_0 using GW events at high redshifts. A similar analysis can also be applied for Type Ia supernovae where the host galaxy cannot be uniquely identified. This will be especially applicable for upcoming large scale surveys such as the Vera Rubin Observatory (VRO), which will identify a large number of supernovae.

Chapter 7

Conclusion

In this thesis, we explored a variety of different problems in the theoretical and observations aspects of cosmology.

In Chapters 2 and 3, we investigated the evolution of perturbations in a bouncing scenario for the early Universe. We showed using a toy model that a bouncing scenario can be realized in Cuscuton gravity, without any catastrophic instability in the cosmological perturbations. The inflationary paradigm has been very successful in explaining cosmological observations. Nevertheless, some open questions remain about the theoretical underpinnings of inflationary theory. Over the last couple of decades, temperature anisotropies from the CMB have been used to put tight constraints on models of inflation. In the future, potential detection of polarization of the CMB may shed more light on the physics of inflation. Nevertheless, it remains unlikely that observations alone will be sufficient to solve the problems associated with inflation. Therefore, further theoretical investigation and potentially unique observational signatures of alternate theories of the early Universe will be crucial in putting inflation and its alternatives through the most stringent test.

On the observational front, upcoming surveys of the large-scale structures will be used to study the Universe with an unprecedented detail. As we saw earlier, detailed study of peculiar velocity in the local Universe is important both as a study of growth of structure at low redshifts, and as corrections for the redshifts in other cosmological studies. Upcoming peculiar velocity surveys, such as the TAIPAN, the WALLABY and upcoming supernovae surveys will provide an order-of-magnitude increase in the quantity of peculiar velocity data. In chapter 4, we used a velocity comparison method to constrain the cosmological parameter combination, $f\sigma_8$. With the increase in volume of peculiar velocity data, we expect the statistical error on the growth parameter, $f\sigma_8$, to shrink, thus increasing the im-

portance of different systematic uncertainties. It would therefore be worthwhile to quantify systematic effects in the measurement of the $f\sigma_8$ using the velocity comparison method. Advancements in peculiar velocity analysis methods may also facilitate new insights. For example, one can imagine using the forward-modelled reconstruction scheme, BORG, to study peculiar velocities in the local Universe. A joint forward-modelled reconstruction of density and velocity field could potentially provide the ideal framework to optimally combine the information from the low-redshift galaxy survey and peculiar velocity surveys. Accurate modelling of non-linear structure formation and higher order statistics of the density field may help in yielding tighter constraints on the cosmological parameters. Furthermore, non-linear structure formation can also help break the degeneracy between f and σ_8. Peculiar velocities are also complementary to redshift space distortion measurements from the upcoming galaxy surveys (Kim & Linder, 2020). RSD measurements provide the strongest constraints on $f\sigma_8$ at high redshifts, while peculiar velocity surveys are effective only at low redshifts. Combining the two can provide strong constraints on the growth index, γ, thus providing a stringent test of modified gravity.

In Chapter 5, we studied the impact of different methods for correcting the peculiar velocity. Comparing reconstruction based and kernel smoothing based methods, we showed that reconstruction based methods are best suited for correcting the peculiar velocity in the local Universe. Such corrections are important for a variety of different cosmological studies, including for correcting the redshift in measuring H_0 from standard distance indicators. Given the current tension in the measurement of H_0, it is worth exploring further the systematic effects that peculiar velocities may have in the measurement of H_0 from the local distance measurement.

One potential route in resolving the current tension in H_0 is by measuring its value with new methods. One such promising method is using the distance estimates from gravitational wave standard sirens. In Chapter 6, we introduced a new statistical method to measure H_0 using a reconstruction from galaxy surveys. We showed that our method provides unbiased estimates of H_0. While the constraints from such statistical methods are necessarily weaker than the measurements with optical counterparts, the statistical method likely gives the only way to utilize the distance measurements from binary black hole events. The statistical method may become more important in case we continue to not observe optical counterparts to the gravitational wave events, as has happened after the initial detection of the GW170817 event. It would be worthwhile to understand the advantages and limitations of the statistical method of measuring H_0.

It would be interesting to see how the current tensions in the measured values of H_0 and σ_8 evolve over the next few years. Beyond these tensions, understanding the nature of dark matter and dark energy continue to challenge cosmologists. With the upcoming

cosmological surveys, potentially we will be able to answer some or most of these questions. Further detection of standard siren events will provide independent measurements of H_0, thus potentially being able to adjudicate whether the tension is due to systematic effects or due to new physics. Probes of weak lensing and cluster abundance from upcoming surveys like Vera Rubin Observatory (VRO), Euclid, and WFIRST will be able to constrain the growth of structure with much smaller statistical and systematic uncertainties. Similarly, measurement of RSD from DESI will complement these probes. The massive increase in data volume poses new challenges in terms of the analysis methods to be used. There are many promising developments in this front as well. All things considered, the prospects of new discoveries in cosmology are therefore brighter than ever.

References

Aaronson M., Huchra J., Mould J., Schechter P. L., Tully R. B., 1982, Astrophysical Journal, 258, 64

Abate A., Lahav O., 2008, Mon. Not. Roy. Astron. Soc., 389, L47

Abazajian K. N., et al., 2009, Astrophys. J. Suppl., 182, 543

Abbott B. P., et al., 2017a, Physical Review Letters, 119, 161101

Abbott B. P., et al., 2017b, Nature, 551, 85

Abbott T. M. C., et al., 2018a, Physical Review D, 98, 043526

Abbott T. M. C., et al., 2018b, Mon. Not. Roy. Astron. Soc., 480, 3879

Abbott T. M. C., et al., 2019, Physical Review Letters, 122, 171301

Abbott B. P., et al., 2020, Astrophysical Journal, Letters, 892, L3

Adams C., Blake C., 2017, Mon. Not. Roy. Astron. Soc., 471, 839

Adams C., Blake C., 2020, Mon. Not. Roy. Astron. Soc.,

Adshead P., Blas D., Burgess C. P., Hayman P., Patil S. P., 2016, JCAP, 1611, 009

Afshordi N., 2009, Phys. Rev., D80, 081502

Afshordi N., Chung D. J., Geshnizjani G., 2007a, Phys.Rev., D75, 083513

Afshordi N., Chung D. J., Doran M., Geshnizjani G., 2007b, Phys.Rev., D75, 123509

Afshordi N., Fontanini M., Guariento D. C., 2014, Phys. Rev., D90, 084012

Alam S., et al., 2017, Mon. Not. Roy. Astron. Soc., 470, 2617

Arnowitt R. L., Deser S., Misner C. W., 2008, Gen. Rel. Grav., 40, 1997

Bacon D. J., Refregier A. R., Ellis R. S., 2000, Mon. Not. Roy. Astron. Soc., 318, 625

Bahcall N. A., Fan X., 1998, Astrophysical Journal, 504, 1

Bahcall N. A., Soneira R. M., 1983, Astrophysical Journal, 270, 20

Balbi A., et al., 2000, Astrophysical Journal, Letters, 545, L1

Bardeen J. M., 1980, Phys. Rev., D22, 1882

Bardeen J. M., Steinhardt P. J., Turner M. S., 1983, Phys. Rev., D28, 679

Baumann D., 2011, The Physics of Inflation, https://www.icts.res.in/sites/default/files/baumann_icts_dec2011.pdf

Behroozi P. S., Wechsler R. H., Wu H.-Y., 2013, Astrophysical Journal, 762, 109

Berlind A. A., Narayanan V. K., Weinberg D. H., 2000, Astrophysical Journal, 537, 537

Bernardeau F., Colombi S., Gaztañaga E., Scoccimarro R., 2002, Physics Reports, 367, 1

Bessada D., Kinney W. H., Stojkovic D., Wang J., 2010, Phys. Rev., D81, 043510

Beutler F., et al., 2012, Mon. Not. Roy. Astron. Soc., 423, 3430

Bhattacharyya J., Coates A., Colombo M., Gümrükçüoğlu A. E., Sotiriou T. P., 2018, Physical Review D, 97, 064020

Blakeslee J. P., Lucey J. R., Barris B. J., Hudson M. J., Tonry J. L., 2001, Mon. Not. Roy. Astron. Soc., 327, 1004

Bocquet S., et al., 2019, Astrophysical Journal, 878, 55

Borde A., Guth A. H., Vilenkin A., 2003, Phys. Rev. Lett., 90, 151301

Borgani S., et al., 2001, Astrophysical Journal, 561, 13

Boruah S. S., Kim H. J., Geshnizjani G., 2017, JCAP, 1707, 022

Boruah S. S., Kim H. J., Rouben M., Geshnizjani G., 2018, Journal of Cosmology and Astroparticle Physics, 2018, 031

Boruah S. S., Hudson M. J., Lavaux G., 2019, arXiv e-prints, p. arXiv:1912.09383

Bouchet F. R., Colombi S., Hivon E., Juszkiewicz R., 1995, Astronomy and Astrophysics, 296, 575

Branchini E., et al., 1999, Mon. Not. Roy. Astron. Soc., 308, 1

Brandenberger R. H., 2010, PoS, ICFI2010, 001

Brandenberger R., Feldman H., Mukhanov V., 1994, in Evolution of the Universe and its Observational Quest. pp 19–30 (arXiv:astro-ph/9307016)

Burns C. R., et al., 2018, Astrophysical Journal, 869, 56

Cai Y.-F., Easson D. A., Brandenberger R., 2012, JCAP, 1208, 020

Cai Y.-F., McDonough E., Duplessis F., Brandenberger R. H., 2013, JCAP, 1310, 024

Cai Y., Wan Y., Li H.-G., Qiu T., Piao Y.-S., 2017a, JHEP, 01, 090

Cai Y., Li H.-G., Qiu T., Piao Y.-S., 2017b, Eur. Phys. J., C77, 369

Campbell L. A., et al., 2014, Mon. Not. Roy. Astron. Soc., 443, 1231

Carrasco J. J. M., Hertzberg M. P., Senatore L., 2012, Journal of High Energy Physics, 2012, 82

Carrick J., Turnbull S. J., Lavaux G., Hudson M. J., 2015, Mon. Not. Roy. Astron. Soc., 450, 317

Charnock T., Lavaux G., Wandelt B. D., Sarma Boruah S., Jasche J., Hudson M. J., 2019, arXiv e-prints, p. arXiv:1909.06379

Costanzi M., et al., 2018, arXiv e-prints, p. arXiv:1810.09456

Coughlin M. W., et al., 2020, Physical Review Research, 2, 022006

Creminelli P., Luty M. A., Nicolis A., Senatore L., 2006, JHEP, 12, 080

Creminelli P., Nicolis A., Trincherini E., 2010, JCAP, 1011, 021

Cui W., Liu L., Yang X., Wang Y., Feng L., Springel V., 2008, Astrophysical Journal, 687, 738

D'Amico G., de Rham C., Dubovsky S., Gabadadze G., Pirtskhalava D., Tolley A. J., 2011, Phys. Rev., D84, 124046

DES Collaboration 2020, arXiv e-prints, p. arXiv:2002.11124

DESI Collaboration et al., 2016, arXiv e-prints, p. arXiv:1611.00036

Dark Energy Survey Collaboration 2018, Physical Review D, 98, 043526

Davis M., Nusser A., Masters K. L., Springob C., Huchra J. P., Lemson G., 2011, Mon. Not. Roy. Astron. Soc., 413, 2906

De Bernardis F., et al., 2017, Journal of Cosmology and Astroparticle Physics, 2017, 008

Deffayet C., Pujolas O., Sawicki I., Vikman A., 2010, JCAP, 1010, 026

Dekel A., 1994, Annual Review of Astronomy and Astrophysics, 32, 371

Dekel A., Bertschinger E., Yahil A., Strauss M. A., Davis M., Huchra J. P., 1993, Astrophysical Journal, 412, 1

Desjacques V., Jeong D., Schmidt F., 2018, Physics Reports, 733, 1

Djorgovski S., Davis M., 1987, Astrophysical Journal, 313, 59

Donahue M., Voit G. M., Gioia I., Luppino G., Hughes J. P., Stocke J. T., 1998, Astrophysical Journal, 502, 550

Doré O., et al., 2018, arXiv e-prints, p. arXiv:1804.03628

Dressler A., Lynden-Bell D., Burstein D., Davies R. L., Faber S. M., Terlevich R., Wegner G., 1987, Astrophysical Journal, 313, 42

Dubovsky S., Gregoire T., Nicolis A., Rattazzi R., 2006, JHEP, 03, 025

Dupuy A., Courtois H. M., Kubik B., 2019, Mon. Not. Roy. Astron. Soc., 486, 440

Easson D. A., Sawicki I., Vikman A., 2011, JCAP, 1111, 021

East W. E., Kleban M., Linde A., Senatore L., 2016, Journal of Cosmology and Astroparticle Physics, 2016, 010

Eddington A. S., 1914, Stellar movements and the structure of the universe. London, Macmillan and co., limited, 1914.

Efstathiou G., Sutherland W. J., Maddox S. J., 1990, Nature, 348, 705

Erdogdu P., et al., 2006, Mon. Not. Roy. Astron. Soc., 368, 1515

Erdoğdu P., et al., 2006, Mon. Not. Roy. Astron. Soc., 373, 45

Feeney S. M., Peiris H. V., Williamson A. R., Nissanke S. M., Mortlock D. J., Alsing J., Scolnic D., 2019, Physical Review Letters, 122, 061105

Fertig A., Lehners J.-L., Mallwitz E., 2016, JCAP, 1608, 073

Fishbach M., et al., 2019, The Astrophysical Journal, 871, L13

Fisher K. B., Davis M., Strauss M. A., Yahil A., Huchra J. P., 1994, Mon. Not. Roy. Astron. Soc., 267, 927

Folatelli G., et al., 2010, Astronomical Journal, 139, 120

Foley R. J., et al., 2018, Mon. Not. Roy. Astron. Soc., 475, 193

Foreman-Mackey D., Hogg D. W., Lang D., Goodman J., 2013, Publications of ASP, 125, 306

Freedman W. L., et al., 2019, Astrophysical Journal, 882, 34

Ganeshalingam M., Li W., Filippenko A. V., 2013, Mon. Not. Roy. Astron. Soc., 433, 2240

Garcia K., Quartin M., Siffert B. B., 2019, arXiv e-prints, p. arXiv:1905.00746

Gibbons G. W., Hawking S. W., Siklos S. T. C., eds, 1983, The Very early universe : proceedings of the Nuffield workshop, Cambridge, 21 June to 9 July, 1982

Goodman J., Weare J., 2010, Communications in Applied Mathematics and Computational Science, 5, 65

Gorski K., 1988, Astrophysical Journal, Letters, 332, L7

Graziani R., Courtois H. M., Lavaux G., Hoffman Y., Tully R. B., Copin Y., Pomarède D., 2019, Mon. Not. Roy. Astron. Soc., 488, 5438

Guth A. H., 1981, Physical Review D, 23, 347

Guth A. H., 2007, Journal of Physics A Mathematical General, 40, 6811

Guy J., et al., 2007, Astronomy and Astrophysics, 466, 11

Hamana T., et al., 2019, arXiv e-prints, p. arXiv:1906.06041

Heymans C., et al., 2013, Mon. Not. Roy. Astron. Soc., 432, 2433

Hicken M., Wood-Vasey W. M., Blondin S., Challis P., Jha S., Kelly P. L., Rest A., Kirshner R. P., 2009, Astrophysical Journal, 700, 1097

Hikage C., et al., 2019, Publications of the Astron. Soc. of Japan, 71, 43

Hildebrandt H., et al., 2017, Mon. Not. Roy. Astron. Soc., 465, 1454

Hinshaw G., et al., 2013, Astrophysical Journal, Supplement, 208, 19

Hockney R. W., Eastwood J. W., 1988, Computer simulation using particles. Taylor & Francis, Inc.

Holz D. E., Hughes S. A., 2005, Astrophysical Journal, 629, 15

Hong T., et al., 2014, Mon. Not. Roy. Astron. Soc., 445, 402

Hong T., et al., 2019, Mon. Not. Roy. Astron. Soc., 487, 2061

Horava P., 2009, Phys.Rev., D79, 084008

Howlett C., Davis T. M., 2020, Mon. Not. Roy. Astron. Soc., 492, 3803

Howlett C., Staveley-Smith L., Blake C., 2017, Mon. Not. Roy. Astron. Soc., 464, 2517

Huchra J. P., Geller M. J., 1982, Astrophysical Journal, 257, 423

Hudson M. J., 1994a, Mon. Not. Roy. Astron. Soc., 266, 475

Hudson M. J., 1994b, Mon. Not. Roy. Astron. Soc., 266, 475

Hudson M. J., Turnbull S. J., 2012, Astrophysical Journal, Letters, 751, L30

Hui L., Greene P. B., 2006, Physical Review D, 73, 123526

Huterer D., Shafer D. L., Scolnic D. M., Schmidt F., 2017, Journal of Cosmology and Astroparticle Physics, 2017, 015

Ijjas A., Steinhardt P. J., 2017, Phys. Lett., B764, 289

Ijjas A., Steinhardt P. J., Loeb A., 2013, Physics Letters B, 723, 261

Jain B., Seljak U., 1997, Astrophysical Journal, 484, 560

Jasche J., Lavaux G., 2019, Astronomy and Astrophysics, 625, A64

Jasche J., Wandelt B. D., 2012, Mon. Not. Roy. Astron. Soc., 425, 1042

Jasche J., Wandelt B. D., 2013, Mon. Not. Roy. Astron. Soc., 432, 894

Johnson A., et al., 2014, Mon. Not. Roy. Astron. Soc., 444, 3926

Johnson A., Blake C., Dossett J., Koda J., Parkinson D., Joudaki S., 2016, Mon. Not. Roy. Astron. Soc., 458, 2725

Jones D. H., et al., 2009, Mon. Not. Roy. Astron. Soc., 399, 683

Jones D. O., et al., 2019, Astrophysical Journal, 881, 19

Joudaki S., et al., 2017, Mon. Not. Roy. Astron. Soc., 465, 2033

Joudaki S., et al., 2019, arXiv e-prints, p. arXiv:1906.09262

Juszkiewicz R., Feldman H. A., Fry J. N., Jaffe A. H., 2010, Journal of Cosmology and Astroparticle Physics, 2010, 021

Kaiser N., 1984, Astrophysical Journal, Letters, 284, L9

Kaiser N., 1987, Mon. Not. Roy. Astron. Soc., 227, 1

Kaiser N., Hudson M. J., 2015, Mon. Not. Roy. Astron. Soc., 454, 280

Kaiser N., Efstathiou G., Saunders W., Ellis R., Frenk C., Lawrence A., Rowan-Robinson M., 1991, Mon. Not. Roy. Astron. Soc., 252, 1

Kashyap R., Raman G., Ajith P., 2019, Astrophysical Journal, Letters, 886, L19

Khoury J., Ovrut B. A., Steinhardt P. J., Turok N., 2001, Phys. Rev., D64, 123522

Kim A. G., Linder E. V., 2020, Physical Review D, 101, 023516

Koda J., et al., 2014, Mon. Not. Roy. Astron. Soc., 445, 4267

Kodi Ramanah D., Charnock T., Lavaux G., 2019, Physical Review D, 100, 043515

Koribalski B. S., et al., 2020, arXiv e-prints, p. arXiv:2002.07311

Kourkchi E., Tully R. B., 2017, Astrophysical Journal, 843, 16

Kourkchi E., Tully R. B., Anand G. S., Courtois H. M., Dupuy A., Neill J. D., Rizzi L., Seibert M., 2020, arXiv e-prints, p. arXiv:2004.14499

Krause E., Eifler T., 2017, Mon. Not. Roy. Astron. Soc., 470, 2100

Kravtsov A. V., Berlind A. A., Wechsler R. H., Klypin A. A., Gottlöber S., Allgood B. o., Primack J. R., 2004, Astrophysical Journal, 609, 35

Krisciunas K., et al., 2017, Astronomical Journal, 154, 211

LIGO and Virgo Collaboration 2019, arXiv e-prints, p. arXiv:1908.06060

LSST Science Collaboration 2009, arXiv e-prints, p. arXiv:0912.0201

Laureijs R., et al., 2011, arXiv e-prints, p. arXiv:1110.3193

Lavaux G., 2016, Mon. Not. Roy. Astron. Soc., 457, 172

Lavaux G., Hudson M. J., 2011a, Mon. Not. Roy. Astron. Soc., 416, 2840

Lavaux G., Hudson M. J., 2011b, Mon. Not. Roy. Astron. Soc., 416, 2840

Lavaux G., Tully R. B., Mohayaee R., Colombi S., 2010, Astrophysical Journal, 709, 483

Lewis A., Challinor A., Lasenby A., 2000, Astrophysical Journal, 538, 473

Li W. D., et al., 2000, in Holt S. S., Zhang W. W., eds, American Institute of Physics Conference Series Vol. 522, American Institute of Physics Conference Series. pp 103–106 (arXiv:astro-ph/9912336), doi:10.1063/1.1291702

Lin C., Quintin J., Brandenberger R. H., 2018, JCAP, 1801, 011

Linde A. D., 1982, Physics Letters B, 108, 389

Lynden-Bell D., Faber S. M., Burstein D., Davies R. L., Dressler A., Terlevich R. J., Wegner G., 1988, Astrophysical Journal, 326, 19

Mackay D. J. C., 2003, Information Theory, Inference and Learning Algorithms. Cambridge University Press

Maddox S. J., Efstathiou G., Sutherland W. J., Loveday J., 1990, Mon. Not. Roy. Astron. Soc., 242, 43

Magoulas C., et al., 2012, Mon. Not. Roy. Astron. Soc., 427, 245

Makiya R., Ando S., Komatsu E., 2018, Mon. Not. Roy. Astron. Soc., 480, 3928

Maldacena J. M., 2003, JHEP, 05, 013

Malmquist K. G., 1920, Lund Medd. Ser II, 22

Mandel I., Farr W. M., Gair J. R., 2019, Mon. Not. Roy. Astron. Soc., 486, 1086

Mantz A. B., et al., 2015, Mon. Not. Roy. Astron. Soc., 446, 2205

Marinoni C., Hudson M. J., 2002, Astrophysical Journal, 569, 101

Martin J., Brandenberger R. H., 2001, Phys. Rev., D63, 123501

Martin J., Ringeval C., Trotta R., Vennin V., 2014, Journal of Cosmology and Astroparticle Physics, 2014, 039

Masters K. L., Springob C. M., Haynes M. P., Giovanelli R., 2006, Astrophysical Journal, 653, 861

Masters K. L., Springob C. M., Huchra J. P., 2008, Astronomical Journal, 135, 1738

Mathews G. J., Rose B. M., Garnavich P. M., Yamazaki D. G., Kajino T., 2016, Astrophysical Journal, 827, 60

Mo H., van den Bosch F. C., White S., 2010, Galaxy Formation and Evolution. Cambridge University Press

Mukhanov V., Winitzki S., 2007a, Introduction to Quantum Effects in Gravity. "Cambridge University Press"

Mukhanov V., Winitzki S., 2007b, Introduction to Quantum Effects in Gravity. Cambridge University Press, https://books.google.ca/books?id=vmwHoxf2958C

Mukherjee S., Lavaux G., Bouchet F. R., Jasche J., Wandelt B. D., Nissanke S. M., Leclercq F., Hotokezaka K., 2019, arXiv e-prints, p. arXiv:1909.08627

Neal R., 1993, Technical Report CRG-TR-93-1. Dept. of Computer Science, University of Toronto.

Neal R., 1996, Lecture Notes in Statistics, No. 118. Springer-Verlag

Neal R. M., 2003, Ann. Statist., 31, 705

Neill J. D., Hudson M. J., Conley A., 2007, Astrophysical Journal, Letters, 661, L123

Neyrinck M. C., Aragón-Calvo M. A., Jeong D., Wang X., 2014, Mon. Not. Roy. Astron. Soc., 441, 646

Nicolaou C., Lahav O., Lemos P., Hartley W., Braden J., 2019, arXiv e-prints, p. arXiv:1909.09609

Nissanke S., Holz D. E., Hughes S. A., Dalal N., Sievers J. L., 2010, Astrophysical Journal, 725, 496

Nusser A., 2017, Mon. Not. Roy. Astron. Soc., 470, 445

Nusser A., Davis M., 2011, Astrophysical Journal, 736, 93

Nusser A., Dekel A., 1993, Astrophysical Journal, 405, 437

Ostriker J. P., Steinhardt P. J., 1995, Nature, 377, 600

Palmese A., Kim A. G., 2020, arXiv e-prints, p. arXiv:2005.04325

Peacock J. A., Dodds S. J., 1994, Mon. Not. Roy. Astron. Soc., 267, 1020

Peacock J. A., et al., 2001, Nature, 410, 169

Peebles P. J. E., 1993, Principles of Physical Cosmology. Princeton University Press

Penzias A. A., Wilson R. W., 1965, Astrophysical Journal, 142, 419

Perlmutter S., et al., 1999, Astrophysical Journal, 517, 565

Pesce D. W., et al., 2020, Astrophysical Journal, Letters, 891, L1

Philcox O. H. E., Ivanov M. M., Simonović M., Zaldarriaga M., 2020, Journal of Cosmology and Astroparticle Physics, 2020, 032

Phillips M. M., 1993, Astrophysical Journal, Letters, 413, L105

Pike R. W., Hudson M. J., 2005, Astrophysical Journal, 635, 11

Planck Collaboration 2016, Astronomy and Astrophysics, 594, A24

Planck Collaboration 2018a, arXiv e-prints, p. arXiv:1807.06209

Planck Collaboration 2018b, arXiv e-prints, p. arXiv:1807.06211

Planck Collaboration 2019, arXiv e-prints, p. arXiv:1905.05697

Press W. H., Schechter P., 1974, Astrophysical Journal, 187, 425

Qiu T., Evslin J., Cai Y.-F., Li M., Zhang X., 2011, JCAP, 1110, 036

Radburn-Smith D. J., Lucey J. R., Hudson M. J., 2004, Mon. Not. Roy. Astron. Soc., 355, 1378

Riess A. G., Davis M., Baker J., Kirshner R. P., 1997, Astrophysical Journal, Letters, 488, L1

Riess A. G., et al., 1998, Astronomical Journal, 116, 1009

Riess A. G., et al., 2011, Astrophysical Journal, 730, 119

Riess A. G., et al., 2016, Astrophysical Journal, 826, 56

Riess A. G., Casertano S., Yuan W., Macri L. M., Scolnic D., 2019, Astrophysical Journal, 876, 85

Romano A. E., 2017, Eur. Phys. J., C77, 147

Sanchez A. G., 2020, arXiv e-prints, p. arXiv:2002.07829

Sato K., 1981, Mon. Not. Roy. Astron. Soc., 195, 467

Schmidt F., Cabass G., Jasche J., Lavaux G., 2020, arXiv e-prints, p. arXiv:2004.06707

Schutz B. F., 1986, Nature, 323, 310

Scolnic D. M., et al., 2018, Astrophysical Journal, 859, 101

Scrimgeour M. I., et al., 2016, Mon. Not. Roy. Astron. Soc., 455, 386

Silverstein E., Tong D., 2004, Physical Review D, 70, 103505

Singer L. P., Price L. R., 2016, Physical Review D, 93, 024013

Soares-Santos M., et al., 2019, Astrophysical Journal, Letters, 876, L7

Spergel D. N., et al., 2003, Astrophysical Journal, Supplement, 148, 175

Springel V., 2005, Mon. Not. Roy. Astron. Soc., 364, 1105

Springob C. M., Masters K. L., Haynes M. P., Giovanelli R., Marinoni C., 2007, Astrophysical Journal, Supplement, 172, 599

Springob C. M., et al., 2014, Mon. Not. Roy. Astron. Soc., 445, 2677

Springob C. M., et al., 2016, Mon. Not. Roy. Astron. Soc., 456, 1886

Starobinsky A. A., 1982, Physics Letters B, 117, 175

Strauss M. A., Willick J. A., 1995, Phys. Rep., 261, 271

Tassev S., Zaldarriaga M., Eisenstein D. J., 2013, Journal of Cosmology and Astroparticle Physics, 2013, 036

Tatekawa T., 2013, Progress of Theoretical and Experimental Physics, 2013, 013E03

The LIGO Scientific Collaboration the Virgo Collaboration Abbott B. P., et al., 2019, arXiv e-prints, p. arXiv:1908.06060

Tripp R., 1998, Astronomy and Astrophysics, 331, 815

Trujillo I., et al., 2019, Mon. Not. Roy. Astron. Soc., 486, 1192

Tully R. B., Fisher J. R., 1977, Astronomy and Astrophysics, 500, 105

Tully R. B., Courtois H. M., Sorce J. G., 2016, Astronomical Journal, 152, 50

Turnbull S. J., Hudson M. J., Feldman H. A., Hicken M., Kirshner R. P., Watkins R., 2012, Mon. Not. Roy. Astron. Soc., 420, 447

Van Waerbeke L., et al., 2000, Astronomy and Astrophysics, 358, 30

Veitch J., et al., 2015, Physical Review D, 91, 042003

Verde L., et al., 2002, Mon. Not. Roy. Astron. Soc., 335, 432

Verde L., Treu T., Riess A. G., 2019, Nature Astronomy, 3, 891

Vilenkin A., 1983, Physical Review D, 27, 2848

Wang L., Steinhardt P. J., 1998, The Astrophysical Journal, 508, 483

Wang H., Mo H. J., Yang X., Jing Y. P., Lin W. P., 2014, Astrophysical Journal, 794, 94

Wang Y. Y., Wang F. Y., Zou Y. C., 2018, Physical Review D, 98, 063503

Watkins R., Feldman H. A., Hudson M. J., 2009, Mon. Not. Roy. Astron. Soc., 392, 743

Westover M., 2007, PhD thesis, Harvard University

White S. D. M., Efstathiou G., Frenk C. S., 1993a, Mon. Not. Roy. Astron. Soc., 262, 1023

White S. D. M., Navarro J. F., Evrard A. E., Frenk C. S., 1993b, Nature, 366, 429

Willick J. A., Strauss M. A., 1998, Astrophysical Journal, 507, 64

Wittman D. M., Tyson J. A., Kirkman D., Dell'Antonio I., Bernstein G., 2000, Nature, 405, 143

Wong K. C., et al., 2019, arXiv e-prints, p. arXiv:1907.04869

Yahil A., Strauss M. A., Davis M., Huchra J. P., 1991, Astrophysical Journal, 372, 380

Yuan W., Riess A. G., Macri L. M., Casertano S., Scolnic D. M., 2019, Astrophysical Journal, 886, 61

d'Amico G., Gleyzes J., Kokron N., Markovic K., Senatore L., Zhang P., Beutler F., Gil-Marín H., 2020, Journal of Cosmology and Astroparticle Physics, 2020, 005

da Cunha E., et al., 2017, Publications of the Astron. Soc. of Australia, 34, e047

de Bernardis P., et al., 2000, Nature, 404, 955

de Jaeger T., Stahl B. E., Zheng W., Filippenko A. V., Riess A. G., Galbany L., 2020, arXiv e-prints, p. arXiv:2006.03412

de Rham C., Melville S., 2017, Phys. Rev., D95, 123523

de Rham C., Motohashi H., 2017, Physical Review D, 95, 064008

van Dokkum P., et al., 2018, Nature, 555, 629

APPENDICES

Appendix A

Detailed derivation of second order action for Cuscuton perturbation

In this appendix, we present some of the intermediate steps of our derivation in section 2.3. After fixing the gauge, we perturb different parts of the action (2.16) to second order in perturbative variables, N_1, ψ, ζ and $\delta\varphi$. We then remove N_1 and ψ using the constraint equations (2.26a) and (2.26b). The result after taking into account the background equations, (2.7a), (2.7b) and (2.11) is

$$\begin{aligned} S^{(2)}_{\rm EH} &= \int d\tau d^3x\, a^2 \left\{ \left[\frac{3\epsilon}{2} - 9\right](\zeta\mathcal{H})^2 - \epsilon(\partial\zeta)^2 + \mu^2 a\delta\varphi \left[\alpha\zeta' - \frac{9}{2}\zeta\mathcal{H}\right] \right. \\ &\qquad \left. -(\mu^2 a\delta\varphi)^2 \left[\frac{\alpha}{2} + \frac{3}{4}\right] \right\} \qquad \text{(A.1)} \\ S^{(2)}_{\varphi} &= \int d\tau d^3x\, a^2 \left\{ \left[6(\alpha-\epsilon) + \left[\frac{3Va^2}{\mathcal{H}^2}\right]\left(1+\frac{\epsilon}{2}\right)\right](\zeta\mathcal{H})^2 + \mu^2 a\delta\varphi \left[\frac{3a^2V}{2\mathcal{H}^2}(\zeta\mathcal{H}) \right. \right. \\ &\qquad \left. \left. -\frac{1}{2}\alpha\zeta' + \frac{\partial^2\zeta}{2\mathcal{H}}\right] + (\mu^2 a\delta\varphi)^2\left(\frac{\alpha}{4}+\frac{3}{4}\right) \right\} \qquad \text{(A.2)} \\ S^{(2)}_{\pi} &= \int d\tau d^3x\, a^2 \left\{ \alpha\zeta'^2 + \left[\left(9 - 6\alpha + \frac{9\epsilon}{2}\right) - \frac{3Va^2}{\mathcal{H}^2}\left(1+\frac{\epsilon}{2}\right)\right](\zeta\mathcal{H})^2 \right. \\ &\qquad \left. +\mu^2 a\delta\varphi\left[\left(\frac{9}{2} - \frac{3a^2V}{2\mathcal{H}^2}\right)\zeta\mathcal{H} - \alpha\zeta'\right] + \frac{1}{4}(\mu^2 a\delta\varphi)^2 \right\} \qquad \text{(A.3)} \end{aligned}$$

Combining these expressions we obtain the expression 2.27,

$$S^{(2)} = \int d\tau d^3x\, a^2 \left[\alpha\zeta'^2 - \epsilon(\partial\zeta)^2 + \sigma\left(\frac{\mathcal{H}\delta\varphi}{\varphi_0'}\right)\left(\alpha\mathcal{H}\zeta' - \partial^2\zeta\right)\right] . \tag{A.4}$$

We then proceeded to eliminate $\delta\varphi$ from above action while continuing our derivation in Fourier space. We substituted for $\delta\varphi_k$ in terms of ζ_k and ζ_k' using equation (2.30) and obtained

$$\begin{aligned}
S^{(2)} &= \int d^4x a^2 \big[\alpha\zeta_k'^2 - \epsilon(\partial\zeta_k)^2 + \sigma\frac{(\mathbf{k}^2\zeta_k + \alpha\mathcal{H}\zeta_k')^2}{\mathbf{k}^2 + \alpha(3-\sigma)\mathcal{H}^2}\big] \\
&= \int d^4x a^2\alpha\Bigg[\left(\frac{\mathbf{k}^2 + 3\alpha\mathcal{H}^2}{\mathbf{k}^2 + \alpha(3-\sigma)\mathcal{H}^2}\right)\zeta_k'^2 - \mathbf{k}^2\left(\frac{\mathbf{k}^2 + (3-\sigma)\epsilon\mathcal{H}^2}{\mathbf{k}^2 + (3-\sigma)\alpha\mathcal{H}^2}\right)\zeta_k^2 \\
&+ \left(\frac{2\mathbf{k}^2\sigma\mathcal{H}}{\mathbf{k}^2 + (3-\sigma)\alpha\mathcal{H}^2}\right)\zeta_k\zeta_k'\Bigg] \\
&= \int d^4x a^2\Bigg[\alpha\left(\frac{\mathbf{k}^2 + 3\alpha\mathcal{H}^2}{\mathbf{k}^2 + \alpha(3-\sigma)\mathcal{H}^2}\right)\zeta_k'^2 - \alpha\mathbf{k}^2\left(\frac{\mathbf{k}^2 + (3-\sigma)\epsilon\mathcal{H}^2}{\mathbf{k}^2 + (3-\sigma)\alpha\mathcal{H}^2}\right)\zeta_k^2 \\
&+ \frac{\mathbf{k}^2}{a^2}\left(\frac{\alpha a^2\sigma\mathcal{H}}{\mathbf{k}^2 + \alpha(3-\sigma)\mathcal{H}^2}\right)'\zeta_k^2\Bigg],
\end{aligned} \tag{A.5}$$

where in the last step we applied integration by parts. After performing the algebraic evaluation of these term and introducing the second slow roll parameters η and β as

$$\eta \equiv \frac{\epsilon'}{\mathcal{H}\epsilon} \tag{A.6}$$

$$\beta \equiv \frac{\alpha'}{\mathcal{H}\alpha} \tag{A.7}$$

we finally get

$$S^{(2)} = \int d^4x a^2\alpha\left[\left(\frac{\mathbf{k}^2 + 3\alpha\mathcal{H}^2}{\mathbf{k}^2 + \alpha\mathcal{H}^2(3-\sigma)}\right)\zeta_k'^2 - \left(\frac{\mathbf{k}^4 + \mathbf{k}^2\mathcal{H}^2\mathcal{B}_1 + \mathcal{H}^4\mathcal{B}_2}{[\mathbf{k}^2 + \alpha\mathcal{H}^2(3-\sigma)]^2}\right)\mathbf{k}^2\zeta_k^2\right], \tag{A.8}$$

where $\mathcal{B}_1$ and $\mathcal{B}_2$ are given by relations

$$\mathcal{B}_1 = 6\alpha + \sigma(\eta + 6 + \beta - 2\sigma - 3\alpha) + \alpha(\eta - \beta) \tag{A.9}$$

$$\mathcal{B}_2 = 9\alpha^2 - \sigma\alpha(3\alpha + 4\sigma - 3(4+\eta)) + 3\alpha^2(\eta - \beta). \tag{A.10}$$

After identifying the coefficient of the kinetic and the gradient terms as z^2 and $z^2c_s^2$, the final action can be presented as (2.31).